FUNDAMENTAL STUDIES OF AEROSOL COMBUSTION

by
Frank Atzler
Diplom Ingenieur (FH)

Submitted in accordance with the requirements for the degree of
Doctor of Philosophy

University of Leeds
School of Mechanical Engineering

February 1999

The candidate confirms that the work submitted is his own and that appropriate credit has been given where reference was made to the work of others

ABSTRACT

The combustion of clouds of fuel droplets is of great importance in many industrial applications, such as gasoline and diesel engines, gas turbines and furnaces. Here, efficient combustion has to be combined with minimum noxious emissions. Aerosols also might produce a particularly hazardous explosion risk.

To optimise their performance a fundamental understanding of the complex processes in aerosol combustion systems is necessary. A fundamental study of aerosol combustion has been conducted to quantify the parameters of importance. For this, a novel aerosol combustion apparatus was developed, that offers a well controlled environment with respect to aerosol properties, temperature, pressure and turbulence. Aerosols were generated using the Wilson cloud chamber principle of expansion cooling, which produces a homogeneously distributed, near monodisperse droplets cloud.

Drop sizes of 10 to 30μm, pressures between 100 and 360kPa and temperatures of 263 to 292K were used. Laminar mixtures between the overall equivalence ratios of 0.8 and 1.2 were studied. A considerable burning velocity enhancement of up to 420% was observed. This enhancement was shown to be a function of drop size and liquid fraction.

From the study, it was concluded that burning velocity enhancement probably is caused by the increase in surface area due to wrinkling, caused by the development of instabilities. At low temperature (<275K) the formation and destruction of wrinkles and cells was random. At higher temperatures (>290K) cell formation and division was progressive and traceable, like that observed in gaseous flames. Cellular acceleration at these temperatures was similar to that of gaseous flames. Stretch appeared to have a damping effect on the instabilities, caused by the aerosol.

Oscillating flames were observed for some experimental conditions and these also showed enhanced flame speeds. These oscillations were possibly caused by aerodynamic interaction between droplets and gas motion ahead of the flame. Also Stretch and radiation probably influenced these oscillations.

Inert glass particles in a gaseous fuel-air mixture had no effect on flame speed or structure. However, water aerosols caused significant burning velocity enhancement (50%). These findings contradict the hypotheses that fuel rich pockets, flame propagation through "easy-to-burn" regions or a "grid-effect" trigger instabilities in aerosols.

Comparison with a linear stability analysis of heat loss from the flame (Greenberg et al., 1998), yielded good qualitative agreement with the data of the present work.

ACKNOWLEDGEMENTS

Although the candidate confirms that this thesis is his own work and nothing but, he still needed advice, motivation and friendship, not to drown in a sea of despair or be overwhelmed by a mountain of work. Therefore, I wish to thank all those, who kept up my spirits and lent me a hand, once in a while, with official and "governmental" work. The list is by no means comprehensive, is in no particular order and I apologise to everybody who feels neglected.

My wife Barbara
Mum (not only because she shelled out so much cash)
Dad (who always was so fond of my plans.... "Get a job, son !")
Prof. C.G.W. Sheppard
Dr. Malcolm Lawes (for reading my endless stream of good quality thesis material)
Prof. Derek Bradley (for the "Kumagai-Idea")
Prof. Barry Greenberg, Faculty of Aerospace Engineering, Institute of Technology, Haifa, Israel
Barry Robertson, Non-Nuclear Energies Panel of the European Commission,
for all his help and efforts to obtain financial support for this project
Prof. Alan Williams and John Taylor, Dept. of Fuel & Energy, for the loan of their Malvern 2600
Steven Ward-Smith and Stephanie Somerset of Malvern Instruments
for the loan of a Mastersizer S and their endless patience.
Bob & Helen Hicks
Rob Woolley & Angela Hepworth
Dave & Jill Barrell
Mark Drake
François-Xavier Demoulin, Université de Provence, Marseille
Rick "Norton" Roper
Prof. J. Griffiths, School of Chemistry
John Groves, Mark Batchelor, Brian Leach, Jonathan Stevenson
Peter Lawes & Lads, (incl. Stuart, who is long gone)
Stan "Grumpy" Cail (who ALWAYS helps, as long as you put up with "a" comment) & Company
Christine, Jay, Pam, Pat, Heather and all other clerical staff, ...very helpful bunch......
Lynne, Glen, Adam, Alasdair, Jim, Big Ade, Marco and all the other colleagues many pints later,.....
and of course those who did not drink, Nazim, Dinçer, Made, Kazem
and last, but not least: Paul Banks, Luciano Bellon, Alan Heald, Robert Guest, Dave Hawkridge,

and Malc's friend Fred Bloggs

CONTENTS

NOMENCLATURE

A	m^2, mm^2	Area
B		Mass transfer number
c	$J\,kg^{-1}K^{-1}$	Heat capacity of a solid
C	m^3/m^3	Liquid volume concentration
$\overline{C}$		Evaporation coefficient
c_p	$J\,kg^{-1}K^{-1}$	Specific heat (at constant pressure)
d	m, mm, µm	Diameter
D	µm	Drop diameter
D_{30}	µm	Mass mean diameter
D_{32}	µm	Sauter mean diameter
$D_{V0.5}$	µm	Volume median diameter
F		Dynamic factor (for Supersaturation)
f	Hz, kHz	Frequency
f	mm	Focal length
G		Group combustion number
h	$W\,m^{-2}\,K^{-1}$	Heat transfer coefficient
k	$W\,m^{-1}\,K^{-1}$	Thermal conductivity
k, k_{cr}		(dimensionless Perturbation-) Wave number, Critical wave number,
l	µm	Drop spacing, Drop centre distance
l	m	Length
L_b		Markstein length
Le		Lewis number
M	kg/kmol, kg/mol	Molecular weight
M		Magnification
n	min^{-1}	Rotational speed
n, n_a, n_f		Number of moles, of air, of fuel
N		Number density of droplets
N_T		Total number of drops in a cluster
p	Pa, kPa, MPa	Pressure
p_1	Pa, kPa, MPa	Pre-expansion pressure

p_2	Pa, kPa, MPa	Pressure during expansion
p_v	Pa, kPa, MPa	Vapour pressure
p_p, p_a, p_f	Pa, kPa, MPa	Partial pressure, of air, of fuel
Q	J	Heat of combustion
r	µm, mm, m,	Radius, Flame radius
R_c	mm	Cloud radius
Re		Reynolds number
R	kJ $kg^{-1}K^{-1}$	Universal gas constant
S		Density factor
S, S_{cr}		(Degree of) Supersaturation, Critical supersaturation
Sc		Schmidt number
S_n	m/s	Normal (stretched) flame speed
S_s	m/s	Unstretched flame speed
S_a	m/s	Aerosol flame speed
t	s, ms	Time
T	K, °C	temperature
T_∞	K, °C	Farfield temperature
T_1	K, °C	Pre-expansion temperature, Temperature at time step 1
T_2	K, °C	Temperature during expansion, Temperature at time step 2
T_f	K, °C	Fluid temperature
T_s	K, °C	Surface temperature
t_0	s	Time constant, Characteristic time
u'	m/s	Turbulence velocity
u_a	m/s	Aerosol burning velocity
u_g	m/s	Gas velocity
u_n	m/s	Laminar burning velocity
u_{nr}	m/s	Burning velocity, based on the appearance of burnt gas
u_x, u_y	m/s	Velocity in x-, y-direction
V	m^3, ml, cm^3	Volume
x_0	mm	Characteristic length
Z		Compressibility factor

Greek Symbols

α	s^{-1}, ms^{-1}	Stretch
α		Accommodation coefficient
γ		Ratio of specific heat capacities
δ_l	m	Flame thickness
δt	s	Time step
δ		Drop loading
ϕ		Equivalence ratio
ϕ_{eff}		Effective equivalence ratio
ϕ_g		Gaseous equivalence ratio
ϕ_l		Liquid equivalence ratio
ϕ_{ov}		Overall equivalence ratio
λ		Evaporation constant
λ	nm	Wave length
Ω		(Perturbation-) Growth parameter
ρ	kg m^{-3}	Density
ρ_b	kg m^{-3}	Burnt gas density
ρ_u	kg m^{-3}	Unburnt gas density

Subscripts

g	Gas
l	Liquid
f	(liquid) Fuel
s	at saturation conditions

Abbreviations

ADC, A/D		Analogue to digital converter
BS		British standard
BSP		British standard pitch
D.I		Direct injection (Diesel)
FDV		Fill & discharge valve
GDI		Gasoline direct injection
PC		Personal computer
PDA, PDV		Phase Doppler anemometry, velocimetry
PIV		Particle image velocimetry
PTS		Principal trigger switch
r.m.s.		Root mean square
S.I.		Spark ignition
SMD	μm	Sauter mean diameter
TTL		Transistor logic

1. INTRODUCTION

1.1 GENERAL INTRODUCTION

The need to improve fuel economy and to reduce emissions have been major drivers for combustion research in the last 3 decades. Although the levels of emissions from individual engines have decreased drastically as a result, this was counteracted by the ever increasing energy demand and a continuously rising number of vehicles on the roads. The European Programme of Emissions, Fuels and Engine Technologies (EPEFE, 1997) investigated possible reductions in road traffic emissions that can be achieved by combining vehicle and engine technologies with advanced fuels. It was concluded that "new measures, derived from scientifically sound data, may be required to meet air quality objectives in the most cost effective way" and "these measures form the basis for the next step in emission legislation for the year 2000".

The concept of lean combustion in piston engines is one method to achieve a reduction in CO and NO emissions as well as in fuel consumption (Fujimoto et al., 1995). However, for spark ignition engines, in which the charge is fully premixed, an inherent disadvantage of this concept is the slow and sometimes unstable combustion of the highly diluted charge (Heywood, 1988). This can be avoided using stratification of the in-cylinder charge, although this does not offer the same reductions in CO and NO in S.I. engines. Diesel and the gasoline direct injection (GDI) engines are inherently suitable for charge stratification, particularly since the advent of electronic control of high pressure injection equipment. The combination of good atomisation from high pressure injection systems and complete flexibility of injection timing offers a wide variety of controls over the combustion event (Su et al., 1995).

In addition to pollution from road transport, emissions from aircraft gas turbines are a major cause for concern. Much research has been invested in aviation gas turbines and present aero-engines operate at much higher combustion efficiencies than are commonly found in reciprocating engines. Further improvements may come from the use of staged combustion systems which allow optimisation of the combustion process for different engine conditions (Brundish et al., 1997). However, a major area for concern is that of altitude relight. As engine operation is pushed to extremes, the risk of flame blow off is increased. In addition the low pressures and temperatures experienced at these conditions offer the most difficult environment for re-ignition. Following spark ignition the flame must develop initially at low pressure and temperature, until the flame is fully established. Only then are normal operating conditions achieved. The present work investigates the combustion of aerosols at conditions pertaining in the early stages of flame development following flame-out and re-ignition (Tian-Yu et al., 1981).

There is also a concern that aerosols might produce a particularly hazardous explosion risk. This is not only due to the much lower limits of flammability of aerosols relative to that of gaseous flames (Hayashi et al., 1981), but also because of an apparently much quicker propagation of the flame (Aslanov et al., 1991).

A fundamental understanding of the combustion process in aerosols is required to optimise the performance of spray combustion systems and to minimise explosion hazards. However, studies in practical systems are unsuitable for this purpose, due to the multiplicity of dependent parameters. The flame propagation rate in the two-phase-environment must be analysed in isolation from the complex processes of fuel injection, distribution and mixing, often within a turbulent flow field. The interaction of those processes does, at present, not allow for adequate mathematical modelling. A fundamental study of droplet cloud combustion is required to investigate and quantify the parameters of importance.

1.2 THESIS OUTLINE

An important pre-requisite for the study of aerosols is an understanding of the experimental concepts and theoretical descriptions of gaseous combustion. Those concepts important for the present work are presented in Chapter 2. Although fundamental data on the burning rate of aerosols is scarce, relative to the wealth of data available on gaseous combustion, there have been a number of important studies and these also are reviewed in Chapter 2. Of particular interest are the works of Burgoyne and Cohen (1954), who used the Sinclair-LaMer method of controlled condensation to conduct one of the first systematic studies of aerosol combustion, and those of Hayashi and Kumagai (1974 & 1976), which, in part, inspired the present work. Due to the formidable complications involved in the experimental study of aerosols, most of the experimental results of earlier works are apparatus specific and are related to experimental conditions that varied vastly between different workers. Therefore, a quantitative comparison of the results of these works is a difficult undertaking. However, these experiments revealed important details of the phenomena governing aerosols combustion and provided qualitative trends of the combustion behaviour of aerosols.

In order to obtain experimental data of a more general applicability, a combustion apparatus was developed by the present author, that allows the generation and combustion of aerosols under well controlled conditions in terms of liquid and gaseous fractions of the fuel, drop size, pressure, temperature and turbulence. This is introduced in Chapter 3. The Wilson cloud chamber method of expansion-cooling is used, to produce aerosols with a homogeneous spatial droplet distribution and drop size. This method was first used for combustion studies in a 1 litre combustion chamber by Hayashi and Kumagai (1974 & 1976). However, its use in the present much larger combustion bomb provides a longer observation period than that of previously used vessels. This is important, because the development of instabilities in flames is a function of propagation distance (and time). The bomb has two 150mm diameter main windows, which were used for flame photography, mainly with the schlieren technique. Laser sheet imaging also was employed to obtain cross sectional images of the developing flame. The vessel is equipped with four fans, driven by electronically controlled motors, which allow combustion experiments to be conducted in a precisely controlled turbulent environment. Although the emphasis of the present work was on laminar combustion, a number of turbulent aerosol experiments also have been conducted.

The aerosols generated in the bomb under laminar and turbulent conditions were characterised using Malvern laser diffraction instruments to measure droplet size and concentration of liquid fuel during the process of expansion cooling. Simultaneously, temperature and pressure were recorded and used as a basis to calculate aerosol properties. The results are presented in Chapter 4.

Results from the combustion studies are presented and discussed in Chapter 5. Most measurements utilised iso-octane-air aerosols, because for this fuel, there is a wide range of existing data available for its gaseous combustion, and these were used for comparison with the results of the present work. The effect of several parameters on the combustion of aerosol was investigated. These include the overall, gaseous and liquid equivalence ratios, droplet size, mixture pressure and temperature. Also, the effect of the presence of droplets on the flame surface was examined, using flame photographs. The importance of flame stretch was assessed, applying the analysis developed for gaseous combustion, and the method of obtaining flame speeds and burning velocities from plots of flame speed against stretch was used to produce these parameters for aerosol flames. For some experimental conditions oscillating flames were observed and several potential causes for this are discussed in Chapter 5.

A number of additional experiments were conducted to elucidate the mechanisms that trigger instabilities in aerosols. These include the combustion of mixtures containing spherical inert particles and, alternatively, water aerosols. Qualitative comparisons are drawn between the experimental results of the present work and a mathematical model (Greenberg et al., 1998 & 1999, to be published), which investigates heat loss from the flame as a source for instability in aerosols.

Chapter 6 summarises the findings of the present study and gives recommendations for future work.

2. BURNING VELOCITY AND FLAME SPEED IN DROPLET-VAPOUR-AIR MIXTURES

A necessary precursor to the understanding of droplet combustion is to understand that of gaseous combustion. There is a wealth of data on the burning rate of homogeneous mixtures, although it is often inconsistent. Early work has been reviewed by Andrews (1972) and James (1987). Fundamental data on the burning rate of aerosols is more scarce. Several workers, Ballal et al. (1981), Nakabe et al. (1988) and Richards et al. (1989), suggested that this is due to the more complex nature of droplet combustion and the resulting increase in the difficulties of experimental work. Nevertheless a significant number of fundamental works have been conducted, which are reviewed in this chapter. Much more work has been undertaken on the combustion of aerosols in specific applications, such as diesel engines and gas turbines. These include the works of Arold et al. (1990), Stroia & Abata (1991) and Edwards et al. (1992). However, the exploration of fundamental parameters in practical combustion systems is difficult due to the multiplicity of dependent variables.

In Section 2.1 a brief review of the burning rate of homogeneous mixtures is presented, since this forms the foundation for the present study. This includes the phenomenon of flame instability in gaseous flames, since instabilities in aerosol flames may be triggered by the same mechanism. In Section 2.2 an overview of the different approaches to aerosol combustion is given. Section 2.3 presents combustion regimes and flame structures, encountered in aerosol flames. A number of fundamental studies are reviewed in Section 2.4 with regard to mixture parameters and their effect on the rate of combustion. A particular detail addressed in the present work is the effect of the presence of droplets on burning velocity. There is some evidence, that droplets can increase the burning rate relative to that of a homogeneous mixture, but the definition of the reference conditions varies considerably and so do the phenomenological explanations. The observation or failure to observe this effect, may be related to turbulence, present in a particular apparatus, and this is discussed in Section 2.5.

2.1 HOMOGENEOUS COMBUSTION

2.1.1 PREVIOUS WORK

The understanding of gaseous combustion is a necessary prerequisite for the investigation of the combustion of heterogeneous systems since many theoretical descriptions and most experimental methods are used for both. There are several techniques for measuring flame speeds and the laminar burning velocity, which have been critically reviewed by Andrews (1972b) and Bradley et al. (1998).

Due to their ease of use, stationary flames in ducts and on burners have been used frequently to obtain flame speeds and burning velocities. However, these flames are often distorted and subjected to turbulence, which causes variations in propagation velocity over the cross section and the length of the flame. Other problems include the divergence of the flow at the burner exit and the drag of the burnt gas on the confining walls of ducts. Also, the evaluation of the flame area or representative flame angle often is problematic. This is because different optical techniques, including direct photography, schlieren, shadowgraphs and laser induced fluorescence yielded significantly different reference surfaces and this lead to different results (Nakabe et al., 1988). Propagating flames observed in tubes suffer from aerodynamic drag and wall quenching effects as well as the occurrence of pressure waves, all of these being a function of vessel dimensions. These effects can be avoided by studying outwardly growing flames in bombs, which make it possible to obtain burning rates at a range of pressures. However, any increase in pressure can trigger the onset of flame instabilities, which can alter the propagation velocity of the flame significantly. Additionally the change of flame thickness with pressure affects the mean burnt gas density as well as the distance of the optical reference surface, used in some measurement techniques, from the reaction zone. Transient pressure effects can be avoided by taking measurements only in the pre-pressure rise period (Bradley et al., 1996). This method will be presented in Section 2.1.2 . Because the laminar burning velocity depends upon the flame stretch rate, the former should not be measured without reference to the latter, preferably at the same reference surface. Andrews et al. (1972) and Bradley et al. (1996) found that failure to account for the effects of stretch was the most probable explanation for the large spread in burning velocity data from various sources, including those for iso-octane (James, 1987, Bradley, 1990).

2.1.2 MEASUREMENT OF LAMINAR BURNING VELOCITY, FLAME STRETCH AND MARKSTEIN LENGTHS

Many of the above mentioned difficulties in the determination of laminar burning rates are avoided by the use of spherically expanding flames to measure flame speeds, defined by *dr/dt*, in the pre-pressure regime. A spherically propagating explosion flame is well suited for measurement purposes, as the flame stretch is uniform and unambiguously defined (Bradley et al., 1996, Dixon-Lewis, 1990, Dowdy et al., 1990). The flame speed is found directly from measurements of flame radius at different times by schlieren cine photography. Provided there is no significant increase in pressure, no other measurement is required. Observation of the flame surface, necessary for the flame propagation measurements, has the further advantage of revealing the onset of instabilities, first as flame cracking then as a developed cellular structure (Bradley & Harper, 1994). In general the published data for burning velocities above atmospheric pressure have been deduced from pressure measurements during explosions in bombs, with no visual observation of the flame (Bradley et al., 1998). In consequence, the effects of any flame distortion and developing flame cellularity, which can enhance the burning rate, have been masked. In addition, pressure measurements tend to record the rate of burning rather than the rate of propagation of the flame into cold mixture. An important observation by Bradley et al. was, that for many mixtures, a cellular flame structure develops during flame propagation as the flame stretch rate is reduced. When the flame surface becomes completely cellular, there is an increase in flame speed and this continues as the flame propagates. It is suggested by the present author, that these instabilities and the phenomenon of flame acceleration are related to those observed in aerosol flames. This is discussed in Chapter 5.

The flame speed, S_n, for a spherical outwardly propagating flame is given by

$$S_n = u_g + u_n \tag{2.1}$$

where u_n is the stretched laminar burning velocity based on the propagation of the flame front and u_g the gas velocity due to the flame expansion, and

$$S_n = \frac{dr}{dt} \tag{2.2}$$

where r represents the flame radius and is more precisely defined as the isotherm that is 5K above the temperature of the reactants. S_n is related to u_n by

$$S_n = \frac{u_n \rho_u}{S \rho_b} \tag{2.3}$$

Here ρ_u is the density of the unburned and ρ_b that of the burned gas at the adiabatic temperature. S is a generalised function that depends upon the flame radius and the density ratio, and accounts for the effect of the flame thickness on the mean density of the burned gases. Bradley et al. (1996) computed a generalised expression for S from modelled methane air flames at 100 kPa over a range of equivalence ratios. The generalised expression is

$$S = 1+1.2\left[\frac{\delta_l}{r}\left(\frac{\rho_u}{\rho_b}\right)^{2.2}\right]-0.15\left[\frac{\delta_l}{r}\left(\frac{\rho_u}{\rho_b}\right)^{2.2}\right]^2 \tag{2.4}$$

where δ_l is the laminar flame thickness, given by

$$\delta_l = \nu / u_l \tag{2.5}$$

Here ν is the kinematic viscosity of the unburnt gas and u_l is the unstretched laminar burning velocity. They did not compute a value for iso-octane-air flames, used in the present work, but they suggested it would be unlikely to be significantly different. Computations for propane-air mixtures suggested that this expression is correct to 10 % for a range of paraffinic fuel conditions. Values of the u_l are based on the extrapolation of S_n to the value of zero stretch and are not sensitive to the value of S.

Because of the finite flame thickness the situation is further complicated by the existence of two possible definitions of burning velocity, each legitimate and of practical significance. The first already derived, u_n, is based on the rate of disappearance of cold, unburned gas, the second, u_{nr}, on the rate of appearance of burned gas. At smaller radii the flame thickness effect is important, but it is less so at larger radii. As the radius tends to infinity, both u_n and u_{nr} tend towards u_l. Differences between these two burning velocities probably are significant for aerosol flames, because of their greater thickness. Because u_{nr} governs the pressure development in engines and, probably, the quenching of turbulent flamelets it is the more pertinent in such contexts. Bradley et al. (1996) expressed it as

$$u_{nr} = \frac{\rho_b}{\rho_b - \rho_u}\left(u_n - S_n\right) \tag{2.6}$$

A burned gas Markstein length (Clavin, 1985) expresses the influence of stretch on the flame speed by

$$S_s - S_n = L_b\alpha \qquad (2.7)$$

where S_s is the unstretched flame speed. For a spherically expanding flame the total stretch rate is defined by

$$\alpha = \frac{1}{A}\frac{dA}{dt} = \frac{2}{r}\frac{dr}{dt} = \frac{2}{r}S_n \qquad (2.8)$$

When $r \rightarrow \infty$, $\alpha \rightarrow 0$ and $S_n \rightarrow S_s$. This yields S_s as the intercept value of S_n at $\alpha = 0$. The gradient of the best straight line fit to the experimental data gives L_b. The unstretched laminar burning velocity is deduced from S_s since, for constant pressure flame propagation, u_l and S_s are related by:

$$u_l = S_s\frac{\rho_b}{\rho_u} \qquad (2.9)$$

2.1.3 FLAME INSTABILITY

Flame instability plays an important role for the investigation of gaseous combustion. The mechanisms of hydrodynamic and thermo-diffusive instability, and their interaction with flame stretch are likely to be important also in aerosol flames. Therefore, a brief review of the analysis of flame instability is presented here.

The mathematical analysis of flame instability for gaseous laminar mixtures is well established (Shivashinsky, 1977, Bradley and Harper, 1994, Ashurst, 1997, Bradley et al., 1998). A gaseous flame advancing into unburnt gas is inherently unstable. This was shown by Darrieus (1938) and Landau (1944). When the unburnt gas moves into the crest of a flame front it diverges and this increases the pressure (Bradley, in preparation). The opposite occurs at the trough of the flame front, and pressure decreases. This system is fundamentally unstable, because it aggravates wrinkling of the flame front, and, with the increased heat release due to the enlarged surface aera, the burning velocity increases. However, thermo-diffusive effects can either reduce or reinforce hydrodynamic instabilities (Bradley & Harper, 1994) and so does flame stretch.

Bradley et al. (1998) measured laminar burning velocities for a range of conditions, using the method described above. An important observation was that a cellular flame structure developed earlier during flame propagation as the initial pressure was increased. As the flame surface became completely cellular there was an increase in flame speed and this continued as the flame propagated. The increase of flame speed after the transition to full cellularity was a function of time and was given by

$$S_n = C\,t^m \tag{2.10}$$

where C is an empirical constant that depends on mixture properties and flame speed at the point of cellular transition. The values of the exponent, m, was between 0.10 and 0.35 (Bradley et al., 1998).

Woolley (1999) observed a cellular surface structure on gaseous, moderately turbulent flames, at similar conditions to those in laminar gaseous flames. However, when the scale of turbulent wrinkling was of the same order as that of the cells, cellularity and turbulent wrinkling could not be distinguished. He also found that it was possible to induce cellularity in otherwise stable flames by use of turbulence.

It is possible that similar instabilities effects are also significant in aerosol flames and that this might be a cause of aerosol flame enhancement. This is discussed in Chapter 5.

2.2 APPROACHES TO AEROSOL COMBUSTION ANALYSES

Various types of study have been undertaken to elucidate the mechanisms of droplet evaporation and combustion. These broadly can be classified into three types: single droplet combustion, combustion of droplet clouds and combustion in more practical situations, such as industrial fuel sprays. These, briefly, are considered in this Section.

2.2.1 SINGLE DROPLET COMBUSTION

Knowledge about the combustion of a single fuel droplet forms the building blocks on which more practical studies can be based. It allows information to be gained on such parameters as evaporation, mixing and burning in a well characterised environment. Godsave (1952) found that the time taken for a single droplet suspended in still air to burn out is a square function of its diameter. He established the so-called D^2-law for the situation in which the difference in temperature between the drop and the surrounding atmosphere is considerable.

$$D^2 = D_0^2 - \lambda t \tag{2.11}$$

Here λ is the fuel evaporation constant, determined directly from the slope of plots of D^2 against t, D_0 and D are the drop sizes initially and at time = t, respectively. Spalding (1952) established the mass transfer number, B, as a means to calculate the evaporation rate from a sphere of liquid fuel in a stagnant atmosphere. He assumed the Lewis number to be unity and evaporation to be the dominant force in the mass transfer. Hence, B is a ratio of heat required to evaporate the droplet to that supplied to its surface by its combustion. It is given by

$$B = c_p\,(T_\infty - T_s)\,/\,Q \qquad (2.12)$$

where, c_p is the specific heat capacity of the liquid fuel drop, T_∞ is the far field temperature, T_s is the surface temperature of the fuel, usually approximated by its boiling temperature, and Q is the heat of combustion, supplied to the drop surface. For a quiescent mixture, B and λ are related by

$$\lambda = \frac{k}{8c_p\rho_f}\ln(1+B) \qquad (2.13)$$

where k is the thermal conductivity of the gas surrounding the drop and ρ_f the liquid density of the fuel. In many situations involving droplet combustion, mixing and burning can, to a first approximation, be assumed to be very fast (Spalding, 1952). Hence, evaporation is the rate determining process. This is particularly so for large droplets, and most of the early experiments were conducted on droplets with diameters of the order of millimetres. These works were reviewed by Faeth (1977) and Law (1982). In many applications the diameters are of the order of a few microns. In these cases the D^2 burning law may not be a good approximation and other factors must be considered (Annamalai & Ryan, 1992).

2.2.2 EVAPORATION BASED DESCRIPTION OF CLUSTER BURNING

The D^2 law fails when several drops are close enough to interfere with their individual evaporation and combustion processes. Research into drop array, cloud or cluster burning has been reviewed by Annamalai and Ryan (1992). They defined a cloud or cluster as having a large number of droplets, usually much higher than 10. They concluded that droplets in clouds can behave very different from isolated ones due to interaction between the droplets, and that this depends on the mixture composition within the cloud. For combustion to take place, liquid fuel must first be vaporised and this results in a complex mixture of fuel droplets, fuel vapour and air. The mixture of fuel and air may or may not be within its inflammability limits and the local proportions of vapour and air determine whether the overall mixture is flammable, and the location of the reaction zone. Conditions in the droplet cloud can be expressed in terms of the liquid volume of fuel present per unit volume of mixture. This is a function of the average size of the droplets and the average interdrop distance. Burgoyne & Cohen (1954) combined the drop diameter D and the interdrop distance l to the non-dimensional drop spacing l/D, to express the limiting conditions for flame propagation, in terms of flammability of the aerosol. This parameter was developed further, to accommodate more complex processes in the cloud. Various definitions have been used to describe the phenomena of evaporation and subsequent combustion conditions in aerosol clouds (Labowski et al., 1978, Chiu et al., 1977 & 1982, Correa et al., 1982). The expression developed by Chiu et al., to characterise different group combustion regimes in aerosol clouds, is given by

$$G = 1.5\, Le\, (1 + 0.276\, Re^{1/2}\, Sc^{1/3})\, N_T^{2/3}\, (D/l) \qquad 2.14$$

where Le is the Lewis number, Sc the Schmidt number, Re is the droplet Reynolds number and N_T denotes the total number of droplets in a cluster. The group combustion number G corresponds to the ratio of the gross droplet evaporation to the inward oxygen diffusion (Akamatsu et al., 1996). Figure 2.1 shows the combustion regimes of aerosol clouds with a given total number of droplets, N, against a non-dimensional drop separation, S. These four different combustion regimes were re-defined into more detailed subsections by Annamalai and Ryan (1992), and their definitions are summarised below, together with the appropriate G-number:

1. isolated group combustion: Each drop burns unaffected by other drops. $G < 0.01$

2a. individual flame combustion: As N increases the flames around individual drops will start to affect each other but still do not merge. $0.01 < G < 0.1$

2b. incipient group combustion: With further increase in N the oxygen consumption by droplet combustion at the edge of the cloud will lower the O_2 concentration in the cloud centre. The flames of individual drops touch each other, as the drop distance l becomes equal to the flame diameter. $0.01 < G < 0.1$

3. partial group combustion: A further increase in N starves the cloud centre of oxygen and a group flame is established at some radius inside the cloud, enveloping the centre. Outer drops still burn individually. $0.1 < G < 1$

4a. critical group combustion: N is so high that the blowing of vapour from the cloud prevents oxygen penetration into the cloud. The flame stands just on the cloud surface. $1 < G < 100$

4b. total group combustion: Due to further increase in N the flame is established outside the cloud. $1 < G < 100$

5. sheath combustion: In very dense clouds a condition is reached, in which the surface temperature of the cloud is at the boiling temperature of the drops. The cloud then behaves as an equivalent drop of the cloud radius R_c. $G > 100$

The above group combustion theory only considers the interaction between droplets in terms of evaporation and the location of the reaction zone is predicted to be a function only of the local mixture composition. The calculation of a burning rate is based solely on these evaluations and does not account for hydrodynamic interaction between the flame and the drop cloud. Nevertheless it gives a valuable insight into the processes of evaporation, fuel vapour accumulation and local mixture composition in a fuel drop cloud. The existence of these group combustion modes was confirmed experimentally by Nakabe et al. (1991b, 1995), Akamatsu et al. (1996, 1997) and Tsushima et al. (1998). This is discussed in Section 2.3.

2.2.3 COMBUSTION OF SRAYS IN INDUSTRIAL APPLICATIONS

The combustion of sprays in industrial applications involves many parameters in addition to those that directly affect combustion. Two reviews by Faeth (1983 & 1996) cover most aspects of two-phase flow, relevant to spray combustion. Hence, only a brief discussion is presented here. In addition to the parameters mentioned above, combustion in practical applications is influenced by the structure of injected fuel jets, drop break-up regimes and drop-turbulence interactions. Flame speeds in these environments are the result of many interacting hydrodynamic, thermodynamic and physico-chemical processes, such as turbulence, evaporation and combustion itself, which influence flame promotion or quenching. The knowledge obtained from experiments in practical applications may be applicable to industrial problems, but it is difficult to single out fundamental parameters to improve the understanding of the basic processes or to facilitate and validate numerical and phenomenological models of these fundamental features. Hayashi & Kumagai (1974) found that, in order to give correct interpretations of observed phenomena in aerosols, idealised simplified systems were needed, referring to monodisperse, uniformly suspended droplets.

2.3 OBSERVATION OF FLAME STRUCTURE

The visual appearance of aerosol flames was frequently used, to try to explain possible mechanisms of aerosol combustion. Three regimes of combustion, premixed, transition and relay, have been observed in aerosol flames. Burgoyne and Cohen (1954) used a dilute cloud of monosized droplets, condensed out of a gaseous mixture flowing through a glass tube. They established that, when the interdrop region was free of fuel vapour, the occurrence of any one of these regimes was primarily dependant on the diameter of the liquid droplets. For drop sizes smaller than 10μm they observed that the flame front was of a blue premixed appearance with no individual flame centres, similar to that observed by Wolfhard & Parker (1949) for a "very fine" kerosene spray. The front was observed to progress smoothly and Burgoyne et al. concluded, that the drops were small enough to evaporate ahead of the flame front and mix with the air before they entered the flame front. Between drop diameters of 10 to 40 μm the flame developed a cellular structure with a bright centre associated with each cell. These flames were described as "thick, with evidence of violent motion indicating turbulent burning". Apparently a premixed front and individual diffusion flames coexist. Burgoyne et al. found that, in this regime, a flame could burn faster than in a fully premixed one. Data are presented in Table 2.1. Beyond a drop size of 40 μm, the continuous flame front no longer exited and Burgoyne et al. observed the flame to be relayed between individually burning centres.

Aerosols, containing a flammable gaseous mixture, were investigated by Mizutani & Nishimoto, using a horizontal duct (1972) and an inverted cone burner (1973a). They observed a smooth blue burner flame outside a bright yellow region, with a rough appearance in the transition region. Schlieren pictures of these flames suggested that a continuous thin reaction zone existed, despite the island like appearance of the flame when observed by short exposure direct photography. The supposedly premixed reaction zone was shown to be distinctly separated from the zone of yellow diffusive burning. It was concluded, that the premixed zone governed propagation of the flame. These workers also investigated outwardly growing, spherical flames (1973b) in a closed vessel. The mixture initially was at room temperature and atmospheric pressure. They observed the transition from a laminar to what they called a "self-turbularised" flame, when they added kerosene aerosol to a propane-air mixture. Also using a bomb, Hayashi and Kumagai (1974 & 1976) confirmed that there was a smooth premixed flame when the droplets were small enough to vaporise ahead of the flame front. However, they found this to be a function of the initial flame speed. In fast burning ethanol mixtures, drops as small as 7μm caused a rough appearance of the flame, growing with the propagation of the flame. They ascribed the cellularity of the flame to local variations in temperature and mixture strength and subsequent differences in burning velocity.

Murphy and Borman (1979) used a device, similar to that of Burgoyne et al. (1954). They observed an increase in flame thickness from 1mm, with 8μm drops, up to 15mm at a drop size of 20 - 25μm, at the point where the flame went into transition. This was confirmed by Koshland and Bowman (1984) who also observed two flame zones, whose detailed structure was a function of overall mixture strength. For rich mixtures a vapour phase flame, resembling a laminar premixed gas flame was followed by a diffuse pale blue flame. For lean mixtures the vapour phase flame was followed by luminous streaks. For all mixtures, the second zone varied in thickness between 3 and 10mm depending on the initial drop size and number density.

Nakabe et al. (1988) used a burner, fed by an air blast atomiser. They confirmed the existence of a thin premixed continuous turbulent flame front from observations of the OH emissions of aerosol flames. Simultaneously recorded C_2 emissions indicated group combustion in the flame core, which suggested that the vapour from the aerosol burned locally rich. Short exposure photographs showed discrete flame lumps around droplets and a gaseous flame propagating randomly in "easy-to-burn" regions. The existence of clusters, burning in the core of the flame, was confirmed for an overall equivalence ratio of only 0.75. In 1991, Nakabe et al. used a "premixed spray burner with low slip velocity" to spatially correlate OH and CH emissions from kerosene-spray-air mixtures with variable amounts of propane gas added. They found that the flame burned in the premixed regime when the spatial correlation of OH and CH emissions was good. When the correlation was poor, diffusion flames and soot were observed. They also correlated OH emissions with laser Doppler velocimetry signals and found that flames propagated preferentially through regions with fewer droplets and higher gaseous equivalence ratio. Measurements of cluster size showed, that an increase of propane gas in the mixture caused the cluster size to increase, with sub-clusters burning in external group combustion mode inside bigger "mother clusters" which burned with a premixed flame. The length scale of the "complex group structure" was drastically reduced under turbulent conditions, due to turbulent mixing and higher slip velocities between droplets and gas (Nakabe et al., 1995). Akamatsu et al. (1996 & 1997), using the same apparatus as Nakabe et al. (1991 & 1995), additionally measured the Mie scattering signal from the drops to identify clusters. Using Eq. (2.14), they calculated a decrease from $100<G<1$ to $1<G<0.01$ when they moved the measurement location from 35 to 130mm downstream of the flame front. Tsushima et al. (1998) confirmed these findings, using laser sheet imaging and a novel optical probe to record OH, CH and Mie signals simultaneously with an improved depth of field. They observed, that clusters formed due to preferential flame propagation at a velocity of approximately 2.5m/s through "easy to burn" regions and that these clusters were then consumed at a much slower rate of approximately 0.5m/s from the outside inwards. This phenomenon of cluster combustion may exist at the experimental conditions investigated by the present author, and may play a role in the explanation of the structure of the observed instabilities. This is presented in Chapter 5.

As discussed in Section 2.2.2, drop spacing was frequently used to explain the occurrence of different combustion regimes in aerosol mixtures. Table 2.2 presents interdrop distances as a function of drop size, for the overall equivalence ratios 0.5, 1.0 and 1.5, for the fuels frequently used in aerosol research, recalculated by the present author in appropriate units. It was assumed that all of the fuel was present in liquid form, comparable to a case of fuel injection, as used in most of the reviewed works. Table 2.3 shows the same data for vapour liquid equilibrium at 20°C. This corresponds to those experiments where condensation was used to generate the aerosol. These data show, that the drop spacing does not vary greatly for the range of experimental conditions, compiled in this review. This may explain why similar effects of aerosols on combustion where observed throughout all experiments, undertaken with different fuels in different experimental apparatus.

2.4 THE EFFECT OF MIXTURE COMPOSITION AND PARTICLE SIZE IN AEROSOLS

To a first approximation only two properties are necessary to fully characterise an aerosol, the mixture composition and the size of the liquid droplets. Since the fuel is present in two phases the mixture composition itself needs to be expressed in terms of those phases. The particle size in an aerosol usually is not uniform which necessitates some form of averaging to find a suitable mean that properly represents the physical properties of that spray (Lefebvre, 1989). This section presents the most commonly used definitions of mixture composition and drop size, followed by experimental evidence of the effect of these parameters.

2.4.1 DEFINITIONS

The simplest parameter, used by most researchers (e.g. Burgoyne et al., 1954, Mizutani et al., 1972, Nakabe et al., 1997) to define an aerosol mixture is the overall equivalence ratio, ϕ_{ov}. This includes all fuel present, irrespective of phase. Since the behaviour of an aerosol flame is primarily dependent on the gaseous equivalence ratio (Myers, 1986), this is a key parameter. Two different equivalence ratios are therefore defined to accommodate the gaseous and liquid phases, ϕ_g and ϕ_l. These are related by

$$\phi_{ov} = \phi_g + \phi_l \tag{2.15}$$

However, the evaporation of droplets ahead of the flame front alters both the liquid and gaseous equivalence ratios. The amount of gaseous fuel available in the reaction zone is represented by the effective equivalence ratio, ϕ_{eff}, which is most difficult to determine experimentally and there were no measurements attempted in the works included in this review. However, this parameter was used in a computational model by Polymeropoulos (1983) to predict the burning velocity in an aerosol. Other workers, e.g. Burgoyne et al. (1954), calculated the change in drop size, and the subsequent change in ϕ_g, in the preheat zone of the flame from the scaled temperature profile of a homogeneous flame. However, this is not without problems since aerosol flames can be much thicker than gaseous flames. Therefore, experimental results usually have been correlated in terms of cold gas parameters.

The parameter most frequently used for the correlation of the combustion behaviour of an aerosol is the drop size. If all drops in an aerosol are of the same size, then the obvious statement is that of droplet diameter. Such an aerosol is termed monosized or monodisperse. However, sprays produced by injectors, are rarely monosized. Different definitions of average particle sizes have been used, the most widely accepted in combustion research being the Sauter mean diameter. This is defined as

$$D_{32} = \frac{\Sigma N_i D_i^3}{\Sigma N_i D_i^2} \tag{2.16}$$

where D is the representative diameter of size class i and N is the number of drops within that size class. The Sauter mean diameter is the diameter of a particle who's volume to surface ratio is equal to that for the whole spray. As such, it is a suitable parameter for evaporation rate limited processes, since the evaporation of the liquid droplet is a function of surface area and the mass consumed by chemical reaction is one of volume (Lefebvre, 1989).

However, the Sauter mean diameter is calculated from the diameter distribution in the aerosol, which itself will change during evaporation. Therefore, the change in Sauter mean diameter over time does not necessarily follow the D^2-Law, given by Eq. (2.11). Using a computational model Silverman and Greenberg (1993) established, that due to preferential evaporation of small droplets the Sauter mean diameter increases with evaporation time. The magnitude of the increase depends on the initial distribution. This can result in significant errors when evaporation rates are calculated using the D^2-Law and a Sauter mean diameter, initially derived from the cold gas diameter distribution. Akamatsu et al. (1997), using Phase Doppler Velocimetry, measured an increase in Sauter mean diameter from 33 to 37.5μm within the combustion zone while the number density dropped from 24000 to 2000 per unit volume. For the evaporation of a monodisperse spray Greenberg et al. (1993) computed D to decrease monotonically, according to the D^2-Law. This is applicable to the work presented in this thesis since, as it was demonstrated by Hayashi et al. (1974 & 1976), the size distribution generated by the Wilson cloud chamber method (Wilson, 1895 & 1911), is close to monodisperse.

2.4.2 MEASUREMENTS OF FLAME SPEED AND BURNING VELOCITY

Flame speeds and burning velocities have been measured by many researchers, in order to investigate the effects of various parameters on aerosol combustion. This Section reviews results, related to the effects of mixture composition and drop size. However, studies of aerosol combustion have been less rigorous than those for gaseous mixtures. The distinction between burning velocity and flame speed, as discussed in Section 2.1.2, is often not made and experimental conditions were often not precisely defined, particularly with respect to turbulence. Indeed, results are often apparatus specific and a direct comparison of results from different workers is difficult. Therefore, a strict separation between laminar and turbulent results was not possible. This is discussed in Section 2.5, where an attempt is made to isolate the effect of turbulence. For these reasons, experimental results, listed in Table 2.1, were compared quantitatively only to baseline burning rates derived from the same apparatus or from works using similar experimental techniques. The baseline burning rate usually was that of a gaseous mixture at the same overall equivalence ratio or that of the aerosol closest to a gaseous mixture, i.e. that with the smallest drop size, investigated for particular conditions.

For most hydro-carbon fuels, the highest burning velocity for gaseous mixtures is found at an air-fuel ratio slightly rich of stoichiometric (Bradley et al., 1998). Myers & Lefebvre (1986) reviewed a number of sources in the field of aerosol combustion. The general consensus was, that aerosol burning velocities were sensitive to the gaseous equivalence ratio, regardless of the overall equivalence ratio. General agreement also prevailed on the correlation of drop size and burning rate for large and for small droplets. For drop sizes bigger than 40μm, the burning rate has been found to be inversely proportional to SMD . For diameters smaller than

10μm, usually a premixed flame is observed and the burning velocity converges with that of a homogeneous mixture of equal overall equivalence ratio. However, in the size range from approximately 10 to 40μm, experimental findings differed, as do interpretations of results. In this size region most researchers observed the transition regime, described in Section 2.3, and experimental evidence suggests, that flames burn faster in this regime than in homogeneous mixtures of equal overall equivalence ratio (e.g. Kumagai et al., 1976, Mizutani et al., 1973a). Results are listed in Table 2.1.

Burgoyne & Cohen (1954) found a clear enhancement of the burning velocity in the transition regime. For a drop size of 17μm and $\phi_{ov} = 0.70$, the burning velocity was nearly 60% higher than that of a stoichiometric mixture at 10μm. This mixture was taken to be the burning velocity baseline for this apparatus. It was assumed that its burning velocity was close to that of a gaseous mixture, because 10 μm drops tend to evaporate completely ahead of the flame front. Since the presence of vapour in the cold gas was assumed to be negligible ϕ_{ov} was assumed to be approximately equal to ϕ_l.

Mizutani et al. (1973a) observed that a small amount of kerosene drops added to a propane air mixture markedly accelerated the burning velocity (see Table 2.1). Smaller droplets raised the flame speed more effectively than bigger ones. The fact that they found a flame speed promotion even for droplets bigger than 40μm does not necessarily conflict with other works. Since they used a mixture of propane gas and kerosene droplets a flammable mixture was provided in the interdrop space. However, in pure kerosene aerosols this situation would exist only when the drop size and number density allow for high evaporation rates in the preheat zone. The liquid equivalence ratio returning the highest burning velocities was $\phi_l = 0.08$ to 0.10 for any gaseous equivalence ratio. The experiments were mainly conducted at lean overall equivalence ratios. Hence, this contradicts the argument by Hayashi et al. (1974) and Richards et al. (1986) that the burning velocity enhancement of an aerosol mixture is caused by providing a gaseous equivalence ratio that is closer to stoichiometric than that of the overall rich mixture. Adding very fine kerosene mist, with a drop size much smaller than 10μm, which supposedly vaporised ahead of the flame front, caused the flame speed to decrease below that of the reference propane-air mixture regardless of ϕ_l.

Polymeropoulos et al. (1975) examined 5 sprays with different drop sizes at a constant equivalence ratio of $\phi_{ov} = 0.8$. Their results are listed in Table 2.1. Due to the inability to accurately count droplets smaller than 30μm, the Sauter mean diameter was estimated by these workers. The finest spray burned with a premixed appearance, indicating a drop size below 10μm. The trends observed by Polymeropoulos et al. and Burgoyne et al. agreed qualitatively, showing an increase of burning rate of approximately 80%, both for lean mixtures, at a Sauter mean diameter of approximately 30μm. However, the values by Polymeropoulos et al. were slightly higher than those by Burgoyne et al., probably due to the presence of turbulence.

Nakabe et al. (1988) observed that the flame speed of a kerosene spray rose above that of propane gas when the drop size decreased below 70μm and ϕ_{ov} was lean. Their data agreed qualitatively with the experimental results of Myers et al. and also with the empirical relationship of Mizutani et al. (1972). They normalised their data with respect to turbulence intensity, since the variation of drop size via the atomising air pressure caused fluctuations of the level of turbulence. The results confirmed the existence of an optimum liquid-to-gaseous fuel ratio for the highest burning rate, as found by Mizutani et al. (1973a). This optimum shifted towards smaller liquid mass fractions with decreasing drop diameter, i.e. higher evaporation rates.

Richards and Lefebvre (1989) investigated the effects of overall equivalence ratio between the limits of 0.37 and 1.84 in a duct burner. As in previous studies it was assumed that the amount of fuel vapour in the fresh mixture was negligible. The highest flame speeds for overall lean and stoichiometric mixtures were reported to occur with the smallest drop size investigated, which was 30μm. At rich equivalence ratios the maximum flame speed shifted towards 50μm droplets and for higher turbulence levels even to 70μm. This supports the assumption that, for rich mixtures and particularly when the Sauter mean diameter is large, the effective equivalence ratio in the combustion zone was closer to stoichiometric, due to the decrease in evaporation rate. This agrees with the findings of Nakabe (1988). As in Myers work, and presumably for the same reasons, no burning rate promotion was observed. In both works the drop size was not decreased far enough into the transition regime and no comparative measurements with all-vapour mixtures were made at the same experimental conditions.

Mizutani et al. (1973b) compared the pressure histories and flame speeds of propane-air-kerosene drop mixtures. They kept the gaseous equivalence ratio, i.e. that of the propane, constant while adding different amounts of kerosene aerosol. In all cases the highest pressures were recorded for slightly rich mixtures but remained essentially unchanged for further increasing mixture strength. The highest burning rate and shortest pressure rise time was recorded at a liquid equivalence ratio of 0.05 to 0.11. However, lean aerosol mixtures, were up to 60% faster than purely gaseous mixtures at equal overall equivalence ratio. In the initial stage of flame growth, the aerosols burned faster at any overall equivalence ratio than their gaseous equivalents.

Hayashi et al. (1974 & 1976) used the Wilson cloud chamber method (Wilson, 1895 & 1911) to produce a variety of monodisperse aerosols in combustion bombs. They generated droplet clouds with particle sizes between 18 and 30μm for Ethanol and 20 to 35μm for n-Octane, similar to those for iso-octane in the present apparatus, discussed in Chapter 4. The overall highest flame speed for ethanol mixtures was obtained for a rich 30μm aerosol and no conclusive burning rate promotion was found. However, the result for n-Octane, compiled in Table 2.1, show an enhancement for any aerosol above an overall equivalence ratio of 0.85.

In a brief review Myers et al. (1986) established that most workers had observed a flame speed or burning velocity promotion for at least some of their experimental conditions (Burgoyne et al., Cekalin, 1962, Mizutani et al., 1972 & 1973, Polymeropoulos et al., 1975, Hayashi et al., 1976, Ballal et al., 1981).

2.5 THE EFFECT OF TURBULENCE ON AEROSOLS

Turbulence exerts a major influence on the burning velocity and flame speed of gaseous mixtures (Abdel-Gayed et al., 1987, Bradley et al., 1993, Merdjani et al., 1993). In aerosols its presence is even more significant, since the time scales of evaporation and diffusion of the fuel and the entrainment of air are shortened radically (Myers et al., 1986). In a homogeneous environment turbulence produces a wrinkled flame which burns faster than a laminar one. It was suggested (Mizutani et al., 1973a) that the enhancement of the burning velocity in an aerosol was the result of a wrinkled flame surface, due to the presence of the drops. However, this would suggest that the mechanisms that lead to an increased burning velocity in an aerosol and in a turbulent flame, might be similar in that both turbulence and droplets wrinkle the flame. Therefore, the fact that some workers found a burning velocity enhancement and some did not, can possibly be explained with the presence of different turbulence levels in the different apparatus, used for their experiments. Turbulence conditions of a number of works are given in Table 2.1.

Mizutani et al. (1972) developed an empirical correlation for results obtained from a duct burner experiments with high flow velocities, and applied this correlation to data obtained from a bunsen-type burner, with much lower flow rates. However, the correlation of drop size and burning velocity, which predicted the burning velocity for the duct burner quite accurately, could only approximately predict the magnitude of the burning velocity for the burner. The burning rates for 70μm drops showed acceptable agreement, but those for smaller sizes were much higher. It is unclear whether the data obtained from the burner experiment possibly indicated a burning velocity enhancement, since the flame speeds for 30μm drops were recorded at overall equivalence ratios too lean to unambiguously show this effect. The highest overall equivalence ratio in both sets of experiments, burner and duct, did not exceed 0.6, and a potential flame speed promotion would not have been be very pronounced. However, it was observed that the ratio of laminar to turbulent burning velocities was considerable smaller for these aerosols than it is for homogeneous mixtures, also combusted in these apparatus at similar turbulence velocities. In their subsequent work Mizutani et al. (1973a) observed that the effect of adding a kerosene aerosol to the propane-air mixture was greater when the flow velocity i.e. the turbulence intensity was low. This indicates that increased turbulence intensities conceal or curb some of the burning rate enhancing effect of the aerosol. At higher turbulence intensities the gain in flame speed by drop addition over that of the homogeneous mixture was proportional to the overall equivalence ratio, whereas at lower turbulence levels the gain was greater at lean overall equivalence ratios and converged towards stoichiometric mixtures. This suggests that better evaporation and mixing at higher turbulence intensity leads to a decreased dependence of mixture formation on drop size and number. This conclusion was confirmed by the findings of Richards & Lefebvre (1989). They observed that, in general, flame speeds increased with increasing turbulence intensity, but that this effect was more prominent for bigger drop sizes (50 and 90μm) i.e. sprays with smaller evaporative surface area. The turbulence velocities in the research of Myers & Lefebvre (1986) and Richards & Lefebvre were similar, approximately 1.2 to 1.7m/s. In both experiments no explicit burning velocity enhancement was observed. One possible reason is, that these workers did not make calibration measurements with homogeneous mixtures in their own apparatus, but used values compiled from other sources (Dugger et al., 1953, Kuehl, 1962). However, Richards & Lefebvre found that the increase of flame speed with turbulence was small compared to that of homogeneous mixtures, which confirmed the observation of Mizutani et al. (1972). The turbulence levels in the work of Nakabe et al. (1988) were very similar to those in their earlier works (Mizutani et al., 1972). However, these workers normalised their measurements against "standard turbulence intensity", which enabled them to find an optimum liquid equivalence ratio for a maximum flame speed for each drop size verified. The increase was, however, rather smaller than that observed in laminar appliances and much more prominent for lean mixtures.

Generally a flame speed enhancement was observed or suspected, when the r.m.s. turbulent velocity was below 0.2 m/s and no apparent effect was found for u' higher than 0.9 m/s.

Source Method	Fuel	p [kPa]	T [K]	ϕ_{ov}	ϕ_g	D_{32} [μm]	Flow velocity *u* [m/s]	*u'* [m/s]	Turbulence intensity [%]	Flame Speed [m/s]	Burning velocity [m/s]	Enhancement [%]
Burgoyne et al. (1954)	Tetralin	100*	295*	1.00		10					0.39	Baseline
Burner, condensation				0.71		9					0.31	-20
				0.96		11					0.42	8
				0.70		17					0.62	59
				0.69		29					0.68	74
				0.55		38					0.58	49
Mizutani et al. (1973a)	Propane plus	100*	295*	0.7	0.7	0	1.2	0.13			0.32	Baseline
Inverted cone burner,	Kerosene drops			0.7		41	1.2	0.13	10.8		0.9	180
Air blast atomiser				0.7	0.7	0	1.9	0.20			0.57	Baseline
				0.7		37	1.9	0.20	10.5		1.2	100
				0.7		60	1.9	0.20	10.5		0.95	66
Mizutani et al. (1973b)	Propane plus	100*	295*	0.7	0.7	0	0	0		1.55		Baseline
Bomb, Ultrasonic atomiser	Kerosene drops			0.72	0.7	0.02	0	0		1.75		13
Flame speed at 50mm flame diameter				0.734	0.7	0.034	0	0		2.2		42
				0.754	0.7	0.054	0	0		2.5		62
				0.817	0.7	0.117	0	0		2.7		74
Polymeropuolos & Das (1975)	Kerosene	100*	295*	0.81		< 15 (est.)	2.66	0.22	8.3		0.50	Baseline
Inverted cone burner with				0.81		54	2.66	0.22	8.3		0.60	20
combination of air blast and				0.81		43 (est.)	2.66	0.22	8.3		0.72	44
ultrasonic atomiser				0.81		33 (est.)	2.66	0.22	8.3		0.91	82
				0.81		25 (est.)	2.66	0.22	8.3		0.60	20

Table 2.1: *Selected extracts of typical aerosol flame speeds and burning velocities. * marked data are estimates by the present author.*

Source Method	Fuel	p [kPa]	T [K]	ϕ_{ov}	ϕ_g	D_{32} [μm]	Flow velocity u [m/s]	u' [m/s]	Turbulence intensity [%]	Flame Speed [m/s]	Burning velocity [m/s]	Enhancement [%]
Hayashi, Kumagai & Sakai (1976)	n-octane	100*	323	1.05	**1.05**	0				2.65		Baseline
Wilson cloud chamber		80*	305*	1.05	0.75	20				2.85		9
(only pre-expansion p and T quoted)		67*	290*	1.1	0.55	23				2.8		5.5
		57*	280*	1.15	0.4	36				2.75		3.7
Nakabe et al. (1988), Burner	Propane			0.9	0.9	0	High atomizing pressure, high u'			3.6		Baseline 30μm
	Propane			0.9	0.9	0	Low atomizing pressure, low u'			2.9		Baseline 60μm
	Propane plus	100*	295*	0.9	0.67	30				4.1		14
	Kerosene drops			0.9	0.62	40				3.8		
				0.9	0.50	50				3.4		
				0.9	0.37	60				3.0		3.5
Richards & Lefebvre (1989)	Kerosene	100*	295*	1.0		50	12.4	1.24*	10*	2.6		-
(similar to Myers & Lefebvre, 1986)				1.0		50	20.5	1.64*	8*	2.8		-
Duct				1.0		50	24.6	1.72*	7*	3.4		-
				1.0		50	33	1.65*	5*	3.4		-
				1.0		30	12.4	1.24*	10*	3.2		-
				1.0		30	20.5	1.64*	8*	3.8		-
				1.0		30	24.6	1.72*	7*	4.0		-
				1.0		30	33	1.65*	5*	3.8		-

Table 2.1 (cont.): *Selected extracts of typical aerosol flame speeds and burning velocities. * marked data are estimates by the present author.*

Substance	Formula	Drop spacing *l* in [µm] @				Non-dimensional dropspacing
		D=10µm	*D*=20µm	*D*=30µm	*D*=40µm	*l/D*
			ϕ=1.0			
Ethanol	C_2H_5OH	*145*	*291*	*437*	*582*	*14.6*
Methane*	CH_4	145	292	438	583	14.6
Propane*	C_3H_6	158	317	475	634	15.8
n-Hexane	C_6H_{14}	163	327	790	653	16.3
n-Octane	C_8H_{18}	166	333	499	666	16.6
iso-Octane	C_8H_{18}	165	331	497	662	16.6
Decane	$C_{10}H_{22}$	168	336	505	673	16.8
Tetralin	$C_{10}H_{12}$	*179*	*358*	*537*	*716*	*17.9*
Decalin	$C_{10}H_{18}$	174	348	521	695	17.4
Kerosene	$C_{12}H_{23}$	175	350	526	700	17.5
Dodecane	$C_{12}H_{26}$	170	339	509	678	17.0
			ϕ=1.5			
Ethanol	C_2H_5OH	183	367	550	733	18.3
Tetralin	$C_{10}H_{12}$	225	451	677	902	22.6
			ϕ=0.5			
Ethanol	C_2H_5OH	127	254	381	508	12.7
Tetralin	$C_{10}H_{12}$	156	312	469	625	15.6

Table 2.2 : *Relationship between D_{32} and drop spacing as a function of fuel and equivalence ratio, calculated by the present author for 20 °C, 1bar, all fuel assumed liquid. Italic print marks the maximum and minimum values. * The liquid densities of Methane and Propane are those at -164 °C and -45 °C respectively.*

Substance	Formula	Drop spacing *l* in [µm] @				Non-dimensional dropspacing
		D=10µm	*D*=20µm	*D*=30µm	*D*=40µm	*l/D*
			ϕ=*1.0*			
Ethanol	C_2H_5OH	295	590	885	1180	29.5
n-Octane	C_8H_{18}	234	469	704	939	23.5
Decane	$C_{10}H_{22}$	174	348	522	697	17.4
Tetralin	$C_{10}H_{12}$	180	360	540	721	18
Dodecane	$C_{12}H_{26}$	170	340	510	681	17
			ϕ=1.5			
Ethanol	C_2H_5OH	173	346	520	694	17.6
Tetralin	$C_{10}H_{12}$	157	314	470	628	15.7
			ϕ=0.5			
Tetralin	$C_{10}H_{12}$	228	457	686	914	22.9

Table 2.3 : *Relationship between D_{32} and drop spacing as a function of fuel and equivalence ratio, calculated by the present author for 293K, 100kPa, vapour-liquid equilibrium.*

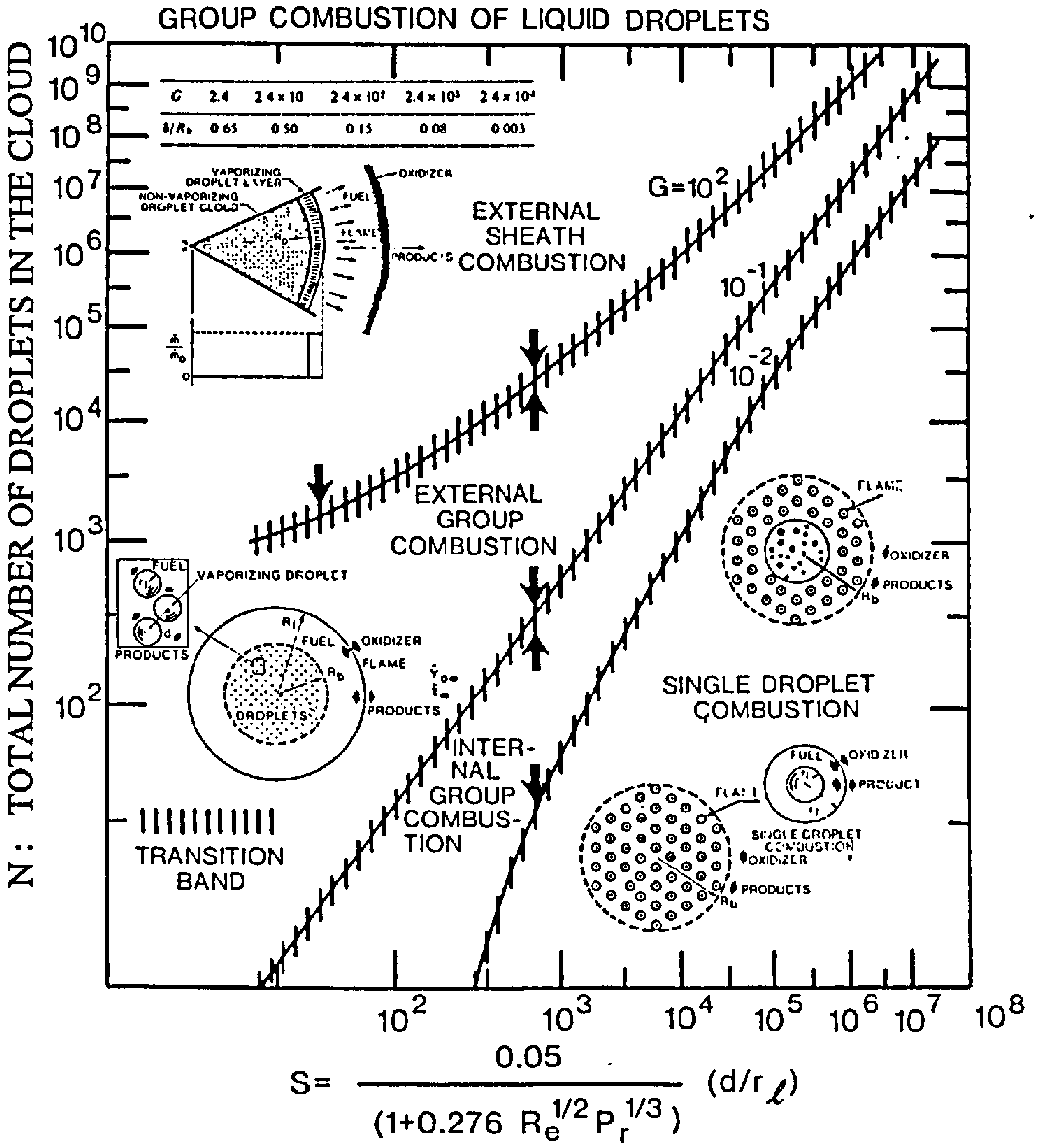

Figure 2.1: *Combustion regimes defined by Chiu et al. (1982), calculated using Eq.(2.14).*

3. APPARATUS AND TECHNIQUES

Described in this chapter are the devices and techniques used for the study of flame propagation in iso-octane and air aerosols at a variety of initial conditions. Aerosols were generated in a combustion apparatus, using the Wilson cloud chamber principle. The apparatus is described in Sections 3.1 and 3.2 and the mixture preparation technique is presented in Section 3.3. Instrument errors that affect mixture properties are discussed in Section 3.4.

Extensive measurements of pressure, temperature and aerosol properties during expansion were undertaken to characterise aerosol properties at the time of ignition. The instrumentation used for this is presented in Section 3.5. Combustion events were recorded, using high speed schlieren photography and laser sheet imaging. These systems also are presented in Section 3.5 and the associated image processing techniques are set out in Section 3.6. Only brief descriptions are given when detailed information exists elsewhere.

3.1 AEROSOL COMBUSTION RIG

For the present research a new aerosol combustion system was commissioned by the present author, in which fuel aerosols were generated, using the Wilson cloud chamber principle, as described by Wilson (1895 & 1911). In this, a homogeneous fuel air mixture is cooled by expansion until the fuel condenses into a fog of liquid droplets. Mixture preparation is explained in detail in Section 3.3. This method was previously used for combustion studies by Hayashi & Kumagai (1974, 1976).

The apparatus comprised the combustion chamber, hereafter called bomb, the expansion tank and interconnecting pipework, various valves and control systems, and measurement instrumentation. Each are discussed below. The system is shown photographically in Fig. 3.1 and schematically in Fig. 3.2.

3.1.1 EXPLOSION VESSEL

The bomb was previously used for studies of gaseous combustion and has been described by Hundy (1969), Andrews (1972) and Lawes (1987). It comprised a cast steel cylinder of 305mm diameter and 305mm length and its working volume was 23.2 litres. Optical quality BK7 windows, 150mm diameter and 39mm thick, were fitted in each end. Four identical eight-bladed fans were fitted, equi-spaced around the central circumferential plane at 45° to the horizontal. For studies of turbulent combustion, they provided the required flow field. They were also used in laminar studies for the mixing of fuel and air, prior to experiments. The fans generated isotropic turbulence within the field of view of the windows and the turbulence velocity was a linear function of fan speed. The vessel turbulence was fully characterised by Lawes (1987). All measurements were taken from within a central sphere of 150mm diameter. The combustion bomb, including the access ports, was essentially the same as that used by previous workers. However, extensive modifications to the rest of the system were made by the author, to allow studies of aerosol combustion. These are detailed below.

Several access ports were required and these are shown schematically in Fig. 3.3. A $^1/_2$" BSP port, in the top of the bomb, was used to connect the bomb to the central fill and discharge valve, FDV, which linked the bomb with the gaseous fuel and air supply and to the exhaust. A pressure transducer, used to monitor the initial mixture pressure, also was connected to this port, as discussed in Section 3.1.3. To prevent exposure of the pressure transducer to combustion pressure, which might result from accidental ignition, an additional isolating valve was fitted immediately adjacent to the port. This valve was equipped with a safety switch which intersected the ignition trigger when the valve was open, thus preventing accidental ignition. The trigger circuits are described in Section 3.2.

Four 1" BSP ports were equi-spaced around the bomb, as shown in Fig. 3.3. The top port was permanently connected to the expansion pipe. All other ports were used as appropriate for ignition, seeding, thermometry and an additional 25.4mm diameter window. Two 1/8" Enots ports, located in the horizontal plane, also were used for thermometry.

New 3-phase 1.5 kW fan motors and electronic motor controllers, Mitsubishi Freqrol Z024-S1.5K, were installed by Drake (in preparation) in 1994, because the original motors (Lawes, 1987) had been removed for use elsewhere.

Previously the vessel contained a 2kW electrical heater, mounted close to the surface of one of the end plates, which was used to raise the vessel temperature to that required for an experiment. However, this configuration was found to be inadequate for the present work because it caused significant temperature gradients within the vessel. This resulted in spatially inhomogeneous condensation and, hence, spatially inhomogeneous mixture properties. Therefore, the heating system of the bomb was extended to include two heating elements, with a total installed power of 4.5 kW. The second heating element was mounted symmetrically opposite to the original heater, on the other end plate. Both heaters were controlled by a CAL Controls Ltd. Model 3200 electronic controller.

3.1.2 EXPANSION SYSTEM

Aerosol mixtures were prepared, as discussed in Section 3.3, by expanding a gaseous pre-mixture from the bomb, into the expansion tank at a controlled rate. The expansion tank comprised an obsolete cylindrical explosion vessel with a volume of 28 litres. Four main ports were fitted at right angles to each other around the vessel circumference. The top port was used to connect the expansion tank to the bomb and the others were unused and blanked off. A mechanical manometer, supplied by Air Products, connected to a ½" BSP port, was used to monitor the internal pressure. The tank was linked to the exhaust system via a Dyna-quip $^{3}/_{8}$" ball valve, connected to a ½" BSP port. Because the expansion tank had originally been designed as a combustion vessel, it was capable of withstanding combustion pressures. Therefore, it was safe to contain the fuel-air mixture expanded from the combustion bomb.

The bomb and expansion tank were connected via a pipeline of 38 mm internal diameter, consisting of a standard water pipe, certified to British Standard 1387,with a safe working pressure of 35 bar. This exceeds the maximum safe working pressure of the bomb and expansion tank. The pipe was flange-mounted to the top ports of the bomb and expansion tank. The total volume of the expansion system, including the pipeline, was 56 litres.

The pipeline held a WOG500 $1^{1}/_{4}$" ball valve of 26 mm internal diameter, which was used to separate the bomb and expansion tank, and was placed immediately outside the combustion bomb. Initially in the present research, the valve was operated manually and care had to be taken to swiftly open the valve at a consistent rate, during experiments, to reduce cycle to cycle variations in mixture expansion (see Section 3.3). For laminar studies, in which mixture expansion took place over a period of 4 seconds, variations in valve opening time had negligible effect on pressure and temperature development and consequently on aerosol properties. However, for turbulent work, in which the expansion duration was only of the order of 0.15 seconds, manual valve operation was not consistent enough. Hence, the valve was converted to pneumatic operation. Acceptable consistency of valve opening times was confirmed from pressure records.

Mixture expansion was controlled by a throttle, which was placed immediately downstream of the expansion valve. It comprised a pipe coupling, which was modified to house interchangeable orifice plates. The standard orifice diameter for laminar combustion experiments was 6 mm, and this resulted in an expansion time to pressure equilibrium of approximately 4 seconds. This long time duration, relative to that for combustion, allowed for easy synchronisation of the spark and diagnostics with respect to the desired state of mixture expansion. The slow expansion also minimised any resulting flow disturbances within the combustion chamber.

For turbulent experiments more rapid expansion was required because the rate of droplet evaporation in the control volume was much higher than for laminar work, due to turbulent heat transfer from the wall region. The expansion time was reduced to 0.15 seconds, by removing the orifice plate from the pipeline.

In the present project iso-octane was the main fuel. It is liquid at room temperature and was delivered into the combustion chamber through a needle valve supplied by Scientific Systems Inc., using a Hamilton precision glass syringe. The needle valve was connected directly to the combustion chamber via a $^1/_{16}$" stainless steel tube. Gaseous fuel and air were supplied to the bomb via a valve panel with $^3/_8$" main valves, RS Ltd., and Nupro fine control and non-return valves.

The exhaust system included a 3-way exhaust valve, which connected both vessels directly to the exhaust line when their pressures were above atmospheric, and to an Edwards Speedivac ED100 vacuum pump for evacuation of the vessels to pressures within 2 kPa of vacuum.

3.1.3 AUXILIARY EQUIPMENT

1. Pressure instrumentation

Measurements of total static absolute pressure and fuel partial pressure, as well as measurements of the pressure change during expansion were performed using a precision pressure transducer-amplifier/readout system, DRUCK Ltd. PDCR 911 and DPI 260. It was fitted immediately behind the isolating valve, as close as possible to the combustion chamber. A snubber protected the transducer from peak pressures that might have occurred during any accidental explosion. The transducer had a range of 0 to 700 kPa absolute, with a resolution of 0.1kPa, and was calibrated by the manufacturer. The response time of the device is significantly faster than required during the fastest expansion performed in the present work. Errors due to temperature variations, within the operating range of the present work of approximately 0 to 30°C, were quoted by the manufacturer to be less than 0.1%. The transducer was found to have no significant shot to shot variation and long term drift was small, even for the small pressure changes (1.5 kPa) measured in some experiments.

2. *Temperature instrumentation*

Temperature measurements during expansion were required to determine the initial conditions for combustion experiments and to enable calculation of aerosol properties using the thermodynamic model, presented in Chapter 4. Two sizes of K-type thermocouples were used. For the required high frequency response during calibration studies of the expanding mixture a 25μm fine wire thermocouple was used. However, fine wires were too fragile to be used during combustion studies. Hence, in all work not requiring a fast response a 200 μm thermocouple was employed. The procedures for transient correction of thermocouples are discussed below. The thermocouples were connected, as required, via a home-built 12-way input selector to a Thermometer, Digitron Ltd, Model 2751-K, with digital display and analogue output. The digital display had a resolution of 0.1°. The analogue output was used for the computer recording of temperature histories. For each experiment, measurements were taken at 3 different locations, as shown in Fig. 3.3. This was required to verify spatial temperature uniformity during the expansion process.

3. *Thermocouple compensation*

Accurate measurements of temperature were an essential prerequisite to accurate characterisation of aerosol properties. Therefore, compensation of thermocouple readings was undertaken, to correct for their finite response to temperature fluctuations. Compensation for the time lag of the 25 μm thermocouple was performed according to Lawton & Klingenberg (1996). The corrected fluid temperature, T_f, is given by

$$T_f = T + t_0 \frac{dT}{dt} \tag{3.1}$$

where T is the measured temperature and t_0 is the characteristic time constant and is given by

$$t_0 = \frac{\rho c d}{4h} \tag{3.2}$$

Here ρ is the density of the wire material, c is its heat capacity, d the wire diameter and h is the heat transfer coefficient. A difficulty in the application of Eqs. (3.1) and (3.2) is the lack of information on the heat transfer coefficient. One may estimate values that range between 25 and 200 $Wm^{-2}K^{-1}$ depending on the assumed flow field during expansion. In the present work, the time constant was estimated by comparing measurements of the temperature during the expansion of dry air in the bomb with those calculated on the assumption of adiabatic expansion. This assumption represents a worst case situation, since any heat transfer from the vessel walls to the expanding gas will reduce the rate of temperature reduction. Comparisons were made under laminar and a range of turbulent conditions. The adiabatic temperature was calculated from pressure records using

$$T_2 = T_1\left(\frac{p_1}{p_2}\right)^{\left(\frac{\gamma-1}{\gamma}\right)} \tag{3.3}$$

where indices 1 and 2 denote the temperature and pressure before and after a given time intervall. The ratio of specific heats, γ, was taken to be 1.4 for dry air.

The best time lag correction was achieved using a characteristic time of 0.1s. This is illustrated in Fig. 3.4, which shows a comparison of measured, corrected and adiabatic temperature histories.

Measured temperature might also differ from the fluid temperature due to heat transfer from the hot junction along the thermocouple wire. Lawton & Klingenberg (1996) suggested that for good accuracy the length of the exposed wire between the thermocouple holder and the hot junction should be at least $6x_0$, where the characteristic length, x_0, is given by

$$x_0^2 = \frac{kd}{4h} \tag{3.4}$$

Here k is the thermal conductivity of the wire. Values of $6x_0$ were between 6 and 8 mm. Therefore, all thermocouples were built with a minimum length of 10mm. For turbulent conditions t_0 was a function of fan speed and values are presented in Table 3.1. Fully corrected temperature histories, with respect to instrument error and time lag are shown in Fig. 3.5 for 500 and 3000 rpm fan speed.

The procedures for instrument and thermocouple correction, as well as the removal of electromagnetic noise, were implemented using Microsoft Excel spreadsheets on a personal computer.

4. Data Acquisition

Pressure and temperature records were digitised on a Keithley Instruments Inc., DAS 801 analogue-to-digital conversion board (ADC), which was installed into an Elonex PC-433 computer. The overall accuracy of data acquisition was typically 0.01% full range ±1 bit. The signal inputs to the ADC were analogue voltages from the thermometer and pressure transducer amplifier. The output sensitivity of the thermometer was 1mV/° and that of the transducer amplifier 1mV/kPa. A typical temperature measurement had a bandwidth of approximately 50°, or 50mV and a typical pressure measurement had one of approximately 100-200 kPa or 100-200mV. The A/D conversion was 4096 bits full range and the most appropriate voltage input range for both pressure and temperature measurements was ±500 mV full range. This returned a resolution of 0.25°/bit, at an accuracy of 0.1° (0.01% full range). In addition to errors associated with the thermometer and ADC systems, the raw data displayed fluctuations of approximately ±1.2° at a frequency of approximately 50Hz, which indicated electro-magnetic noise from the mains electricity supply. This was minimised, using of a 5-point moving average smoothing routine, which reduced the fluctuations to approximately ±0.2°. The overall accuracy of data acquisition resulted in a maximum error of the temperature measurement of ± 0.55°. A similar analysis of the pressure records yielded a maximum error of ± 0.45 kPa. These values are used in Section 3.4, to asses the overall accuracy of the data produced from the present apparatus and instrumentation.

3.1.4 IGNITION SYSTEM

At the start of the present work, two ignition systems were available. One was a conventional 12V automotive coil system, with a spark energy of approximately 50 mJ. This was not sufficient to ignite aerosol mixtures at the low temperatures and pressures used in the present work. The other system was an aviation gas turbine ignition unit, provided by Rolls Royce plc. Initial experiments showed that the spark energy of approximately 5J was too high, resulting in significant spark enhanced flame propagation. Therefore, this system was replaced by a new one, which was designed in the electronics workshop of the School of Mechanical Engineering. It produced a spark with an energy of approximately 300 - 400 mJ and was found to offer a reasonable compromise between reliable ignition and minimal ignition induced combustion overdrive. The new system is shown in Fig.3.6. It consisted of a capacitor discharge unit and a discharge trigger. The trigger produced a small coil generated spark at the spark plug. This provided an ionised electrical path for the release of the capacitor charge, which supplied the main spark. The capacitor was charged, typically, to between 35 and 40V, using an adjustable DC power supply. A volt meter was used to monitor the voltage across the capacitor. An exact knowledge of spark energy was not required for the present research.

The mixture was ignited centrally in the bomb using a Miniglo model spark plug. This was held on an extension screwed into one of the horizontal 1" BSP ports of the bomb (see Fig. 3.3). The spark influence of the new system on flame development was shown to be not significantly greater than that of a conventional 12V coil ignition system at similar initial conditions.

3.2 INSTRUMENT SYNCHRONISATION

Accurate control of experimental conditions and data acquisition required the precise synchronisation of measurement equipment and data acquisition systems with the expansion and combustion events. The datum parameter for all experiments was the start of expansion. All equipment was triggered from a principal trigger switch, PTS, fitted to the expansion valve. This consisted of a micro switch which was actuated by the expansion valve lever, within 2° of lever movement and before the actual start of valve opening. Consistency of valve opening times is discussed in Section 3.1.2.

3.2.1 CALIBRATION EXPERIMENTS

Measurements of pressure, temperature and aerosol properties were synchronised with the start of expansion. The circuit is shown in Fig. 3.7. The PTS triggered a TTL pulse generator, which in turn started data collection on both, the ADC and the Malvern particle sizer. The Malvern was then triggered internally to take the desired number of measurements at a chosen sampling rate (see Section 3.5.1).

3.2.2 HIGH SPEED SCHLIEREN PHOTOGRAPHY

A Hitachi high speed camera was used for schlieren photography (see Section 3.5.2). The start of the high speed camera and the time of ignition were synchronised with the expansion process. The circuit is shown in Fig. 3.8. The PTS started an Omron H5CR countdown timer. This timer determined the time from the start of expansion to the start of the high speed camera, which was triggered by the Camera Controller, Model 'Gordon', Bowen Electronics. .The camera motor required some time to accelerate the film to the required framing rate. A trigger circuit in the camera controller was set to "10 metres of film", which was the length of film required to reach a framing rate of approximately 5000/s. The acceleration time for this setting was 0.53s. After a count of 10 metres of film, the controller delivered a trigger pulse to the ignition interface, which supplied a signal to the ignition unit to trigger the spark. The delay between the ignition interface relay and the breakdown of the spark was of the order of 2 ms. The greatest timing error in this system was that between the start of expansion and ignition, and it arose from the acceleration time of the camera, ±0.01s. However, this was negligible in terms of its effect on pressure, temperature and aerosol properties at the ignition event.

3.2.3 LASER SHEET IMAGING

Laser sheet imaging is discussed in Section 3.5.3. It required synchronisation of a rotating drum camera, copper vapour laser and the spark with the expansion. The circuit is shown in Fig. 3.9. The device for synchronising the drum camera shutter and the laser operation was a N-shot-controller, developed and built by Brian Leach, Thermodynamics Laboratory, with help from Oxford Lasers.

The sequence was started when the manually adjusted rotational speed of the drum camera was correct (Section 3.5.3). The PTS initiated the countdown timer, whose signal was fed into a 4-channel timer/pulse generator. From this a signal was released to the ignition interface and a TTL pulse started the N-shot-controller. A conventional shutter was used on the drum camera, to allow for film exposure during a time window, long enough for a burst of 43 laser pulses. The overall exposure time was set at the shutter in standard photographic increments. Prior to an experiment, the copper vapour laser had to be continuously pulsed to maintain correct operation temperature. This was facilitated with the laser's internal trigger. The N-shot-controller switched the internal trigger off, before opening the camera shutter via the drum camera controller. Then it triggered a burst of 43 laser pulses at the required framing frequency. After a pre-set time, to accommodate the closing of the camera shutter, the controller switched the laser back to its default mode (10kHz, internally triggered). The sequence of trigger events was checked on a LeCroy 9310A digital transient recorder.

3.3 MIXTURE PREPARATION

The preparation of aerosol mixtures consists of three parts including the pre-heating of the bomb to the initial temperature, the preparation of the gaseous pre-mixture, and the expansion process that generates the aerosol. These procedures are presented in this Section. Characterisation of the aerosol and the thermodynamic principles of the Wilson method are presented in Chapter 4.

The principal fuel used for this research was iso-octane, which is the closest single component fuel to gasoline. It was chosen because data for its gaseous combustion have been obtained for a wide range of experimental conditions at Leeds and are available for comparison with results from the present research. Additionally the evaporation and condensation properties of iso-octane were suitable for use in the current research apparatus, with regard to temperature and pressure limitations of the bomb. Iso-octane, 2-2-4-trimethylpentane, was supplied by Ultrafine Ltd and was specified to be at least 99.99% pure with 50 ppm maximal water content. Its molar mass was 114.23 kg/kmol.

For some experiments, discussed in Chapter 5, gaseous propane, substance no. N2.0, of 99% purity, supplied by BOC Ltd., was used. Propane was supplied at the required partial pressure to the bomb from bottles in the same manner as for bottled air.

Bottled industrial grade dry air was used in the fuel-air mixtures to minimise the possibility of water droplet generation during the expansion process, which might occur if inadequately dried air from the laboratory's compressed air supply were used. It was supplied by BOC Ltd., substance no. 1002, with a specified composition of: $H_2O < 250$ ppm, $CO < 10$ ppm, $CO_2 < 500$ ppm and oil < 1ppm. The oxygen content was 21 ±0.5% , and its molar mass 28.96 kg/kmol. Because both air and fuel were pure, the effects of foreign species on combustion were assumed to be negligible.

3.3.1 PRE-HEATING OF THE BOMB

Prior to experiments the bomb was heated, with its internal heaters, to a temperature between 303 and 348K, according to the experimental requirements. This ensured complete evaporation, when liquid fuel was used. It also provided the required temperature datum to enable comparison with the data of other workers, for both gaseous and aerosol experiments.

In order to ensure spatially homogeneous condensation, a homogeneous temperature distribution throughout the mixture was required. For this, the bomb was heated to a preliminary value above the desired initial temperature and then left to cool and homogenize for approximately 1 hour. During this period, the heaters and fans were switched off, because this yielded a more homogeneous temperature distribution. Temperature uniformity was ascertained by monitoring the temperature on the outside of the bomb in three locations, as shown in Fig. 3.3. Good temperature homogeneity across the bomb was assumed when the difference between the measurements was less than 2°.

3.3.2 PREPARATION OF GASEOUS PRE-MIXTURES

Before the introduction of fresh combustible mixture, the bomb was evacuated and flushed with air to remove residuals from previous experiments. Liquid iso-octane was injected into the bomb at a pressure close to vacuum, to aid complete and fast evaporation. The fans were run at 1500 rpm to improve atomisation of the liquid fuel. The appropriate volume of liquid fuel for given initial conditions in terms of temperature, pressure and overall equivalence ratio, was calculated using the stoichiometric equation and the ideal gas law. This procedure is described in Chapter 4. The fuel was introduced into the bomb, using either 5 ml or 10 ml Hamilton Microliter^{TM} glass syringes. The accuracy of the injected volumes was better than ±0.015 ml and ±0.03 ml, respectively, yielding an equivalence ratio accuracy within ±0.5%. The pressure in the bomb was monitored during fuel injection to provide an independent check of the equivalence ratio and to ensure complete fuel vaporisation. At higher initial temperatures, above 323 K, the pressure measurement was in good agreement with the pressure expected for the given volume of fuel injected, which indicated complete vaporisation of the liquid fuel. However, most experiments were performed at initial temperatures of 303 and 313 K. At these conditions the fuel partial pressure was up to 10 % less than expected. A possible reason for this was fuel impingement on the walls. To investigate this, large fuel drops that inevitably dripped from the tip of the injection pipe during fuel injection were collected in a tea spoon, which was fixed underneath the pipe tip. At a fan speed of 1500 rpm the time taken to completely evaporate one tea spoon full of fuel was between 5 and 7 minutes. This clearly demonstrates that there is a possibility of non-evaporated fuel adhering to the wall. However, the amount of this is limited to that which is represented by the difference in measured and calculated partial pressure. To minimise the possibility of fuel being absorbed into deposits on the bomb walls, they were cleaned extremely carefully by physical and chemical means. However, the problem could not be resolved completely and a compromise was applied. In such cases where the partial pressure measurement was more than 5% too low, additional fuel was injected, such that the required equivalence ratio was equal to the average of those calculated by the two methods. Hence, the overall accuracy of mixture strength for the initial temperatures 303 and 313 K was ±5%. For higher initial temperatures it was ±0.5%.

After fuel injection air was added in two stages, first up to atmospheric pressure, where the initial experiment temperature was conditioned, and than up to the initial pressure for the experiment, typically 2 bar. This is explained below.

3.3.3 LEAKAGE

Due to the complexity of the bomb and auxiliary equipment, it was not possible to prevent leakage. This caused errors in mixture preparation of the gaseous pre-mixture during the filling process and due to the inability to fill the bomb isothermally to a precise target pressure and temperature. Although these errors were small, and might be neglected for gaseous mixtures, it was very important for the present work to adequately take them into consideration since the aerosol properties are a strong function of pre-expansion temperature and equivalence ratio.

Under near vacuum (approximately 2 kPa) leakage into the bomb was approximately 0.15 kPa/minute, which was acceptable, because fuel injection took place over only approximately 10s and the rise in partial pressure due to fuel evaporation was typically 3.2kPa, several orders of magnitude greater than the change in pressure due to leakage. However, leakage was a potentially more serious problem at elevated pressures, at which the seals were not as effective as at low pressures. Fuel and air leaking out of the bomb during the filling process from atmospheric to the target pressure reduced the equivalence ratio. The filling process typically took approximately 10 seconds for a target pressure of 210 kPa. The rate of pressure loss at this pressure was approximately 0.25 kPa/s and assuming a linear pressure increase during filling, the average rate of pressure loss during filling was half that at target pressure. For a filling pressure of 210 kPa the displacement of mixture with air was equivalent to 1.2 kPa, 0.6% of the target pressure. Since this affects fuel and air proportionally, 0.6% of fuel was displaced with air, which is acceptable.

Because there is no leakage, when the bomb pressure is equal to the atmospheric pressure, the mixture was initially made up at atmospheric pressure with the correct quantity of fuel, but only part of the required air. The mixture was held at this pressure for some time to ensure maximum evaporation of the fuel and best temperature homogeneity. The temperature at atmospheric pressure had to account for the temperature drop when switching the fans off and for the decrease of temperature caused by slow expansion due to leakage. The bomb was then swiftly filled to the required target pressure above the pre-expansion pressure, to keep mixture loss during filling to a minimum.

For typical initial conditions, at the start of expansion, of T_I = 303 K and p_I = 200 kPa the gas temperature inside the bomb was conditioned at 305.5K at atmospheric pressure with the fans running at 1500 rpm and with an outer bomb wall temperature of 301 to 302 K. The bomb was swiftly filled with air to 210 kPa, where the fans were switched off immediately, which caused a drop in mixture temperature of approximately 1° - 1.5°. After a leakage period of approximately 40 seconds, from 210 to 200 kPa, this led to a temperature of 303 K. With some experience this method returned an accuracy of T_i better than ±0.5 ° at a p_i within ±3 kPa of the target. The effect of these tolerances on overall apparatus accuracy is assessed in Section 3.4.

3.3.4 GENERATION OF AEROSOLS

The Wilson cloud chamber method (Wilson, 1895 & 1911) was used to generate a homogeneously distributed aerosol in the cloud chamber with a near monosize droplet diameter distribution. The expansion process causes negligible levels of turbulence, which allows for the investigation of laminar aerosol combustion. Following mixture preparation as described above, the expansion valve was opened and the mixture allowed to expand into the expansion vessel. When the temperature became lower than the saturation temperature of the fuel, condensation occurred. The drop diameter, number density and liquid fraction were a strong function of pre-expansion conditions and expansion duration. A detailed thermodynamic analysis of the process is given in Chapter 4, as are pressure and temperature histories for laminar and turbulent conditions.

For combustion studies, the aerosol was ignited at selected times after the start of expansion, allowing the variation of the initial conditions at ignition, in terms of liquid and gaseous equivalence ratio. Combustion occurred while the mixture was expanding. However, since the combustion duration was short relative to the expansion duration, typically of the order of 20 to 60ms, quasi steady state was assumed with respect to the unburnt mixture.

For turbulent experiments, the expansion duration to pressure equilibrium was approximately 0.15 seconds. The quick entrainment of warm air from the chamber wall regions, when the fans were switched on, only allowed the maintenance of an aerosol for a very short period. Therefore, ignition was triggered at the point of lowest temperature, which was close to the point of pressure equilibrium. Temperature increase after that was slow, relative to the combustion duration, and pressure was nearly constant. The combustion duration was typically less than 10ms and, hence, the assumption of quasi steady conditions also could be applied for turbulent conditions.

3.4 SUMMARY OF MIXTURE PREPARATION ERRORS

Errors, caused by the use of equipment described in this chapter, have been estimated and the combined errors affect temperature, pressure and mixture strength accuracy. Individual errors are given in each section. However, in any given situation it is likely that some of these will cancel each others out. Therefore the 95% confidence interval on errors in pressure, temperature and mixture strength was calculated. A summary of errors is given in Table 3.2 and these combined errors are discussed in Chapter 4 in relation to the variations in aerosol properties. Subsequent variation in combustion parameters due to fluctuations in mixture properties are discussed in Chapter 5.

3.5 INSTRUMENTATION FOR AEROSOL AND FLAME ANALYSIS

Aerosol properties were determined with Malvern particle sizing equipment, and by equilibrium calculations based on pressure, temperature and overall equivalence ratio, as discussed in Chapter 4.

The flame growth in an aerosol mixture was recorded with high speed schlieren cine photography, to obtain flame speeds and burning velocities, and with laser sheet imaging.

3.5.1 AEROSOL CHARACTERISATION

For the present research, characterisation of the aerosol at the time of ignition was required. Parameters of importance were the drop size and the liquid fuel fraction. With the equipment available to the author, full characterisation in situ was not possible. Instead a Malvern 2600 and a Mastersizer S were available. This Section is based on the technical specification and nomenclature used for the Malvern 2600. Differences with respect to the Mastersizer S, are explained where appropriate.

1. Principle of operation

A good description of the principle of operation is given in Jones (1993) and in Taylor (1992). When a beam of light strikes a particle, the light is scattered by reflection and refraction in all directions. The spatial distribution of the scattered light is a function of the wavelength of the incident light and the particle size. An example for a 6μm diameter liquid droplet is shown in Fig. 3.10. If the wavelength of the incident light, λ, is small compared to the diameter of the particle, D, the shape of the forward scattered lobe is not sensitive to refractive index or shape of the particle, and thus is a unique function of particle size (Hodkinson, 1966). For sufficiently large particles the forward-scatter can be adequately described by the Fraunhofer theory of diffraction.

The beam geometry of a Malvern particle sizer is shown in Fig. 3.11. A collimated beam of laser light is traversed through the measurement volume, in which some light is scattered by droplets, and then onto an detector array of concentric annular detectors. The unscattered light is focused to the axis at the detector, where it is recorded to allow the concentration of the sample to be determined. Light that is scattered from particles is detected on the array at locations away from its axis (Taylor, 1992). The scattering distribution yields the size distribution. The instrument response was checked using particles of known size distribution, as discussed below in Paragraph 4.

2. *Measurements with the Malvern 2600*

In the present arrangement the Malvern 2600 was used in situ. The transmitting and receiving modules were located separately on adjustable tables on either side of the bomb, as shown in Figs. 3.1 & 3.2. Measurements were performed along the central axis of the bomb.

The minimum particle size that can be detected by the Malvern 2600 is determined, among other parameters, by the focal length of the receiver lens. The focal length of 300 mm, used throughout the present work, allowed the measurement of particles down to 5.8 μm. The distribution of droplets below this size was estimated from the measured light distribution by a mathematical algorithm, that was incorporated in the Malvern analysis software. Details of the algorithm were not documented in relevant user handbooks. Errors due to the inability to measure small droplets were assumed to be small, because most droplets were probably above the 5.8 μm limit. However, it had implications for calibration measurements with spherical glass particles by the present author, some of which were smaller than 5.8μm. This is discussed in Paragraph 4.

A further potential error in the present work was caused by the necessary large optical path length, due to the dimensions of the bomb. This resulted in some "vignetting", which is the scattering of light beyond the reach of the receiving lens. This leads to an under representation of the smallest drop diameters. Vignetting occurs, when a particle is too far away from the receiving lens, at a given scattering angle, as shown in Fig. 3.10. The effect of vignetting on the volume distribution could not be quantified precisely. However, it was estimated to be less than 5%.

Erroneous measurements can also occur under turbulent conditions or in the presence of temperature gradients. Here, the resulting density gradients in the dispersant gas produce a scattering signal that indicates the presence of very large particles. These erroneous sizes were filtered, when necessary, using the built-in functions of the Malvern. Results were checked against measurements in which density gradients were negligible.

The Malvern 2600 was capable of one measurement every 1.5 seconds, which yielded 3 measurements per expansion event of approximately 4.5 seconds duration. Time resolution was improved by taking 3 such series of measurements, each one offset from the previous by 0.5

seconds. This returned a set of 9 data points at 0.5 second intervals. Results are presented in Chapter 4.

Further descriptions and technical specifications of the instruments are available in the appropriate Malvern instruction manuals.

3. Accuracy

The primary outputs of a Malvern particle sizer are size distribution, based on particle volume, and the attenuation of the laser beam. The accuracy of the volume median diameter, $D_{V0.5}$, of the Malvern 2600 was ± 4%, that of the Mastersizer S was better than ±1%. These accuracies were much better than the error caused by temperature and pressure variations in the mixture.

The liquid volume concentration, C, in the measured aerosols, was calculated, using the Beer-Lambert law, from the attenuation of the laser beam and the size distribution. This is given in the Malvern 2600 manual by

$$C = \frac{100\ln(1 - Ob)}{-\frac{3}{2}b\sum\frac{V_i Q_i}{d_i}} \qquad (3.5)$$

where Ob is the obscuration of the laser beam and b is the effective beam length, which is defined as that length of the beam in which there are particles. Q_i is the extinction coefficient for a drop diameter D_i. V_i is the volume occupied by droplets of diameter D_i. The obscuration of the laser beam is given by

$$Ob = 1 - \frac{\textit{Incident Laser power}}{\textit{Laser power at centre detector}} \qquad (3.6)$$

The most significant error in the application of Eq. (3.5) is the determination of b. The distance between the windows was 390mm, and it was estimated that, due to heat exchange between the walls and the mixture, there was a “droplet free” zone of approximately 30mm at each end plate of the bomb. Therefore, the effective beam length was estimated to be 320mm. The error of measurements of liquid volume concentration, due to the uncertainty in this was estimated to be ±10%.

4. Calibration measurements

Hollow spherical glass beads, Sphericel$^{\text{TM}}$ 110P8 (Potter Industries Inc.), with a mean density of 1,1 g/cm^3 were used to investigate the accuracy of measurements with the Malvern 2600. Shown in Figure 3.12 are the size distributions of the beads measured by the present author and as specified by the manufacturer. The crossed represent measurements with a microscope, by the present author. The solid curve shows the average of several measurements in the bomb with the Malvern 2600. The microscope measurements were obtained by placing a small quantity of beads on a microscope slide and then measuring their diameters with a NIKON V-16-D Profile Projector at a magnification of 50. The in situ bomb measurements were obtained after injection of 5ml of glass beads into the bomb, using a small amount of compressed dry air. The beads were distributed quickly and with no visible inhomogeneities throughout the bomb volume, regardless whether the fans were turned on or not. Clearly there was a significant difference between the three sets of data, with the specification supplied by the manufacturer differing considerably from both sets of measurements by the present author. However, there is a discrepancy between the distribution and the value of D_{32} that were provided by the manufacturer. The claimed value of D_{32} was 11.7 µm, but its value calculated from the provided size distribution by the present author was only 7.7 µm. The average value of D_{32} obtained from the current Malvern measurements was 10.4 µm. Hence, it is probable that the manufacturer's distribution was erroneous. The difference in the shape of the distributions for the present Malvern and microscope measurements probably is due to agglomerations of particles, which were observed but neglected during microscope measurements, but would have been recorded as one large particle by the Malvern 2600. Also, particles smaller than approximately 5 µm could not be recorded by either the Malvern or the microscope. However, the Malvern software provided an estimate of the volume contained in particles smaller than the detectable range, which is represented in Fig. 3.12 by the non-zero initial data point. It can be concluded, that the present implementation of the Malvern system produced acceptable data.

The effect of the following parameters on size and size distribution measurements were investigated:

- deposition of particles on the windows
- laser obscuration
- instrument settings
- different levels of turbulence

Deposition of particles on the windows was inevitable, particularly when the fan were used. Measurements of deposited seed on the windows, with the bomb being fully evacuated, provided an estimate of the effect of deposition on measurements. Measurements of the deposition layer had the same size distribution and similar values of D_{32} than those of suspended particles in the bomb. Measurements of laser obscuration, due to deposition alone, showed a loss of light of up to 33% with fan speeds of up to 3000 rpm. Therefore, measurements were taken immediately after seed injection, when window deposition was low. Deposition when the fans were switched off, only caused obscuration of up to 3%.

Different amounts of beads were used to assess the effect of obscuration. Measurements with obscuration values up to 80 % usually were consistent with those at optimum obscuration levels of up to 50%. Measurement reliability became progressively more worse at higher obscuration rates. The effect of other parameters was not significant.

5. Measurements with the Mastersizer S

As discussed above, the Malvern 2600 could produce only three sets of measurements within a single expansion event. Therefore, Malvern Instruments Ltd. kindly made a Mastersizer S available to the present author. This had a much higher measurement frequency of up to 500 Hz, which was in excess of that required for the present work. However, a serious limitation of the system was its short optical path length of only 84 mm. Therefore, it was not possible to use the system in situ. Instead it was used in conjunction with an auxiliary bomb, initially used for combustion studies by Witchell (1973). It consisted of a stainless steel cylinder, internal diameter 51 mm and 51 mm length. Both ends were covered by schlieren quality glass windows. The aerosol mixture was extracted from the combustion bomb via a 25mm diameter by 380 mm long copper pipe into the auxiliary bomb, and finally through a $^3/_8$" exhaust pipe. The arrangement is depicted in Fig. 3.13. The flow resistance in the exhaust pipe lead to an expansion time that was similar to that of an expansion through the 6 mm orifice plate into the expansion tank. It was not possible to quantify the influence on the aerosol of the flow through the pipe to the auxiliary bomb. Therefore, these measurements were used mainly to observe trends in aerosol characteristics. Results are presented in Chapter 4.

3.5.2 HIGH SPEED SCHLIEREN PHOTOGRAPHY

The rate of flame growth was recorded, using high speed schlieren cine photography. The system is shown in Fig. 3.14. It was previously used by various researchers which include Lawes (1987), Bradley et al. (1998) and Haq (1998).

A Uniphase 20 mW helium-neon laser, with a wavelength of 632 nm, was used as the light source. The laser light was expanded up to a diameter of 150 mm by an Olympus A40 microscope objective, where it was collimated by a 150 mm diameter x 1000 mm focal length lens. After passing through the two windows of the explosion vessel, a second, identical lens was used to refocus the parallel beam onto a 2mm diameter pinhole. A Hitachi model HM16 high speed camera, fitted with a lens Nikkor 50mm/1:2, was positioned behind the schlieren focus to record flame propagation on 16mm B/W film, Ilford HP4 or HP5. For analysis, the films where back projected onto an opaque screen, where their image, magnified by a factor of approximately 40, was measured in detail. Schlieren photography produces a projection through the flame, which readily allows for the derivation of flame growth rate. However, it produces a two-dimensional picture of a three-dimensional structure and, hence, silhouetting leads to a loss of detail. The analysis of flame structure can be improved, using laser sheet imaging, which is discussed in Section 3.5.3.

3.5.3 LASER SHEET IMAGING

Planar Mie Scattering uses a thin sheet of laser light to produce a cross-sectional two dimensional image of a three dimensional flame. The light is scattered from seed particles, which may be fuel droplets or some arbitrarily introduced seed. The seed evaporates, burns or sublimes as it crosses the flame front and consequently does not scatter light, while the seed in the unburnt mixture scatters light. A planar cross-section of the flame is imaged, perpendicular to the incident light sheet and the flame is identified as the frontier between the bright unburned, and the dark burned regions in the illuminated zone (Durao and Heitor, 1990). The arrangement is shown in Fig. 3.15.

The system used in the present work was fully described by Gillespie (1998), and only brief details are given here. A drum camera, Cordin 321, equipped with a lens UV-Nikkor 105mm/1:4.5, was used in conjunction with a copper vapour laser, supplied by Oxford Lasers Ltd., Model LS20-50. The laser wavelength was 510.6 nm (green), and the light energy was 2 mJ/pulse, which provided sufficient light for flame photography. Further technical details of laser and camera are provided in the appropriate user manuals.

Unlike a continuous wave laser, the copper vapour laser produced light pulses of approximately 15ns width, which were utilised by the drum camera instead of a shutter. In the present work each pulse gave one exposure and the camera's own shutter prevented exposure before and after a burst of pulses. The framing rate was 2000 Hz and 43 images per event were recorded on 35mm Kodak Tmax 3200 ASA b/w film. This provided a 21.5ms sequence of the flame development. Because a typical combustion event was of 30 to 40 ms duration, only part of such an event could be included. Therefore, the laser was triggered at some time after ignition, to record the main section of flame development. The trigger circuit is described in Section 3.2. The laser beam, 25mm in diameter, was manipulated, using a combination of a spherical bi-convex lens to focus the laser beam, $f = 1000$ mm, and a plano-convex cylindrical lens, $f = 1000$ mm, to expand the beam in one plane to form a sheet, as shown in Fig. 3.15. The sheet passed through a vertical plane in the centre of the bomb, orthogonal to the direction of flame observation. The sheet thickness was approximately 0.3 to 0.5 mm, which is thin enough, relative to the overall dimensions of the flame, to provide a true 2-dimensional image. However, the beam width was restricted by the use of the side window. Figure 3.16 shows the laser sheet and the location of the images recorded in the present work. The field of view was 45 x 45 mm, which provides a sufficiently large, yet detailed image for analysis.

Initially aerosol droplets were the sole source of scattered light. Since, this only showed the evaporation boundary ahead of the flame front, cigarette smoke was added in some experiments, to revealed details of the flame front. Wirth et al. (1993) found, that tobacco particles burned out immediately at the flame front, to generate good contrast between burned and unburned regions. However, the use of smoke affected the process of condensation. It provided condensation nuclei, which caused the generation of an aerosol cloud, which was too dense to visualise the sheet image on film. The number density of droplets and the liquid fraction were probably much higher, relative to experiments without smoke. However, these effects could not be quantified with the present instrumentation. Only small quantities of smoke were used, which produced only a very weak contrast at the flame front. With the aerosol properties unknown, only a qualitative analysis of the images was possible. This is discussed in Chapter 5.

3.6 IMAGE PROCESSING

3.6.1 SCHLIEREN

Films, obtained as described in Section 3.5.2, were developed by the present author, using a Bray Film Processor. Flame images were viewed with a Vanguard Projector, which back projected the 16mm film onto a 30×50cm opaque screen. Flame diameters were measured in three axes, horizontal, vertical and at 45°, and the average was used in the subsequent analysis. A calibration mark, attached to the bomb window and representing a distance of 60mm, was used to scale the measurements to true distances. The time between frames on the film was established using timing marks, which were produced by a light emitting diode, that was built into the camera, flashing at a constant frequency of 1kHz.

From time and distance measurements flame radius against time data were calculated. These were analysed to derive flame speed and burning velocity. This is discussed in Chapter 5.

3.6.2 PLANAR LASER SHEET IMAGES

Images obtained with the laser sheet imaging technique, discussed in Section 3.5.3, were digitised, using a Nikon LS-1000 35mm film scanner at a resolution of 50pixels/mm. They were processed to yield flame speed from consecutive images and to obtain the velocity of the droplets ahead of the flame front.

Particle image velocimetry, PIV, was used to obtain droplet velocities ahead of the flame front. The principle of PIV is explained in Section 3.6.3. This was undertaken in collaboration with Dr. Robert Woolley, a Research Fellow in the School of Mechanical Engineering, and Mr. Francois-Xavier Demoulin, a visiting research student from the Universitė de Provence, Marseille. The present author gained only a rudimentary knowledge of the technique, the full detail of which are documented in Atashkari (1997), who used it for gaseous combustion in S.I. engines and on a V-burner. PIV analysis was performed, using a software package, VISIFLOW (AEA Technology, 1997).

3.6.3 PARTICLE IMAGE VELOCIMETRY

A good description of the principle of particle image velocimetry was produced by Atashkari (1997). PIV comprises a class of flow measuring techniques, that is characterised by the recording of the displacement of small particles suspended in a fluid. A number of reviews of this technique have been published (e.g. Lauterborn, 1984, Buchave, 1993). The principle of PIV is, to illuminate the flow with a strong light source and to record the scattered light from tracer particles, in the present work on 35mm b/w film as described in Section 3.5.3. In order for the tracer particles to provide detailed information on the flow, they must be present in sufficient concentration, and have the right size to accurately follow the flow field. Therefore, the choice of seeding particle and the method of introducing them into the flow are important aspects of PIV.

The measurement of velocity involves the measurement of a travelled distance in a known time interval. The arrangement shown in Fig. 3.17 illustrates the basic principle of the recording process. Two spatially coincident laser sheets at a known time separation provide two images of particles on a recording medium. The laser sheets must be dimensioned so that the sheet thickness is thicker than the cross plane displacement of the particles between image pairs, and thin enough for the flow to be assumed to be two dimensional.

As shown in Fig. 3.18(a) the image plane is divided into equal interrogation areas, which are usually regularly spaced, and their size determines the spatial resolution. Providing the dimensions of the interrogation area are larger than the maximum particle displacement, there will be particle image pairs relating to the motion of the recorded flow. In most practical cases an interrogation area will include many particle image pairs along with some single images (due to particles crossing the plane) and stray light from the surrounding flow (not reflected from optic components). The usual procedure is to examine consecutively individual interrogation areas to evaluate a velocity vector for each area. Figure 3.18(b) illustrates an idealised interrogation area including two pairs of images and no single particle images. The horizontal and vertical displacements in the object plane, the plane at which the sheet intersects the flow, Δx_0 and Δy_0, are found by determining the displacements in the image plane (Fig. 3.17), Δx_i and Δy_i, on the recording medium. Knowing the magnification, M, of the optical system, and the time separation between the two sheets, Δt, the velocity projections on the measurement plane, u_x and u_y, can be evaluated

$$u_x = M\frac{\Delta x_i}{\Delta t} \qquad (3.7)$$

$$u_y = M\frac{\Delta y_i}{\Delta t} \qquad (3.8)$$

After processing, these yield an essentially continuous distribution of velocity vectors, as shown in Fig. 3.19. Because of the random distribution of particles in the flow, a sufficient seed concentration, to ensure at least one particle image pair in each interrogation area, will result in most interrogation areas having considerably more than one pair. Hence, the evaluation of displacement can no longer simply rely on the measurement of the separation of a single image pair. More sophisticated methods, involving probability analysis or correlation techniques must be applied. These have been discussed e.g. by Atashkari (1997). In case of double exposed single pictures an auto correlation is applied. This technique does not yield information about the direction of velocity vectors, hence a method is needed to resolve the directional ambiguity. If the image information is recorded in two separate pictures, one for the first illumination and one for the second, a cross correlation can be applied to find the displacement without directional ambiguity.

The objective of PIV in the present work was, to find the velocity field of the droplets, rather than that of the gas. The droplets had excellent scattering properties and their number density was suitable for PIV. The droplet motion was analysed directly and no additional seeding was required.

T_I [K]	303	323	323	323	323	323	323
p_I [kPa]	200	440	440	440	440	440	440
Fan Speed [rpm]	500	500	1000	1500	2000	2500	2500
u' [m/s]	0.83	0.83	1.67	2.5	3.33	4.17	5
t_0 [s]	0.04	0.027	0.02	0.016	0.014	0.012	0.011
$6\,x_0$ [mm]	3.7	3.25	3.1	2.8	2.6	2.5	2.35
Correction Tolerance	-1°	-0.5°	-0.25°	>0.1°	>0.1°	>0.1°	>0.1°

Table 3.1: *Thermocouple compensation parameters x_0 and t_0 and estimated compensation errors for turbulent initial conditions examined in the present work. The overall equivalence ratio was 1.0 in all cases.*

TEMPERATURE

Accuracy of K-type thermocouple	max. ±0.3°
Mixture preparation	max. ±0.5°
Data acquisition accuracy	max. ±0.55°
95% confidence interval on 6 data points	max. ±0.7°

PRESSURE

Accuracy of transducer / amplifier combination	±0.1% = ±0.2 kPa at 200 kPa
Mixture preparation	max. ±3 kPa
Data acquisition accuracy	max. ±0.45kPa
95% confidence interval on 6 data points	max. ±2.5 kPa

EQUIVALENCE RATIO

Initial equivalence ratio decrease du to leakage	0 - 0.6%max
Accuracy of injected fuel volume	±0.5%
Accuracy of compensation of fuel loss due to wall impingement	±5%
95% confidence interval on 6 data points	±4%

Table 3.2: *Estimated maximum errors on temperature, pressure and overall equivalence ratio.*

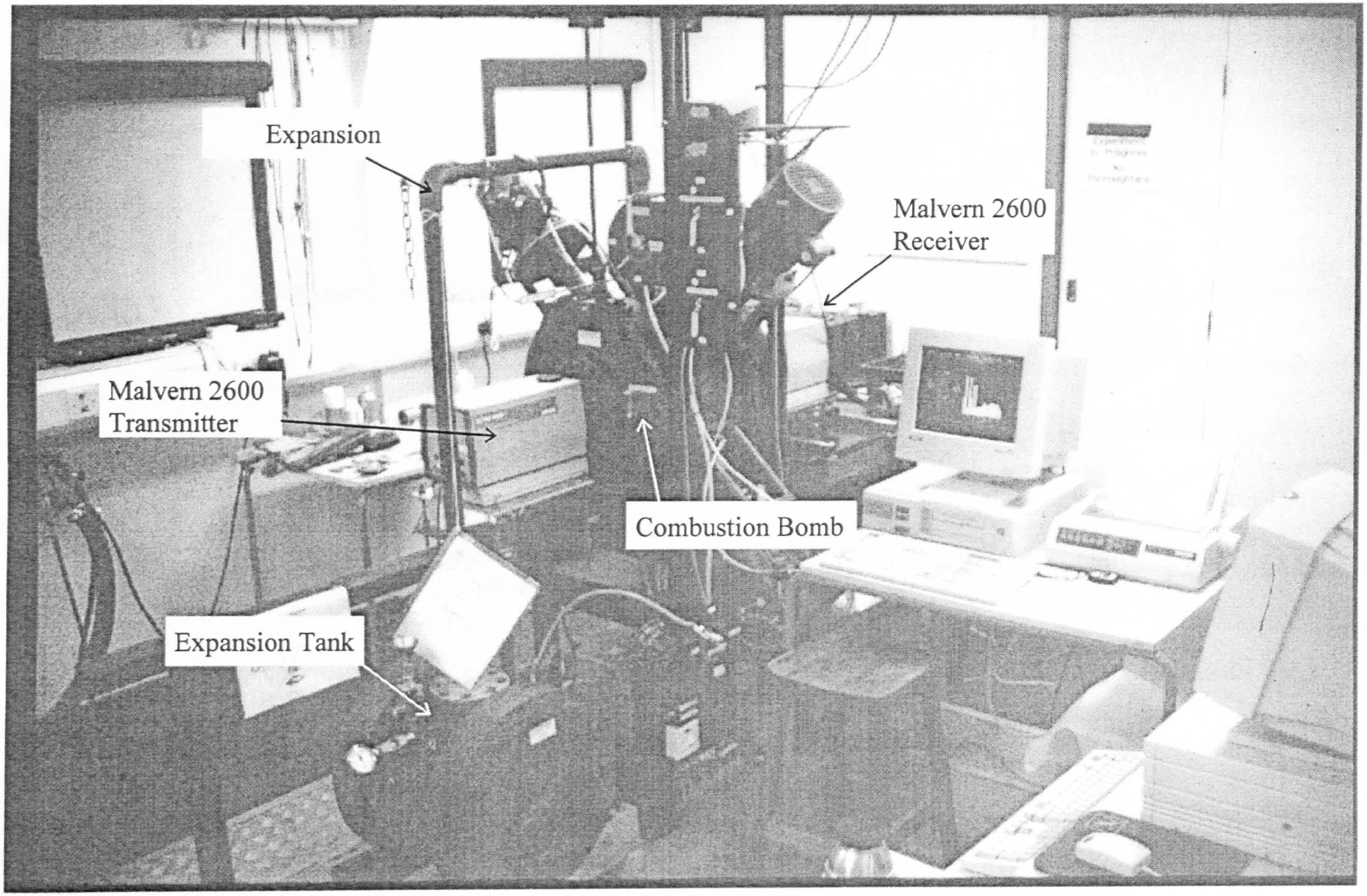

Figure 3.1: *Aerosol combustion apparatus with Malvern 2600 particle sizer and auxiliary equipment.*

Figure 3.2: *Schematic of aerosol combustion apparatus with schlieren system and in-situ Malvern particle sizing equipment.*

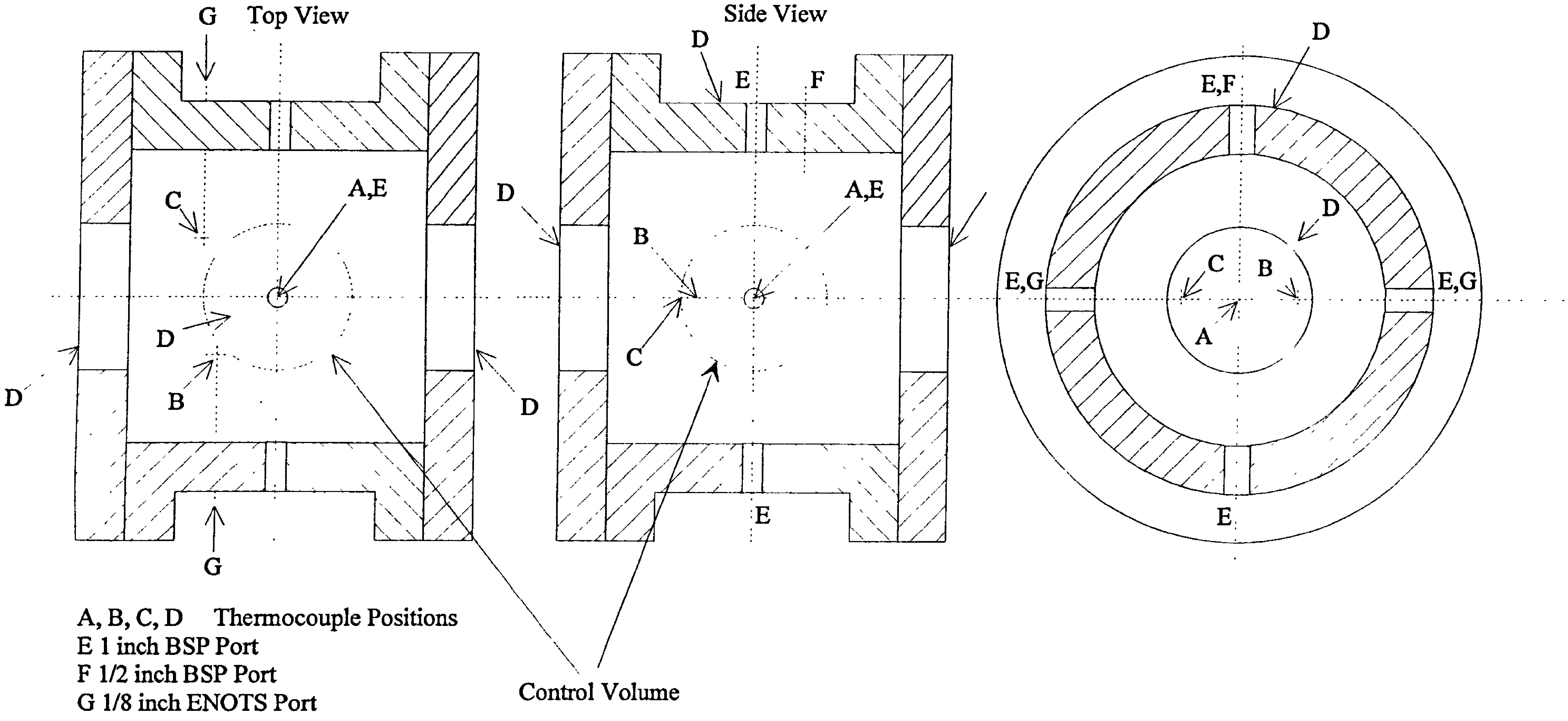

Figure 3.3: *Schematic of combustion bomb with ports and thermocouple locations.*

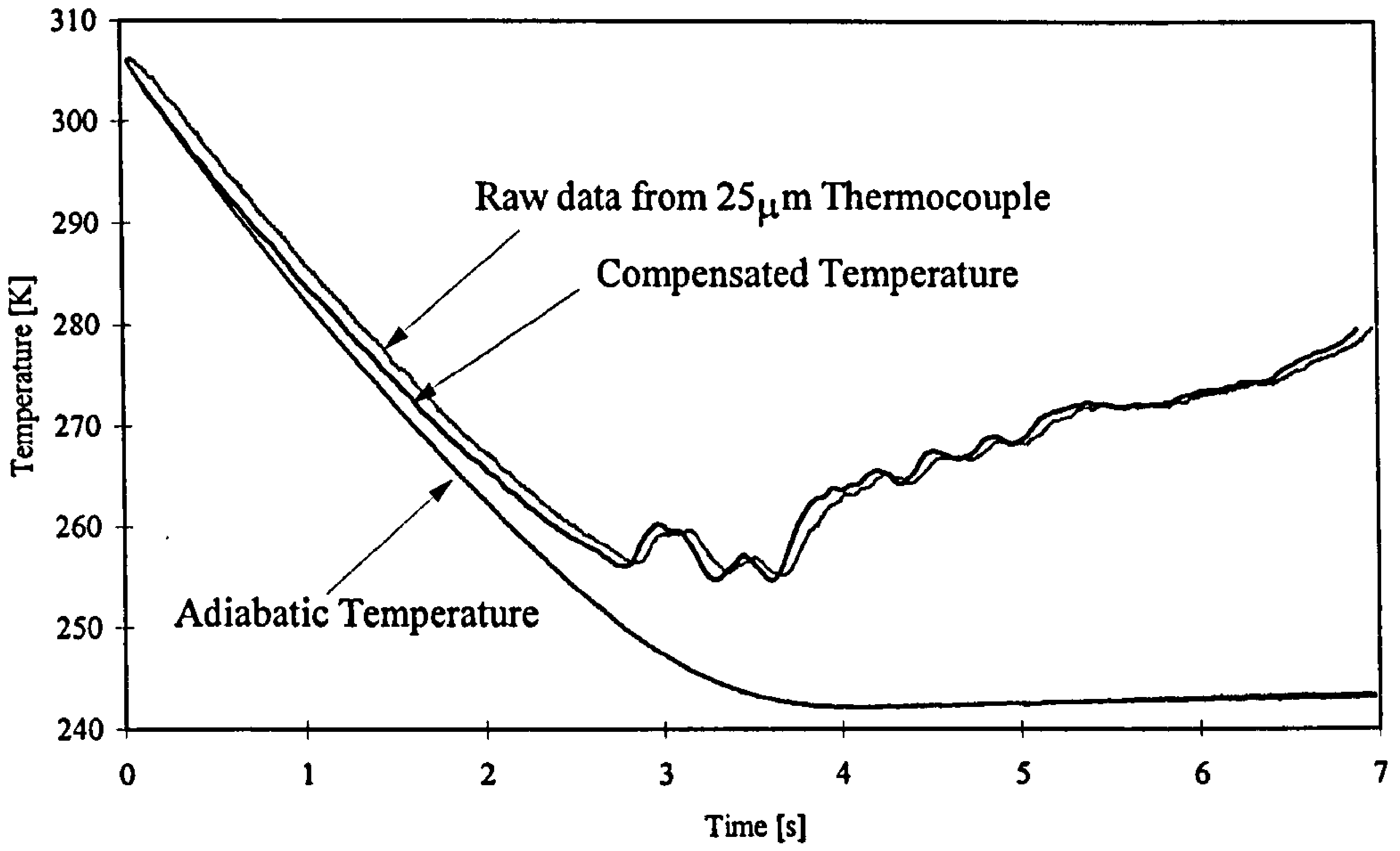

Figure 3.4: *Thermocouple compensation for laminar temperature records.*

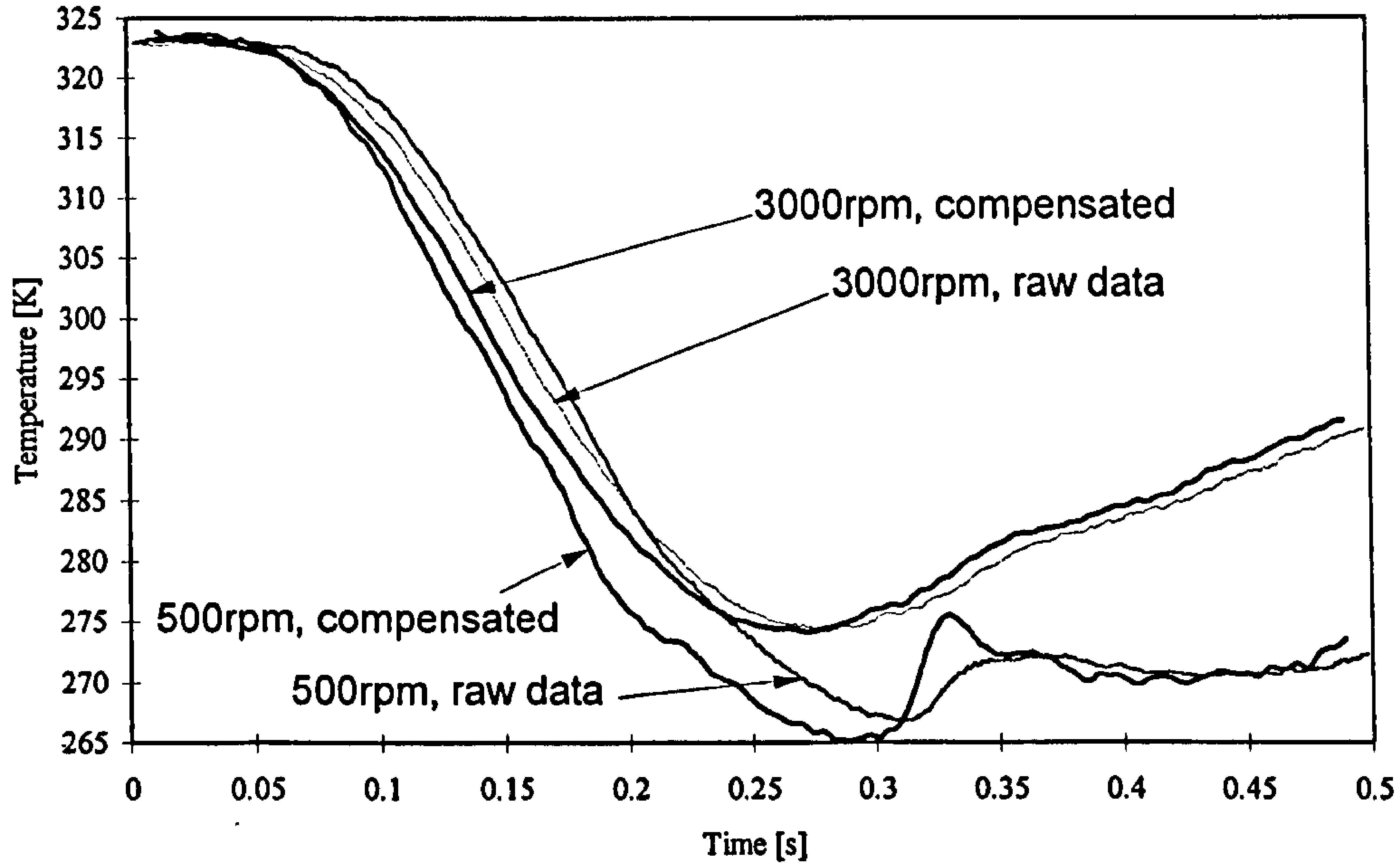

Figure 3.5: *Temperature histories during expansion under turbulent conditions; Raw data and compensated measurements are shown.*

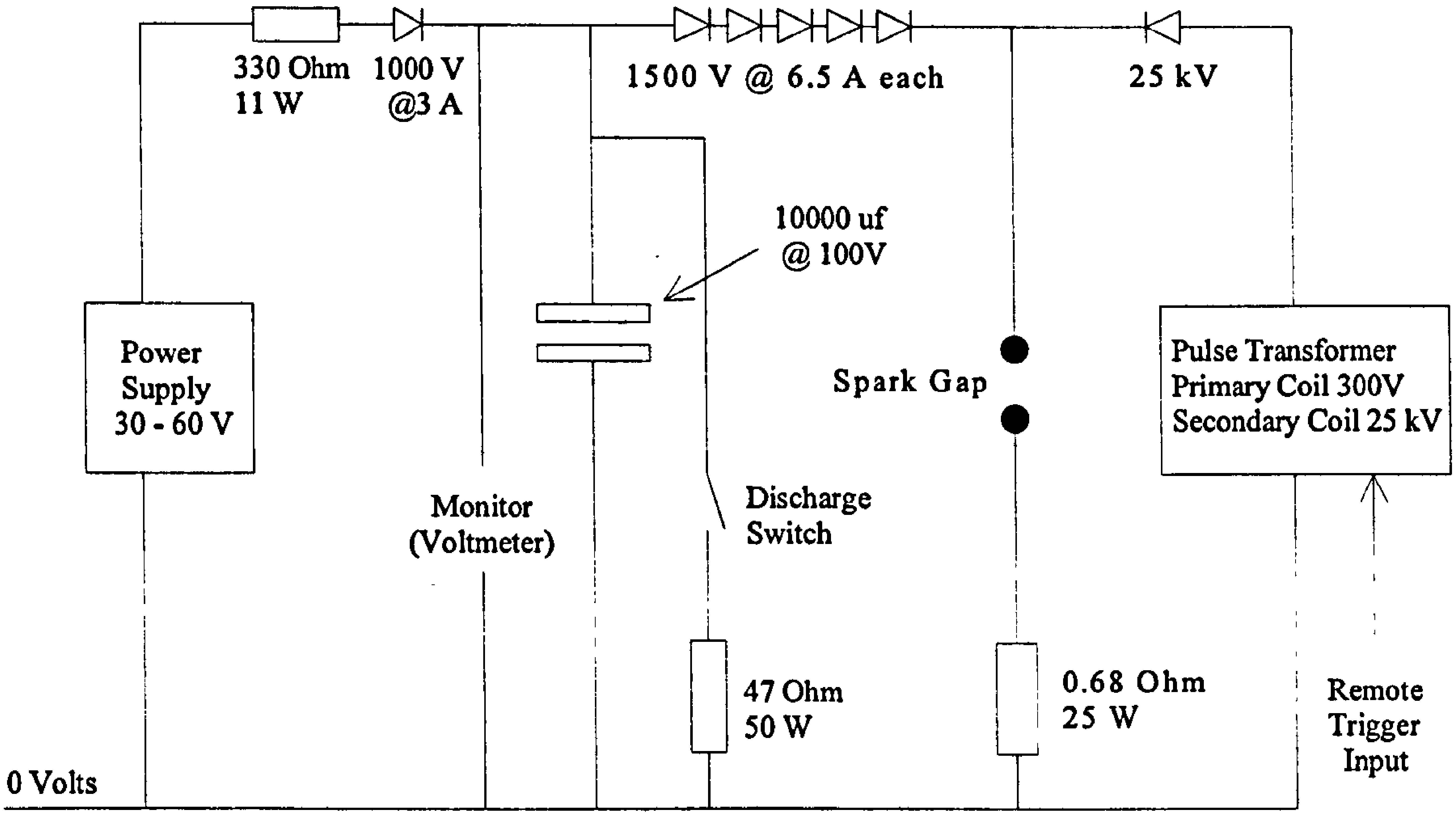

Figure 3.6: *Ignition system.*

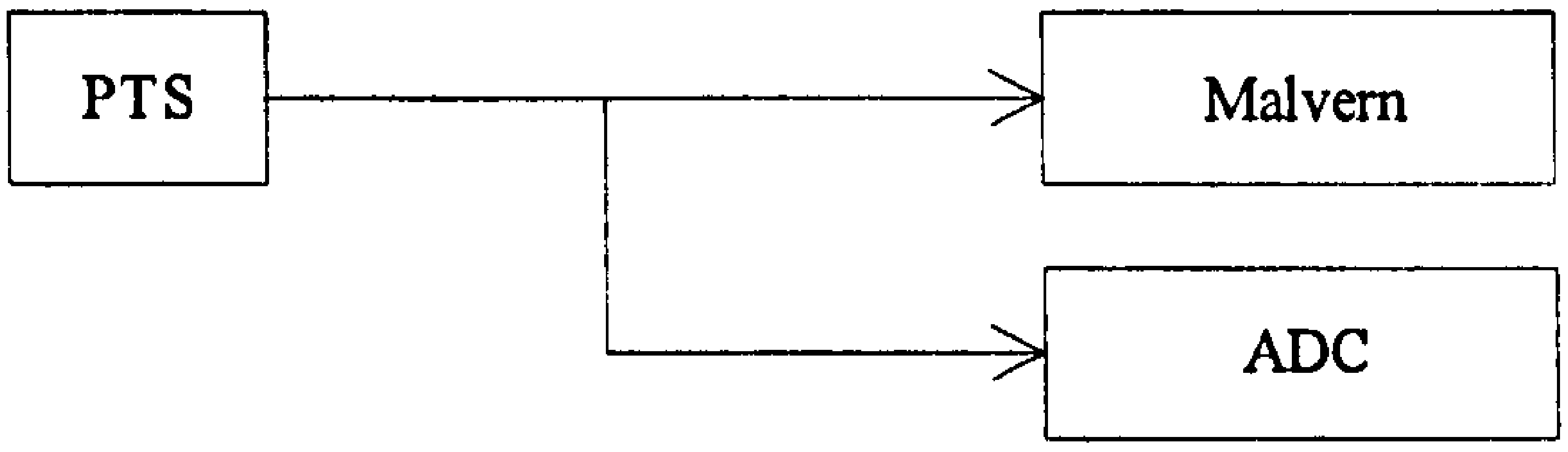

Figure 3.7: *Trigger circuit for temperature and pressure recording, and for aerosol data acquisition in non-combustion experiments.*

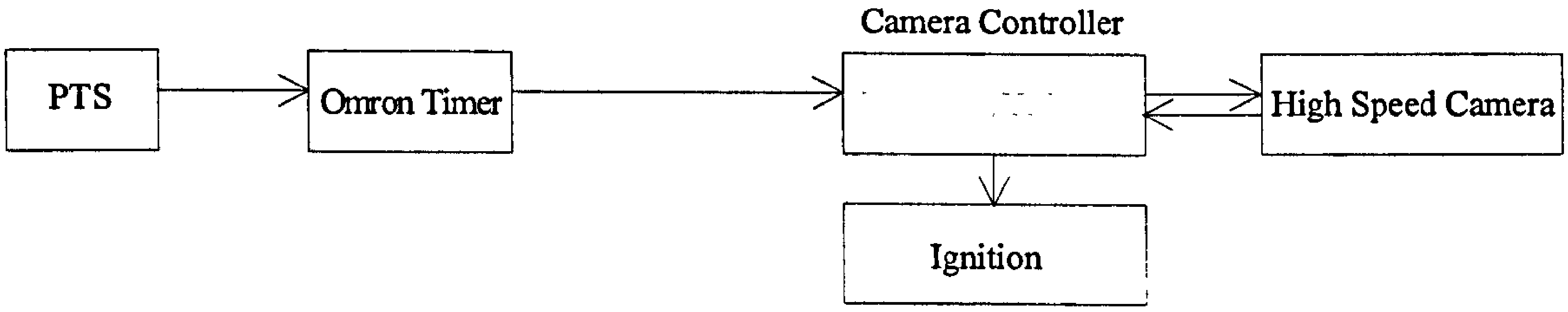

Figure 3.8: *Trigger Circuit for Schlieren System.*

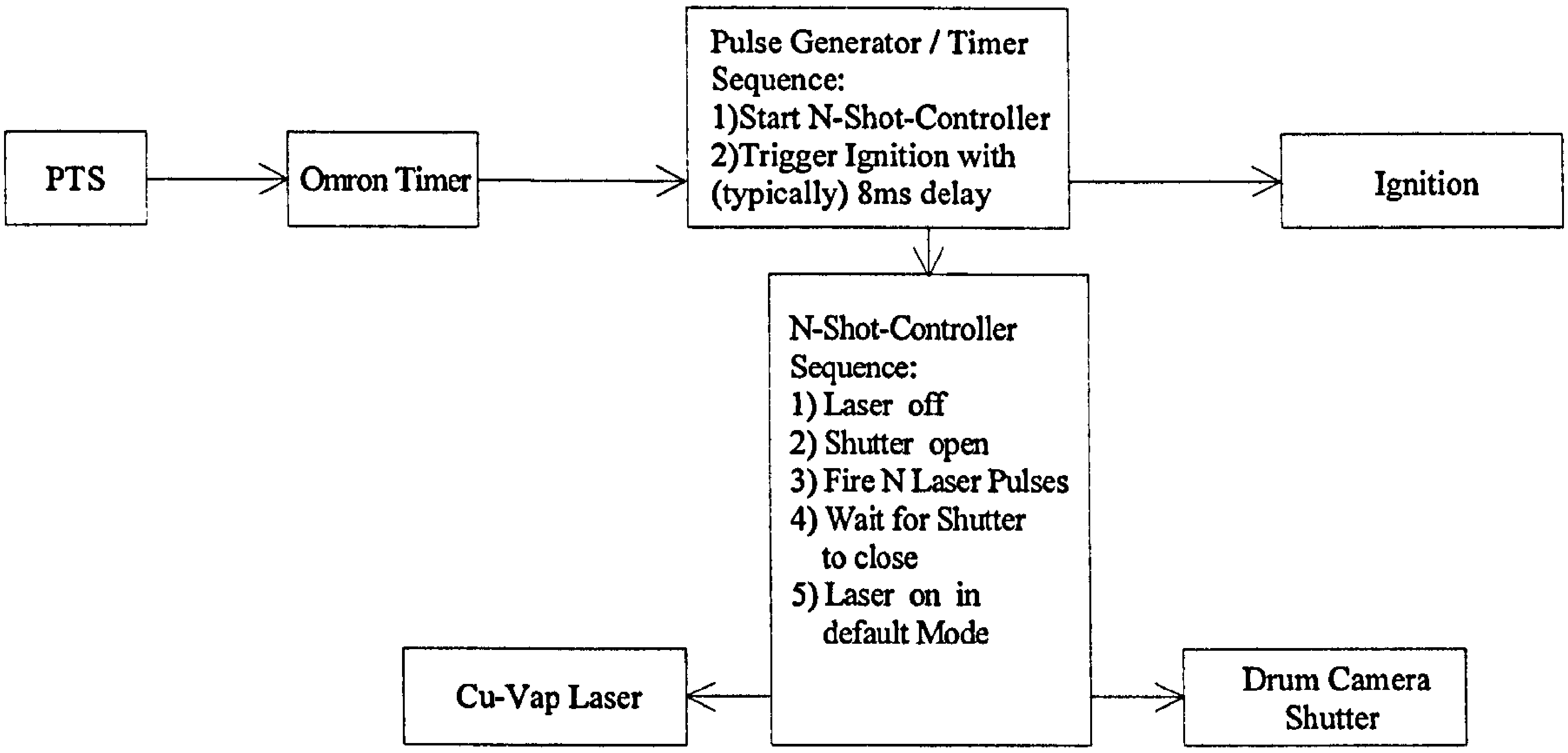

Figure 3.9: *Trigger Circuit for Laser Sheet Imaging.*

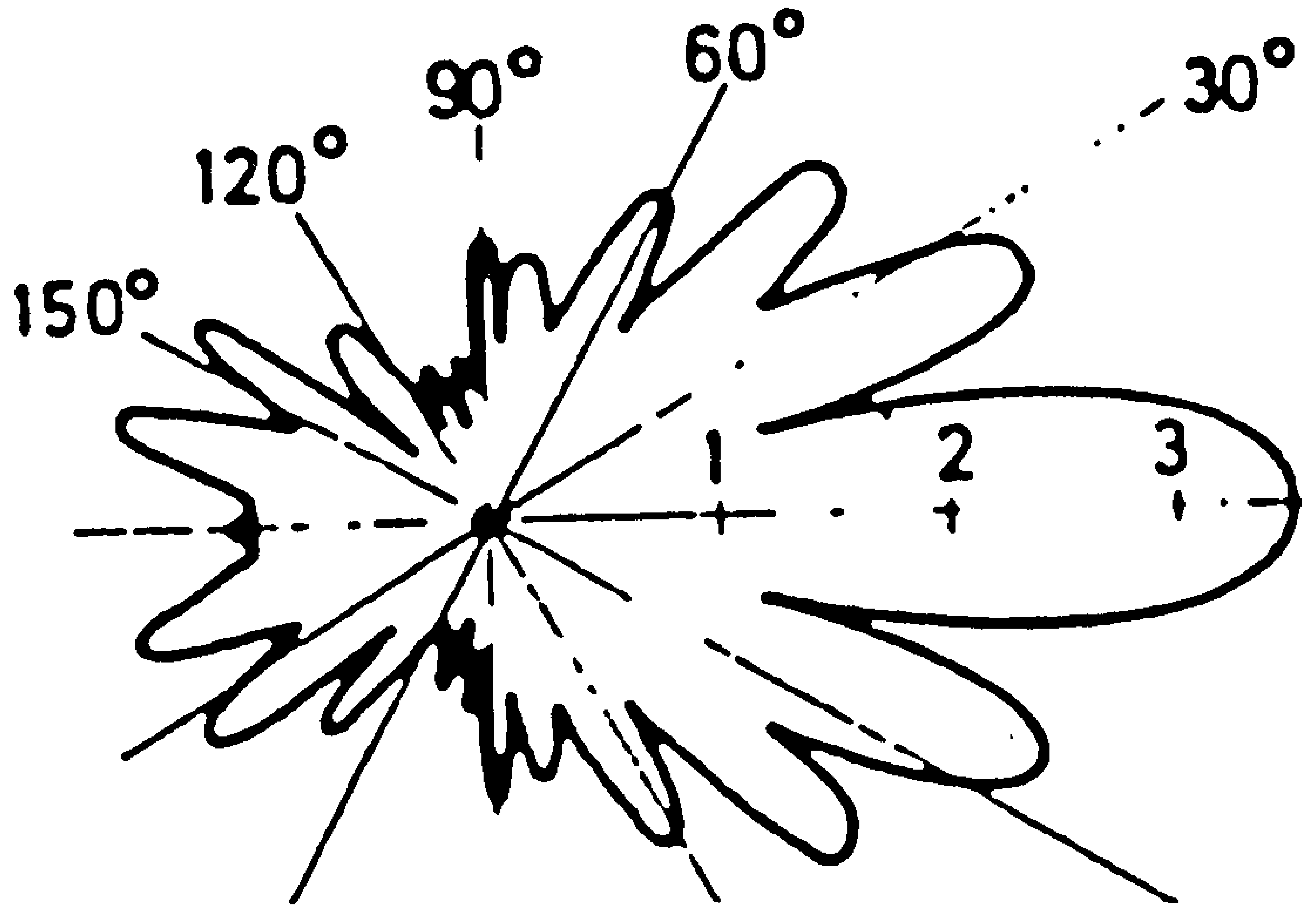

Figure 3.10: *Angular distribution of light intensity scattered a sphere (Reproduced from Taylor, 1992).*

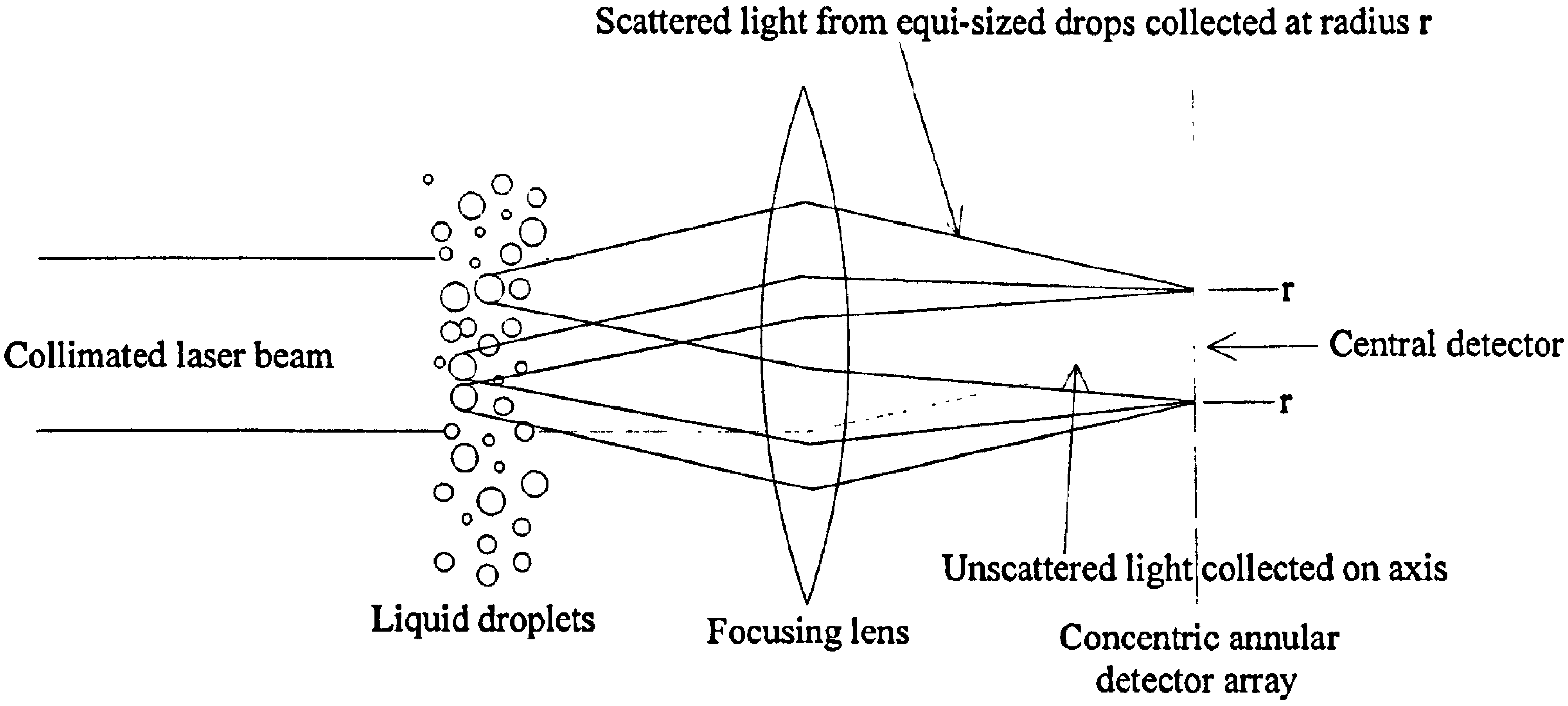

Figure 3.11: *Schematic of particle sizing technique (Malvern, 1992).*

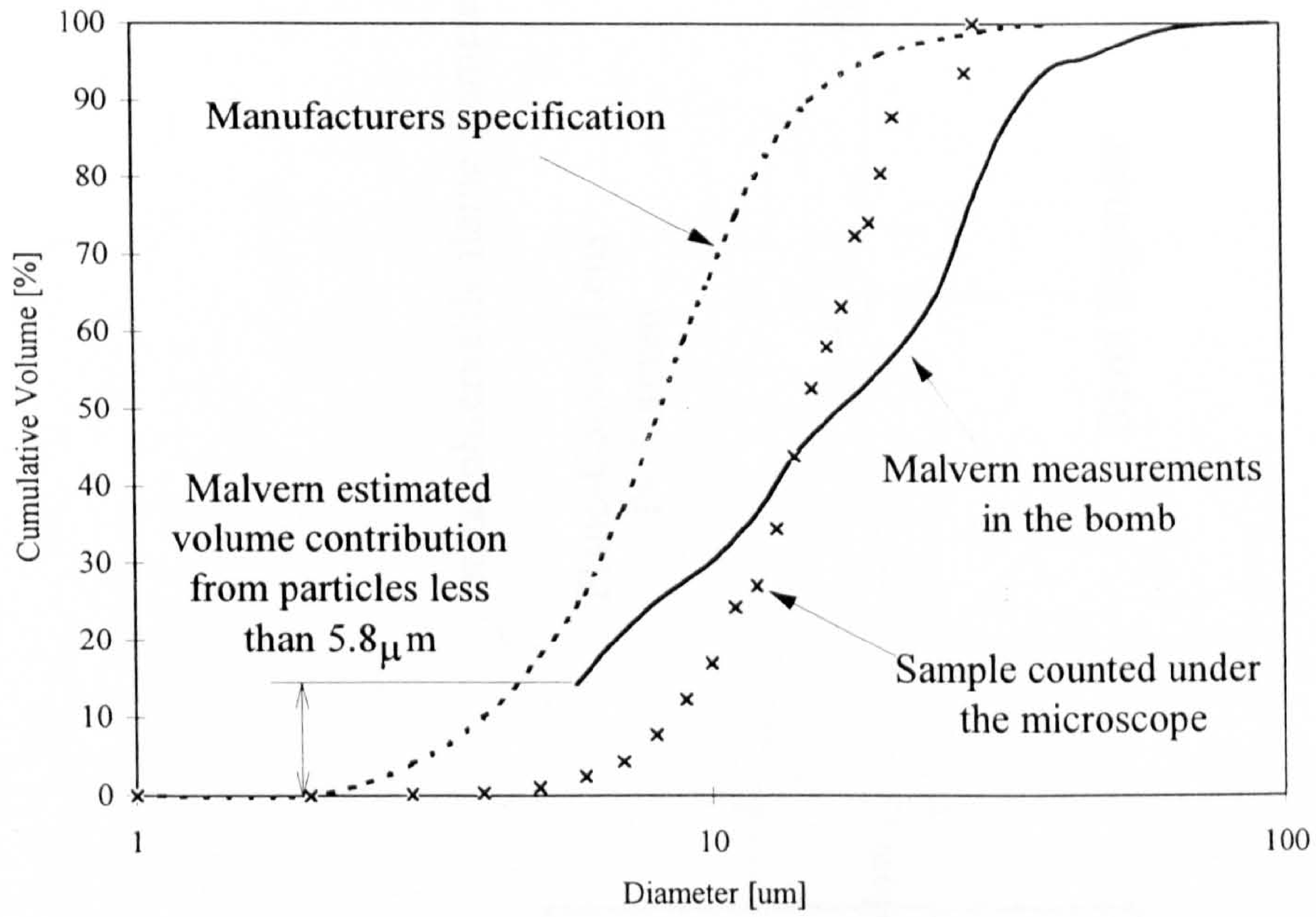

Figure 3.12: *Size distributions of* Sphericel™ 110P8 *hollow glass beads measured by the present author and by the manufacture.r*

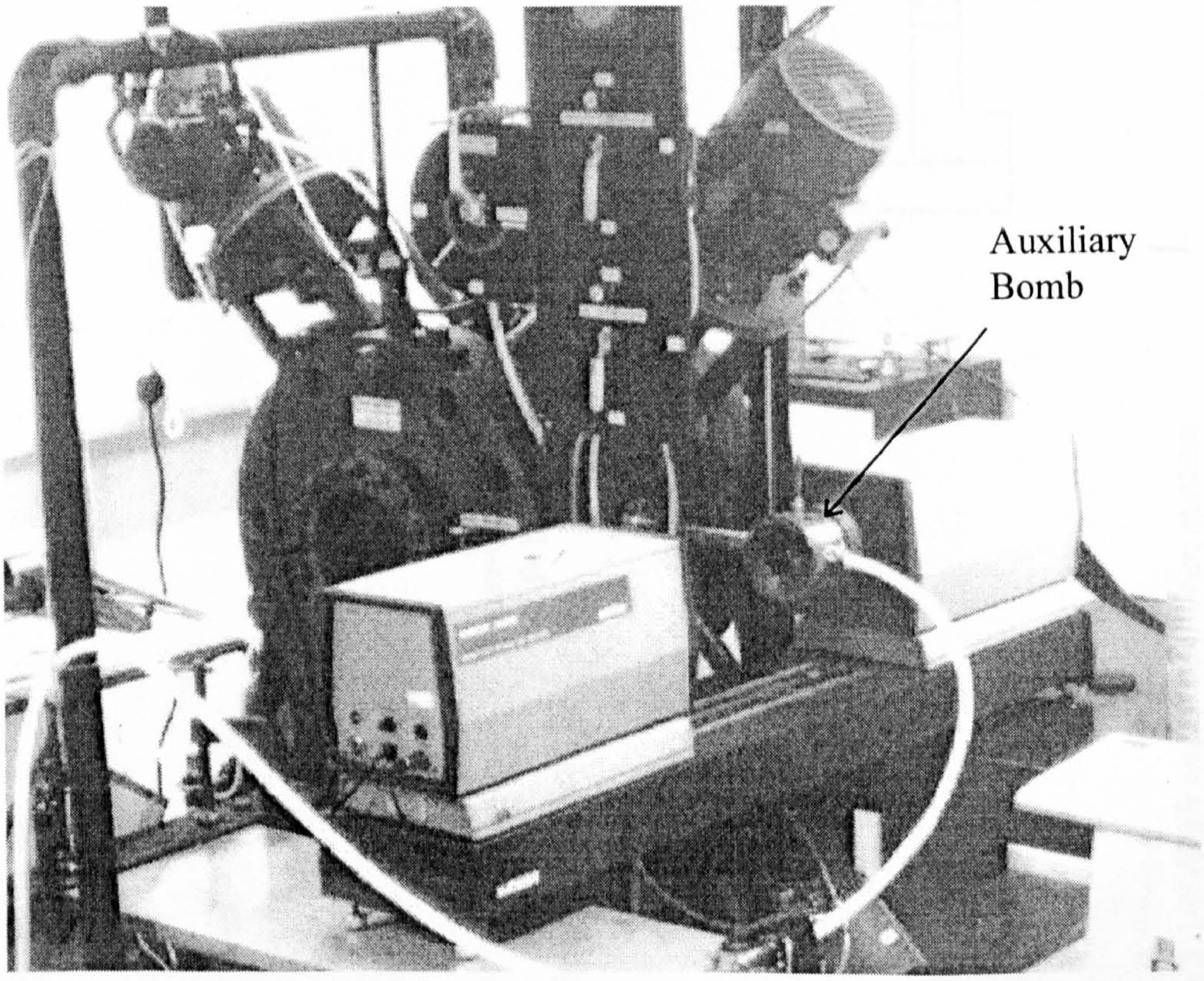

Figure 3.13: *Malvern Mastersizer S and auxiliary bomb.*

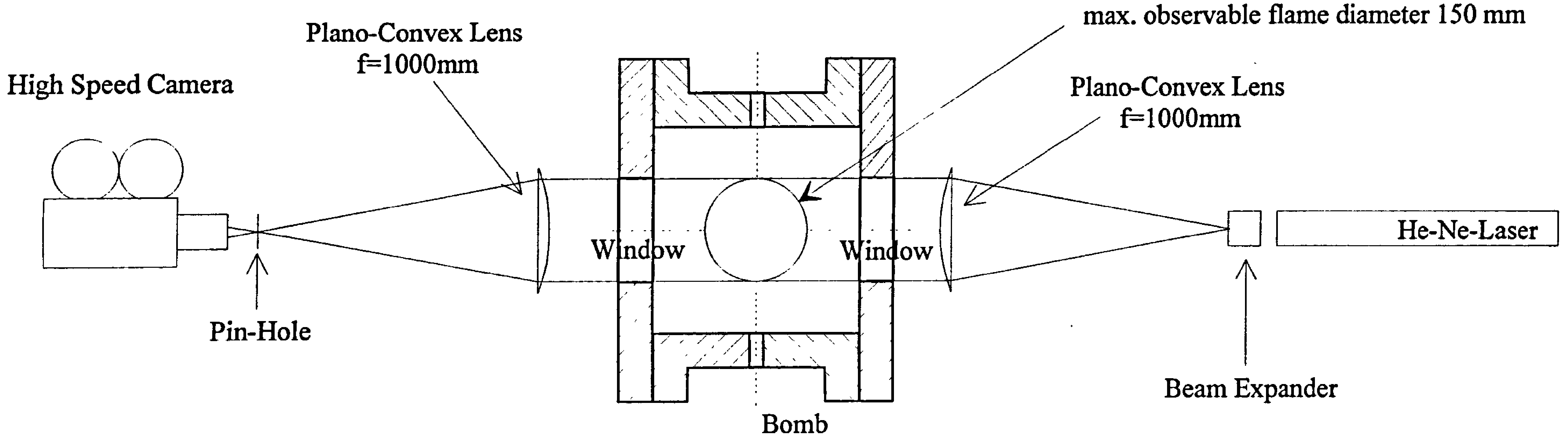

Figure 3.14: *High speed schlieren system.*

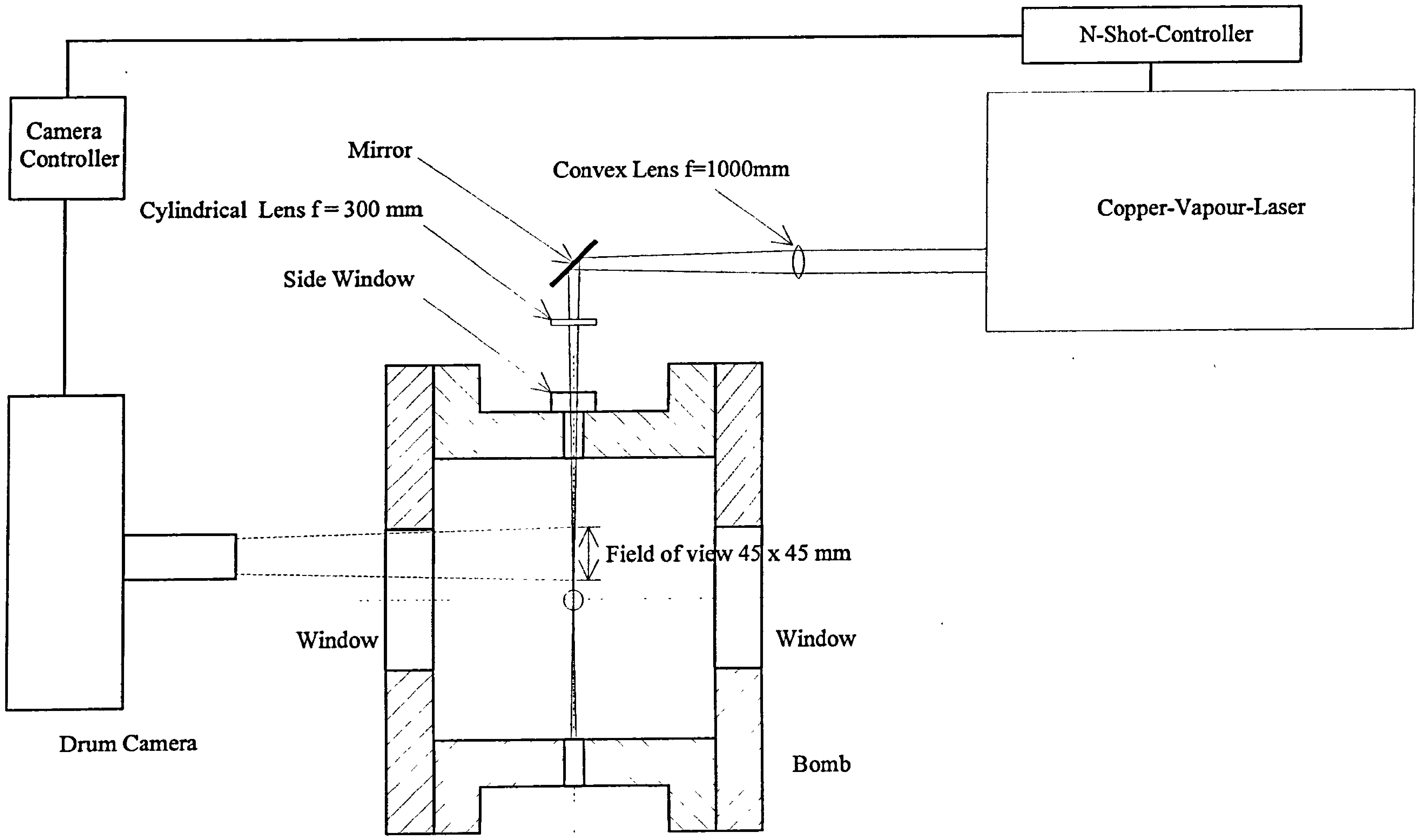

Figure 3.15: *Planar laser sheet imaging system.*

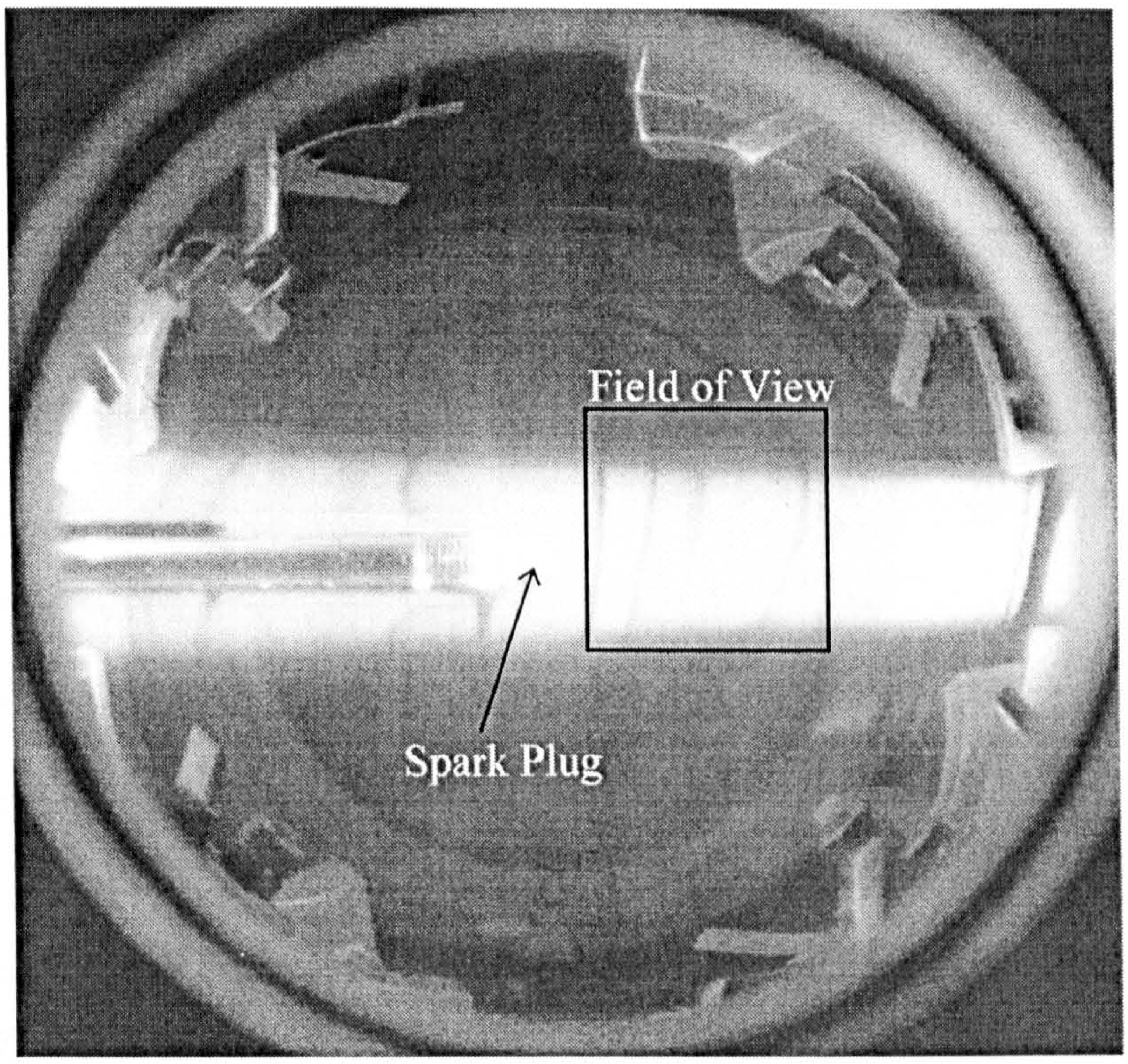

Figure 3.16: *Laser sheet through side window and field of view of the drum camera.*

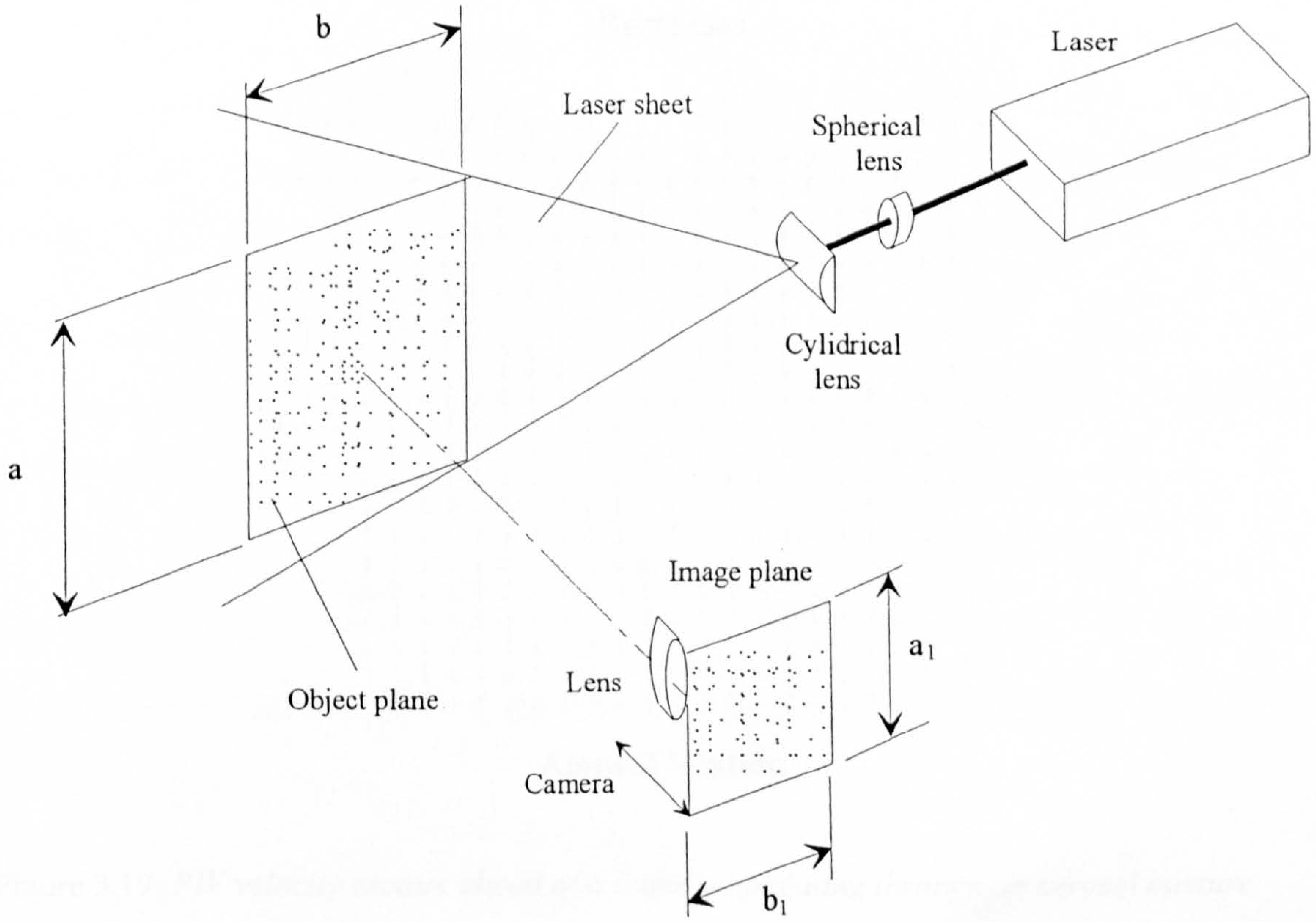

Figure 3.17: *The principle of PIV (Reproduced from Atashkari, 1997).*

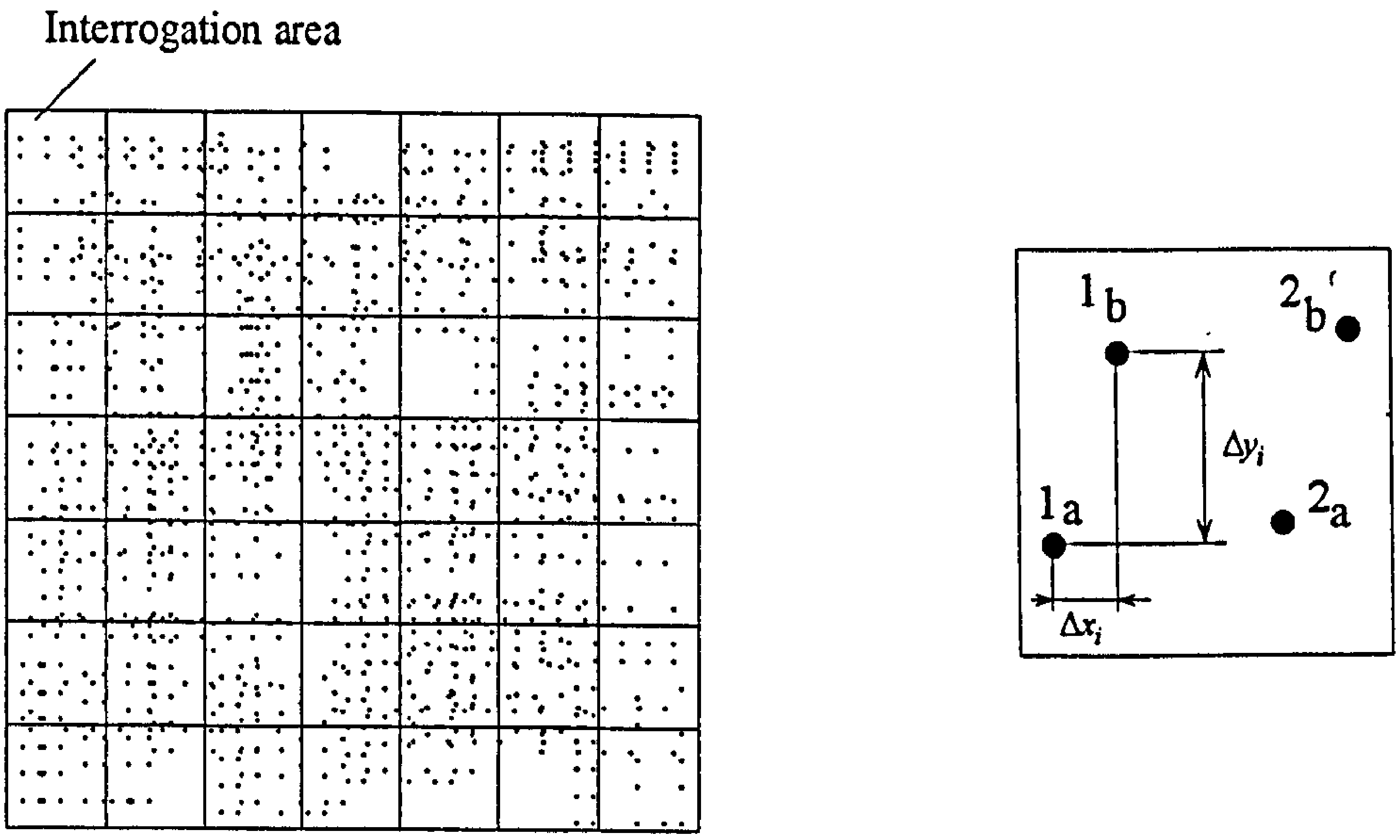

Figure 3.18 a: *Regularly spaced interrogation area; b: Ideal interrogation area (from Atashkari, 1997).*

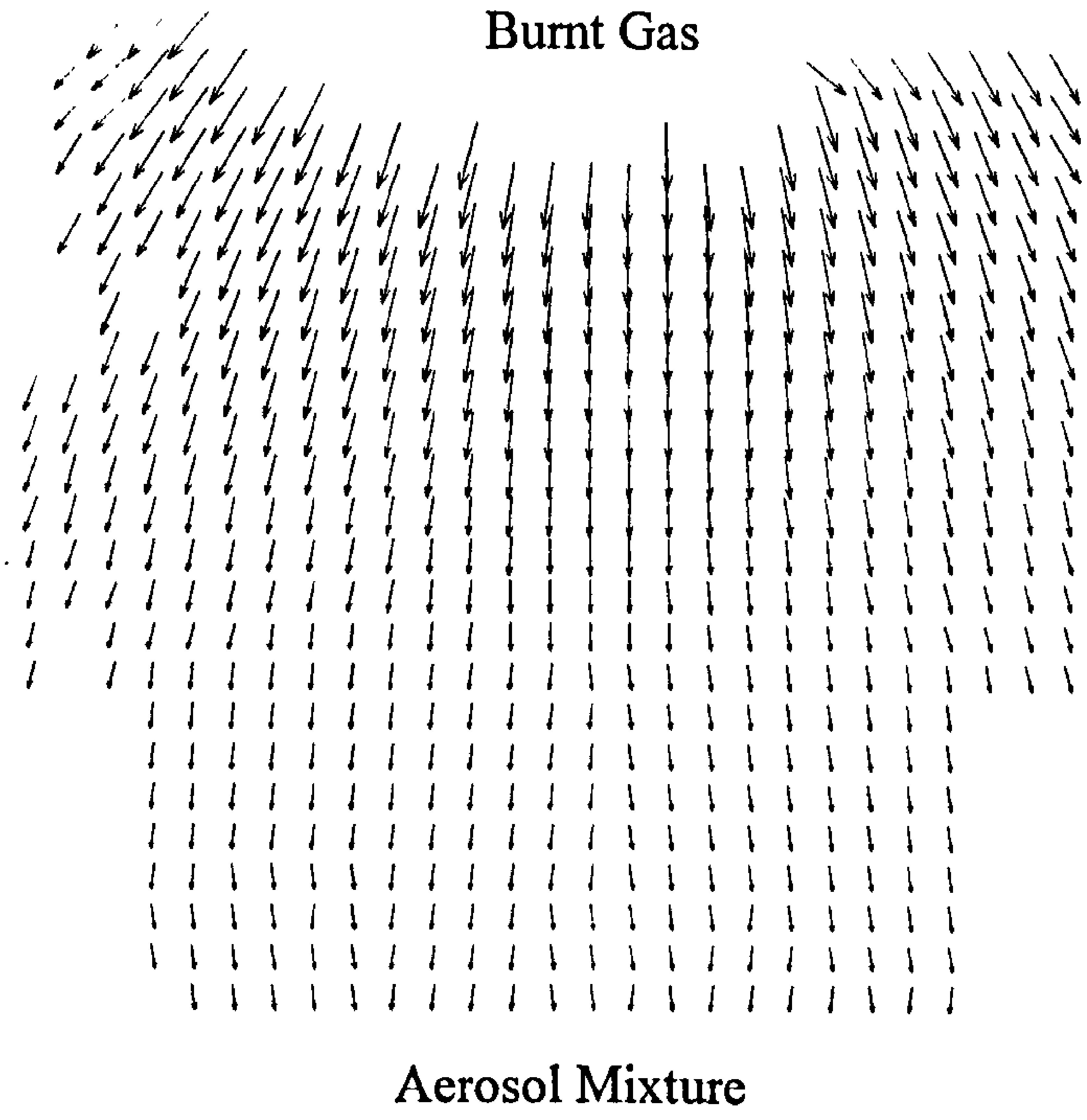

Figure 3.19: *PIV velocity vectors ahead of a flame propagating through an aerosol mixture.*

4. CHARACTERISATION OF AEROSOLS

This Chapter presents an analysis of the two-phase mixture composition in terms of gaseous and liquid fractions of the fuel and drop size, as a function of time during the expansion process. In Section 4.1, a theoretical analysis is presented. It is based on the thermodynamic principle that, given any two properties of a system, in this case pressure and temperature, any other property, here the liquid fraction, can be calculated. In Section 4.2, experimental data on temperature and pressure during expansion of iso-octane air mixtures are presented. These data are used as inputs to the model to predict the two-phase mixture composition as a function of time during expansion. The results of aerosol property measurements, using a laser diffraction technique, are shown in Section 4.3. A comparison of measured and predicted aerosol properties, together with some conclusions, is given in Section 4.4. Errors on measurements and calculation are analysed in Section 4.5. The combustion studies, presented in Chapter 5, make use of the data presented in here.

4.1 AEROSOL PROPERTY CALCULATIONS

The fractions of liquid and vapour phase of a substance are important parameters for the determination of the aerosol properties. The model, presented in this Section, is used in Section 4.4 to calculate these fractions for a mixture of iso-octane and air. It is based on a knowledge of system pressure and temperature, the vapour pressure and the amount of the fuel present. It is then applied to the expansion system, described in Chapter 3.

4.1.1 GAS PHASE IN EQUILIBRIUM

The molar composition of a stoichiometric mixture of iso-octane and air can be calculated from the stoichiometric equation

$$C_8H_{18} + 12.5\ O_2 + 47\ N_2 \rightarrow 8CO_2 + 9H_2O + 47\ N_2 \qquad (4.1)$$

For a non-stoichiometric mixture, the reactants on the left hand side of Eq. (4.1) can be expressed as

$$\phi\ C_8H_{18} + 59.5\ Air \qquad (4.2)$$

where ϕ is the equivalence ratio. Normalised to one mole of mixture, this is

$$1 \text{ mole reactants} = \frac{\phi}{59.5+\phi} C_8H_{18} + \frac{59.5}{59.5+\phi} Air \tag{4.3}$$

From Eq. (4.3), the mole fractions of air and fuel are

$$\frac{n_a}{n} = \frac{59.5}{59.5+\phi} \tag{4.4}$$

and

$$\frac{n_f}{n} = \frac{\phi}{59.5+\phi} \tag{4.5}$$

where n_a, n_f and n are the numbers of moles of air, fuel and the total mixture. The sum of the partial pressures, p_i, of all species, i, in the mixture is equal to the total static pressure p

$$p = \Sigma p_i \tag{4.6}$$

and the ratio of the partial pressures of two species is equal to their mole fractions, such that

$$n_a / n_f = p_a / p_f \tag{4.7}$$

Following from Eqs. (4.5), (4.6) and (4.7), the partial pressure of the fuel can be expressed as

$$p_f = p \frac{\phi}{59.5+\phi} \tag{4.8}$$

4.1.2 SATURATION AND CONDENSATION IN A THERMODYNAMICALLY IDEAL SYSTEM

When a system undergoes phase change, the process is necessarily associated with a departure from equilibrium. However, because it is assumed that the system moves towards an equilibrium state, the conditions corresponding to the equilibrium state are of considerable practical importance (Carey, 1992). This Section considers equilibrium in the process of condensation. The effects of the compressibility of a gas close to saturation conditions and the non-equilibrium behaviour, i.e. supersaturation, in the wet region are discussed in Section 4.1.3.

The state at which the fuel is completely vaporised and superheated, such that it is well away from saturation conditions, is defined by the ideal gas law.

$$p_f V = n_f RT \tag{4.9}$$

where V is the volume occupied by the mixture and R is the universal gas constant. In an ideal system, saturation of the fuel vapour is reached when its partial pressure is equal to its vapour pressure. In the wet region the partial pressure of the gaseous fuel cannot be derived from Eq. (4.8). However, it can be calculated from the vapour pressure function

$$p_f = p_v \tag{4.10}$$

where the subscript v denotes the vapour pressure of the fuel. This is calculated from the mixture temperature, using a function of the form:

$$p_v = 133.3224 \times 10^{(A+B/T+C\log T+DT+ET^2)} \tag{4.11}$$

with the coefficients A = 50.3422, B = -3278.9, C = -1.6111, D = 0.007426 and E = -9.1804E-14, (Yaws, 1993). The constant, 133.3224, accounts for the conversion of pressure from *mm Hg* to *Pa.*

It is assumed that the decrease in volume, due to the condensation of fuel, is negligible. With Eq. (4.9), and using the vapour pressure of the fuel to represent its partial pressure in the wet region, Eq. (4.10), the number of moles of gaseous fuel in the wet mixture is

$$n_{fg2} = \frac{p_v V}{RT_2} \tag{4.12}$$

Here, suffix 2 denotes the state of the mixture at any time after the start of expansion and g the vapour state.

The liquid molar fraction of fuel can be expressed in terms of the gaseous fraction

$$\frac{n_{fl}}{n_f} = \frac{\left(n_f - n_{fg}\right)}{n_f} = 1 - \frac{n_{fg}}{n_f} \tag{4.13}$$

were the subscript *l* denotes the liquid state.

Unlike in cloud chambers where a piston mechanism is used, the expansion of the mixture from a fixed-volume chamber into an expansion tank introduces an additional problem. The total amount of mixture in the combustion chamber decreases during the process. It is assumed, that the air-fuel ratio in the combustion chamber, irrespective of the state of matter of the fuel, remains constant during expansion. This assumption is reasonable on the grounds that condensed drops and the remaining fuel-vapour-air mixture are essentially at the same temperature. As droplets condense from the gas phase at the local flow velocity, they are transported out of the bomb at the same rate as the gaseous mixture. The total number of moles of fuel in the expansion chamber at the start of expansion, when all the fuel is fully vaporised can be expressed using Eqs. (4.8) and (4.9)

$$n_{f1} = \frac{p_{f1}V}{RT_1} = \frac{\phi}{59.5+\phi}\,\frac{p_1 V}{RT_1} \tag{4.14}$$

where suffix 1 denotes the state of the mixture immediately prior to the start of expansion. However, n_f in the condensation region must be calculated by assuming a constant mixture composition, since the former method does not account for the liquefied fuel. Constant mixture composition implies

$$n_{a1} / n_{f1} = n_{a2} / n_{f2} \tag{4.15}$$

Hence

$$n_{f2} = n_{f1} \frac{n_{a2}}{n_{a1}} \tag{4.16}$$

The number of moles of air in the wet region is

$$n_{a2} = \frac{p_{a2}V}{RT_2} = \frac{(p_2 - p_v)V}{RT_2} \tag{4.17}$$

The initial number of moles of air, using Eq. (4.4), is

$$n_{a1} = \frac{59.5}{59.5+\phi}\,\frac{p_1 V}{RT_1} \tag{4.18}$$

Substituting Eqs. (4.14), (4.17) and (4.18) into Eq. (4.16) yields

$$n_{f2} = \frac{\phi}{59.5}\,\frac{(p_2 - p_v)V}{RT_2} \tag{4.19}$$

Substitution of Eqs. (4.12) and (4.19) into Eq. (4.13), returns

$$\frac{n_{fl2}}{n_{f2}} = 1 - \frac{59.5}{\phi}\,\frac{p_v}{(p_2 - p_v)} \tag{4.20}$$

The mass of fuel present in the expansion chamber at condition 2 can be calculated, from its molar mass M_f

$$m_{f2} = n_{f2} \times M_f \tag{4.21}$$

where n_{f2} is obtained from Eq. (4.19).

4.1.3 NON IDEAL SYSTEMS

- Compressibility

Non ideal systems, in the present context, are those close to saturation conditions or in the wet region. Here the ideal gas law must be modified to account for the changed compressibility of the gas. This is done, using the compressibility factor Z. The equation of state becomes

$$p\,V = Z\,n\,R\,T \tag{4.22}$$

In the present work, for the partial pressures of iso-octane, Z was always very close to unity, as shown in Fig. 4.1. Here, it was necessary to extrapolate the compressibility chart, which was reproduced from Wylen & Sonntag (1985), to the "worst case" partial pressure used in the present work. It yielded a value of Z of 0.98. Typical values of Z were between 0.99 and 1. Therefore, Z was disregarded in the present model.

- Supersaturation

Condensation, in a non-ideal system, does not begin precisely when saturation is reached. A critical supersaturation, is needed to initiate the process (Amelin, 1967). Supersaturation, S, is defined as the ratio of fuel partial pressure in the supersaturated mixture, p_{fs}, to its vapour pressure

$$S = p_{fs} / p_v \tag{4.23}$$

This implies, that the mixture is dry when $S < 1$, saturated at $S = 1$, and supersaturated for $S > 1$. The magnitude of supersaturation needed to initiate any condensation process is the critical supersaturation, S_{cr}. Two different mechanisms of condensation are distinguished. In heterogeneous condensation a substance condenses on foreign nuclei, which may be present in the mixture, e.g. dust or ions. Homogeneous condensation occurs when the mixture is free of foreign nuclei and the substance condenses onto spontaneously formed molecular agglomerates. Amelin found that S_{cr} was several times higher for homogeneous than that for heterogeneous condensation. After its onset, the rate of vapour condensation on the surface of the growing droplets can be expressed by the Maxwell formula (Maxwell, 1890), with the correction for the influence of the drop radius, r, by Fuks (1934)

$$\frac{dm}{dt} = \frac{4\pi DrM}{RT\varphi} \left(p - p_v\right) \tag{4.24}$$

where D is the diffusion coefficient of the vapour. The coefficient φ is a function of several parameters, including the velocity differential between droplets and vapour, the accommodation coefficient, α, and others. Both, critical supersaturation and supersaturation during the process of condensation are functions of numerous variables, including surface tension of the liquid fuel, electric charge and radius of the nucleus, the coefficient φ and others, most of which were unknown for the present apparatus. Therefore the supersaturation was determined from an empirical relationship

$$S = S_{cr} + S_d \tag{4.25}$$

where S_d is the dynamic component of supersaturation during condensation. At the onset of condensation $S = S_{cr}$ and $S_d = 0$. During condensation S_d is a function of the ratio of the theoretical partial pressure of the fuel, calculated from Eq. (4.8), and the vapour pressure. The maximum supersaturation of any mixture is limited by p_f, the minimum by p_v. When $p_f = p_v$, the mixture is saturated, i.e. $S = 1$. If condensation occurs, p_{fs} must be smaller than p_f. Rearranging Eq. (4.25) for S_d and substitution of S from Eq. (4.23) yields the dynamic supersaturation

$$S_d = \frac{p_{fs}}{p_v} - S_{cr} \tag{4.26}$$

If the degree of supersaturation in the mixture is not known S_d can, to a first approximation, be estimated, using the theoretical partial pressure, such that

$$S_d = \left(\frac{p_f}{p_v} - S_{cr} \right) F \tag{4.27}$$

where F is an empirical constant, hitherto called the dynamic factor, that determines the magnitude of the dynamic component, and which can assume values between zero and one. Both F and S_{cr} were obtained from a comparison of calculated and experimental data, as discussed in Section 4.4.

In Eqs. (4.12) and (4.20) the equilibrium vapour pressure was used to calculate the gaseous and liquid fractions of fuel in the wet region. In non-equilibrium circumstances, this is replaced by p_{fs}, obtained by rearranging Eq. (4.23)

$$p_{fs} = S \times p_v \tag{4.28}$$

Substituting Eqs. (4.25) and (4.26) into Eq. (4.28) yields

$$p_{fs} = \left(S_{cr} + \left(\frac{p_f}{p_v} - S_{cr}\right)F\right)p_v \qquad (4.29)$$

In the above model, pressure and temperature were determined experimentally. From these, and the overall equivalence ratio p_f and p_v were derived for substitution into Eq. 4.29.

4.2 TEMPERATURE AND PRESSURE MEASUREMENTS

Temperature and pressure are the key parameters for the determination of liquid and gaseous fractions of fuel, present at any instant during expansion. In addition to mixture composition they are essential prerequisites for the analysis of the combustion process, discussed in Chapter 5.

Temperature measurements were performed at different locations in the control volume, to establish the spatial variation, and several measurements were taken at each location to account for temporal fluctuations. Temperature and pressure histories during expansion, at a range of initial pressures, temperatures and overall equivalence ratios, were obtained for use in the model, presented in Section 4.1, and for the prediction of ignition conditions in terms of pressure, temperature, liquid fraction and drop size.

4.2.1 LAMINAR TEMPERATURE RECORDS

Laminar temperature histories have been recorded at a number of pre-expansion conditions, as given in Table 4.1. Figure 4.2 shows the variation of temperature during the expansion of an iso-octane air mixture of ϕ_{ov}=1, T_i=303K and p_i=200kPa. Measurements were recorded sequentially at locations A and B, as defined in Chapter 3. Three measurements are presented at each location. Following the start of expansion the temperature at each location reduces in a smooth predictable manner. After 1.5 seconds, the temperature curves for position B become more erratic and similar effects occur at location A after 2.7 seconds. This is possibly the result of bulk flow motion or the onset of turbulence, which entrained warmer mixture from the wall region into the centre of the bomb. At A, these fluctuations were of the order of ±10°. Similar characteristics were obtained at location B. However, fluctuations were slightly greater than at location A. Variations shown in Fig. 4.2 were typical at all conditions studied. Maximum cycle to cycle and spatial variations were approximately 10K.

Temperature histories for identical conditions, from 3 individual measurements at each location, were averaged to yield spatially and temporally characteristic temperature histories for the whole of the control volume. Averaged temperature histories for equivalence ratios from 0.8 to 1.3 and for dry air are shown in Fig. 4.3. Up to 1.3 seconds after the start of expansion mixtures at all equivalence ratios exhibit similar trends to that of dry air. After this point variations in gradient as a function of equivalence ratio were observed. This is because of the release of latent heat of condensation, which increases with equivalence ratio due to the increased mass of fuel present in the mixture. The lowest temperature in the bomb was reached, typically, after approximately 3.5s. Figure 4.4 shows temperature histories as a function of initial pressure and temperature, at an overall equivalence ratio of 1.0 . They were not a strong function of pressure. These temperature histories were used to estimate the temperature as a function of time, irrespective of initial pressure, throughout the present work.

4.2.2 LAMINAR PRESSURE RECORDS

Pressure records were obtained simultaneously with each temperature record. Cycle to cycle variations and variations with equivalence ratio were negligible. Figure 4.5 shows the pressure histories for 200, 250, 300, 440, 600 and 700 kPa initial pressure. These were used to estimate the pressure as a function of time throughout the present work.

4.2.3 TEMPERATURE AND PRESSURE RECORDS UNDER TURBULENT CONDITIONS

Temperature and pressure histories were recorded at initial conditions given in Table 4.2. Pressure histories for all measured conditions are shown in Fig. 4.6. These were nearly identical, and this indicates a negligible effect of condensation on pressure development. The variation between all measurements was 8kPa between 0 and 0.2seconds and 5kPa after pressure equilibrium was reached. These variations were considered to be negligible. Temperature histories are shown in Fig. 4.7. Aerosol parameters calculated from these temperature and pressure histories and estimated errors are listed in Table 4.2.

4.3 AEROSOL PROPERTY MEASUREMENTS

Drop size and mixture composition, in terms of gaseous and liquid fractions of the fuel, are important parameters in the combustion of aerosols. This Section presents measurements of size distribution, Sauter mean diameter and volume concentration of liquid fuel in the aerosol during the expansion process. These measurements were obtained with Malvern particle sizing equipment, discussed in Chapter 3. Most measurements were taken in situ, using the

Malvern 2600. These results were complemented with measurements in the auxiliary bomb, performed with the Mastersizer S.

4.3.1 DROP SIZE DISTRIBUTION AND DISTRIBUTION HISTORY

Using the Malvern 2600, three measurement sequences at each condition, each containing 3 measurements, were performed at times 1, 1.5 and 2 seconds after the start of expansion. Figure 4.8 shows a series of eight typical histograms, recorded at an initial temperature and pressure of 303K and 200kPa and an overall equivalence ratio of 0.8. Also indicated on each Figure are the Sauter mean diameter, the volume concentration. The span, indicated in Figs. 4.8(b) to (d), is defined as

$$S = \frac{D_{v0.1} - D_{v0.9}}{D_{v0.5}} \qquad (4.30)$$

$D_{V0.1}$, $D_{V0.5}$ and $D_{V0.9}$ are the diameters at which 10, 50 and 90% of the particle volume are contained. A span of 0.2, at a mean diameter of 20µm, indicates that 80% of the particles, by volume, are within the range of ±2µm of the mean diameter.

All histograms obtained at $t = 1.5$ seconds, after the start of expansion, were very noisy as indicated by the volume concentration value of zero in Fig. 4.8(a). The cut off peak at the 500µm limit and the small peak at 100µm were due to beam steering effects caused by refraction due to density gradients in the bomb. At $t = 2$s, as shown in Fig. 4.8(b), a narrow histogram appeared with a span of 0.22, representative for a near monosize distribution. The Sauter mean diameter was 10.6µm and 80% of the droplet volume was contained in droplets between 9.5 and 12µm. The subsequent histograms, up to $t = 3$s had an increase in particle diameter, but maintained the narrow distribution. From $t = 3.5$s, Fig. 4.8(e), a small peak to the left of the main histogram indicated the appearance of small droplets. These probably originated from the onset of turbulent motion in the bomb, which caused re-evaporation. These small droplets probably do not affect combustion, because they evaporate ahead of the flame front (Chapter 2). However, the inclusion of these particles in the measurement affected the calculation of the Sauter mean diameter. Therefore, the aerosol data were filtered as described in Chapter 3, to obtain a representative value of D_{32} for those droplets, that are relevant for combustion. The size distribution tended to widen at later times, due to drop interaction and re-evaporation.

4.3.2 SAUTER MEAN DIAMETER AND LIQUID VOLUME CONCENTRATION

Figure 4.9 shows a typical set of histories of liquid volume for overall equivalence ratios 0.8 to 1.3 at an initial pressure and temperature of 200kPa and 303K. They were measured with the Malvern 2600. Typically droplets begin to form between 1.5 and 2 seconds after the start of expansion, as a function of equivalence ratio. The maximum liquid fuel concentration occurs between 2.5 and 3 seconds after the start of expansion. Typical histories of D_{32} are presented in Figs. 4.10(a), (b) & (c) for the initial pressures of 200, 250 and 300kPa, at an initial temperature of 303K and an overall equivalence ratio of 1.0. In all cases, the experimental data follow the same trends as the liquid volume data in Fig.4.9. The solid symbols represent in situ measurements with the Malvern 2600 and the open symbols were obtained with the Mastersizer S. Also shown are curves calculated from the model, described in Section 4.1, which are discussed in Section 4.4. Although the data obtained with the Malvern Mastersizer S were not measured in situ, their agreement with the other experimental data is good. An error analysis on Sauter mean diameter and liquid volume concentration is presented in Section 4.5.

4.4 COMPARISON OF MEASUREMENTS AND EXPANSION MODEL

This Section compares results of the thermodynamic model, presented in Section 4.1, with experimental measurements. Both Malvern measurements and model calculations yield average mixture properties across the control volume. Also, measurements of aerosol properties, pressure and temperature were performed simultaneously, which allows for a direct comparison of the former with the model calculations based on the latter.

The liquid volume concentration was calculated from the liquid molar fuel fraction (Eqs. (4.16) and (4.20)). It is given by

$$C = \frac{n_{fl2}\, M_f}{\rho_f\, V} \tag{4.31}$$

The drop diameter history was calculated using an arbitrary number of droplets, N, which was assumed to be constant throughout the processes of condensation and re-evaporation

$$D = \left(\frac{m_{fl2}\, 6N}{\rho_f\, \pi}\right)^{1/3} \tag{4.32}$$

Presented in Fig. 4.11 is the fitting procedure, that considers the phenomenon of supersaturation. Shown are data for the expansion of an overall stoichiometric fuel-air mixture from T_i=303K and p_i=200kPa. The thin solid curve in Fig. 4.11(a) shows model predictions of condensation at equilibrium vapour pressure, i.e. S=1. If supersaturation is not considered, the model over predicts the amount of fuel condensed from the gas phase. The thin dashed curve was calculated using a constant critical supersaturation of 1.1. Although the start of condensation coincides with that of the experimental data, the liquid concentration during further expansion is still over predicted. The bold curve shows the result, for a critical supersaturation of 1.1 and a dynamic factor of 0.3, which agrees with the experimental data. Figure 4.11(b) shows a family of curves for the same pre-expansion conditions and the overall equivalence ratios of 0.8, 1.0 and 1.2. The experimental results were well predicted using an S_{cr} of 1.1 and F varying between 0.3 and 0.5.

For all experiments of the present work, typical values of critical supersaturation varied between 1.0 and 1.4, indicating heterogeneous condensation. Condensation nuclei probably originated from contamination of the mixture components, the devices used to introduce them into the bomb or from the bomb walls and fans. F typically varied between 0.25 and 0.55. Due to considerable scatter of the experimental data, it was not possible to establish a consistent trend of the values of S_{cr} and F throughout the range of initial conditions used in the present work. However, both parameters were functions of the overall equivalence ratio.

The measured and calculated curves of Sauter mean diameter for initial conditions of 200kPa and 303K, are shown in Fig. 4.12. Good agreement of measured and calculated data was obtained at all conditions for times less than 3 seconds. After this time, which approximately corresponds to the start of droplet evaporation, the predictions were less accurate, probably because the values of supersaturation, used in the calculation, were those for condensation, not evaporation. Sauter mean diameters were affected, additionally, by drop agglomeration, which was not considered in the model. The gaseous equivalence ratios, calculated for that condition, are presented in Fig. 4.13.

Liquid volume concentration and drop sizes were measured under turbulent conditions only near the coldest point within the expansion process. This limitation was due to the resolution limitations of the Malvern 2600. Therefore, a similar scaling process to that described in Section 4.1 for laminar data, was not possible. However, the model was used to calculate overall supersaturation values and mixture composition for the measured data points.

The calculated and measured data are used in the analysis of the combustion experiments in Chapter 5. Errors are discussed below.

4.5 ERRORS IN CALCULATED AEROSOL PROPERTIES AND SCATTER OF EXPERIMENTAL DATA

From the experimental data alone it is difficult to quantify the variations of aerosol properties, associated with fluctuations of pre-expansion temperature and pressure, as discussed in Chapter 3. Therefore the model, described in Section 4.1, was used to simulate the effect of temperature and pressure deviations. Experimental errors were discussed in Chapter 3.

Figure 4.14 shows the effect of a temperature and pressure change of 1K and 2.5kPa for the overall equivalence ratios of 0.8 and 1.2, presented in Fig. 4.11(b). The deviation of liquid volume concentration was 10 to 20% of the maximum value. This was comparable with the estimated error of ±10% for liquid concentration measurements with the Malvern 2600 (Chapter 3). The scatter in Sauter mean diameter, shown in Figure 4.15 was ±1 to ±2μm, which is ±5 to ±10% of the maximum value measured. This compares well with the accuracy quoted by the manufacturer of ±4% and the additional error in equivalence ratio of ±4%, discussed in Chapter 3. Figure 4.16 shows the gaseous equivalence ratio and its error bands for the data shown in Figs. 4.15 and 4.16. The gaseous equivalence, varied by up to ±0.08, which is ±10%. This is consistent with the results for liquid concentration.

The time at which condensation commenced could be determined only within 0.5 seconds. Also, in the initial stage of droplet formation their growth rate was very high. Hence, accurate determination of mixture properties within the first 2 seconds after the start of expansion was not possible. At times longer than 2 seconds, particle size and mixture composition were determined to an acceptable accuracy for use in combustion analysis. Better temperature control in the bomb as well as more reliable pre-mixture preparation are required to improve this situation.

The accuracy of mixture characterisation under turbulent conditions was difficult to estimate, since no trend analysis was possible. However, estimates of gaseous equivalence ratio were possible and are presented in Table 4.2.

T_l [K]	303	303	303
p_l [kPa]	200	250	300
ϕ_{ov}	Dry air, 0.8, 0.9, 1.0, 1.1, 1.2, 1.3	0.7, 0.8, 0.9, 1.0	0.7, 0.8, 0.9, 1.0

T_l [K]	313	323	333	348
p_l [kPa]	300	440	600	700
ϕ_{ov}	1.0	1.0	1.0	1.0

Table 4.1: *Laminar initial conditions examined in the present work.*

T_l [K]	303	323	323	323	323	323	323
p_l [kPa]	200	440	440	440	440	440	440
Fan Speed [rpm]	500	500	1000	1500	2000	2500	3000
u' [m/s]	0.83	0.83	1.67	2.5	3.33	4.17	5
liquid volume concentration [$m^3/m^3 \times 10^{-6}$]	17 ±2.5	19 ±2.5	24 ±4	23 ±5	20 ±6.5	20 ±9	15 ±10
D_{32} [μm]	20 ±1	20 ±1	22 ±1	22 ±1.5	20 ±2.5	20 ±3	19 ±4
ϕ_g	0.865 ±0.01	0.9 ±0.01	0.9 ±0.01	0.9 ±0.01	0.91 ±0.03	0.92 ±0.04	0.93 ±0.04

Table 4.2: *Properties of aerosols under turbulent conditions. Also shown are estimated errors.*

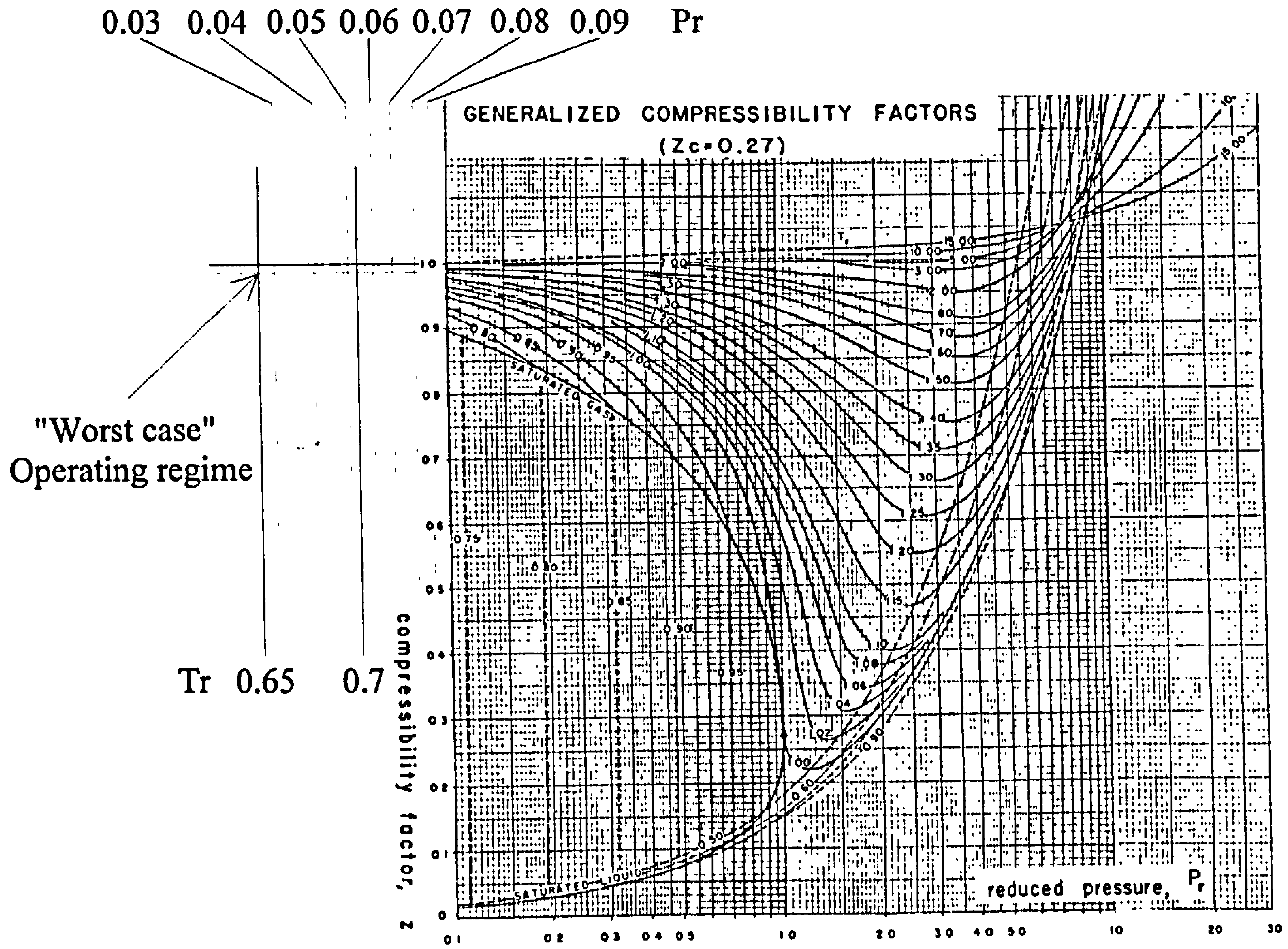

Figure 4.1: *Compressibility factor for iso-octane vapour at saturation conditions with extrapolations to the present operating regime (reproduced from Van Wylen et al., 1985).*

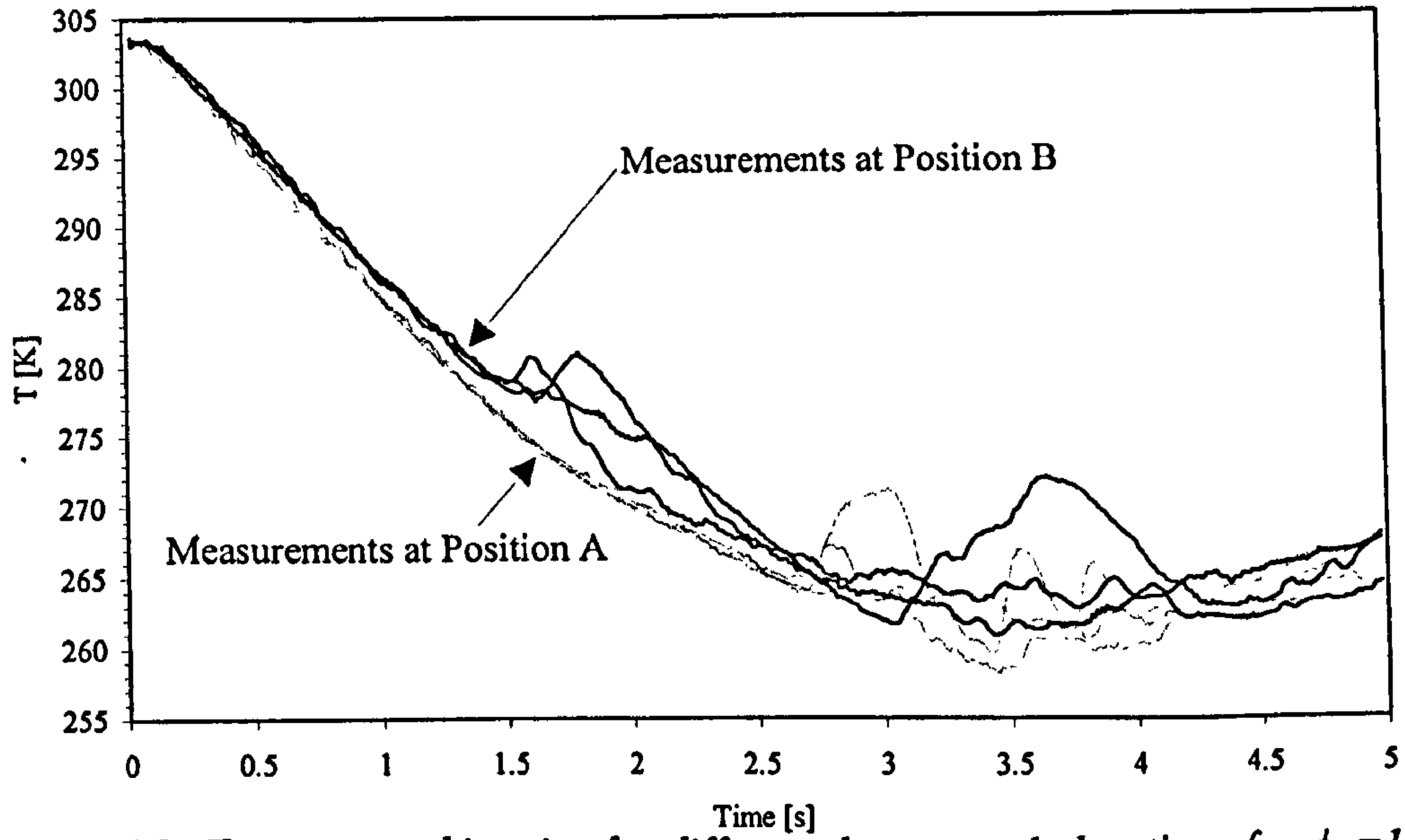

Figure 4.2: *Temperature histories for different thermocouple locations for $\phi_{ov}=1$, $T_i=303K$ and $p_i=200kPa$.*

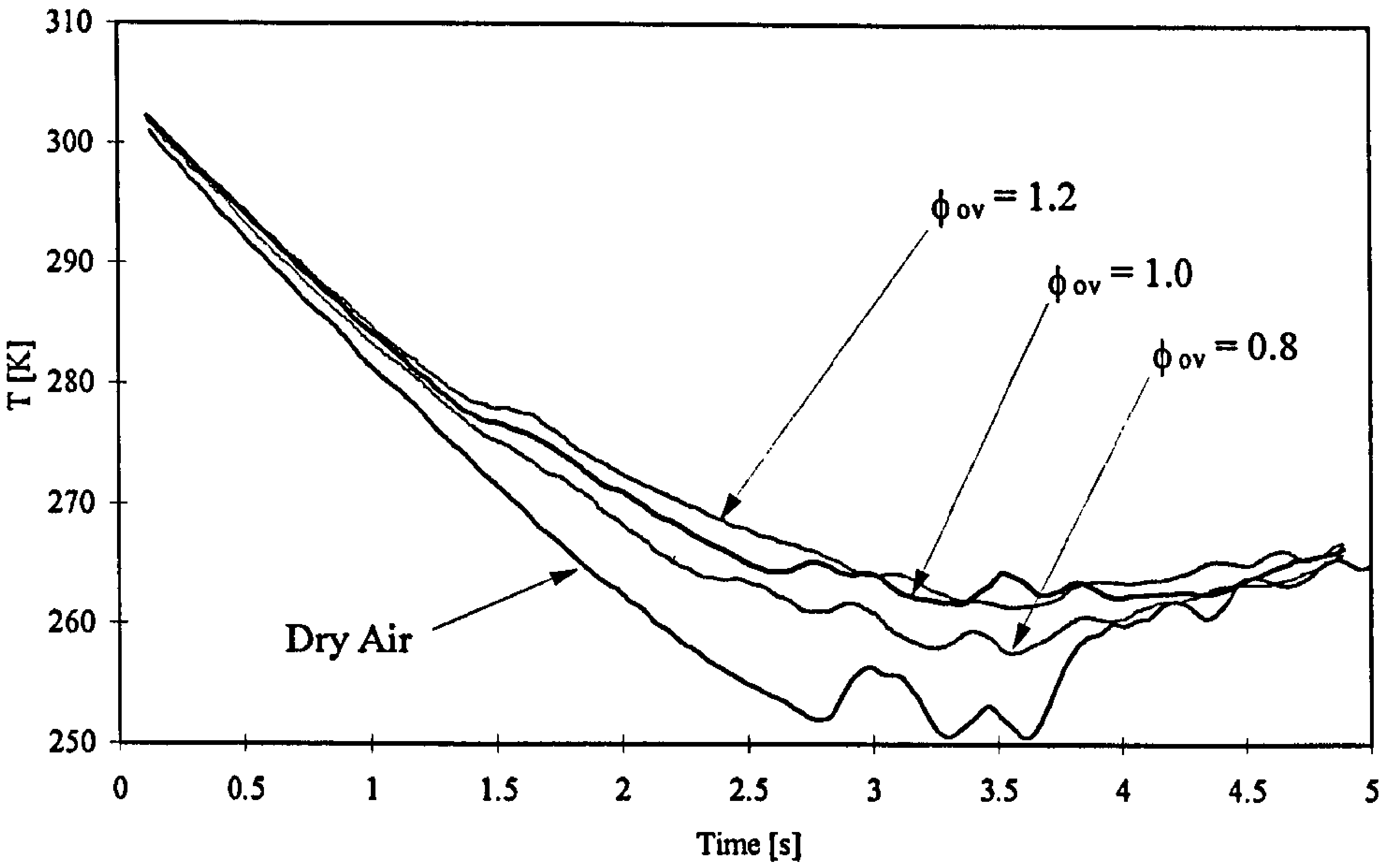

Figure 4.3: *Averaged temperature histories for iso-octane aerosols as function of equivalence ratio and dry air.*

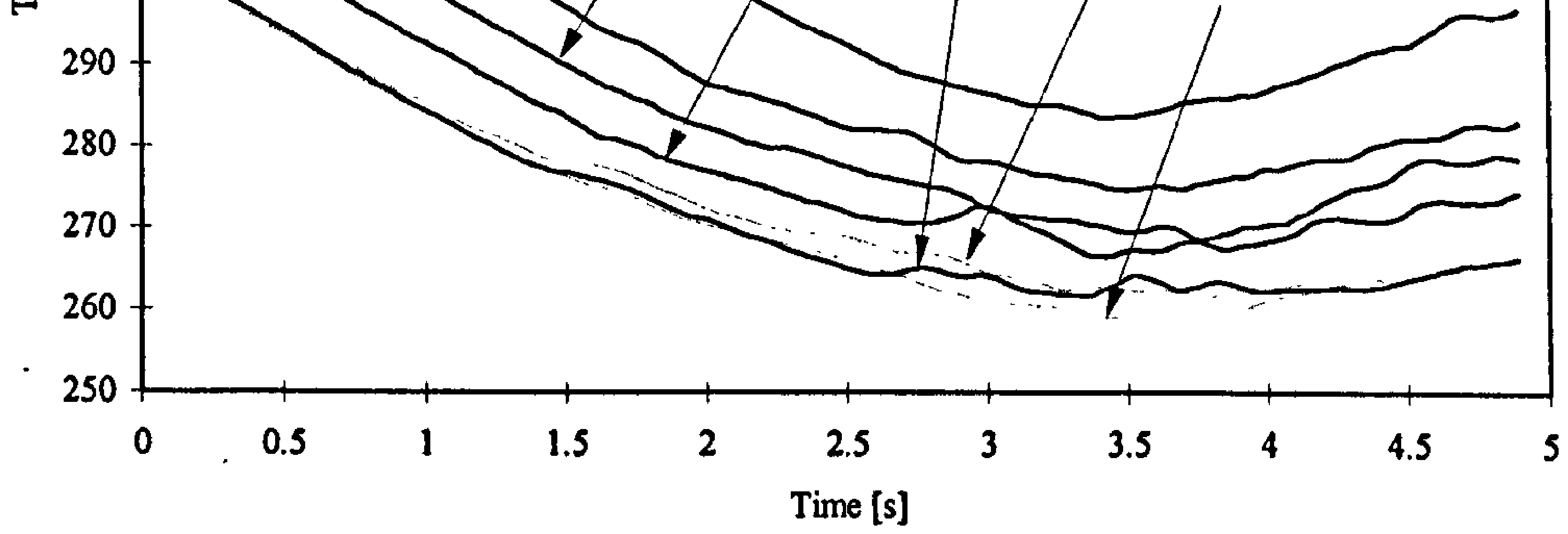

Figure 4.4: *Temperature histories for various initial temperatures and pressures.*

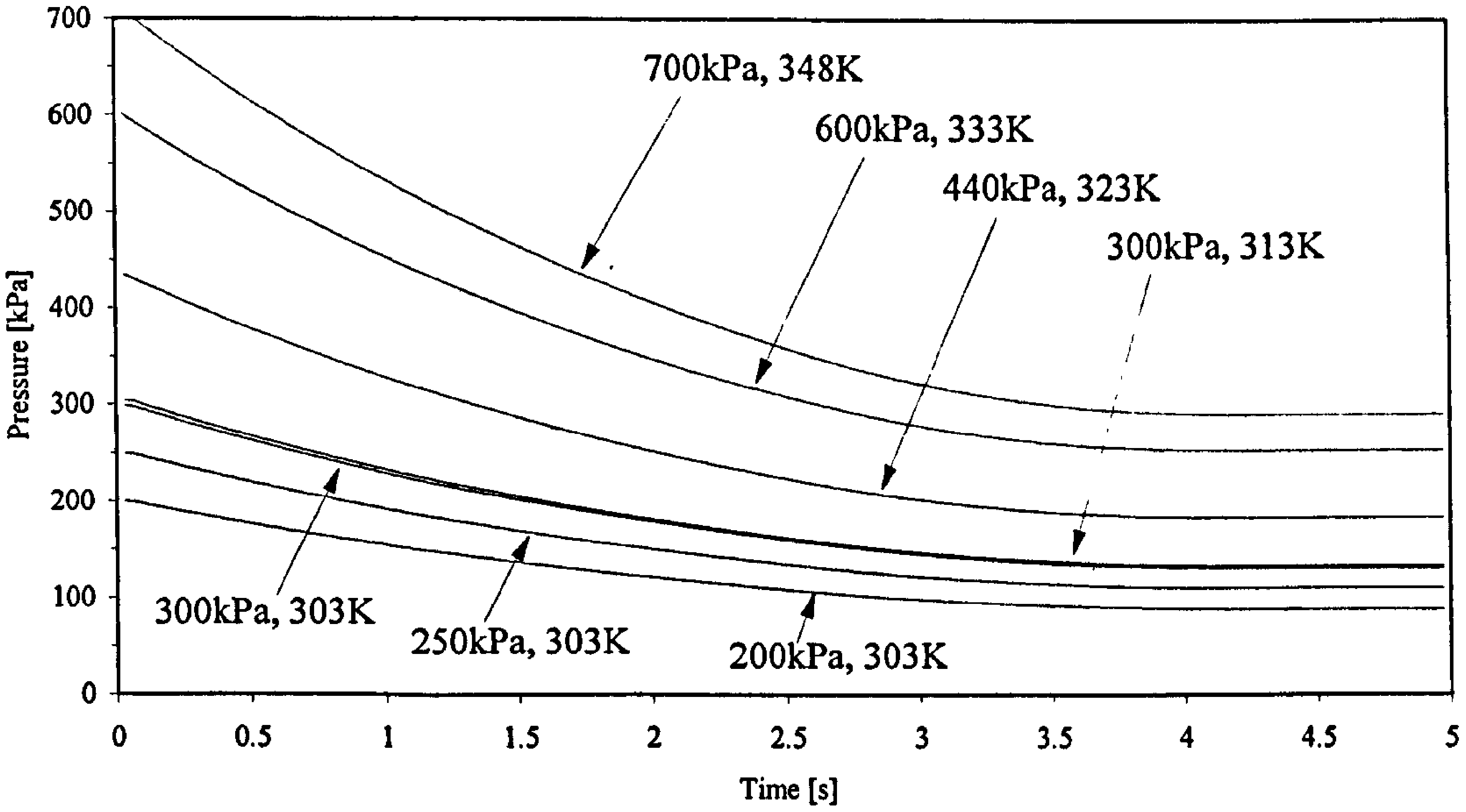

Figure 4.5: *Pressure histories for various initial temperatures and pressures.*

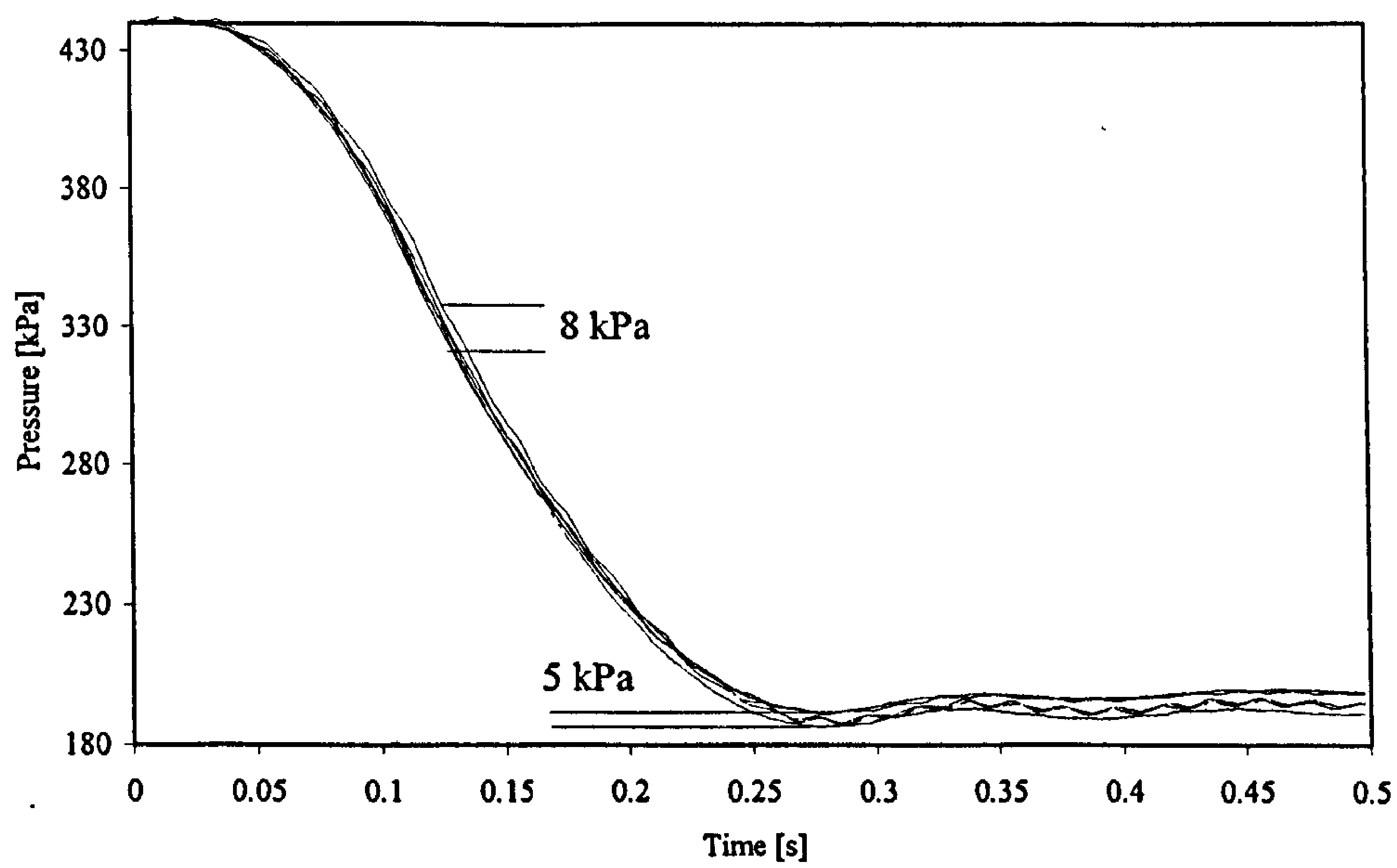

Figure 4.6: *Pressure histories as function of fan speed for 500 to 3000 rpm, in increments of 500, for* p_l*=440kPa and* T_l*=323K.*

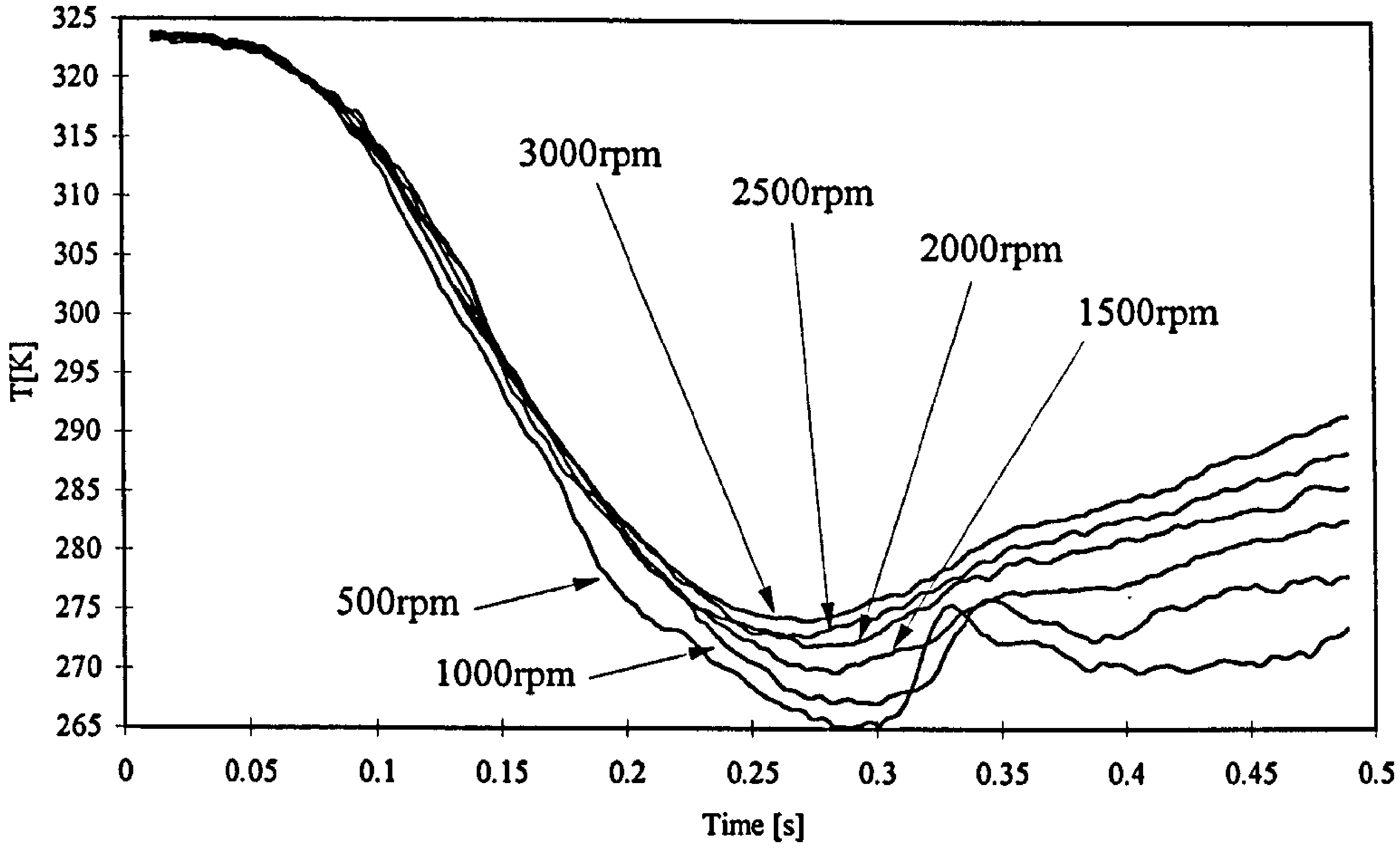

Figure 4.7: *Temperature histories as function of fan speed for 500 to 3000 rpm, in increments of 500, for* p_I*=440kPa and* T_I*=323K.*

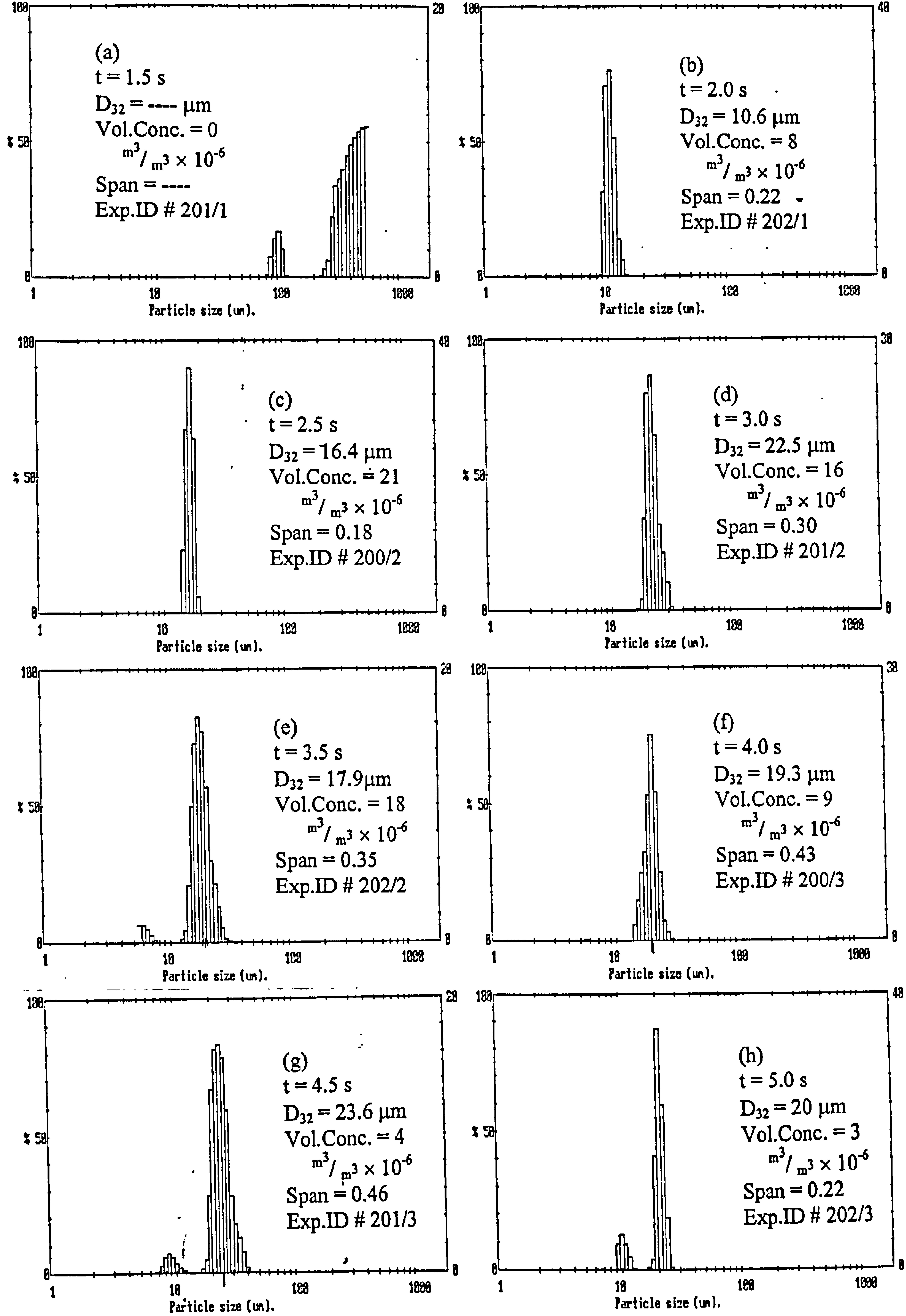

Figure 4.8: *Typical Malvern 2600 size distribution history.*

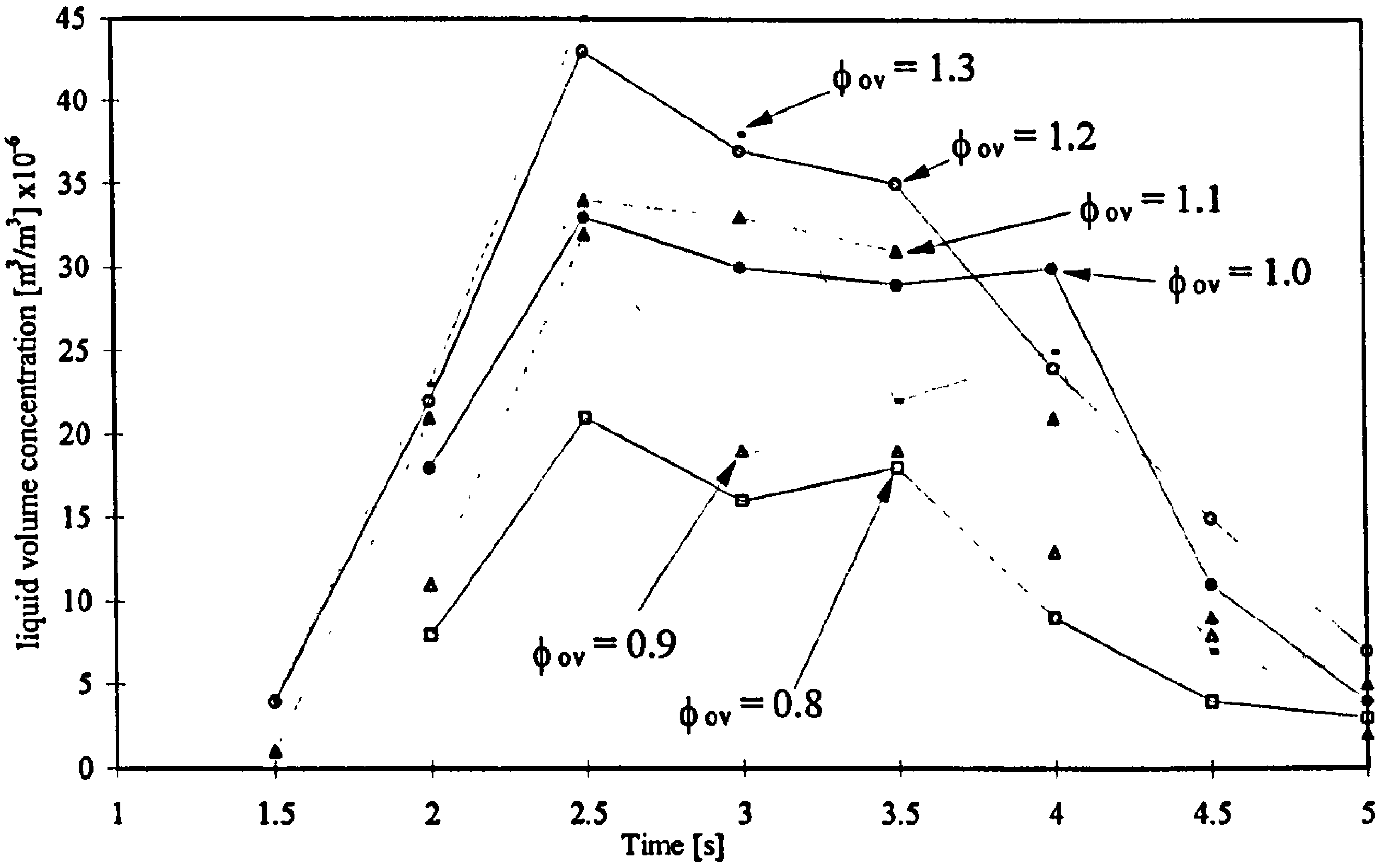

Figure 4.9: *Liquid volume concentration as function of time for different overall equivalence ratios, p_l=200kPa & T_l=303K; lines are shown for clarity.*

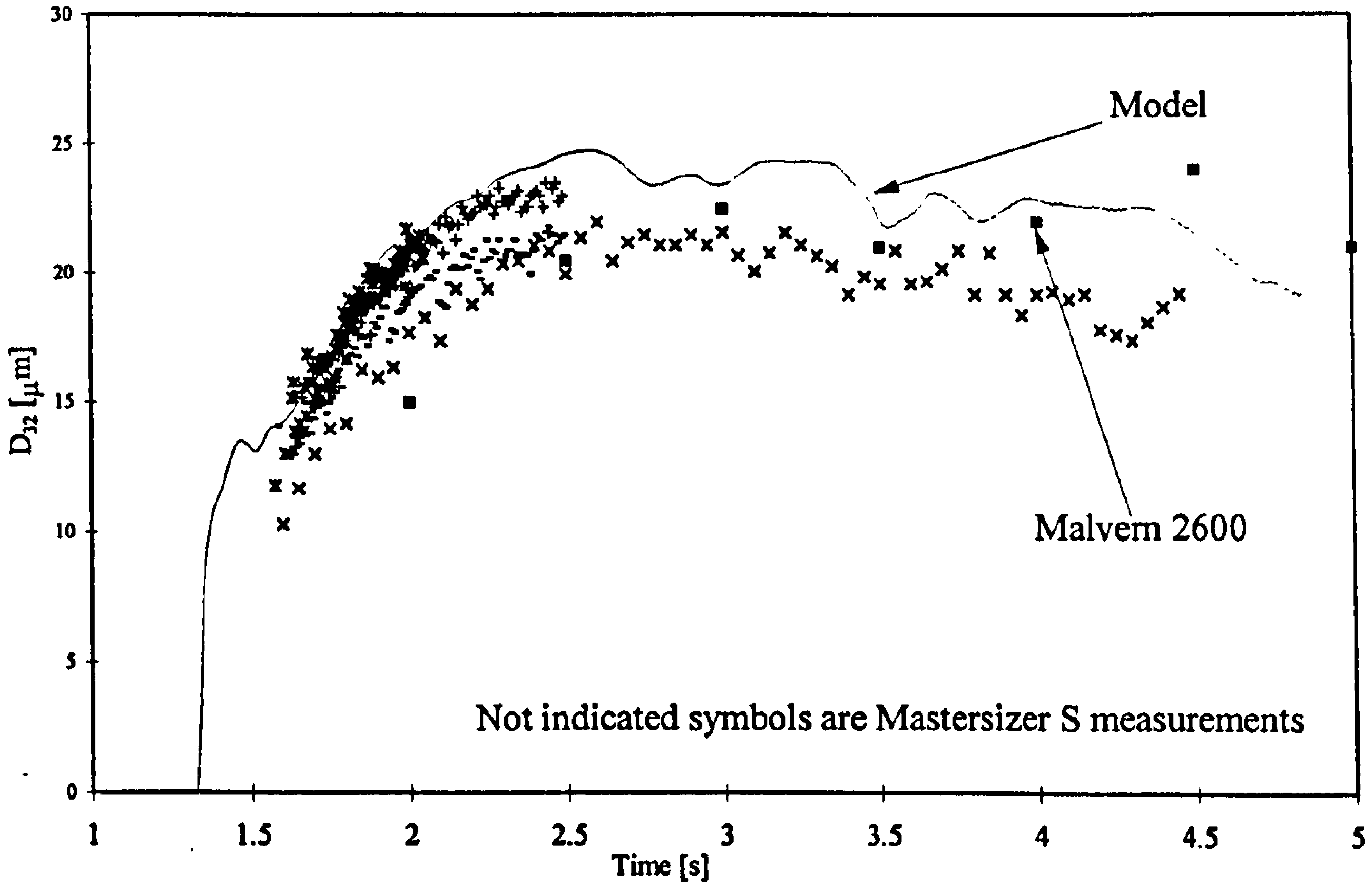

Figure 4.10(a): *Comparison of measurements of D_{32} from Malvern 2600 and Mastersizer S for p_l=200kPa & T_l=303K; also shown are model predictions (discussed in Section 4.4).*

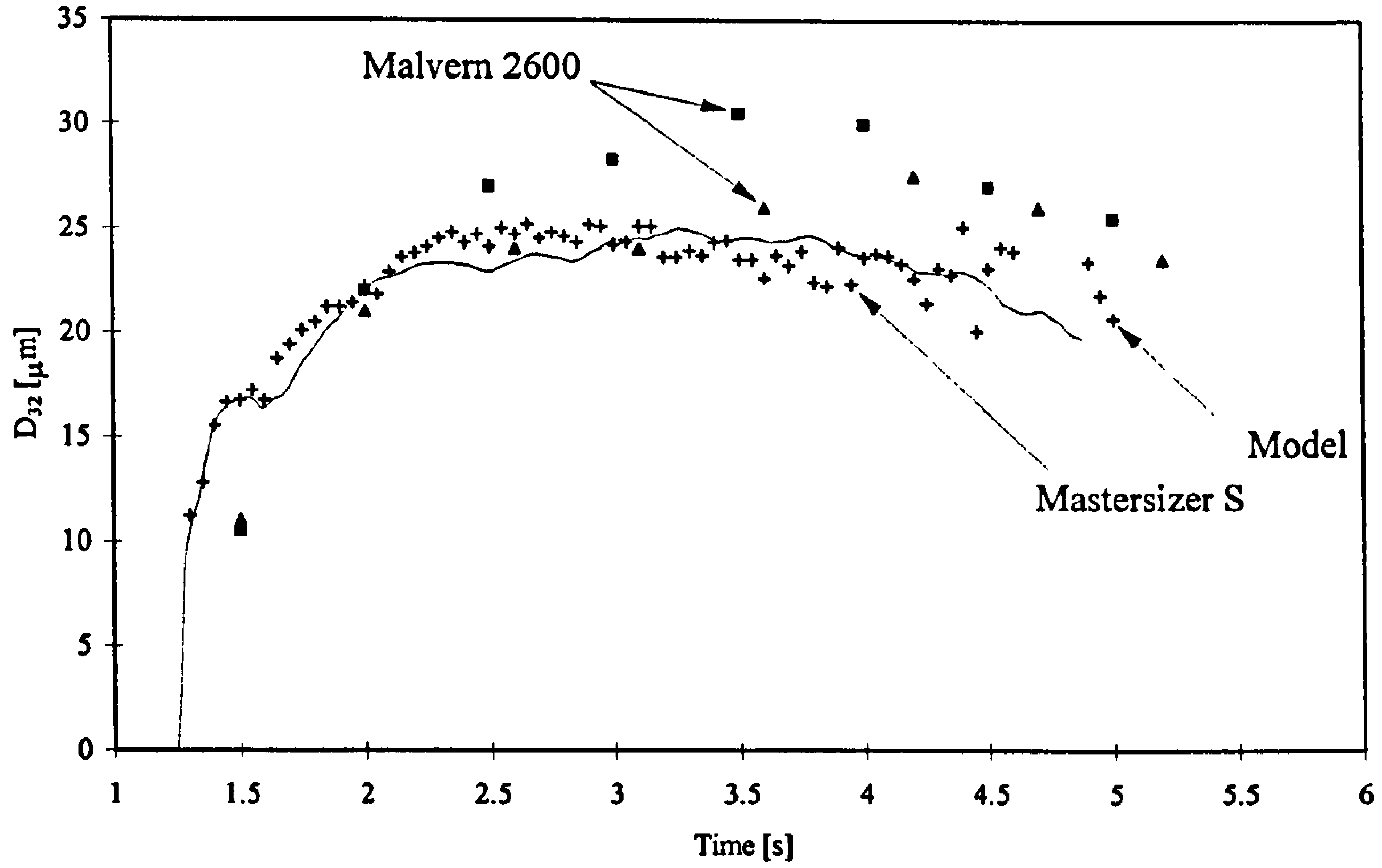

Figure 4.10(b): *Comparison of measurements of D_{32} from Malvern 2600 and Mastersizer S for p_l=250kPa & T_l=303K; also shown are model predictions (discussed in Section 4.4).*

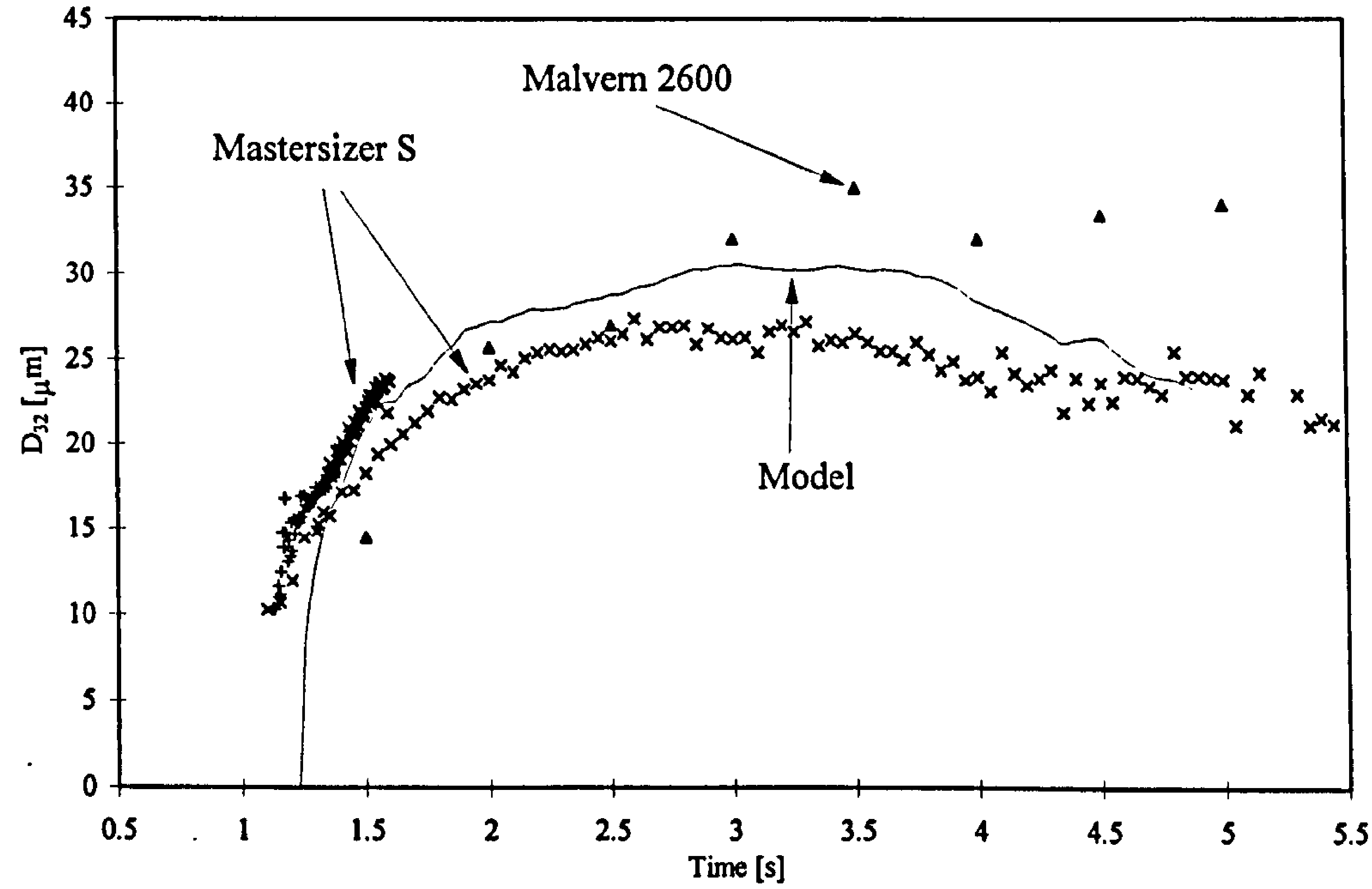

Figure 4.10(c): *Comparison of measurements of D_{32} from Malvern 2600 and Mastersizer S for p_l=300kPa & T_l=303K; also shown are model predictions (discussed in Section 4.4).*

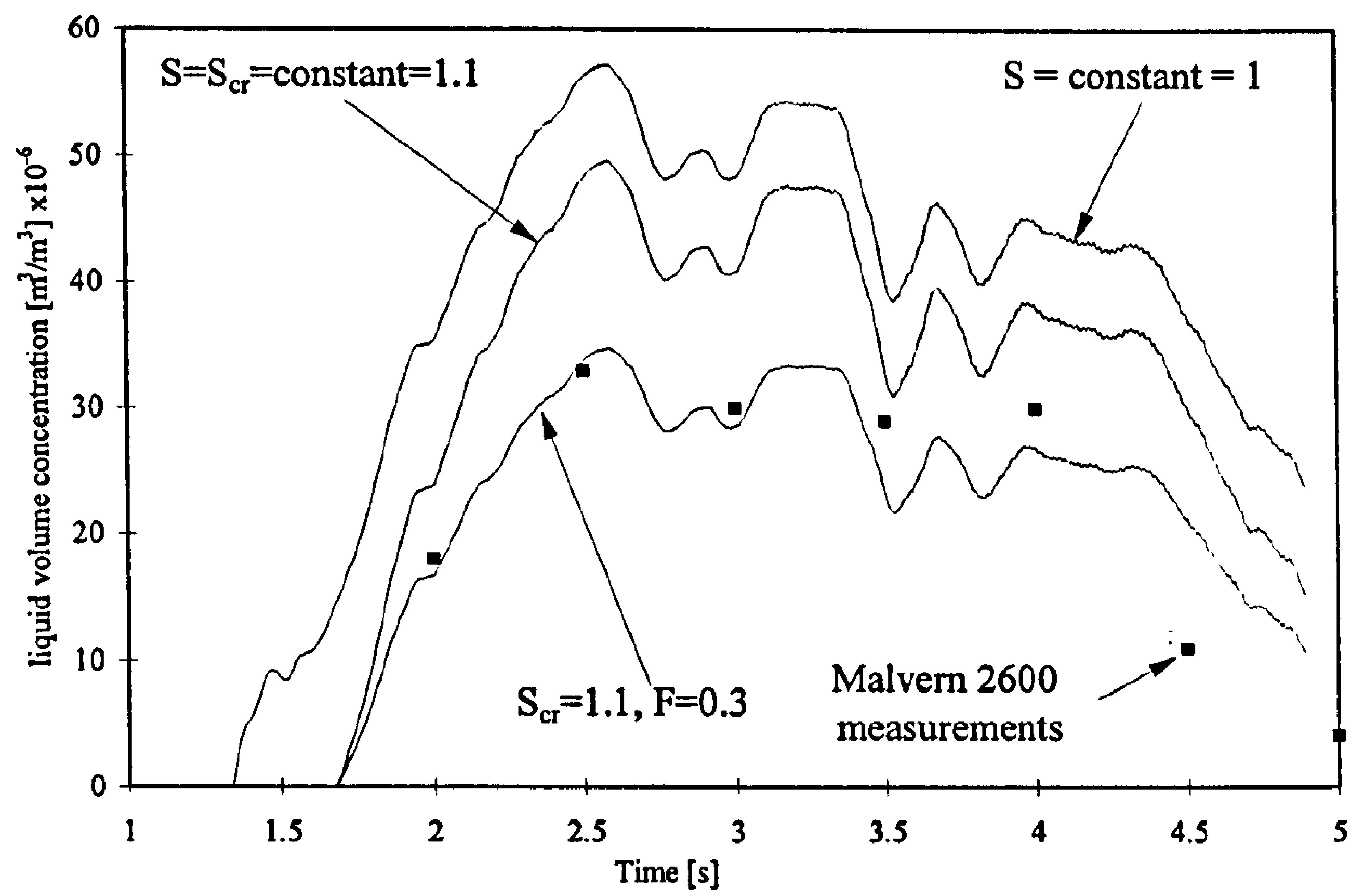

Figure 4.11(a): *Determination of* S_{cr} *and F to fit model calculations to experimental results for* $\phi_{ov}=1.0$, $p_i=200kPa$ & $T_i=303K$.

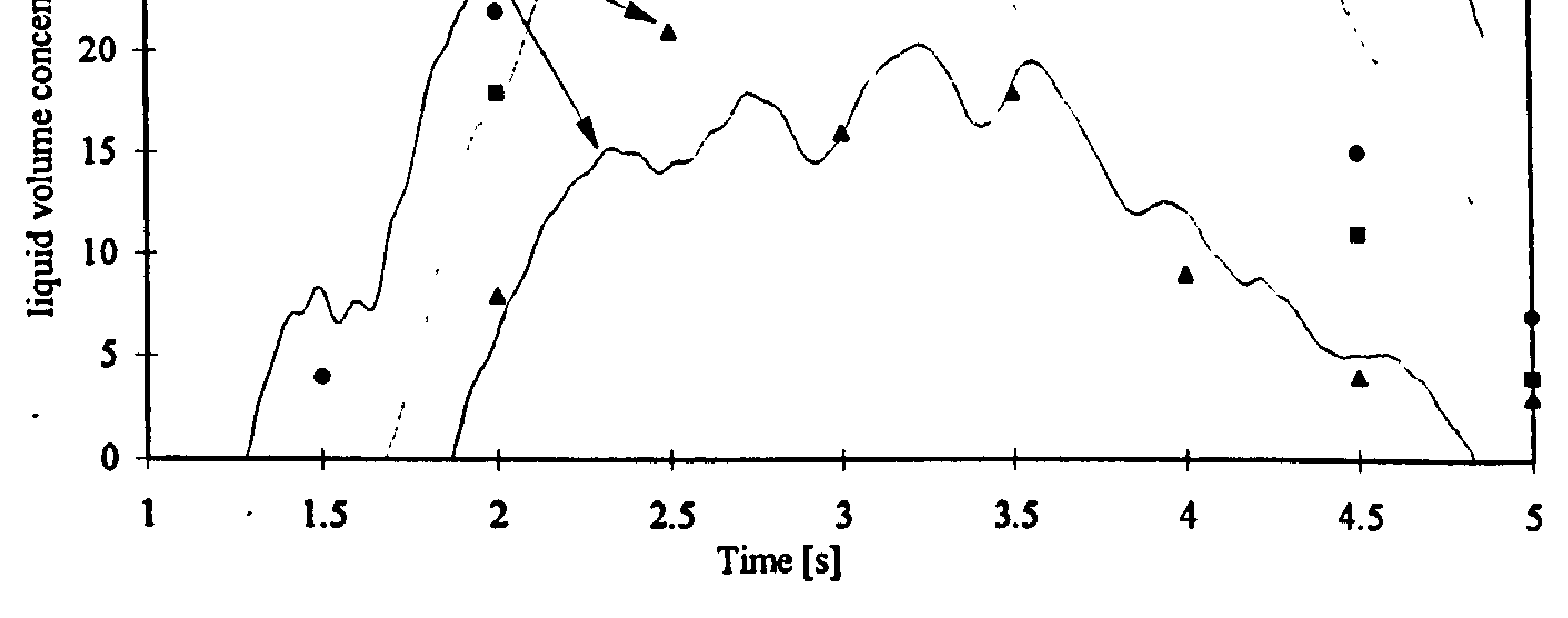

Figure 4.11(b): *Calculated and measured values of liquid concentration as function of time and overall equivalence ratio for* $p_i=200kPa$ & $T_i=303K$; *also shown are supersaturation parameters.*

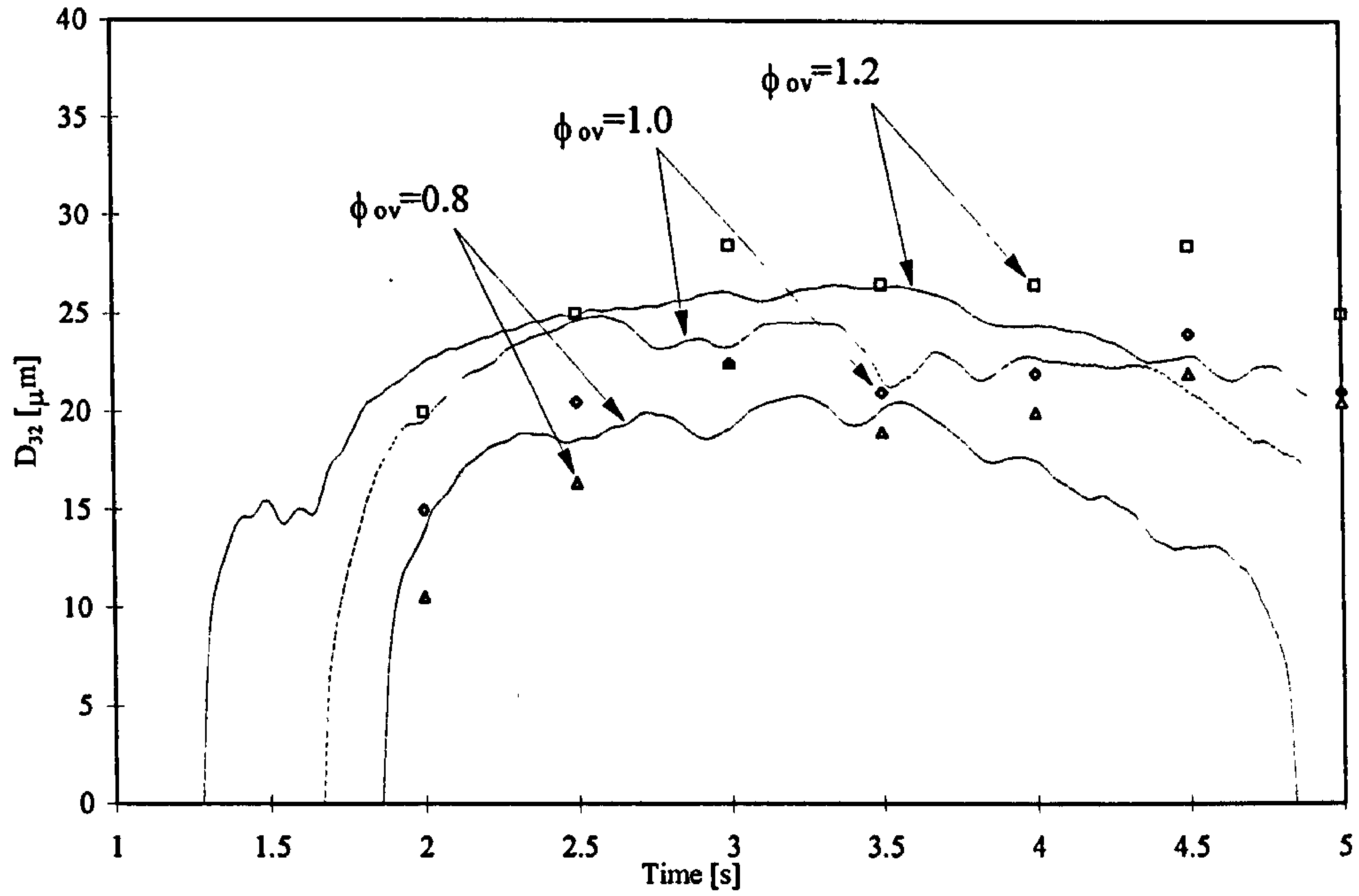

Figure 4.12: *Calculated and measured values of D_{32} as function of time and overall equivalence ratio.*

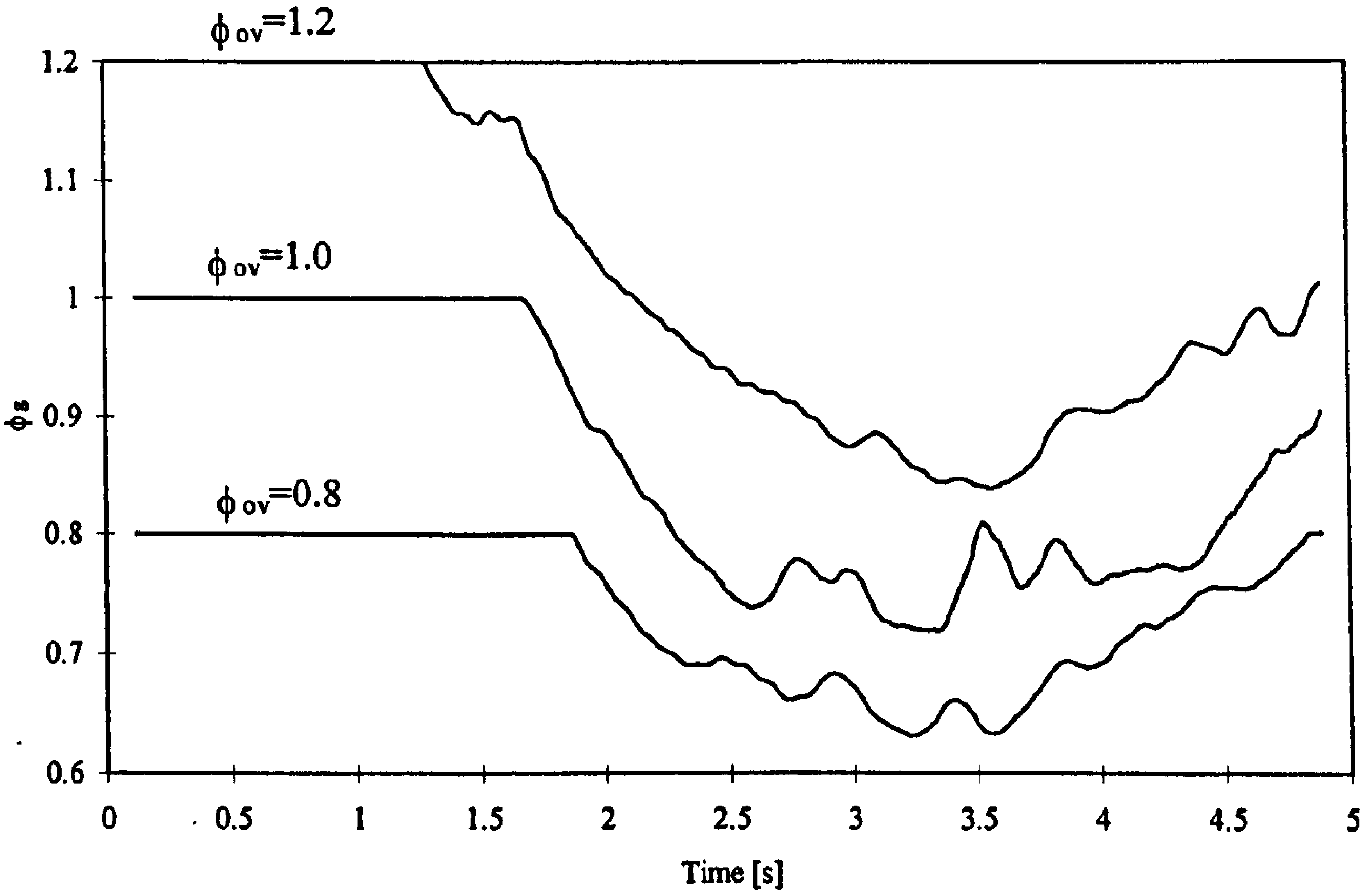

Figure 4.13: *Calculated values of gaseous equivalence ratio as function of time and overall equivalence ratio.*

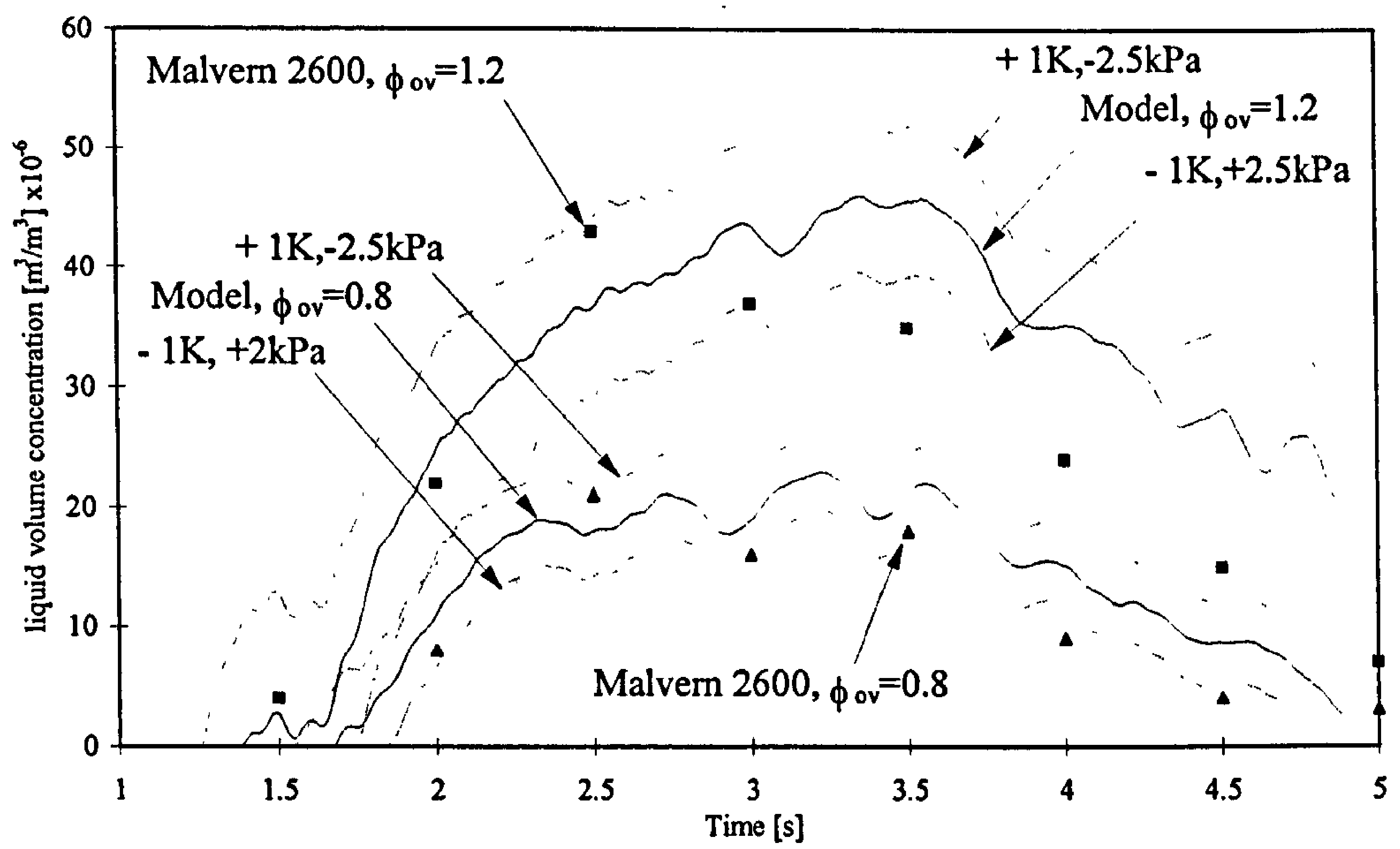

Figure 4.14: *Error bands of liquid volume concentration as function of time for deviations of 1K and 2.5kPa from the baseline calculation,* p_l*=200kPa &* T_l*=303K.*

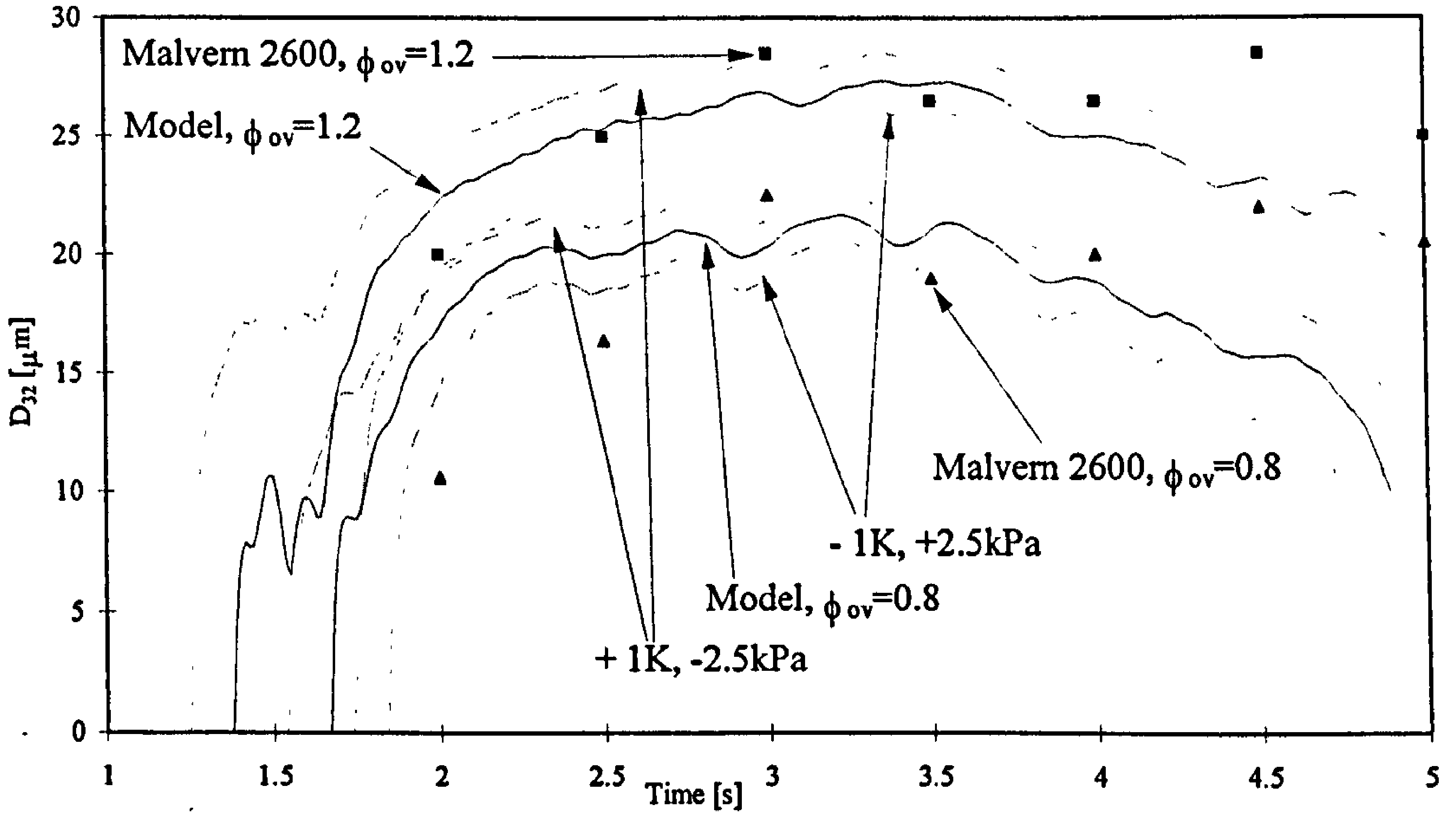

Figure 4.15: *Error bands of Sauter mean diameter as function of time for deviations of 1K and 2.5kPa from the baseline calculation,* p_l*=200kPa &* T_l*=303K.*

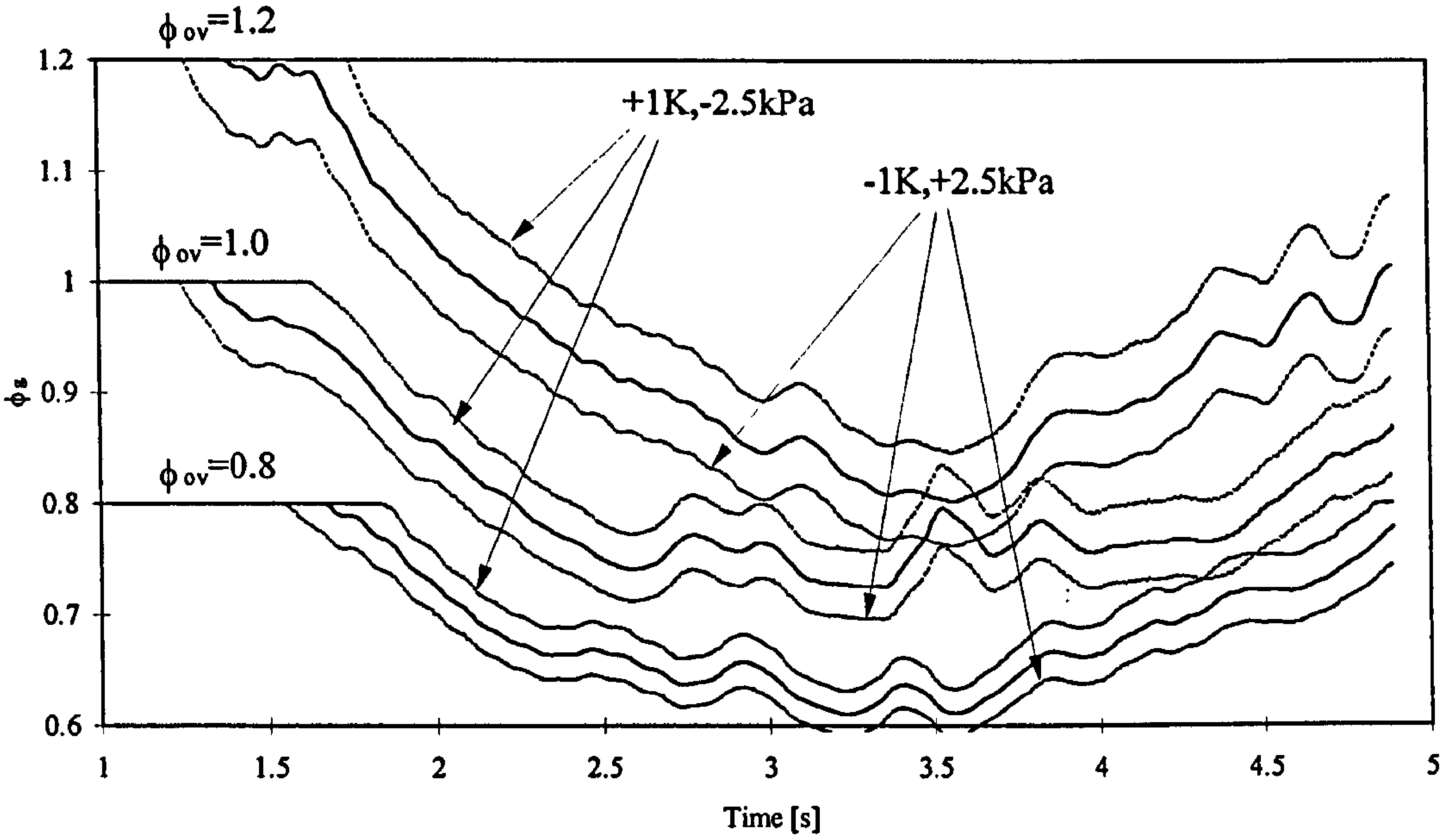

Figure 4.16: *Error bands of gaseous equivalence ratio as function of time for deviations of 1K and 2.5kPa from the baseline calculation,* p_i*=200kPa &* T_i*=303K.*

5. COMBUSTION OF AEROSOLS

Aerosol mixtures were combusted in the apparatus described in Chapter 3, mainly at laminar conditions, to investigate flame structure and quantify burning rates. Burning rates of aerosol flames have been derived from spherical expanding flames, a technique well established for gaseous combustion, which is discussed in Chapter 2. Previously published work about aerosol combustion has been presented in a less rigorous manner (Chapter 2), often with insufficient experimental detail, than that for gaseous flames.

In a first study, such as the present work, the number of experiments conducted is limited to a few conditions and are inadequate for full characterisation. Also, the concepts of stretch and flame instability, well established for gaseous combustion, can only be applied tentatively to aerosols, since there are many additional variables to consider. Nevertheless, important aspects of aerosol flame structure and burning rates have been revealed by the present work.

Photographs of aerosol flames, at a range of initial conditions, are presented and discussed in Section 5.1. Burning rates are presented in Section 5.2, and conclusions are drawn relating to the phenomenon of burning velocity enhancement, or increase in burning rate due to the presence of aerosols. The results are discussed in Section 5.3. Evidence is presented for the hydrodynamic and thermo-diffusive effect of various particles on flame structure, and the significance of each for fuel aerosols is discussed. The effect of flame stretch is argued, particularly with respect to the onset of instabilities. Also, two theoretical approaches to aerosol combustion are presented. The first relates the thermo-diffusive mechanism to instabilities in aerosol flames, and the second associates the phenomenon of aerosol flame oscillation to aerodynamic interaction of the flame front and the droplets.

The surface structure of flames presented in this Chapter is described in terms of wrinkling and cellularity. Cells in this context are surface perturbations which are separated from each other by what appears to be a crack. Here, the word "crack" describes its physical appearance and no inference regarding its detailed structure is implied. However, there is some evidence (Bradley et al., 1996b) that "crack" is a valid descriptive term, since there is, indeed, a reduction in chemical activity in flame cracks. Although cells in aerosols look very similar to those seen in some gaseous mixtures, they are not necessarily the same. The most revealing technique to investigate them, laser induced fluorescence LIF, was not available during the present work.

5.1 FLAME OBSERVATIONS

This Section presents sequences of flame photographs for gaseous and aerosol flames at a range of initial conditions. They were obtained mainly by the schlieren technique described in Chapter 3 and they demonstrate a wide variety of flame structures. Also presented are Planar laser sheet images of aerosol flames, which reveal details of the flame front and the properties of the aerosol mixture. These were analysed with PIV (Chapter 3) to obtain droplet velocities and this is discussed in Section 5.2.2.

Figure 5.1 shows a typical laminar flame, for a stoichiometric gaseous iso-octane-air mixture at T=328K and p=100kPa. Also shown with each photograph are the flame radius and the time from ignition, t_c. The flame surface is smooth, without wrinkles or cells, and displays only one shallow crack, which originates from perturbations caused by the spark plug. This flame is typical of those presented by Bradley et al. (1998) at similar conditions. However, for richer mixtures and higher pressures, they observed that flames become cellular and they showed that this is probably a function of flame stretch and Markstein length (Chapter 2).

The profound effect of pressure on stoichiometric and rich gaseous iso-octane-air flames is shown in Fig. 5.2. Figures 5.2(a) & (b) show a stoichiometric flame at different stages in its development at a pressure of 250kPa and a temperature of 358K. There are some large scale cracks in the flame surface but no cells, and this persists throughout the growth of the flame. The flame shown in Figs 5.2(c) & (d) at 500kPa is cellular throughout its development. Cells are larger in the early stage of flame growth and become smaller by cross-cracking while the flame grows. This is discussed by Bradley et al. (1998). Figure 5.3 shows the pattern of cell division during flame growth, in intervals of 2ms, for the flame shown in Fig 5.2. Figure 5.3(b) corresponds to Fig. 5.2(c). The history of cell division is presented exemplary for selected cells. It clearly shows the growth and subsequent division of cells, and the cell history can be traced at least over a significant part of the flame growth.

Figure 5.4 shows the growth of an aerosol flame, at ϕ_{ov}=1.2, ϕ_g=1.18 and $D_{32}\approx$10μm. The mixture was at p=137 kPa and T=278K. Initially the kernel was laminar. First signs of a change in flame surface structure were observed at a radius of 50mm, Fig. 5.4(d), with an increase in the number of shallow cracks (bright lines). At a radius of 60mm the flame surface is fully cellular. The cell size, which is of the order of several millimetres, subsequently decreases and becomes more pronounced. The cell boundaries appear to be associated with valleys between wrinkles.

Figure 5.5 shows a sequence of aerosol flame photographs at similar global conditions to those in Fig. 5.4 (ϕ_{ov}=1.2, p=122kPa, T=273K). However, the droplet size is larger, at

D_{32}=20μm, and the gaseous equivalence ratio lower, at 1.03 . The flame kernel displays a cellular surface structure immediately after ignition and the cells remain smaller and more pronounced than those at equivalent times and radii in the previous flame. Figure 5.6 shows the schematic enlargement of the flame shown in Fig. 5.5. It highlights the features from Figs. 5.5(e) & (f). Deep crack-like cusps divide the flame surface into large cell-like structures. These structures are hitherto called cracks and cells. Smaller wrinkles are superimposed on bigger ones. The brush like structure is probably an artefact of the schlieren technique, since it is centred around the axis of the schlieren system. Therefore this structure is disregarded in further discussion.

The cell history of an aerosol flame, at similar conditions to that shown in Fig. 5.5 (ϕ_{ov}=1.2, ϕ_g=0.93, D_{32}=25μm, p=108kPa, T=268K), is shown in Figure 5.7 . It reveals a different behaviour than that of a gaseous flame shown in Fig. 5.3. There is a random pattern of cell formation and destruction while the flame propagates. The range of cell sizes does not change significantly over the period of flame growth of 10ms shown in the Fig. 5.7.

Figure 5.8 displays a sequence of twelve frames from an aerosol flame at ϕ_{ov}=1.0, ϕ_g=0.75 p=108kPa and T=265K. This mixture, in the gas phase, is much closer to the lean flammability limit than the previous ones. It is unusual, although very repeatable, in that it exhibits periodic fluctuations of flame structure and speed during its growth. The flame kernel develops a wrinkled structure very quickly after ignition, shown in Figs. 5.8(a) to (d). However, this structure begins to fade at a flame radius of 24mm, Fig. 5.8(e), and at r=35mm the flame is completely smooth. At r=42mm, cells reappear in the upper part of the flame and quickly, within 2ms, they cover all of the surface with a very small scale cellular structure. The appearance of cells first at the top of the flame probably is due to buoyancy effects, also observed in Figs. 5.8(k) and (l). There the flame approaches the top edge of the window faster than the bottom edge. At a radius of 59mm only large scale wrinkles are observed, without the cellular cracks, present in Fig. 5.8(k). At 67mm the flame again becomes completely covered in cells. The cell size is of the same magnitude than that in Fig. 5.8(h). However, it is much smaller than the underlying wrinkled surface. These changes in flame structure are accompanied by large changes in flame speed, which are discussed in Section 5.2.2. The phenomenon of flame oscillations was also observed by Hanai et al. (1998) in clouds of Polymethylmetacrylat (PMMA) particles near the lean limit of flammability. In the present study oscillating aerosol flames, in which surface perturbations cyclically appeared and disappeared, were also observed near the gaseous phase lean limit.

Presented in Fig.5.9 are overall stoichiometric flames at approximately similar flame radii and time from ignition. It shows the change in combustion behaviour with increasing liquid equivalence ratio (decreasing ϕ_g) and drop size from Fig. 5.9(a) to (f). However, as a result of the expansion method, the change in drop size and liquid fraction is accompanied by a change in initial pressure and temperature, in this case from 205kPa and 284K for Fig. 5.9(a) to 154kPa and 270K for Fig. 5.9(f). (This demonstrates a limitation in the present technique, in that it is not possible to vary a single parameter independently of others). The effects of changes in pressure and temperature are discussed in Section 5.2.

Figure 5.9(a) displays an essentially smooth flame, for which the drop size was estimated to be approximately 15μm. In Fig. 5.9(b), at a drop size of 20μm and a gaseous equivalence ratio of 0.92, first indications of wrinkles are observed in the centre of the picture and at the top and bottom edge of the flame. In Figs. 5.9(c), (d) & (e) the drop size increases from 24 to 27μm and the ϕ_g reduces from 0.89 to 0.84. The surface structure becomes progressively more unstable. A further decrease in gaseous equivalence ratio (and mixture temperature) in Fig. 5.9(f) causes the onset of oscillations, similar to those shown in Fig.5.8.

The patterns of large scale cracks in Figs. 5.9(a) to (c) are all very similar, as is the instability on the top left edge of all flames in Fig. 5.9. This might be caused by the expansion process. This similarity of global patterns of surface structure for different initial conditions indicates, that the combustion behaviour in the bomb was very repeatable, if not totally homogeneous.

Figure 5.10 shows an overall stoichiometric aerosol flame, ignited at a rather higher temperature and pressure of 292K and 322kPa, than the aerosols shown in Figs. 5.4 to 5.9. Although the pressure is significantly lower than that for the gaseous mixture shown Figure 5.2(b), 500kPa, the cells are of similar size. In the early stages of flame development the cells of the aerosol flame (Fig. 5.10) are much more pronounced than those for the gaseous mixture. Also, the cell size for the gaseous flame decreases while the flame grows, whereas that for the aerosol flame appears to remain constant. The aerosol flame shown in Fig. 5.10 behaves much more like a gaseous cellular flame, than the aerosol flames previously presented in Figs. 5.4 to 5.9, which were ignited at temperatures between 284 and 263K and pressures between 205 and 108kPa. Although the wrinkles and cracks in the flame surface, emerge in a gradual and random manner during flame propagation, as seen in the previously described aerosol flames, the cells in the fully developed cellular flame surface, shown in Fig. 5.10(b), maintain their size and position throughout the rest of the flame growth and the cells resemble that of the gaseous cellular flame shown in Fig. 5.2(b).

Figure 5.11 shows two sequences of laser sheet images. Figure 5.11(a) displays photographs of an oscillating aerosol flame at the same conditions as that presented in Fig. 5.8, (ϕ_{ov}=1.0, ϕ_g=0.75, p=108kPa, T=265K, D_{32}=20μm). The drop spacing, measured directly from these pictures, was on average 0.5-0.6mm, which compares well with the calculated drop spacing for a diameter of 20μm (Table 2.2). Particle image velocimetry measurements of this flame are presented in Section 5.3.4 . Figure 5.11(b) shows images of a flame at ϕ_{ov}=1.2, ϕ_g=0.93 and D_{32}=20μm, similar to that shown in Fig. 5.5. For both flames shown in Fig. 5.11 the boundary at which droplets are fully evaporated is clearly visible. Although a precise determination of the evaporation zone thickness is not possible, it was estimated to be several millimetres wide. The cellular flame structure can be seen in both Figures and it is more intense in the overall rich case. However, small scale wrinkling superimposed on larger cells, as shown in Fig. 5.6, is not resolved, because the spacing of the droplets is of the same scale. All images shown in Fig. 5.11 display a near homogeneous droplet distribution, as found by other workers (Chapter 2) who used the Wilson cloud chamber method (Wilson, 1895). Also, the visibly uniform scattering properties of the drops indicate a near homogeneous drop size, as is often attributed to this method.

The effect of the presence of particles on the flame was investigated, using a laminar gaseous iso-octane-air mixture, which also contained hollow glass spheres with similar physical properties as the droplets used in the present research. The flame is shown in Figure 5.12 . It is completely smooth and very similar to that shown in Fig. 5.1, for the same equivalence ratio, pressure and temperature, but without glass particles. Burning rates of both mixtures are presented in Section 5.3.1 and the effect of particles on the flame is discussed in Section 5.3.

The effect of heat loss from the flame through drop evaporation was investigated. However, the evaporation of fuel drops also causes high gradients in mixture strength, which might have an effect on the flame (Chapter 2). Therefore, water aerosol was used, which was generated by expansion-cooling, in the same manner as fuel aerosols (Chapter 3). Because this also would have caused the condensation of iso-octane, propane was used for these experiments. The effect is discussed in detail in Section 5.3. Figure 5.13 shows the flames of three different laminar propane-air mixtures, with and without water aerosol added. The equivalence ratio was 1.3 in all cases. Figure 5.13(a) shows the flame of a mixture containing no water aerosol. Although it has multiple cracks, its surface does not become cellular. Figure. 5.13(b) shows the flame of a mixture that contains a water aerosol with "medium" number density of droplets. There is a well developed surface structure at a radius of 60mm, and its precursors are observed already at a radius of 35.5mm. The flame shown in

Fig. 5.13(c) contains a water aerosol with "high" number density of droplets. At a radius of 33mm the flame displays multiple cracks, but few cells. Its surface is much less perturbed than that for the "medium dense" aerosol mixture. At the same combustion duration the radii of the flames shown in Fig. 5.13(c) are smaller than those shown in Fig. 5.13(b), indicating a lower flame speed. At large flame radii the cell size for the "medium dense" aerosol mixture is significantly smaller than that for the "very dense" aerosol. The amount of water evaporated and condensed in these experiments was not closely controlled. However, the difference in droplet number density between "medium dense" and "very dense" water aerosols was clearly visible. The cell structure does not show a superposition of different scales of wrinkles, as that of the aerosol flames presented in Figs. 5.4 to 5.8. Also, the pattern of cell division is traceable throughout the cellular part of flame growth, similar to that of a gaseous flame, as shown in Fig. 5.3.

The effect of droplets on turbulent flames was examined at different turbulence velocities. Turbulent flame wrinkling and wrinkling caused by the presence of droplets may affect each other, as was discussed in Chapter 2. Figure 5.14(a) shows a turbulent gaseous iso-octane-air flame at ϕ=1.0, u'=0.6 m/s, p=100kPa, T=358K, and Fig. 5.14(b) shows one at u'=1.2m/s at otherwise identical conditions. The flame at the higher turbulence velocity shows much smaller wrinkles. The effect of the presence of droplets becomes evident from a comparison between the flame structure of the turbulent gaseous mixtures shown in Fig. 5.14 and turbulent aerosols shown in Fig. 5.15. Figure 5.15 shows two turbulent iso-octane-air aerosols at 265K and 90kPa. The turbulence velocity in Fig. 5.15(a) is 0.83m/s, that in Fig. 5.15(b) is 1.67m/s. As seen in Fig. 5.14, the wrinkled structure of gaseous flames becomes finer with increasing turbulence. Comparison between the gaseous flame at u'=1.2m/s in Fig. 5.14(b) and the aerosol flame at u'=0.83m/s in Fig. 5.15(a), shows that the structure of aerosol flames is much smaller in magnitude, than that for equivalent gaseous flames at, in this case, even higher turbulence. Due to the big difference in mixture temperature between the flames shown in Figs. 5.14 & 5.15, a quantitative analysis is not possible.

5.2 BURNING RATES

Burning rates of aerosol mixtures were measured at a range of initial conditions. These were compared, where possible, to burning rates of gaseous mixtures, obtained from the present apparatus and from a similar vessel at Leeds (Bradley et al., 1995, 1997 & 1998). To ensure comparability of measurements from both vessels, calibration measurements of gaseous mixtures at identical conditions were performed. These are presented in Section 5.2.1. Flame speeds and burning velocities were also measured for gaseous mixtures close to saturation conditions. These are also presented in Section 5.2.1 and provide a baseline against which aerosol data are compared in Section 5.2.2.

5.2.1 GASEOUS ISO-OCTANE-AIR MIXTURES

In the present study, flame speeds are obtained from measured radius against time data, and burning velocities are derived from these. This method, which is discussed in Chapter 2, is illustrated in Figs. 5.16 & 5.17 . Shown in Fig. 5.16 is the variation of flame speed with radius for the two gaseous stoichiometric flames presented in Fig. 5.1, at a pressure of 100kPa and temperature of 328K, and in Fig. 5.2(b), at a pressure of 500kPa and a temperature of 358K. Figure 5.17 presents a graph of flame speed against stretch, for the same data. The point of ignition in Fig. 5.17 is located to the right, at high stretch rates, and flame propagation proceeds from the right to the left. The mixture at p=100kPa and T=328K, marked by square symbols in Fig. 5.16 and a solid line in Fig. 5.17 clearly exhibits four regimes of flame development, as discussed by Ali et al. (1993). Initially, between points (1) and (2), indicated in Figs. 5.16 & 5.17, the spark causes rapid thermal growth of the flame kernel. However, high stretch rates cause the flame speed to decrease rapidly when the thermal energy of the spark is dissipated into the gas. At point (2), a propagating flame probably is not established yet. Between points (2) and (3), spark plasma dynamics and flame stretch are operative in a regime of spark assisted flame propagation. Between points (3) and (4), flame speed increases as the rate of stretch reduces. Not all flames exhibit this typical behaviour. The mixture marked by triangular symbols in Fig. 5.16 and a short dashed line in Fig. 5.17, ignited at a pressure of 500kPa, does not exhibit these regimes. A possible reason for the apparent lack of the regimes (1) to (3) on this flame is that for this mixture flame stretch aids flame propagation. This has been shown by Bradley et al. (1998). The unstretched flame speed is derived by a linear extrapolation to zero stretch, which is indicated by the long dashed lines in Fig. 5.17. The laminar burning velocity is calculated from the unstretched flame speed as discussed in Chapter 2. The gradient of the extrapolation is the burnt gas Markstein length, L_b. A positive value of L_b, i.e. increasing flame speed with decreasing stretch rate, indicates a flame with little tendency to instabilities, a mixture with negative L_b tends to develop instabilities much quicker.

The unstretched flame speed, and hence the laminar unstretched burning velocity, must be derived from flame speed data for which the flame surface is smooth. This condition is ascertained from schlieren photographs, as presented in Section 5.1.

In such cases when the flame becomes cellular, as shown in Fig. 5.2(b), the flame speed increases. This can clearly be seen in Fig. 5.17, in which the short dashed curve rapidly accelerates at a stretch rate of approximately 0.1 ms^{-1}. This part of the data must be excluded in the derivation of the unstretched laminar flame speed.

The increase of flame speed after the transition to full cellularity is a function of time. This was discussed in Chapter 2. To a first approximation, a linear extrapolation is sufficient to estimate the effect of cellularity on flame speed, but will probably underpredict this effect. Since extrapolation to zero stretch is equal to an extrapolation to infinite flame radius, a burning velocity can be calculated using the same method as that used for the unstretched laminar burning velocity. This burning velocity, is a function not only of the initial mixture composition, pressure and temperature, but also of the increased surface area and, hence, heat release rate due to the presence of cells.

The use of such flame speeds and burning velocities is important with regard to aerosol flames, and is further discussed in Section 5.2.2. Generally, the behaviour of the flames shown in Figs. 5.16 & 5.17 and of aerosol flames, presented in Section 5.2.2, is very similar.

An objective of the present work is to investigate the difference in burning velocity between single and two-phase mixtures. Figure 5.18 shows, for stoichiometric iso-octane-air mixtures, the variation of unstretched laminar burning velocity with reactant temperature. Triangular symbols mark the experimental results, at a pressure of 100kPa, of Bradley et al. (1998). Also shown are measured data of Drake (in prep.) and of the present author, both obtained in the present bomb, and measurements by Mokhtar (in prep.) in another Leeds fan stirred bomb, all at 100kPa. The solid line in Fig. 5.18 is a curve fit through these data and shows good agreement between the measurements of different workers.

Ideally, burning velocity measurements for gaseous mixtures should be obtained at the same conditions as those for the aerosols. However, it is not possible to have single phase mixtures at the same conditions as the present thermodynamically generated aerosols. Hence, Fig. 5.18 presents data for gaseous mixtures, at a pressure of 100kPa and down to 284K, which is 11K above saturation conditions. These were then extrapolated to the temperatures pertaining in the aerosol studies. The trend of the low temperature data indicates a significant drop in burning velocity, when the mixture temperature approaches the saturation limit.

5.2.2 ISO-OCTANE-AIR AEROSOLS

A summary of the aerosols investigated in the present research, and their properties, is presented in Table 5.1. It includes burning rates, Markstein lengths and brief descriptions of the combustion regimes during flame growth. Figure 5.19 shows the flame speeds of various aerosol mixtures plotted against flame radius. Also indicated are their values of ϕ_{ov}, ϕ_g and D_{32}. Unlike in gaseous iso-octane-air mixtures, the overall rich aerosol mixtures burn faster than overall stoichiometric ones. A probable reason, for this is that the overall rich aerosol burns at a gaseous equivalence ratio that, being leaner than ϕ_{ov}, is closer to that for the highest burning rate than ϕ_g for the overall stoichiometric aerosol. The peak burning velocity for gaseous iso-octane-air mixtures occurs at an equivalence ratio of approximately 1.05 (Bradley et al., 1998). This was suggested in earlier works (Chapter 2) as the mechanism for burning velocity enhancement in rich mixtures. Another probable reason is that the overall rich aerosol flames of the present research develop a more pronounced cellular structure than the overall stoichiometric ones. This is illustrated on the photographs presented in Section 5.1. The mixture marked by crosses (ϕ_{ov}=1.2, ϕ_g=1.03, D_{32}=20μm), shows the highest acceleration of the flames presented in Fig.5.19.

Figure 5.20 shows the data presented in Fig. 5.19 plotted against flame stretch. As flame stretch decreases, flame speed increases for most mixtures. Clearly visible is the acceleration of the aforementioned mixture (ϕ_{ov}=1.2, ϕ_g=1.03, D_{32}=20μm), here plotted with a bold line. Although these plots are very similar in appearance to typical plots for gaseous mixtures, it was not possible to derive an unstretched flame speed by extrapolation to zero stretch, because these aerosol flames have a wrinkled or cellular structure, whose amplitude is a function of liquid equivalence ratio and the Sauter mean diameter. However, as discussed in the previous section, the linear extrapolation nevertheless yields a flame speed which allows for the calculation of a burning velocity and these parameters are henceforth termed aerosol flame speed, S_a, and aerosol burning velocity, u_a. Flame speeds and burning velocity obtained in the present work are listed in Table 5.1.

All mixtures presented in Figs. 5.19 & 5.20 were ignited at temperatures between 277K and 265K. Figure 5.21 shows plots of flame speed against stretch for two aerosol mixtures ignited at 286K and 292K. Also shown is the gaseous mixture at ϕ_{ov}=1.0, p=500kPa, T=358K, presented in Fig. 5.17. The difference in flame speed between the aerosols and the gaseous mixture is probably due to the difference in initial mixture temperature of about 70K. Both aerosols show a similar acceleration of flame speed at a stretch rate of 0.1ms^{-1} to that of the gaseous mixture. As described in the previous Section, the acceleration for the gaseous mixture is due to the onset of cellularity. This also appears to be the case in the aerosol mixtures. Figure 5.10 shows photographs of one of the aerosols presented in Fig.5.21 (ϕ_{ov}=1.0, ϕ_g=0.9, D_{32}=16μm, p=322kPa, T=286K). At a radius of 40mm the flame is on the verge of full cellularity, at a radius of 63mm it is fully cellular. Unfortunately, the generation of an aerosol with the cloud chamber method, does not allow independent variation of pressure and temperature. Hence, an increase in temperature affects also an increase in pressure (Chapter 3). Therefore, the appearance of a cell like structure in the aerosol mixture might, in part, be attributed to the increase in pressure. However, the size of the cells of the aerosol at 322kPa and the gaseous mixture at 500kPa is very similar, and one might conclude that the cell size of the aerosol mixture at 322kPa is much finer than would be observed for a gaseous mixture at similar conditions.

Figure 5.22 shows aerosol burning velocities plotted against initial mixture temperature for overall stoichiometric aerosols. Also shown is the gaseous baseline burning velocity at 100kPa. Mixture pressures for the aerosol data shown varied between 205 and 108kPa and this clearly has an effect on the burning velocities. In gaseous mixtures a pressure drop of 100kPa effects an increase in u_l of approximately 15% (Bradley et al., 1998) and this magnitude of pressure dependence was assumed for the aerosol mixtures. Correction for the effect of pressure, from a datum value of 100kPa, is shown by a long dashed line in Fig.5.22. By extrapolating the experimental gaseous burning velocities to the temperatures of the aerosol experiments, a considerable enhancement of the aerosol burning velocities is suggested and this increases with both Sauter mean diameter and liquid equivalence ratio (although these effects may not be independent).

For other aerosols, investigated in the present research, baseline burning velocities for gaseous mixtures were not available. This includes the overall stoichiometric aerosols at 286K, 322kPa and 292K, 358kPa, as well as the aerosol mixtures at ϕ_{ov}=0.8 and ϕ_{ov}=1.2. For these mixtures the enhancement was estimated as follows.

The burning velocity for a gaseous stoichiometric mixture at 100kPa and 290K is obtained from Fig. 5.22, and is approximately 0.25m/s. An increase in pressure from 100kPa to 300kPa reduces u_l by approximately 20% (Bradley et al., 1998), which yields an estimate of u_l at 300kPa & 290K of approximately 0.17m/s. Values of u_a for the experiments performed at 286K, 322kPa and 292K, 358kPa are between 0.28 and 0.71m/s, which returns an enhancement of approximately 70 to 420%. Although data scatter at these condition was high, as listed in Table 5.1, it clearly suggests a strong enhancement of burning velocity, as previously found by other workers, given in Table 2.1.

Figure 5.23 shows u_a against temperature for mixtures at ϕ_{ov}=1.2 and ϕ_{ov}=0.8. Also shown are the data points for overall stoichiometric aerosols from Fig. 5.22. The data for ϕ_{ov}=0.8 appear to show a similar trend to those for ϕ_{ov}=1.0. However, in the absence of a baseline value of u_l at these temperatures for this equivalence ratio a conclusion as to whether an enhancement exists is not possible.

The values of u_a for ϕ_{ov}=1.2 indicate a maximum value at a drop size of 20μm. A tentative comparison may be possible with the mixture with a drop size of approximately 10μm and a gaseous equivalence ratio of approximately 1.18. The burning velocity is 0.29m/s for the mixture with ϕ_g=1.18, $D_{32}\approx$10μm, and 0.41m/s for that at ϕ_g=1.03, D_{32}=20 μm, which yields an enhancement of 40%. The decrease in gaseous equivalence ratio from 1.18 to 1.03 accounts for approximately 10% of the increase in burning velocity (Bradley at al., 1998). However, the photographs of both mixtures, shown in Figs. 5.4 & 5.5, display a highly cellular structure for both flames. Also, the plots of flame speed against stretch for these mixtures, shown in Fig. 5.20, suggest a much greater acceleration for the mixture at ϕ_g=1.03, D_{32}=20μm from an initially lower flame speed than for that at ϕ_g=1.18, $D_{32}\approx$10μm. Therefore, it is likely that an enhancement relative to a smooth flame would be much greater than 40%.

Aerosol combustion, performed at temperatures lower than approximately 270K, exhibits huge oscillations of flame speed during the growth of the flame. The fluctuations in flame speed are accompanied by the appearance and disappearance of a cell like flame surface, as shown by the schlieren photographs of an oscillating aerosol flame in Fig.5.8. Figure 5.24 shows plots of flame speed against time from ignition. The period of oscillation of any one flame appears to be constant throughout flame propagation for a given condition and this is marked on each curve in Fig. 5.24. Acoustic waves in the bomb are unlikely to be the cause of these oscillations since the acoustic frequency is of the order of 20-30Hz, which is not consistent with the flame oscillation frequencies of 50-125Hz.

Figure 5.25 shows a plots of flame speed against stretch for various oscillating flames. The gaseous equivalence ratios and mixture temperatures suggest that these flames are close to the lean limit of flammability. Relative to non-oscillating flames of the same overall equivalence ratio, the peak flame speeds of the oscillating flames have similar values. These are given in Table 5.1. Irrespective of the difference in equivalence ratio, both pairs of flames in Fig. 5.25, for ϕ_{ov}=1.0 and ϕ_{ov}=0.8, show a very similar pattern and one flame for each equivalence ratio is presented in greater detail in Figs. 5.26 & 5.27. Figure 5.26 shows the plot of flame speed against stretch for a flame at ϕ_{ov}=1.0, ϕ_g=0.75, D_{32}=20μm, T=265K and p=108kPa. Schlieren photographs of this flame are shown in Fig. 5.8 and laser sheet images for a mixture combusted at identical conditions are presented in Fig. 5.11. The changes in the flame surface structure during flame development are marked in Fig. 5.26. After the spark effect has ceased at point (1) in Fig. 5.26, the flame speed increases. Initially stretch does not vary greatly and the flame surface becomes cellular at point (2). The cellular structure remains as the flame stretch reduces until the flame speed reaches its first maximum at point (3). Although stretch continues to decrease, as does the flame speed between points (3) & (4), the flame surface begins to smoothen and at a stretch rate of 0.05ms^{-1} no perturbations were observed. After this, the flame speed increases as does the flame stretch. At a stretch rate of approximately 0.1ms^{-1} a cellular structure appears. It remains until after the second maximum in flame speed at point (5). At the end of the observation period the flame was still wrinkled (Fig. 5.11k) but the cellular cracks had disappeared. At a flame radius which was just outside the field of view of the window the flame again became highly cellular (Fig. 5.11h). A possible mechanism for this flame oscillation is flame stretch and this is discussed in Section 5.3. Figure 5.27 shows the plot of flame speed against stretch for a mixture at ϕ_{ov}=0.8, ϕ_g=0.66, D_{32}=17μm, T=263K and p=108kPa. This is different from the previous flame in that values of flame speed and hence stretch, are much lower due to the lower equivalence ratio. The onset of wrinkling coincides with the two peaks of flame speed, when stretch begins to decrease, and wrinkling disappears when stretch increases, on the branch rising to the second flame speed maximum. The argument that an increase in surface area, due to surface perturbations, causes an increase in flame speed, is only supported by the graph shown in Fig. 5.26, where the flame speed increases with the onset of wrinkling. It is not supported by the graph shown in Fig. 5.27, in which this mechanism appears to be completely out of phase.

Figure 5.28 shows particle image velocimetry (PIV) measurements for a mixture combusted at identical conditions to those shown in Fig. 5.26. The solid square symbols denote drop speeds directly ahead of the flame front, obtained from the same series of images as those shown in Fig. 5.11(a). The solid line is a curve fit to the drop speed data. The triangular symbols mark the flame speed, and they were derived from the measured flame edges on the same images as those used for PIV. The short dashed line is a curve fit through the flame speed data. The long dashed line shows flame speed measurements, obtained from the schlieren photographs shown in Fig. 5.8. The magnitudes of flame speeds derived from laser sheet and schlieren images agree well, as do the periods of the oscillation. The phase difference between the two sets of flame speed data is probably due to them being obtained from different experiments. The droplet speed shows a similar oscillation period to those of the flame speeds. At a flame radius of approximately 30mm the flame speed, obtained from the laser sheet images, is about 2.4m/s. The drop speed at this point attains a maximum of approximately 1.7m/s, which yields a droplet entrainment velocity of 0.7m/s. However, this entrainment rate is not constant, and at a flame radius of 46mm the drops move at the same speed as the flame front, and hence the entrainment rate is zero. The trends of flame speed and droplet speed indicate that, as the flame progresses, the flame speed falls behind that of the drops. This possibly implies a complex aerodynamic interaction between the drops and the flame front. A simple model was used to investigate this and this is discussed in Section 5.3.4.

5.3 DISCUSSION

Various mechanisms for the enhancement of aerosol burning velocities have been suggested in previous works. These are discussed in Chapter 2. This Section uses the evidence presented in Sections 5.1 & 5.2, to discuss the cause of burning velocity enhancement in Section 5.3.1. Some additional experimental evidence from the present work is used in subsequent Sections to discuss the significance of various mechanisms for the occurrence of instabilities in aerosol flames. Section 5.3.2 presents the effects of inert, non-evaporating glass particles on a flame. Section 5.3.3 shows experiments with water aerosol, added to gaseous fuel-air mixtures. Water is essentially chemically inert and a water aerosol introduces the effect of heat absorption due to drop evaporation into the combustion system, without the locally varying heat input through their chemical reaction. Section 5.3.3 also briefly discusses a linear stability analyses of aerosol flames (Greenberg et al., 1998 & in prep.). In Section 5.3.4 the mechanisms possibly responsible for the occurrence of oscillations in aerosol flames are considered and a simple model, simulating aerodynamic interaction between drops and the movement of gas ahead of the flame front is presented. Finally, the important points of this discussion are summarised in Section 5.3.5

5.3.1 BURNING VELOCITY ENHANCEMENT

In earlier works, discussed in Chapter 2, the phenomenon of burning velocity enhancement was often attributed to "self-turbularisation" of the flame, or to a "rugged, undulated and thickened" flame surface. The photographs and measurements presented in the present work also indicate that changes in flame surface structure is important. These images do not support the proposition of a self-turbularisation. However, this is not conclusive, since it is possible that turbulence generation requires a longer development time than was available in the current vessel (Bradley, in prep.). A comparison of flame development of gaseous cellular flames with aerosol flames, presented in Section 5.1 & 5.2, suggests that the same or similar mechanisms thought responsible for the increase of the flame speed in gaseous cellular flames is also the cause of burning velocity enhancement in aerosol flames, namely the increase in flame surface area. However, the mechanism that causes the change in flame surface structure is not yet understood. As laid out in Chapter 2, a number of mechanisms have been suggested and these are discussed below.

5.3.2 HYDRODYNAMIC INSTABILITY

Hydrodynamic instabilities occur in several ways in aerosol flames. As discussed in Sections 5.1 & 5.2 the tendency of both aerosol and gaseous flames to become unstable increases with mixture pressure. However, it appears that the presence of droplets triggers instabilities earlier in aerosols than in equivalent gaseous mixtures at similar overall equivalence ratio, pressure and temperature.

In earlier works, droplets were often thought of as obstructions in the path of the flame, that distort and lacerate the flame surface (Chapter 2). It was suggested that a flame that propagates through a droplet matrix is turbularised and that this causes the increase in burning velocity. This mechanism was investigated in the present work, by seeding a stoichiometric gaseous iso-octane-air mixture with hollow spherical glass beads. These particles had properties similar to those of iso-octane droplets in a combustion environment. Their Sauter mean diameter was 10-12μm, which represents the size of a partly evaporated droplet when it enters the reaction zone. The density was 1.1 g/cm^3, which is approximately 50% heavier than iso-octane. Due to the increased inertia, the glass spheres were expected to have a greater effect than drops of similar size. The total volume of particles added to the mixture, 5 cm^3, was similar to the total volume of fuel used for a typical aerosol experiment. Therefore it was assumed that the number density and spacing of particles was similar to those of an aerosol mixture, in which all the fuel is present in liquid form. Figure 5.29 shows plots of flame speed against stretch for these experiments. The dashed lines are the experiments with 5cm^3 of beads added, the solid line is a mixture with no particles. Both mixtures containing glass spheres burn at a similar rate to their respective unseeded mixture and their flame development is very similar. Experiments with only 1cm^3 of particles added to the mixture, to simulate a partly condensed mixture, yielded similar results. Photographs of a flame seeded with 5 cm^3 are shown in Figure 5.12. It is very similar to that shown in Fig. 5.1, for an unseeded gaseous iso-octane-air mixture at otherwise identical conditions. The observations presented in Figs. 5.12 and 5.29 suggest that the so-called "grid-effect" does not play a mayor role with respect to flame instability for aerosols comparable to those used in the present work.

5.3.3 THERMO-DIFFUSIVE INSTABILITY

Previous workers have suggested a number of mechanisms linked to the mixture properties in terms of fuel-air ratio (Chapter 2). It has been assumed that wrinkling of the flame front is caused by preferential flame propagation through areas of optimum equivalence ratio. This is discussed in Chapter 2. For gaseous flames, it has been observed, that rich flames develop instabilities earlier than lean flames (Bradley et al., 1998). Therefore, it might be assumed that fuel rich areas in aerosols, close to evaporating drops, could possibly trigger instabilities. In order to investigate these hypotheses, experiments were conducted using water aerosols in a gaseous fuel-air mixture. The aerosol was generated by expansion-cooling, in the same way as the fuel aerosols investigated in this thesis (Chapter 3). Since this causes a significant drop in mixture temperature, and hence the condensation of iso-octane, propane was used, because it does not condense in the range of temperatures that occurred in the present work. The equivalence ratio was in all cases 1.3 . Woolley (1999) observed that propane-air mixtures at this equivalence ratio did not become unstable at 100kPa, but that an increase in equivalence ratio did induce instabilities at this pressure. Figure 5.30 shows plots of flame speed against stretch for propane-air mixtures containing different amounts of water aerosol. The thick solid line represents a mixture with a "medium dense" water aerosol, the thin solid line is for a "very dense" water aerosol and the long dashed line shows a mixture with no water. This mixture was expanded in the same way as the aerosol mixtures to reduce its temperature to a similar value. Also shown, for comparison, is a mixture that contained no water and was not cooled by expansion. This is marked by a short dashed line. Mixture conditions are given in the Figure. Photographs of these flames are shown in Fig. 5.13, and these, as well as the aerosol terminology are presented in Section 5.1.

Initially, the expansion-cooled gaseous mixture, shown in Fig. 5.30, burns at a higher flame speed than both aerosol mixtures. This agrees with the observations of Bradley et al. (1995) who found that the addition of water vapour reduced the burning rate. They also observed an increase in L_b which suggests that these mixtures are more stable than mixtures without water vapour. However, at a stretch rate of 0.15 ms^{-1} the flame speed of both aerosol mixtures rises drastically, and this is causes by the onset of instabilities, as illustrated in Fig. 5.13. The increase in flame speed is particularly strong for the "medium dense" water aerosol, which at a stretch rate of 0.1ms^{-1} attains the same flame speed as the gaseous mixture that was not cooled by expansion. The burning velocity for the expansion-cooled gaseous mixture is 0.253m/s, that for the "medium dense" aerosol mixture is 0.385m/s, and this yields an enhancement of 52%. However, the "very dense" aerosol mixture returns a value of u_a of only 0.269m/s and the enhancement is only 6%. This suggests that there is an optimum amount of aerosol for an optimum burning rate, as suggested by previous workers (Chapter 2). The use of a water aerosol contradicts the argument that rich pockets might trigger the instabilities. It also weakens the hypothesis of preferential flame propagation, although the local dilution of mixture by evaporating water drops might have a similar effect.

Greenberg et al. (1998, in prep. & 1999) mathematically investigated the instability of aerosol flames, using linear stability analysis. The model is based on the similarity of flame structure observed in cellular gaseous flames and aerosol flames and examines the effect of heat loss due to evaporation as a primary factor involved in the instability in flames. The analysis follows the lines of Shivashinsky (1977) for gaseous flames and considers only heat and mass transfer, without considering the hydrodynamics in detail. Velocity differences between the drops and the gas ahead of the flame front are disregarded. This assumption was found by Greenberg et al. to be relevant only quantitatively and did not affect the qualitative prediction. The model predicts the occurrence of cellularity for given conditions and also gives an indication as to what the cell size will be. The stability of a mixture is expressed in terms of the growth parameter Ω. If $\Omega<0$ the mixture is stable, $\Omega>0$ implies that a perturbation will grow and $\Omega=0$ means that a perturbation will neither grow nor decay. Figure 5.31 shows a plot of Ω against the dimensionless critical wave number k_{cr}, which is a measure of the length scale of the perturbation. Three curves are shown for different drop loadings, δ. At a drop loading of zero there are no droplets in the mixture, at $\delta=1$ all the fuel is liquid. Figure 5.31 shows that, when a gaseous mixture, $\delta=0$, is stable, aerosol mixtures, $\delta>0$, at the same conditions in terms of mixture pressure and temperature and overall equivalence ratio are not. The intercept of the curves with the x-axis at $\Omega=0$ yields a value of k_{cr} that allows for an estimate of the cell size. For conditions similar to those of the present research Greenberg et al. computed cell sizes of the order of 10 to 15mm, which agrees with those measured from the images presented in Section 5.1. Figure 5.32 shows the effect of aerosol density on cell size. The critical wave number is inversely proportional to the cell size. The evaporation coefficient $\overline{C}$ describes the aerosol properties in terms of number density and volatility. Increasing values indicate less dense aerosols, given that the volatility is constant. The arrow indicates the qualitative change in $\overline{C}$ and δ for the propane-air-water aerosols presented above. It suggests that the cell size increases with aerosol density and drop loading. This effect can clearly be seen in Fig. 5.13(b) &(c). Figure 5.33 shows a plot of lewis number against k_{cr}. Shown are two mixtures with the same overall equivalence ratio. One mixture is gaseous, $\delta=0$, in the other one all fuel is liquid, $\delta=1$. For equal Lewis numbers k_{cr} is always greater for the aerosol. This indicates that an aerosol always develops a finer surface structure than an equivalent gaseous mixture, even if that gaseous mixture is cellular itself. This effect can be seen in Figs. 5.2 & 5.10. This analysis of Greenberg et al. yields good qualitative agreement with the experimental results of the present work, which indicates that heat loss due to the evaporation of droplets might play a dominant role in the manifestation of instabilities in aerosol flames. However, linear analysis cannot predict the amplitude of a surface perturbation and, hence, the increase in surface area, which is responsible for the burning velocity enhancement in aerosol flames. For this purpose a non-linear analysis is needed.

5.3.4 OSCILLATING AEROSOL FLAMES

1. Stretch

A possible mechanism for the flame oscillations presented in Figs. 5.8, 5.25, 5.26 & 5.27 is flame stretch. Bradley et al. (1998) concluded from their experimental observations of gaseous flames, that stretch has an effect on the onset of instabilities, and that this effect is a function of Markstein length which itself is a function of equivalence ratio. This may also be applicable to aerosol flames.

The oscillating flame shown in Fig. 5.26, is briefly described in Section 5.2. From point (1) in Fig. 5.26 the flame speed increases, probably due to the development of cells. However, between points (1) & (2), the increasing flame speed increases the stretch. This increasing stretch will tend to stabilise the flame and, hence, reduce the cellular structure as the flame propagates towards and past point (3). Subsequently the magnitude of flame speed reduces towards point (4). From point (4) the cycle begins again since here low stretch and low flame speed offer conditions favourable to flame instability. The delayed onset of instabilities, between points (4) and (5) might be ascribed to the time required for the surface perturbations to develop. This tentative explanation of flame oscillations shows some promise. The hypothesis that an increase in surface area, due to surface perturbations, causes an increase in flame speed, is supported by the graph shown in Fig. 5.26, where the flame speed increases with the onset of wrinkling. However, the overall lean flame for which the flame speed against stretch is shown in Fig. 5.27, somewhat contradicts the above argument. The onset of wrinkling coincides with the two peaks of flame speed, when stretch begins to decrease, and, on the branch rising to the second flame speed maximum, wrinkling disappears when stretch increases. However, this flame has much lower values of stretch and flame speed than the previous one. The flame oscillations in both flames might be related, at least in part, to flame stretch and some, as yet unexplained, history effect. This history effect would be greater for the leaner flame because of the lower values of stretch and flame speed, coupled with a lower propensity to cellularity. It is probable that other causes, such as aerodynamics and radiation are also significant. These are discussed below.

2. Aerodynamics

The effect of drop inertia leading to a time dependant variation of equivalence ratio at the flame front was shown theoretically by Clavin and Sung (1991) and a comparison between experiment and theory was conducted by Clanet et al. (in prep.). In both works an acoustic oscillation of a planar flame, burning in a tube, was amplified significantly when an aerosol was present. To the author's knowledge no such analyses has been performed hitherto for a spherical flame. In the present work the presence of an acoustic interference is unlikely, as discussed in Section 5.2. However, it is possible that oscillations due to instabilities are exaggerated at the low burning velocities pertaining at the low temperatures in the present work. A first excitation of an oscillation could, possibly, be induced by the electric discharge of the spark. In the course of the present work, Demoulin (1999), a visiting research student from the Université de Provence, in collaboration with the present author, developed a simple model to assess whether the oscillations in flame speed might be caused by aerodynamic interaction of the gas motion ahead of the flame front and the drops. The main assumptions used in the model are presented below.

The droplets were assumed to be initially stationary. The gas velocity immediately ahead of the flame front was calculated from Eq. 2.1. The decay of the gas velocity with increasing distance from the flame front was estimated from mass conservation. From the velocity distribution ahead of the flame front the acceleration of the droplets was calculated, using Stokes law, and assuming a drag coefficient appropriate for spherical solid bodies. Knowledge of the drop velocity immediately ahead of the flame front and the flame speed allows the calculation of an entrainment rate of liquid fuel into the flame. This yields the effective equivalence ratio at the flame front. Values for the initial gaseous equivalence ratio and the initial number density of droplets in the mixture were obtained from measurements with the Malvern particle sizer and from calculations using the thermodynamic model presented in Chapter 4. Results of both methods also are presented in Chapter 4. Burning velocities were obtained from Bradley et al. (1998). The increase in flame speed due to the onset of cellularity was modelled by applying a scaling factor to adjust the amplitude of the calculated oscillation to that experimentally measured.

Figure 5.34 shows measured data of flame speed against radius for mixtures at ϕ_{ov}=1.0 and 0.8. The mixture at ϕ_{ov}=1.0, ϕ_g=0.85 and D_{32}=15μm burns without significant oscillation. The mixture at ϕ_{ov}=1.0, ϕ_g=0.75 and D_{32}=20μm oscillates severely. (Photographs of this flame are shown in Figs. 5.8 and PIV data for these initial conditions are presented in Fig. 5.28). In terms of the aerodynamic model described above, the oscillations are caused by the slight drop in gaseous equivalence ratio, which results in a decrease of the burning velocity and a change in drop size. The curve for the lean mixtures exhibits the same trend.

Figure 5.35 shows modelled curves of flame speed against radius, again for overall equivalence ratios of 1.0 and 0.8. The same qualitative behaviour as that of the measured curves is observed. A decrease in gaseous equivalence ratio apparently leads to the onset of oscillations for both overall equivalence ratios.

The modelled aerodynamic interaction between drops and gas motion ahead of the flame front is shown in Figs. 5.36 & 5.37. Presented in Fig. 5.36 are calculated curves of drop speed and drop entrainment velocity for the stoichiometric non-oscillating case shown in Fig. 5.35. Also shown is the flame speed at this condition from Fig. 5.35. The drop entrainment velocity is the difference between flame speed and drop speed. The drop speed increases with flame radius (and time), from an assumed initial value of zero. The drop entrainment velocity and, hence, the mixture composition at the flame front changes accordingly and reaches a fairly constant value at a flame radius of approximately 70mm. Shown in Fig. 5.37 is the stoichiometric oscillating case, presented in Figs. 5.35. The flame speed fluctuates in phase with the drop entrainment velocity. This suggests that the flame speed increases when the drop entrainment rate increases and vice versa, and there are at least two effects which are probably responsible for this. One is the change in effective equivalence ratio from lean towards stoichiometric, which causes an increase in flame speed (e.g. James, 1987, Bradley et al., 1998), and the other is the change in liquid equivalence ratio, i.e. a change in the number density of droplets in the local mixture. When the flame encounters fewer droplets, indicated in Fig. 5.37 by a decrease in drop entrainment velocity, the effect of droplet enhancement decreases. When the entrainment velocity falls below zero, the drops in fact move away from the flame front and droplet enhancement ceases completely. These effects are clearly illustrated in Figs. 5.8 and 5.26, for similar boundary conditions to those used in the model calculations presented here. The occurrence of an aerodynamic effect is also supported by the PIV measurements presented in Fig. 5.28.

3. Radiation from burning particles

Another mechanism that may play a role in the occurrence of flame oscillations is that of radiation by burning particles. This was observed by Hanai et al. (1998) in clouds of Polymethylmetacrylat (PMMA) particles at similar conditions to those of the present research, near the lean limit of flammability. These workers suggested, that particles, which are not burnt completely in the reaction zone, pass through the flame front, absorbing heat and thus causing a reduction in flame speed. Behind the flame front these particles burn in a second luminous flame front, which emits heat to the particles and the gas in the unburnt mixture. Therefore the flame burns rapidly into this preheated zone and consumes it. The length of the preheated zone was assumed, by Hanai et al., to be of the order of the absorption length in the particle cloud. When the flame reaches the zone of cold, not preheated mixture, the flame speed slows down and a new cycle begins. The phenomenon of flame oscillations was observed by these workers for a range of equivalence ratios of 0.75 to 1.3 for particles smaller than 13.5μm, and up to ϕ=1.8 for 30μm particles. It was strongest for the smaller particles, between the equivalence ratios of 0.7 and 0.9, and ceased when particles were bigger than approximately 50μm.

Greenberg (1999) also suggested, that radiation might be important for the onset of oscillations in aerosols. However, the mechanism of flame propagation in dust flames is different from that in aerosols, in that the temperature of the droplets is limited by the boiling temperature, whereas dust particles can be heated to much higher temperatures (Strehlow, 1985). Therefore, radiation plays a dominant role in dust flames, but probably not in aerosols. This is also indicated by the thickness of the particle flames observed by Hanai et al., which was of the order of tens of millimetres. This is much larger than that estimated for aerosols in earlier works (Chapter 2) and in the present work (Fig. 5.11). Although radiation may have an effect in aerosol flames, in the opinion of the present author it is unlikely to be dominant.

5.3.5 TURBULENCE

The most likely reason for the increase in flame speed and burning velocity in aerosols is the increased heat release rate due to the increase in surface area. This is discussed in Section 5.3.1. The same mechanism probably is responsible for the increase in flame speed in turbulent flames, if caused by a different mechanism. This implies, that the enhancing effects of instabilities triggered by the presence of an aerosol and turbulent flame wrinkling may conceal each other. Therefore it might be argued that burning velocity enhancement is significant in low turbulence flames but becomes progressively less important as turbulent wrinkling becomes dominant. However, even for highly turbulent flames, droplet enhancement might be important because, as shown by Abdel-Gayed et al. (1984 & 1987), following ignition all flames start laminar and time is required for the development of a turbulent flame structure.

5.3.6 SUMMARY

It was suggested by earlier workers, that the increase in surface area of the flame front, due to the presence of droplets, probably was the mechanism responsible for the phenomenon of burning velocity enhancement. The comparison of flame development of gaseous cellular flames and aerosol flames, presented in Section 5.1 & 5.2, supports and reinforces this hypothesis.

Several causes of flame wrinkling in aerosols have been investigated in the present work. In earlier works, droplets were often thought of as obstructions in the path of the flame, that distort and lacerate the flame surface (Chapter 2). It was suggested that a flame that propagates through a droplet matrix is turbularised and that this causes the increase in burning velocity. The observations presented in this thesis suggest that the so-called "grid-effect" does not play a mayor role with respect to flame instability for aerosols comparable to those used in the present work.

It has also been assumed in previous works that wrinkling of the flame front is caused by preferential flame propagation through areas of optimum equivalence ratio. Also, in gaseous flames, it has been observed, that rich flames develop instabilities earlier than lean flames (Bradley et al., 1998). Therefore, an initial assumption in the present study was, that fuel rich areas in aerosols, close to evaporating drops, could possibly trigger instabilities. However, the triggering of instabilities through the use of a water aerosol probably contradicts both arguments.

Greenberg et al. (1998 & 1999) mathematically investigated the instability of aerosol flames, using linear stability analysis. The model is based on the similarity of flame structure observed in cellular gaseous flames and aerosol flames and follows the lines of Shivashinsky (1977) for gaseous flames. It, essentially, considers heat and mass transfer between the flame and the aerosol. It yields good qualitative agreement with the experimental results of the present work, and this indicates that heat loss due to the evaporation of droplets might play a dominant role in the manifestation of instabilities in aerosol flames.

Several causes of flame speed oscillations are considered in the present work. Flame stretch is likely to delay the onset of instabilities and could, therefore, have an important influence on the occurrence of oscillations. However, the observations of the present work are not entirely conclusive and further investigation is required.

The role of aerodynamic interaction between the drops and the gas motion ahead of the flame front was investigated, using a simple semi-empirical model. The results support the hypothesis that this effect might be important, possibly dominant. The occurrence of an aerodynamic effect is also supported by the PIV measurements conducted in the present work.

Radiation plays a dominant role in dust flames, but possibly not in aerosols. Although radiation may have an effect in aerosol flames, in the opinion of the present author it is unlikely to be dominant.

From the observations of earlier workers and those of the present work, it is concluded that burning velocity enhancement is significant in low turbulence flames but becomes progressively less important as turbulent wrinkling becomes dominant. However, since all flames start laminar and time is required for the development of a turbulent flame structure, droplet enhancement might be important in the initial stages of combustion in engines. The time scales of the development of a wrinkled flame structure possibly are shortened significantly through the use of aerosols, and this may be important for Diesel and GDI engines as well as for gas turbines. However, the present work was mainly occupied with the investigation of laminar aerosol flames and more work is required to investigate mutual effects of turbulence and aerosols.

ϕ_{ov}	ϕ_g	p_i [kPa]	T_i [K]	D_{32} [μm]	S_n [m/s]	u_a [m/s]	L_b [mm]		p_I [kPa]	T_I [K]	t_i [s]	Exp. ID
1.0	0.97	136	277	≈10	2.01	0.23	-0.18		200	303	1.5	231
large scale cracks, otherwise smooth												
1.0	0.92	128	274	13	2.11	0.24	+1.45		200	303	1.75	240
large scale cracks, otherwise smooth												
1.0	0.85	121	271	15	2.00	0.226	-0.67		200	303	2.0	232
shallow wrinkles, slightly more intense from r≈ 55mm												
1.0	0.79	114	268	20		--	--		200	303	2.25	241
oscillating, maximum flame speed = 1.9m/s												
1.0	0.75	108	265	20	--	--	--		200	303	2.5	233
oscillating, maximum flame speed = 2.6m/s												
0.8	0.79	135	275	<10	1.10	0.143	+0.68		200	303	1.5	234
smooth												
0.8	0.79	127	272	<10	1.27	0.145	+0.866		200	303	1.75	242
smooth												
0.8	0.73	120	268	11	1.17	0.148	+2.67		200	303	2.0	235
smooth, top section of flame becomes cellular at r≈ 57mm												
0.8	0.67	113	265	15	--	--	--		200	303	2.25	243
oscillating, maximum flame speed = 0.95m/s												
0.8	0.66	108	263	17	--	--	--		200	303	2.5	236
oscillating, maximum flame speed = 0.9m/s												
1.2	1.18	137	278	≈10	2.54	0.29	+0.12		200	303	1.5	237
smooth after ignition, first shallow cracks at r≈ 50mm, fully developed but shallow cells from r≈ 60mm												
1.2	1.11	129	276	18	2.80	0.318	+1.71		200	303	1.75	244
wrinkled from r≈ 10mm, develops gradually into fully cellular from surface at r≈ 50mm												
1.2	1.03	122	273	20	3.64	0.41	+6.21		200	303	2.0	238
wrinkled from r≈ 10mm, develops gradually into fully cellular from surface at r≈ 50mm												
1.2	0.97	115	270	23	3.07	0.345	+3.18		200	303	2.25	245
wrinkled from r≈ 10mm, develops gradually into fully cellular from surface at r≈ 50mm coarser cells than #244 & #238												
1.2	0.93	109	268	25	2.72	0.30	+0.31		200	303	2.5	239
fully cellular at r≈ 10mm, more pronounced cells than #238 & #245,												
1.0	0.97	205	284	17	2.07	0.243	+1.86		300	313	1.5	246
smooth												
1.0	0.92	193	280	20	2.05	0.237	+1.35		300	313	1.75	247
smooth												
1.0	0.89	182	277	24	2.06	0.236	+1.25		300	313	2.0	248
essentially smooth, very faint shallow wrinkles												
1.0	0.86	171	275	25	2.02	0.230	+0.54		300	313	2.25	249
essentially smooth up to r≈29mm, cracking and wrinkling up to r≈55mm, then cellular												
1.0	0.84	162	272	27	2.00	0.226	+0.40		300	313	2.5	250
faint wrinkling after ignition disappears at r≈43mm, onset of shallow cellularity from r≈54mm, start of oscillation from r≈60mm												
1.0	0.82	154	270	28	2.09	0.236	+0.55		300	313	2.75	251
faint wrinkling after ignition, onset of shallow cellularity from r≈41mm, start of oscillation from r≈59mm												
1.0	0.81	147	268	30	2.18	0.243	+0.89		300	313	3.0	252
faint wrinkling after ignition, onset of shallow cellularity from r≈ 32mm, start of oscillation from r≈ 60mm												
1.0	0.9	322	286	16	1.81	0.71	+0.73		700	348	3.0	255
small scale wrinkling from ignition, cell division to full cellularity from r≈43-46mm												
1.0	0.9	322	286	16	1.8	0.41	+0.57		700	348	3.0	256
small scale wrinkling from ignition, cell division to full cellularity from r≈ 32-36mm												
1.0	0.95	358	292	13	1.60	0.51	-0.1		700	348	2.5	257
smooth up to r≈ 38mm, gradual onset of cellularity, fully cellular from r≈53mm												
1.0	0.95	358	292	13	1.83	0.28	+0.9		700	348	2.5	258
smooth up to r≈ 42mm, gradual onset of cellularity, fully cellular from r≈ 62mm												
PROPANE-AIR MIXTURES WITH AND WITHOUT WATER AEROSOL												
1.3	--	108	265*	--	2.33	0.385	+0.93		200	297	2.5	282
"medium dense" water aerosol, cracking starts at r≈32mm, fully cellular at r≈42mm												
1.3	--	108	265*	--	2.37	0.269	+1.24		200	302	2.5	283
"dense" water aerosol, cracking starts at r≈ 30mm, fully cellular at r≈ 54mm												
1.3	--	108	255*	--	2.34	0.253	+0.49		200	297	2.5	285
no water aerosol, large cracks, no cells												

Table 5.1: *Laminar aerosols investigated in the present work.*

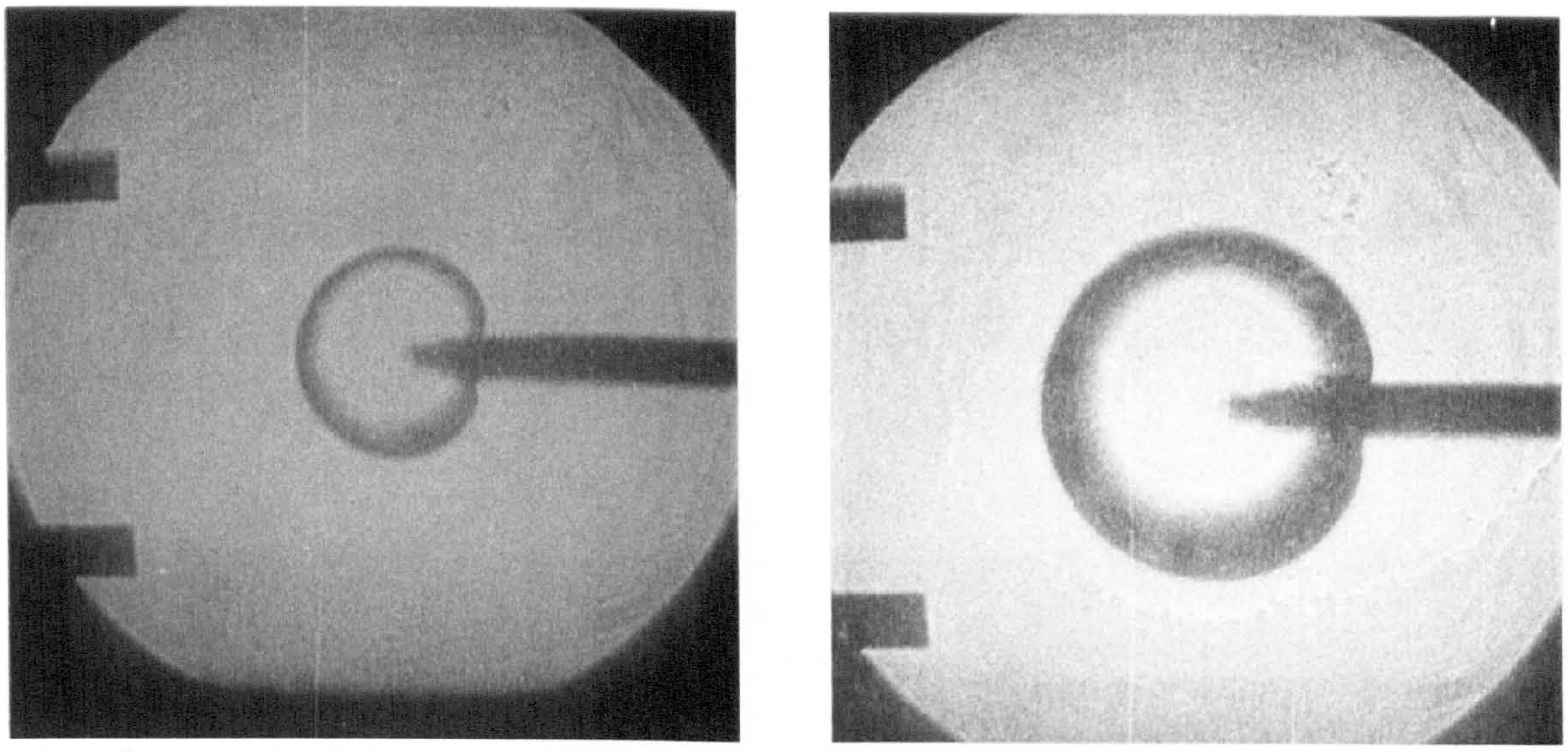

(a) t_c=8ms, r=10mm (b) t_c=12ms, r=19mm

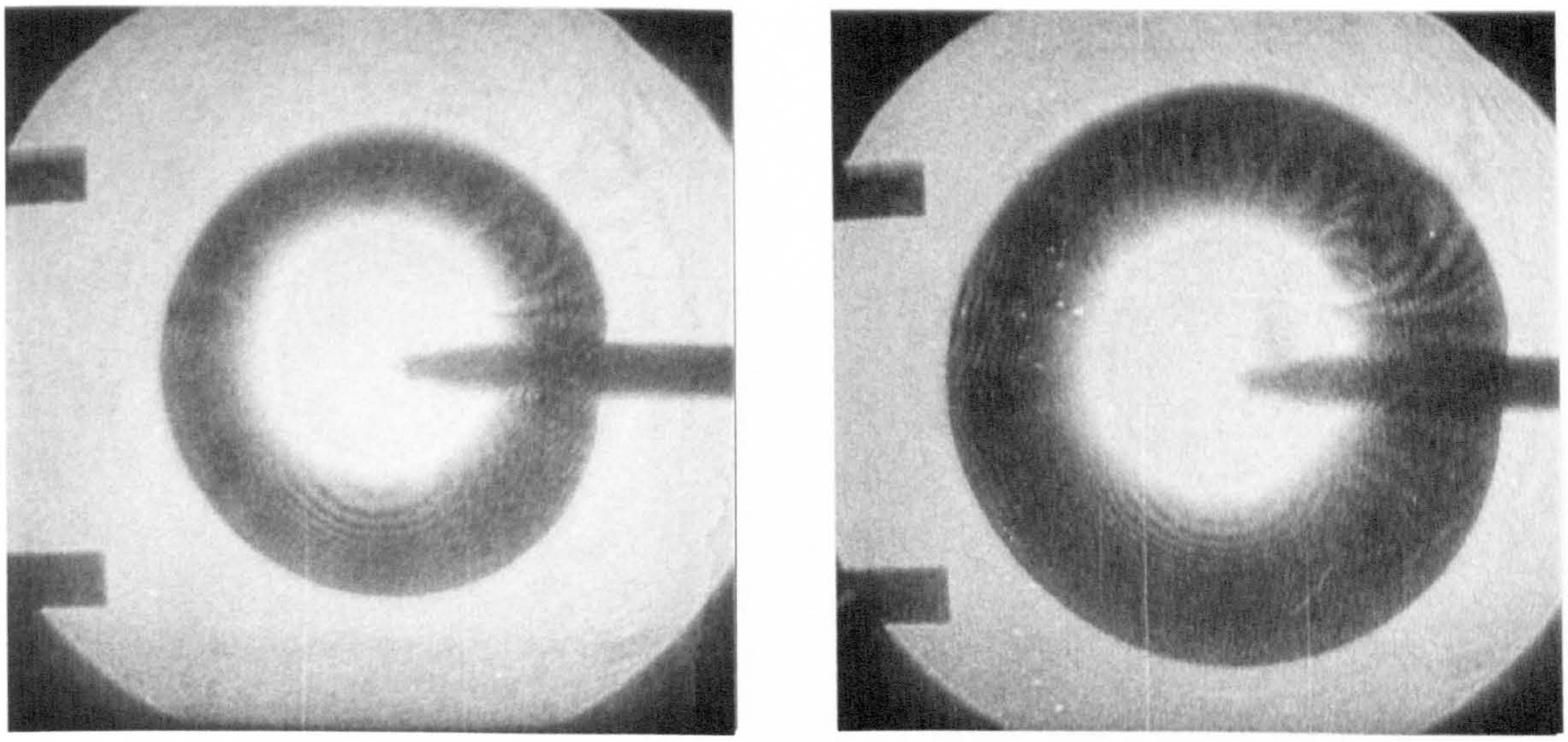

(c) t_c=16ms, r=29mm (d) t_c=20ms, r=39mm

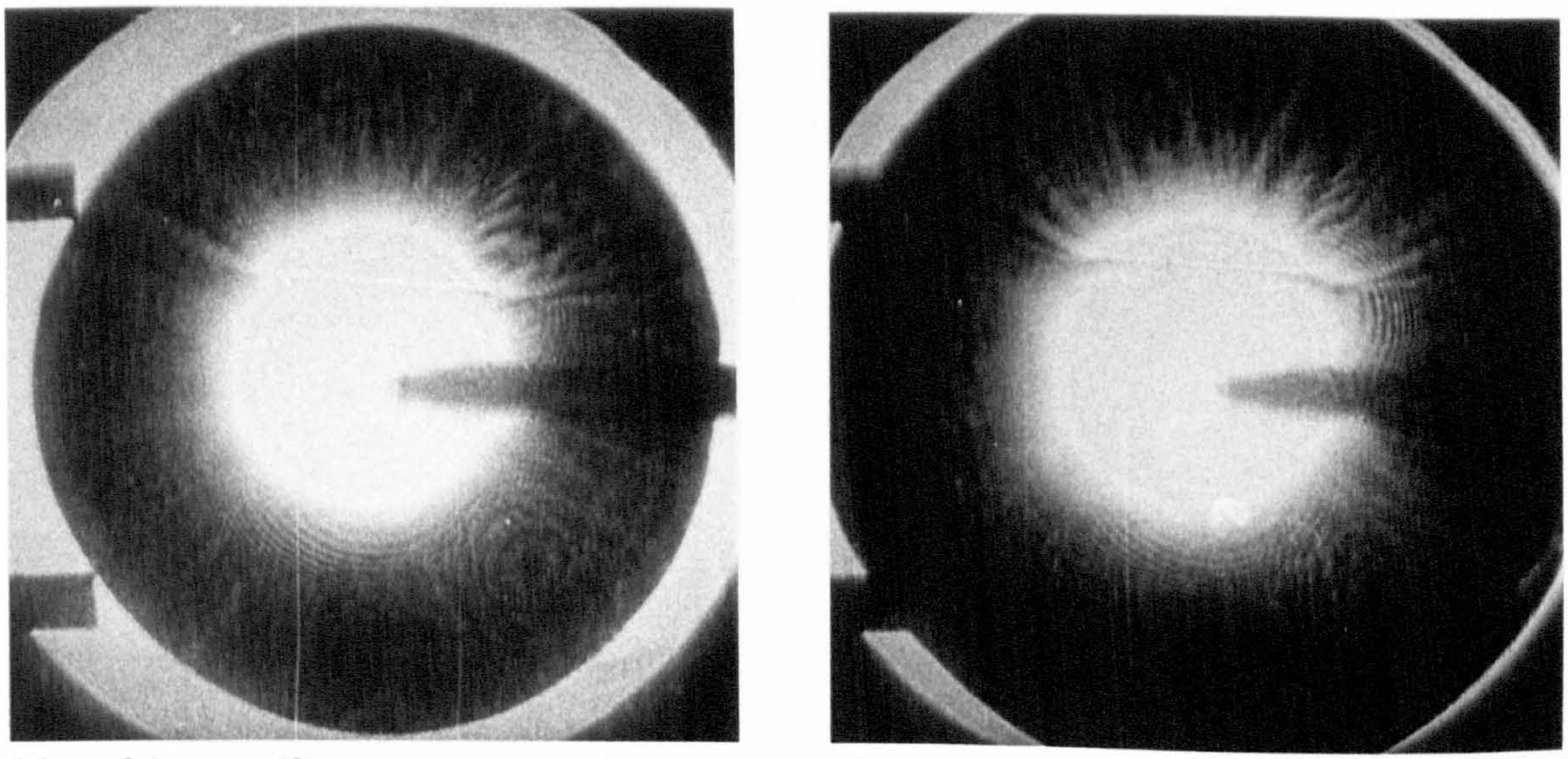

(e) t_c=24ms, r=49mm (f) t_c=28ms, r=59mm

Figure 5.1: *Sequence of schlieren photographs for a laminar gaseous iso-octane-air flame at* ϕ=1.0, p=100kPa, T=328K.

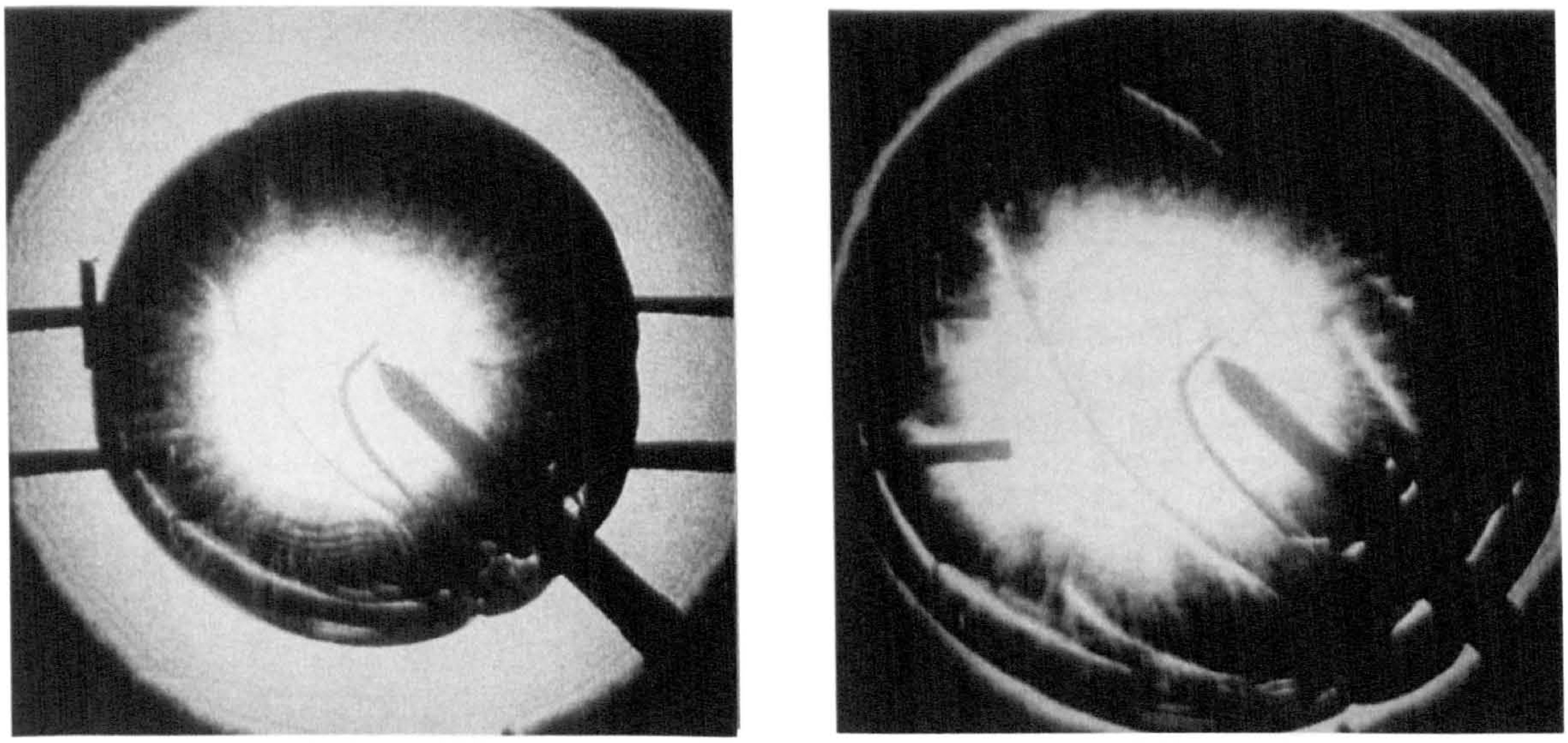

(a) $r=105mm$, $p=250kPa$

(b) $r=142mm$, $p=250kPa$

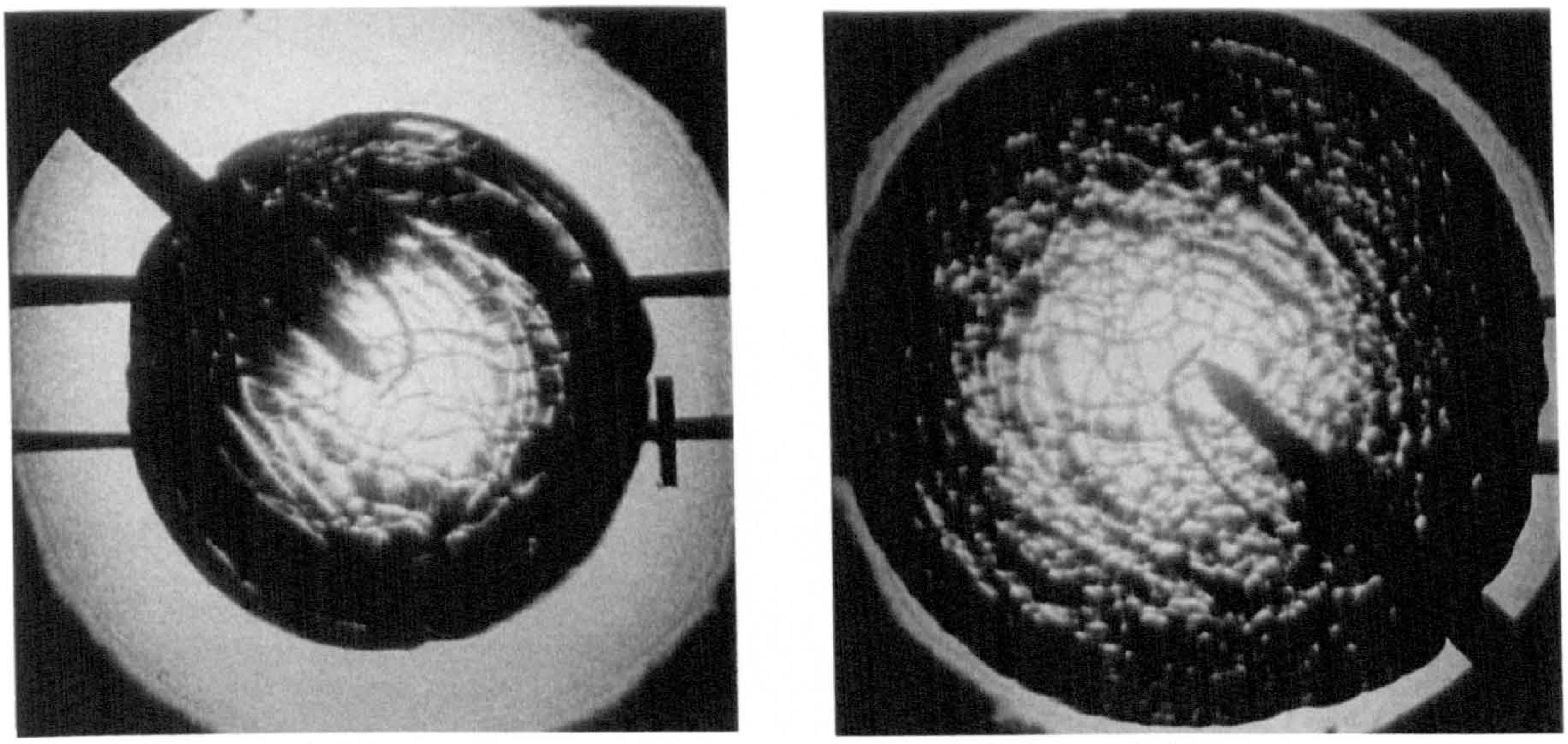

(c) $r=102mm$, $p=500kPa$

(d) $r=138mm$, $p=500kPa$

Figure 5.2: *Effect of pressure on the structure of stoichiometric gaseous iso-octane-air flames at an initial temperature of 358K, Bradley et al. (1998).*

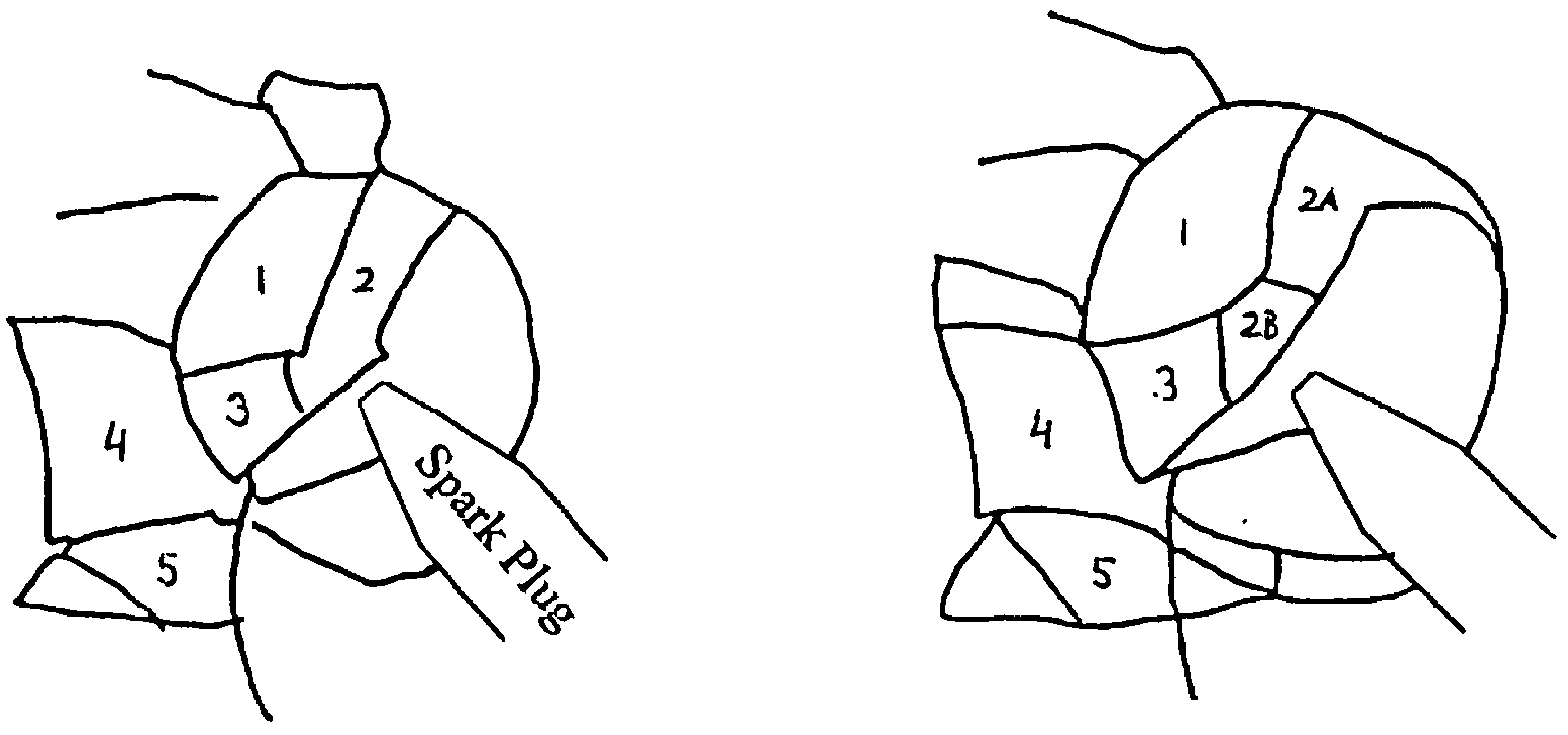

(a) *t=+0ms,* (b) *t=+2ms,*

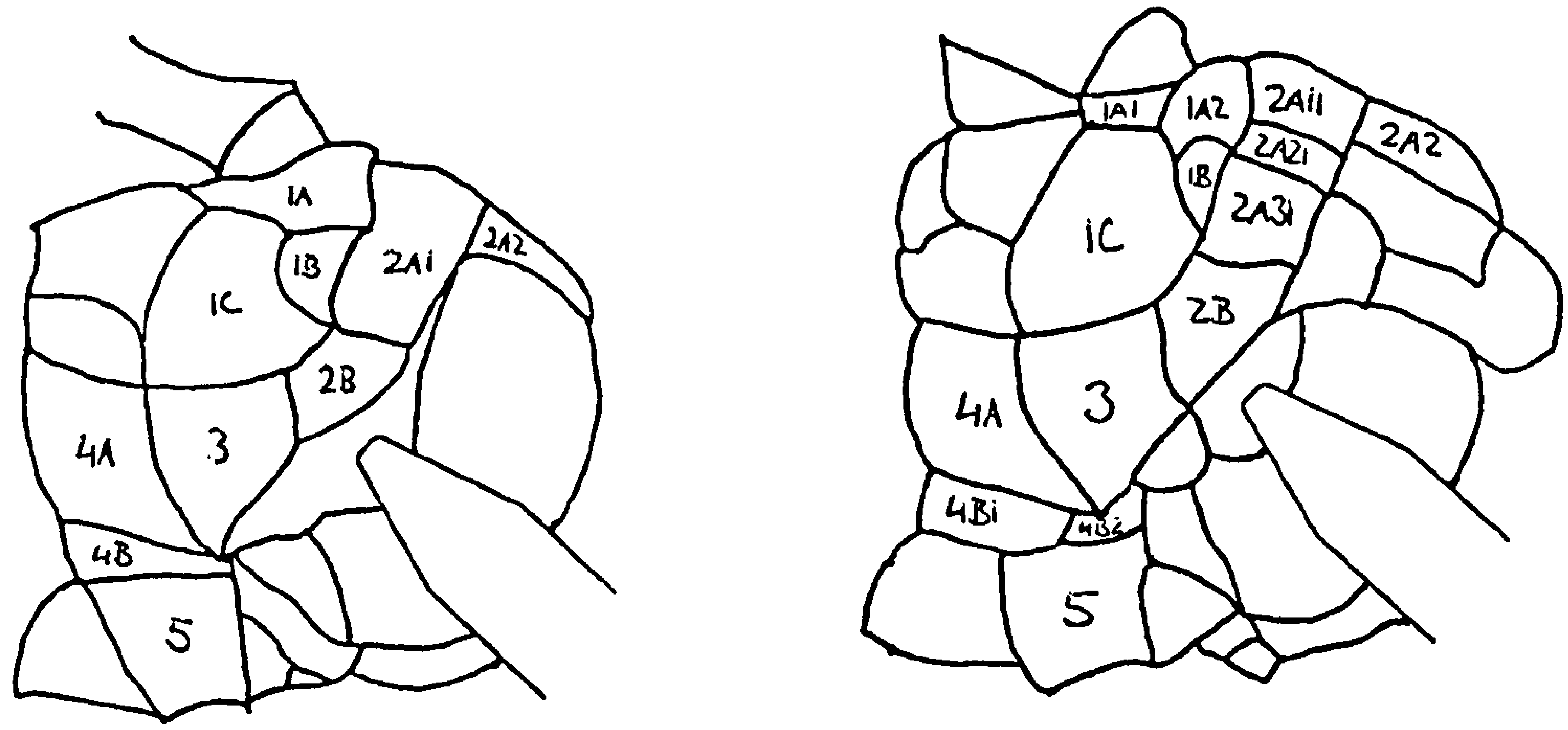

(c) *t=+4ms,* (d) *t=+6ms,*

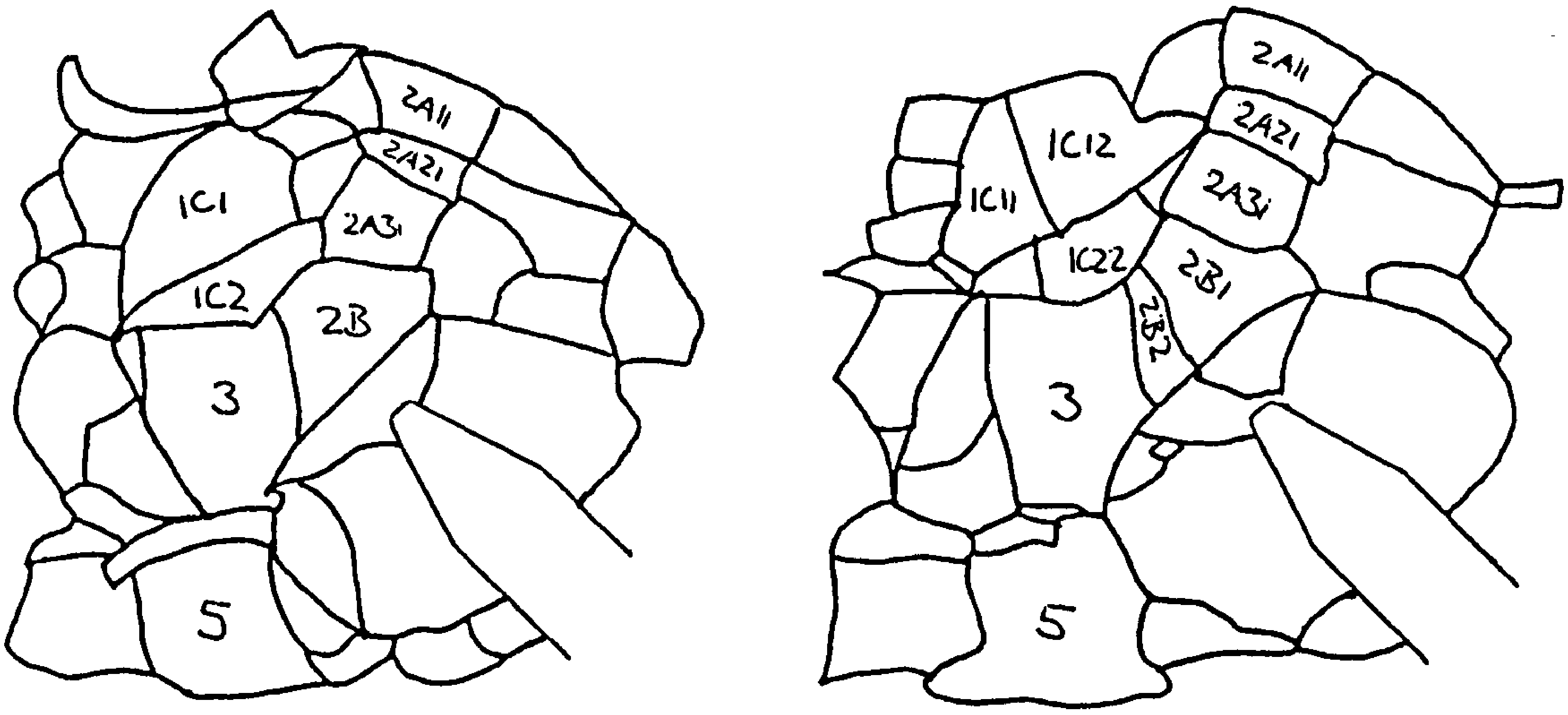

(e) *t=+8ms,* (f) *t=+10ms,*

Figure 5.3: *Cell growth and division in a gaseous iso-octane-air flame, ϕ=1.0, p=500kPa, T=358K, (Photographs of this flame are shown in Fig. 5.2).*

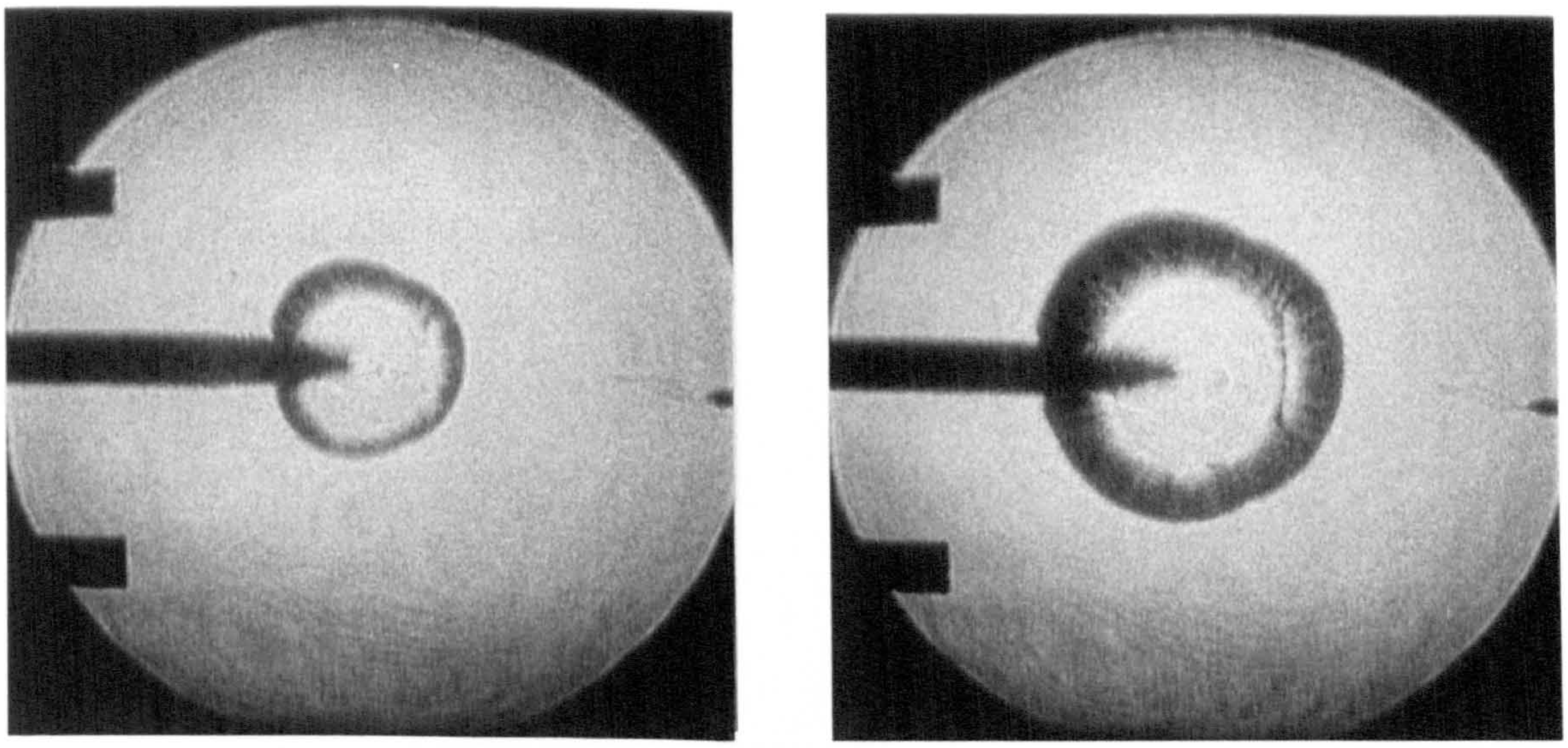

(a) t_c=8ms, r=19mm (b) t_c=12ms, r=29mm

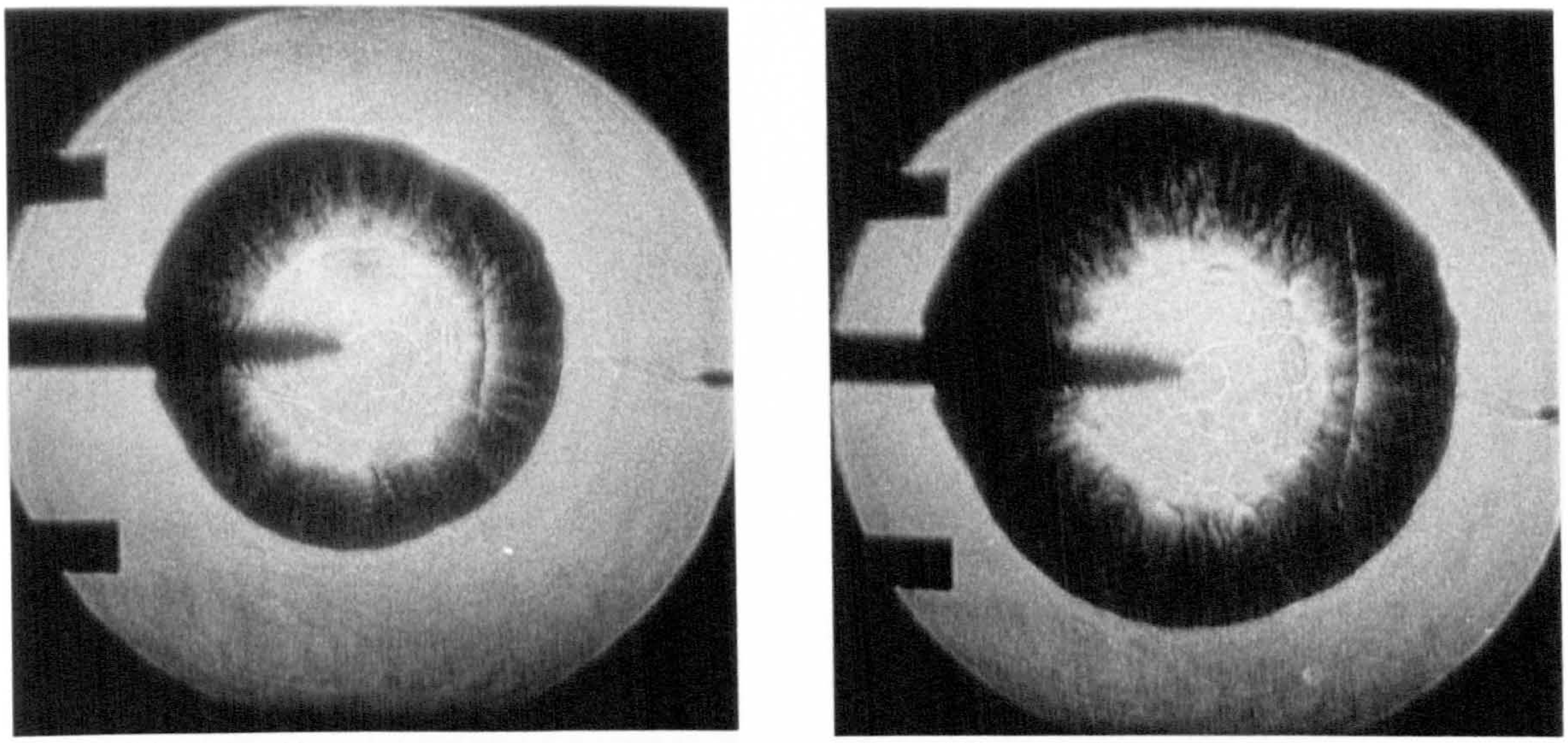

(c) t_c=16ms, r=40mm (d) t_c=20ms, r=50mm

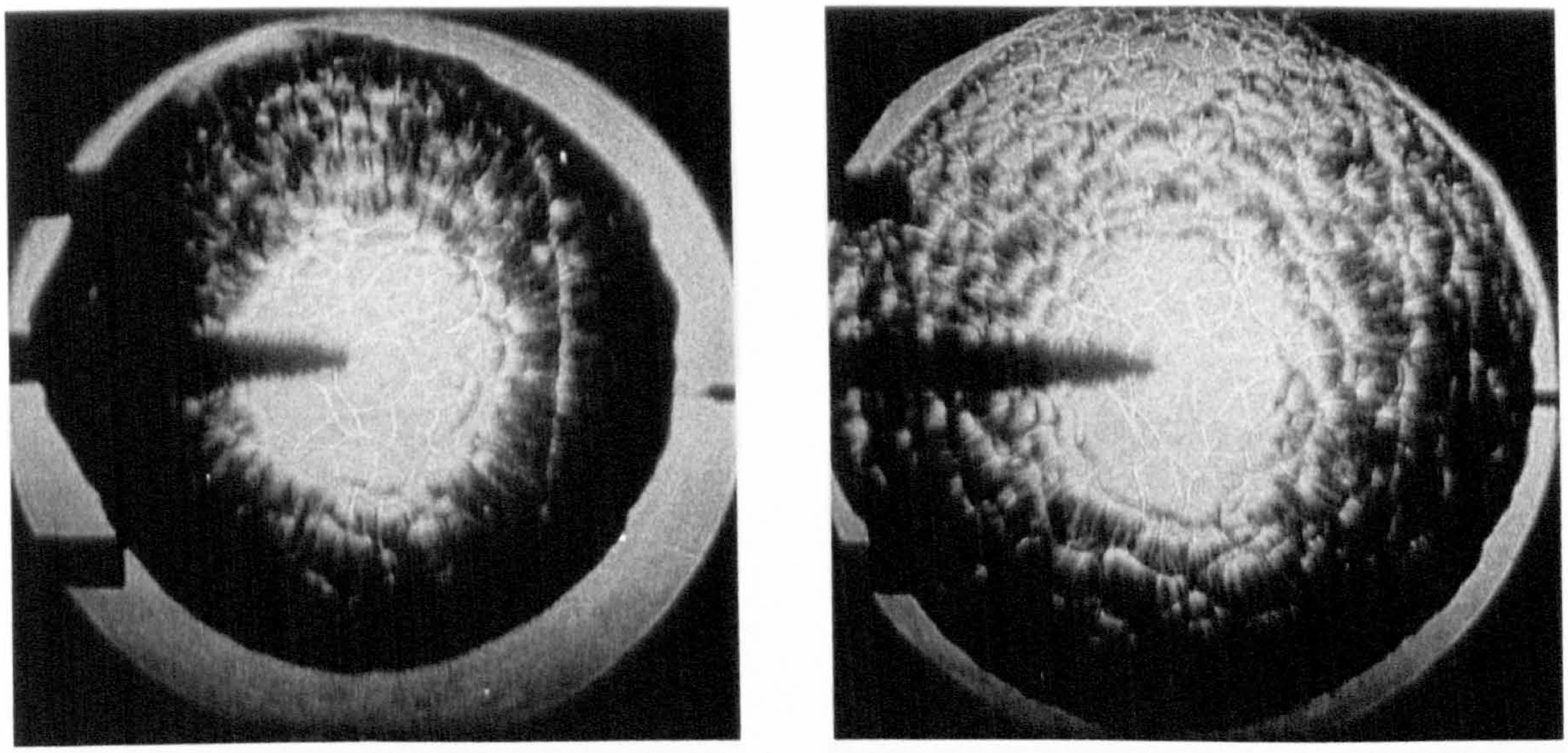

(e) t_c=24ms, r=60 mm (f) t_c=32ms, r=70 mm

Figure 5.4: *Sequence of schlieren photographs of a laminar iso-octane-air aerosol flame,* $\phi_{ov}=1.2$, $\phi_g=1.18$, $D_{32}\approx10\mu m$, $p=137kPa$, $T=278K$.

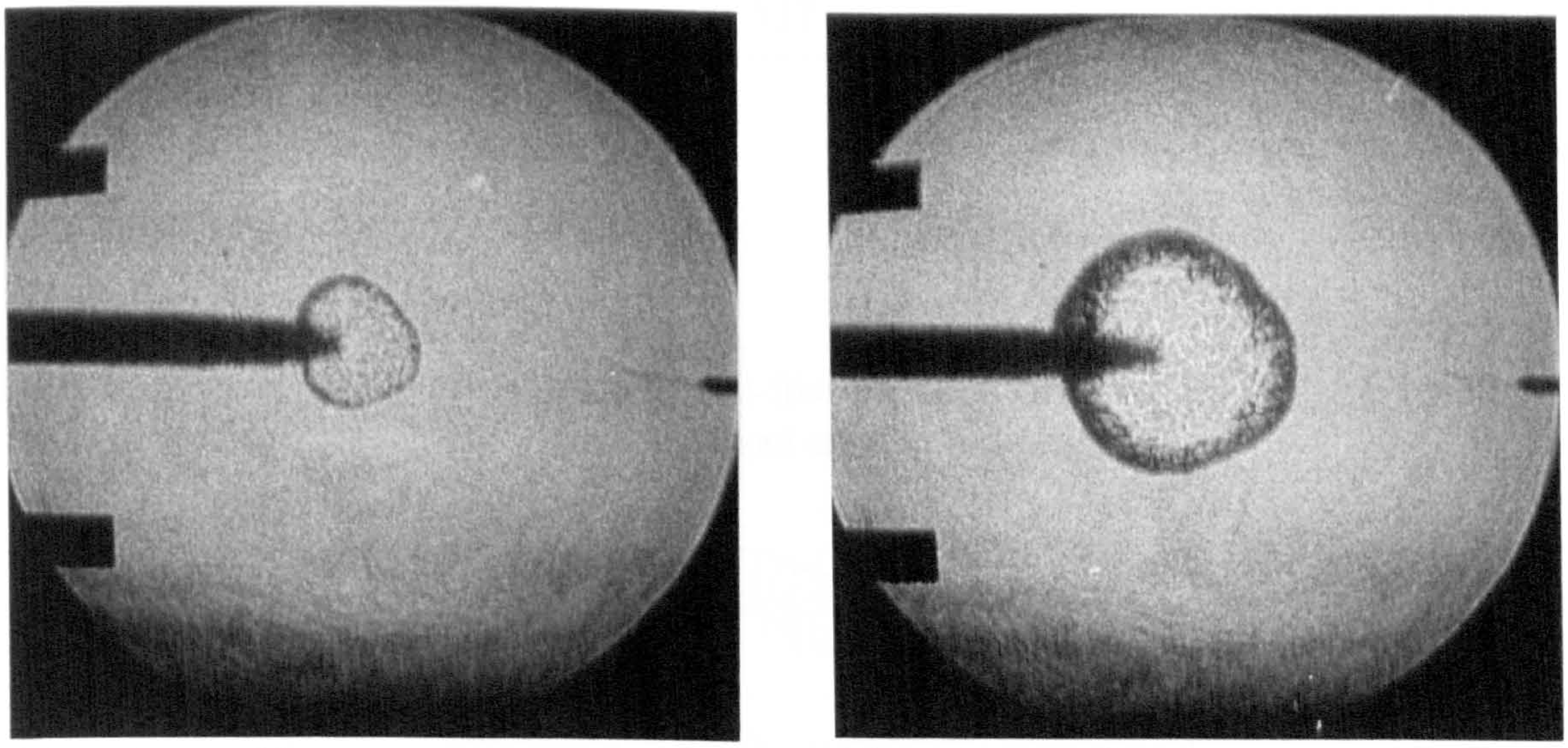

(a) t_c=*4ms, r=10mm* (b) t_c=*8ms, r=18mm*

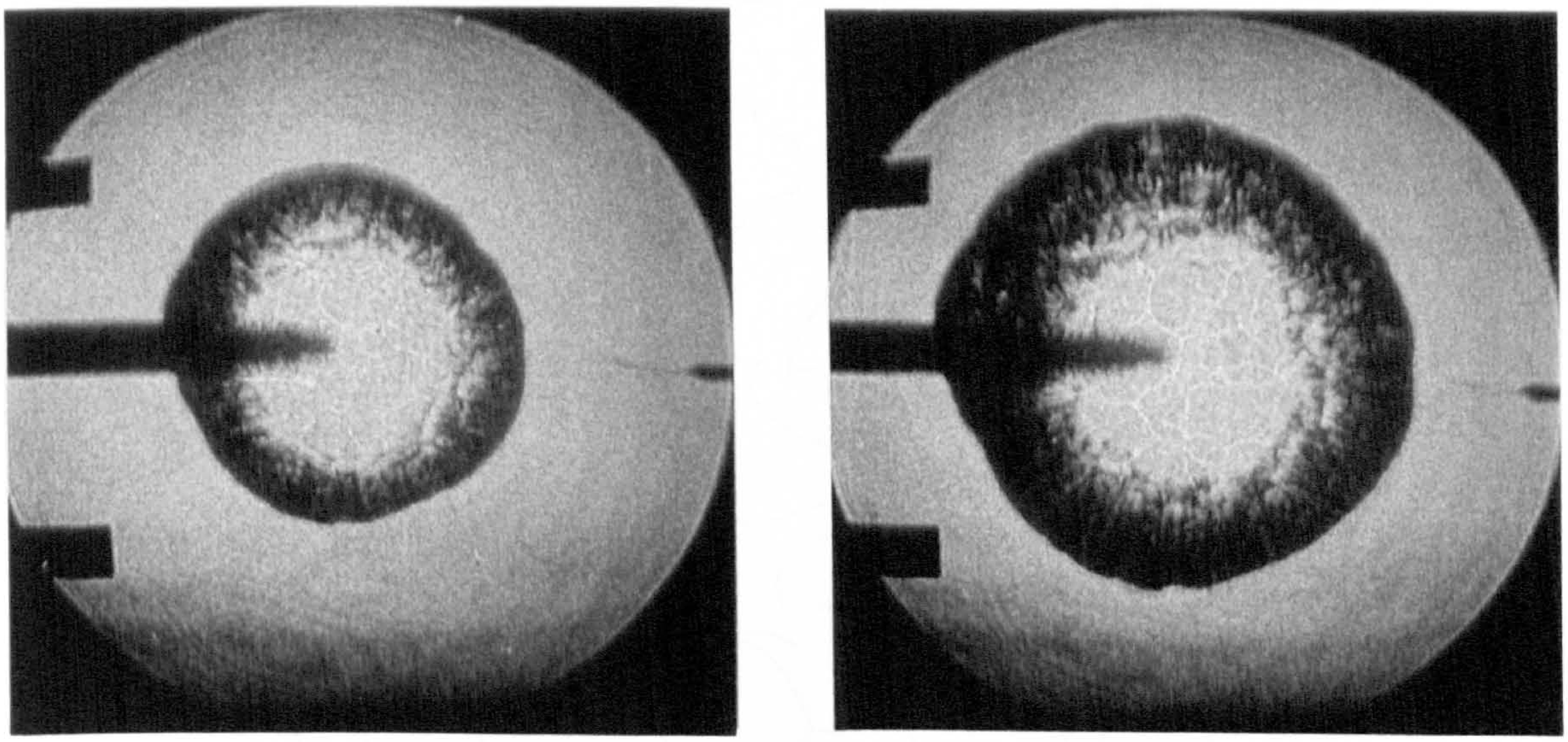

(c) t_c=*12ms, r=27mm* (d) t_c=*16ms, r=38mm*

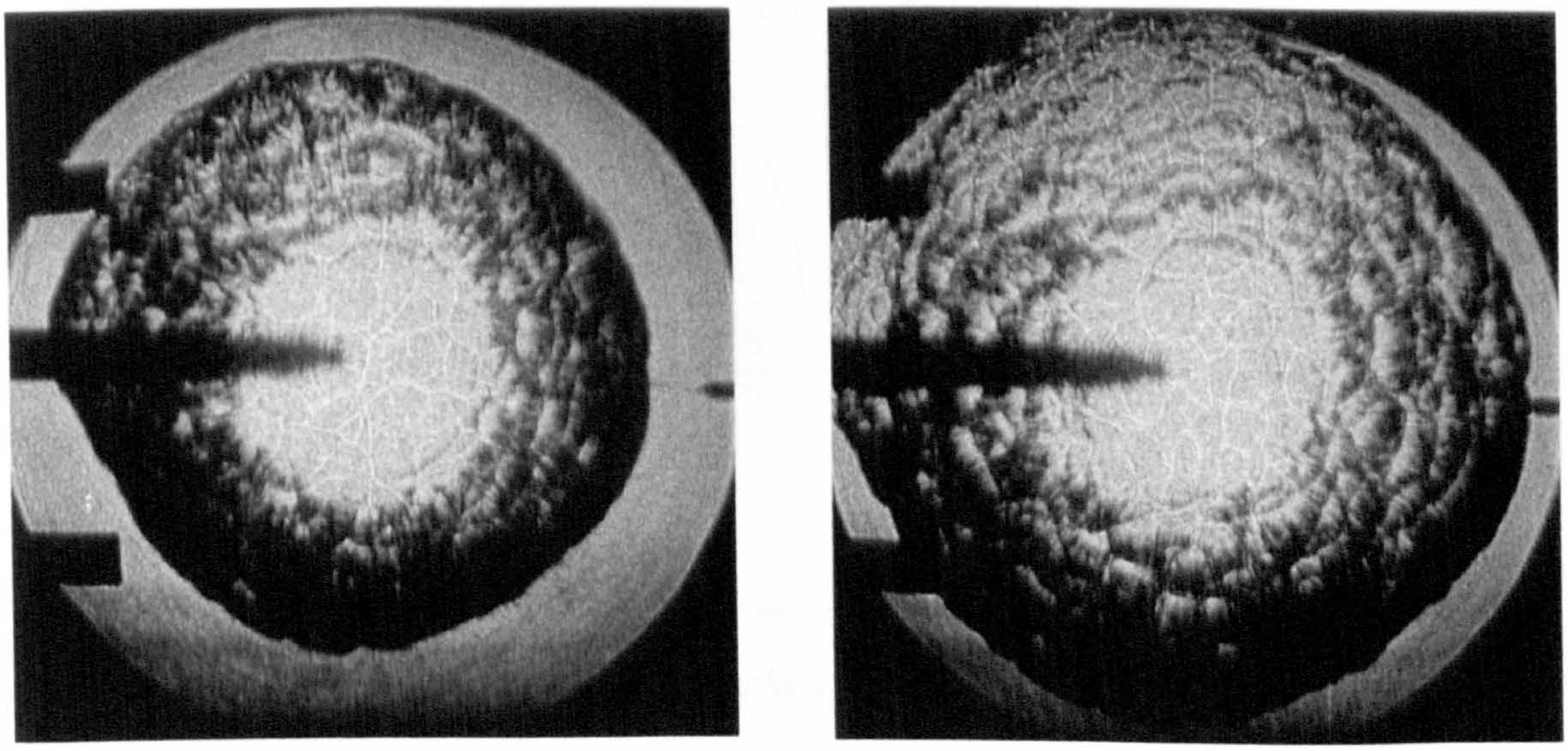

(e) t_c=*20ms, r=50 mm* (f) t_c=*24ms, r=61 mm*

Figure 5.5: *Sequence of schlieren photographs of a laminar iso-octane-air aerosol flame,* $\phi_{ov}=1.2$, $\phi_g=1.03$, $D_{32}=20\mu m$, $p=122kPa$, $T=273K$.

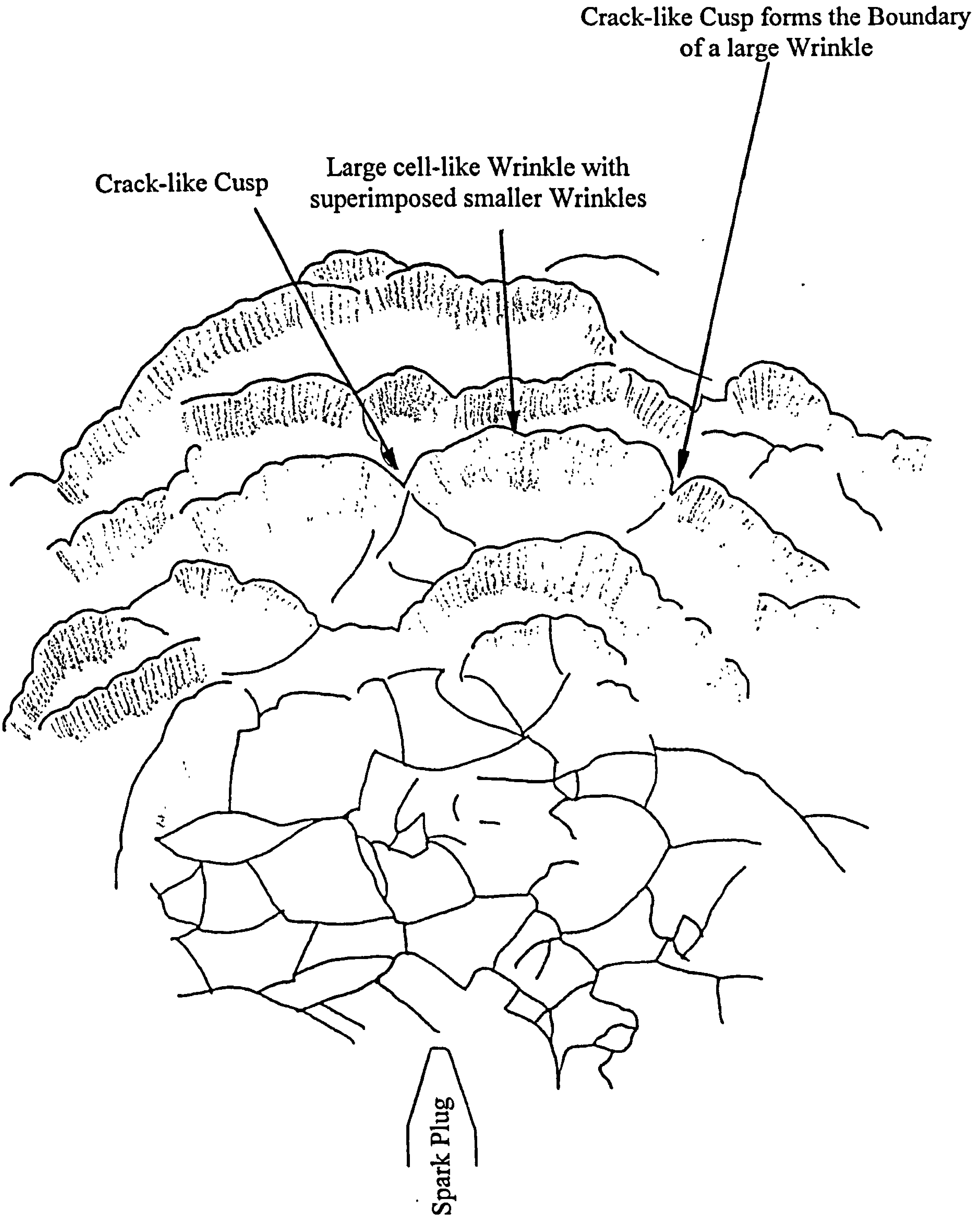

Figure 5.6: *Schematic of a laminar iso-octane-air aerosol flame,* $\phi_{ov}=1.2$, $\phi_g=1.03$, $D_{32}=20\mu m$, *p=122kPa, T=273K, (Photographs of this flame are shown in Fig. 5.5).*

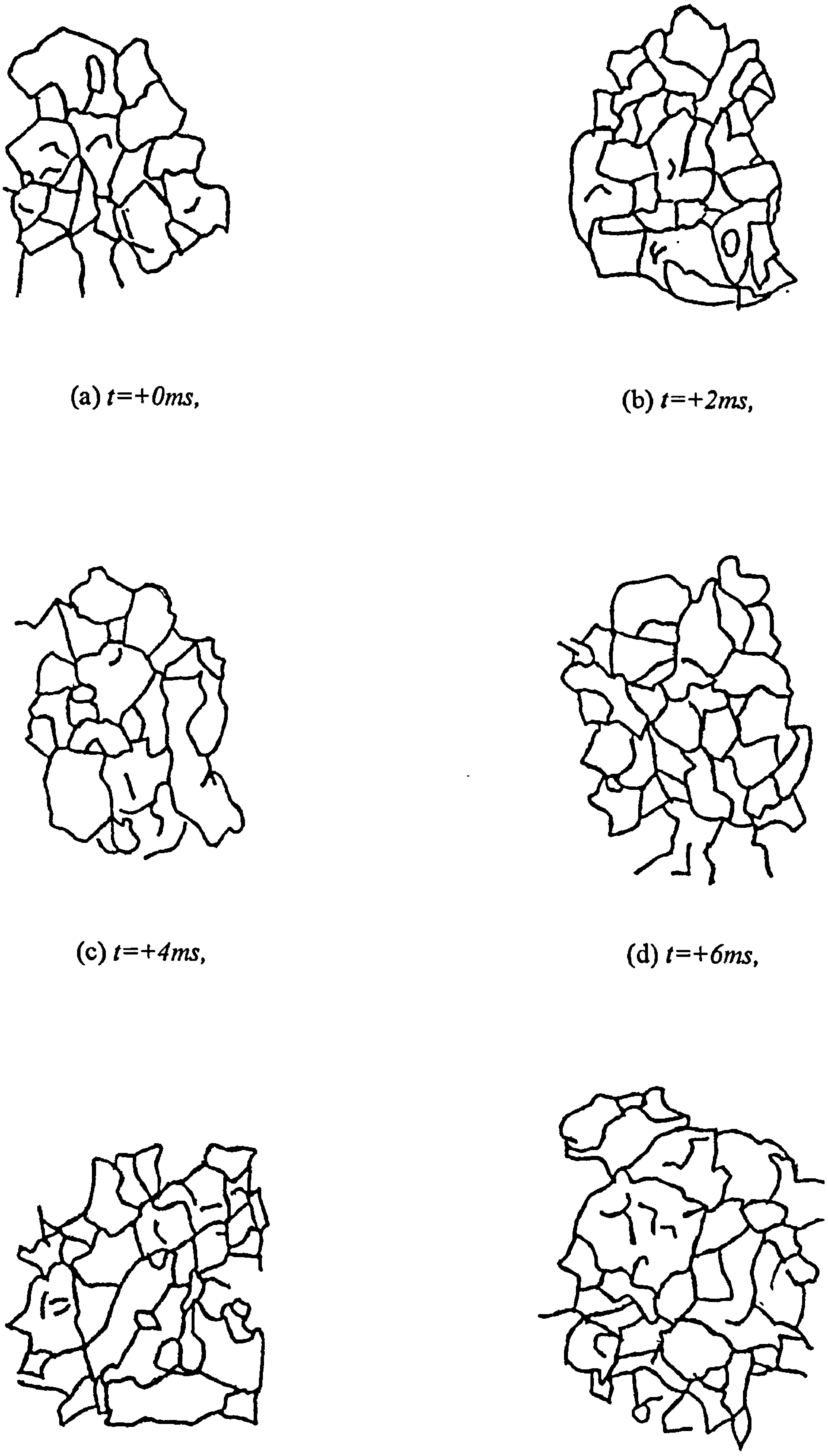

(a) *t=+0ms,*

(b) *t=+2ms,*

(c) *t=+4ms,*

(d) *t=+6ms,*

(e) *t=+8ms,*

(f) *t=+10ms,*

Figure 5.7: *Cell formation and destruction in an iso-octane-air aerosol flame,* $\phi_{ov}=1.2$, $\phi_g=0.93$, $D_{32}=25\mu m$, $p=108kPa$, $T=268K$.

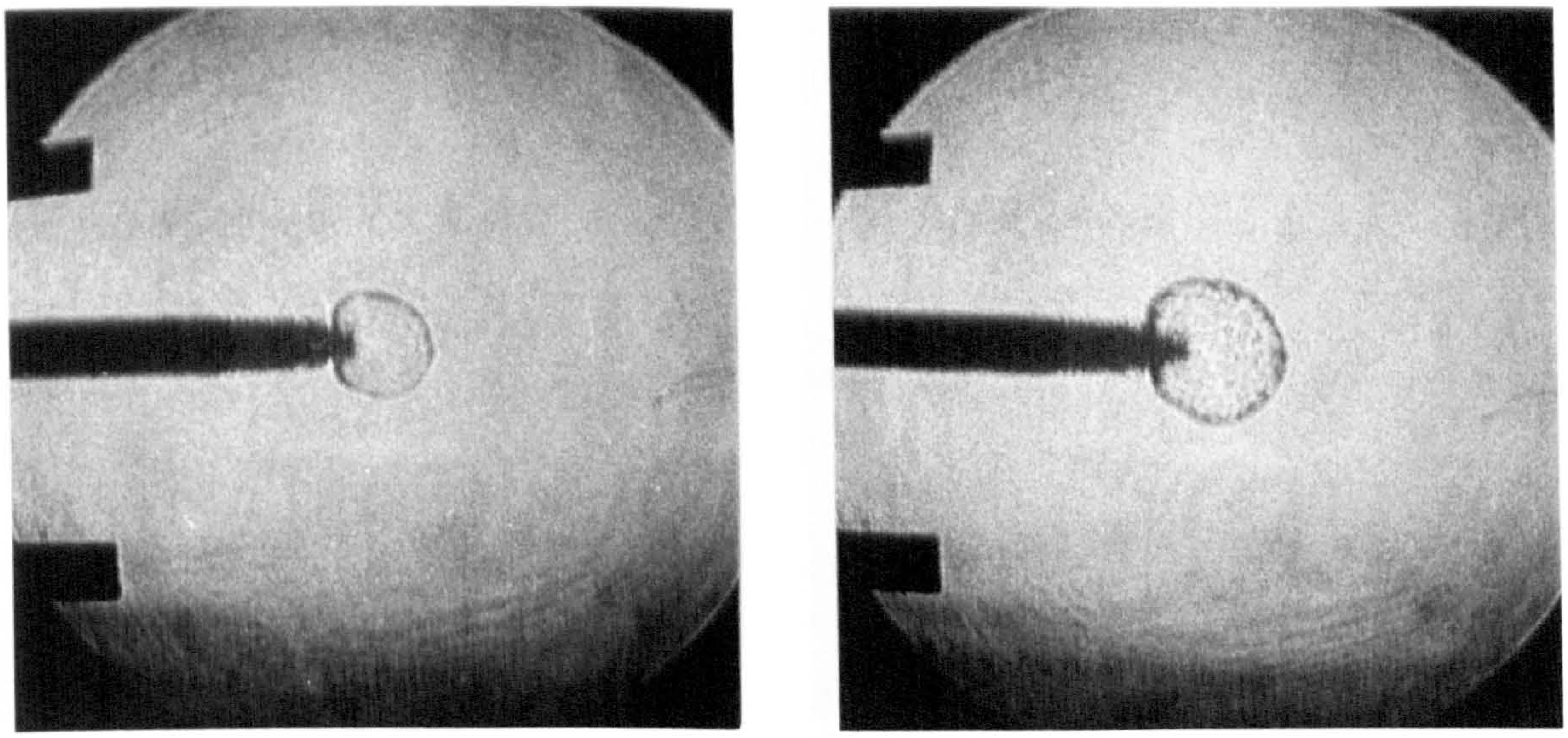

(a) $t_c=5ms,\ r=9mm$ (b) $t_c=7ms,\ r=12mm$

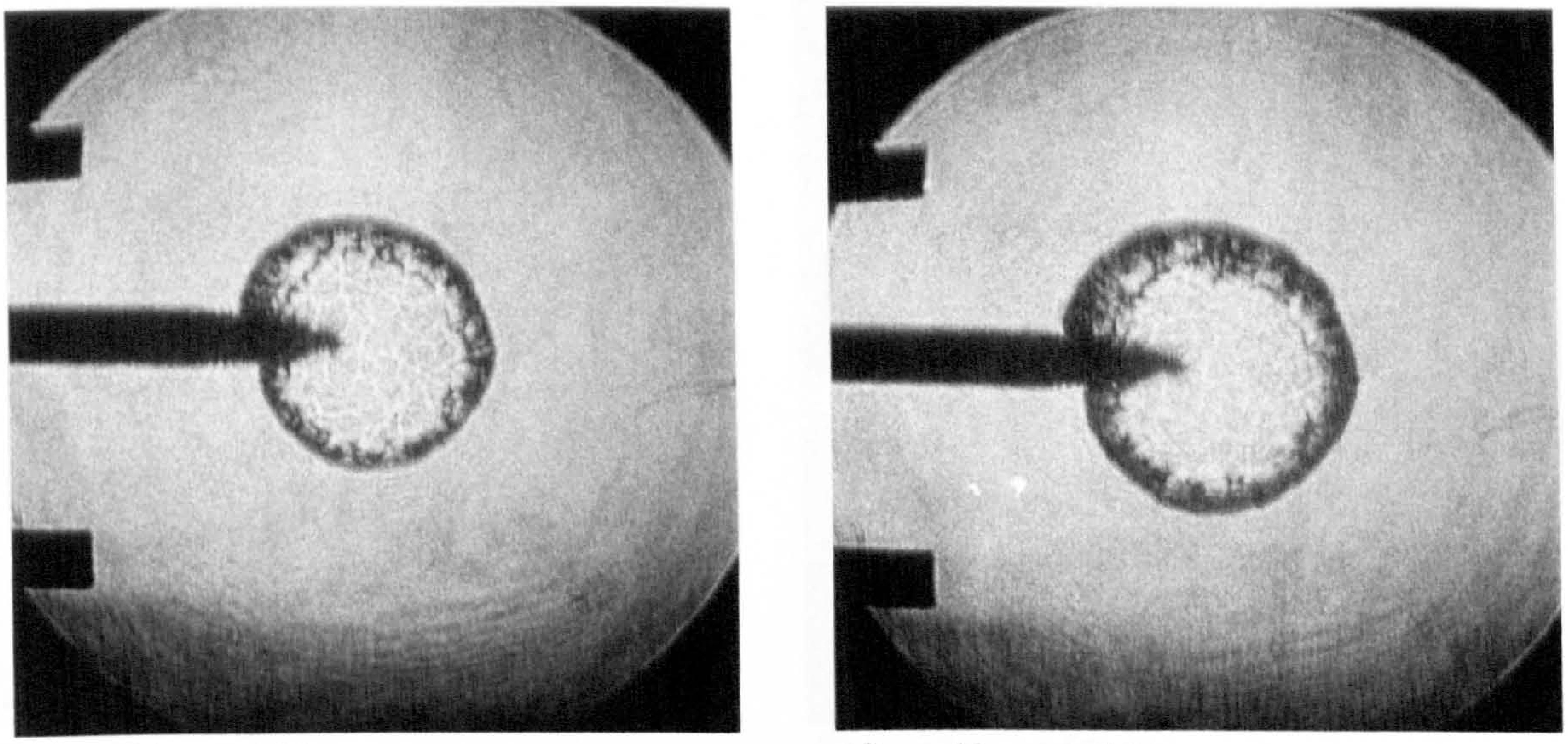

(c) $t_c=11ms,\ r=22mm$ (d) $t_c=12ms,\ r=24mm$

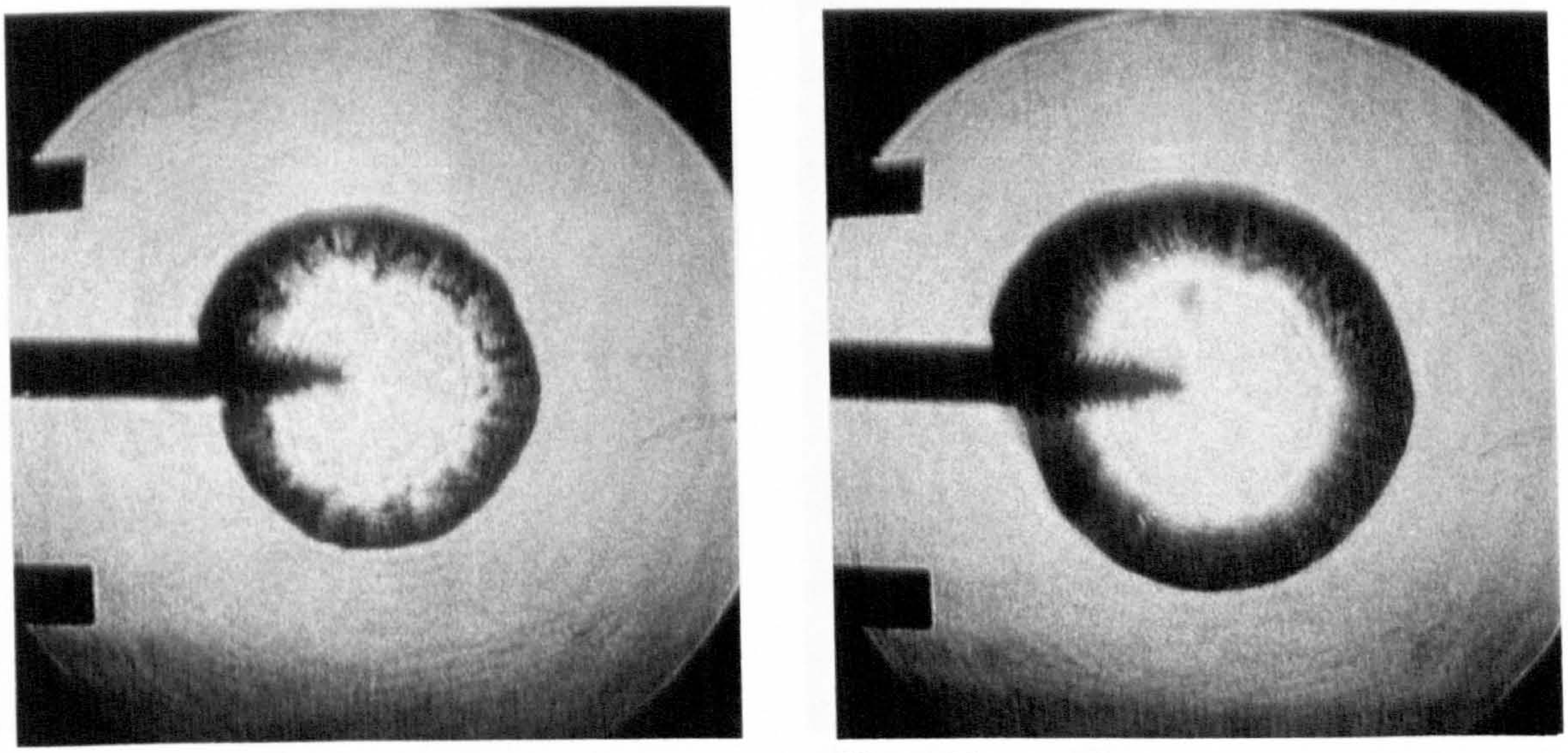

(e) $t_c=14ms,\ r=30\ mm$ (f) $t_c=19ms,\ r=35\ mm$

Figure 5.8: *Sequence of schlieren photographs of a laminar iso-octane-air aerosol flame,* $\phi_{ov}=1.0$, $\phi_g=0.75$, $D_{32}=20\mu m$, $p=108kPa$, $T=265K$, *continued on next page.*

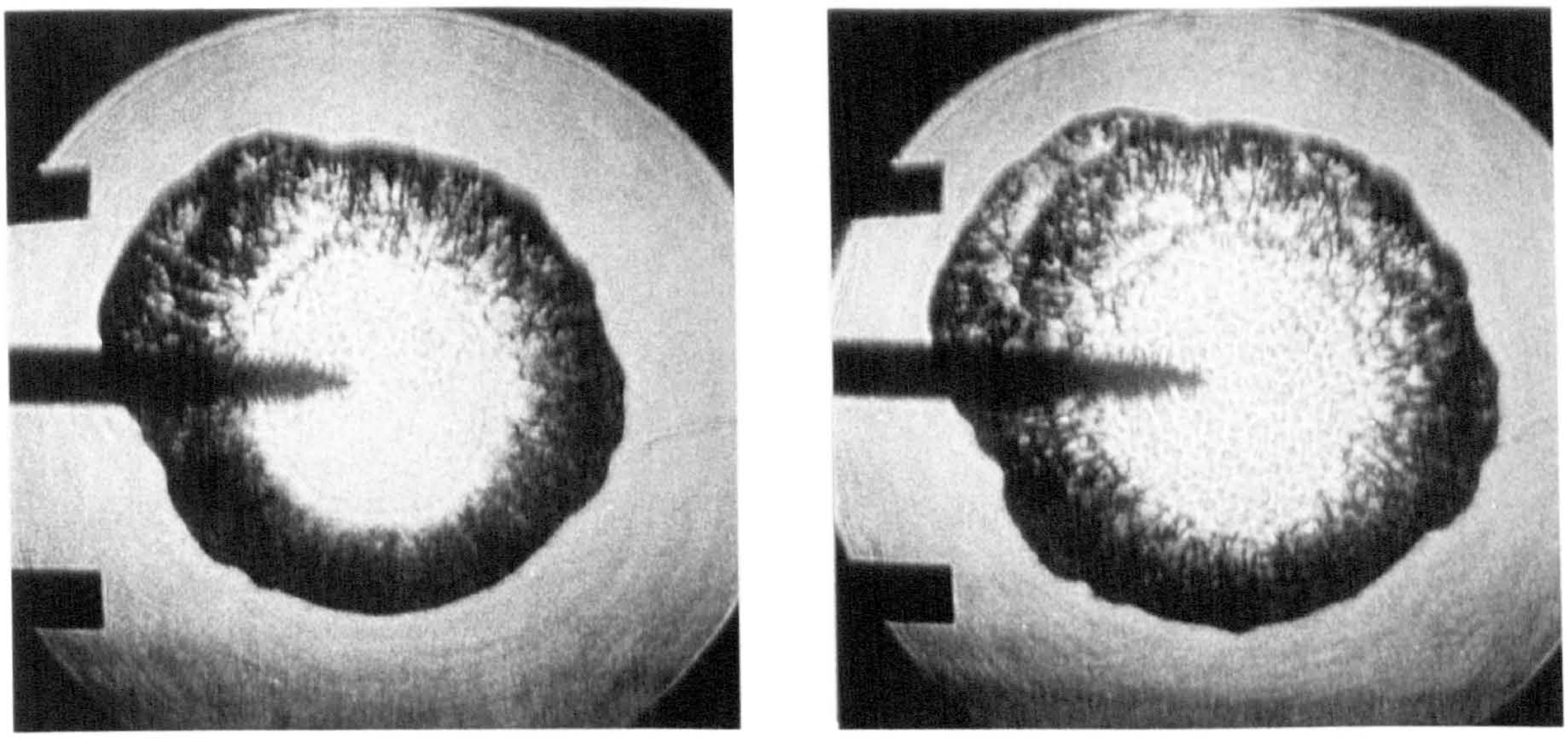

(g) $t_c=25ms$, $r=42mm$

(h) $t_c=26ms$, $r=45mm$

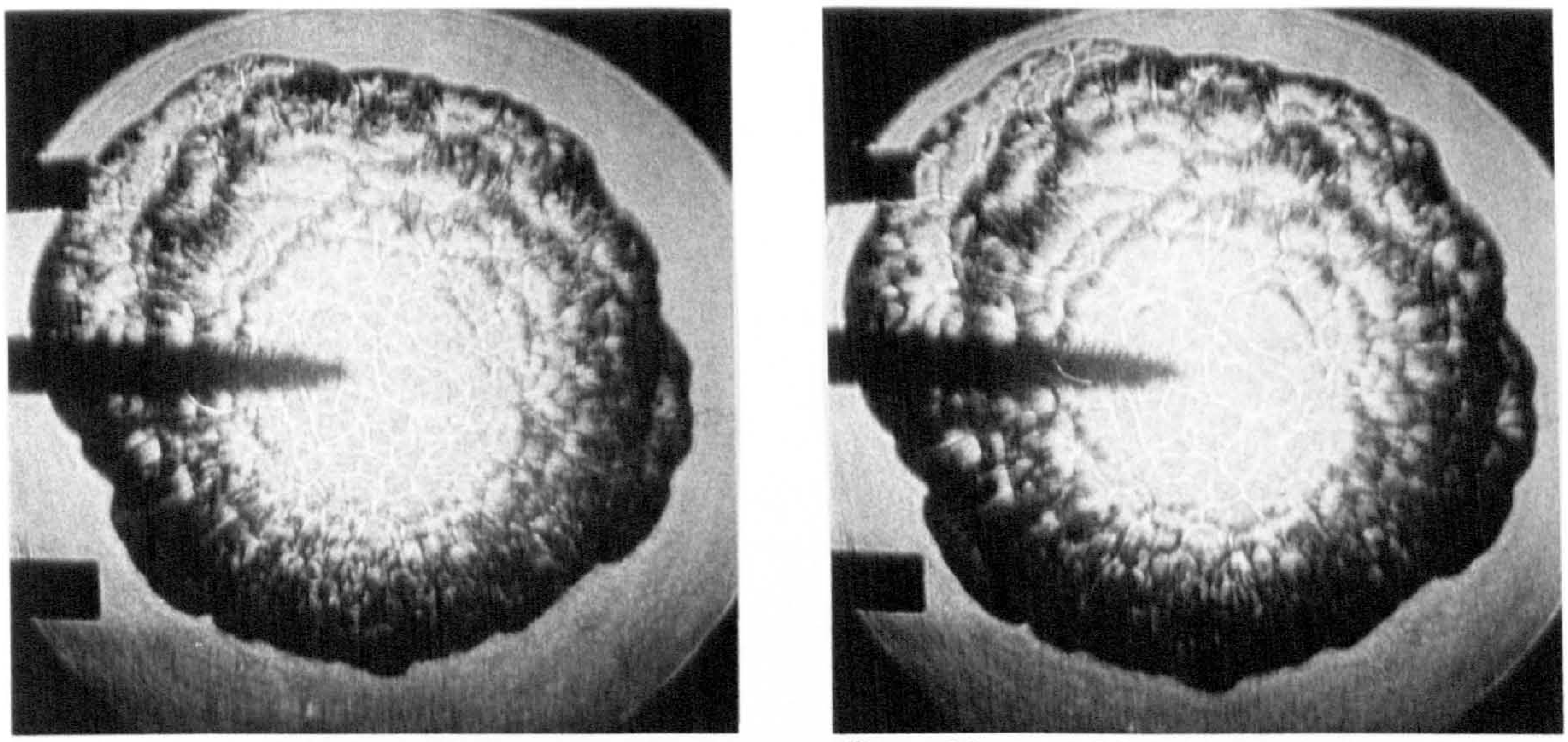

(i) $t_c=29ms$, $r=33mm$

(j) $t_c=30ms$, $r=56mm$

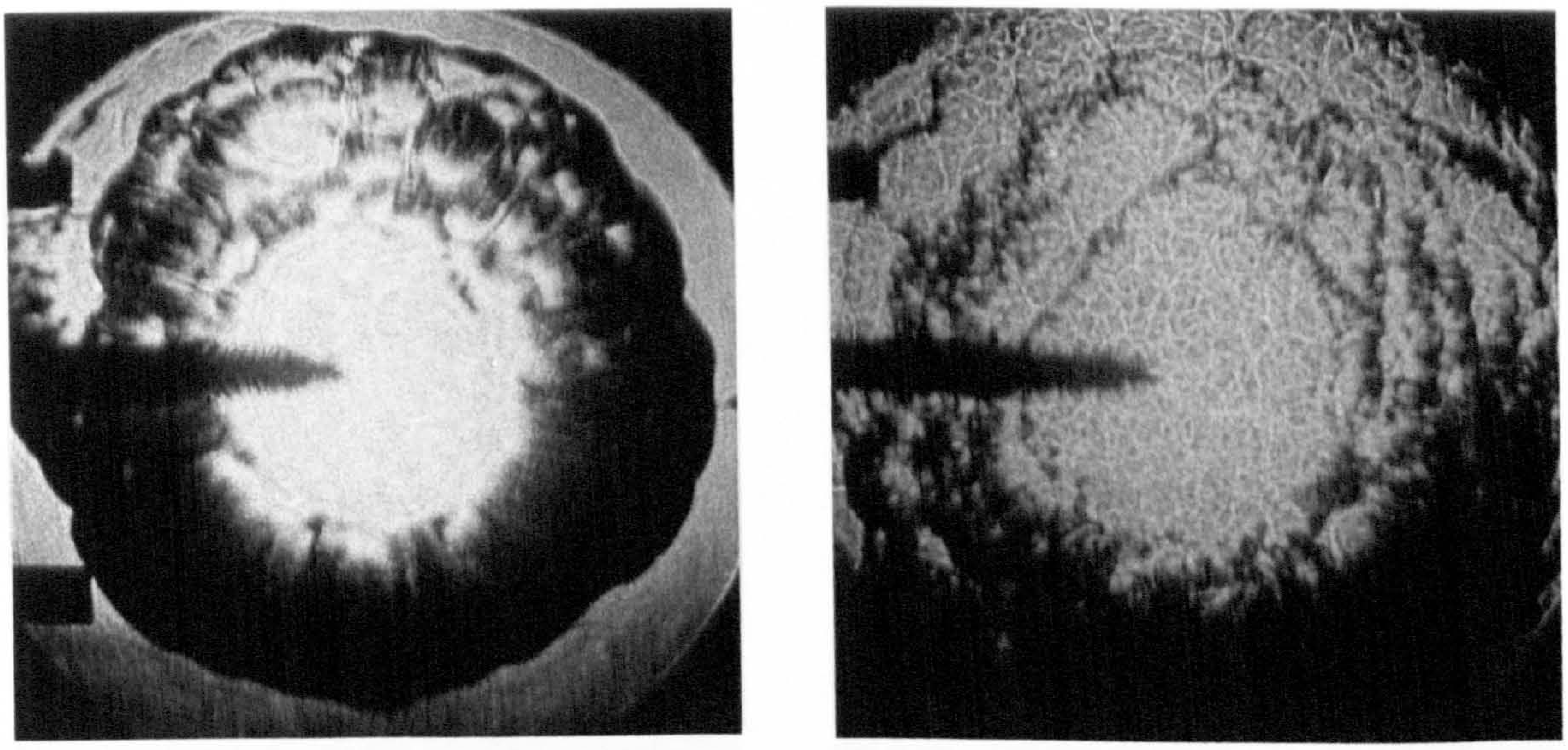

(k) $t_c=32ms$, $r=59$ mm

(l) $t_c=44ms$, $r=XX$ mm

Figure 5.8 (cont.): *Sequence of schlieren photographs of a laminar iso-octane-air aerosol flame,* $\phi_{ov}=1.0$, $\phi_g=0.75$, $D_{32}=20\mu m$, $p=108kPa$, $T=265K$.

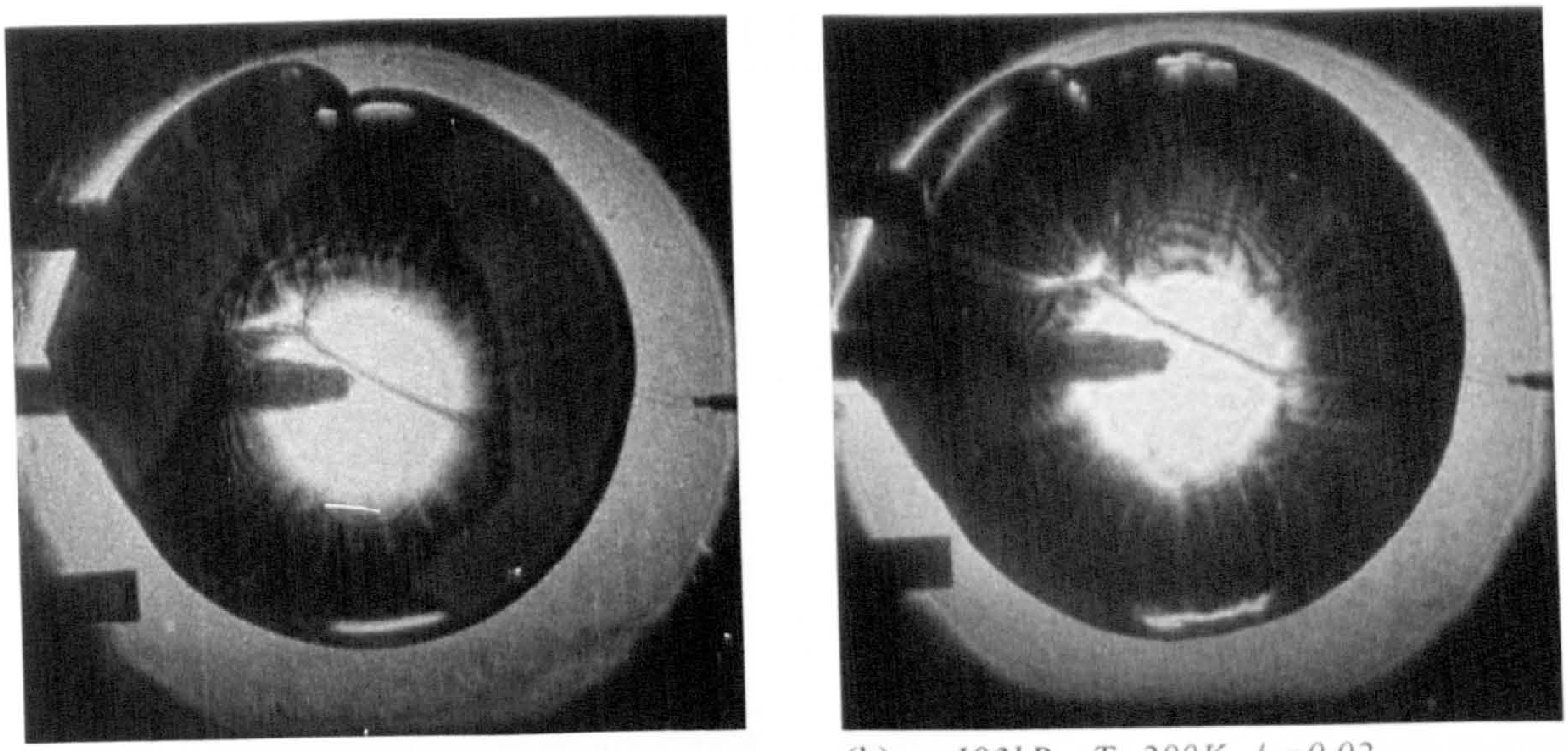

(a) p=205kPa, T=284K, ϕ_g=0.97, D_{32}=17μm, t_c=32ms, r=55mm,

(b) p=193kPa, T=280K, ϕ_g=0.92, D_{32}=20μm, t_c=33ms, r=56.5mm,

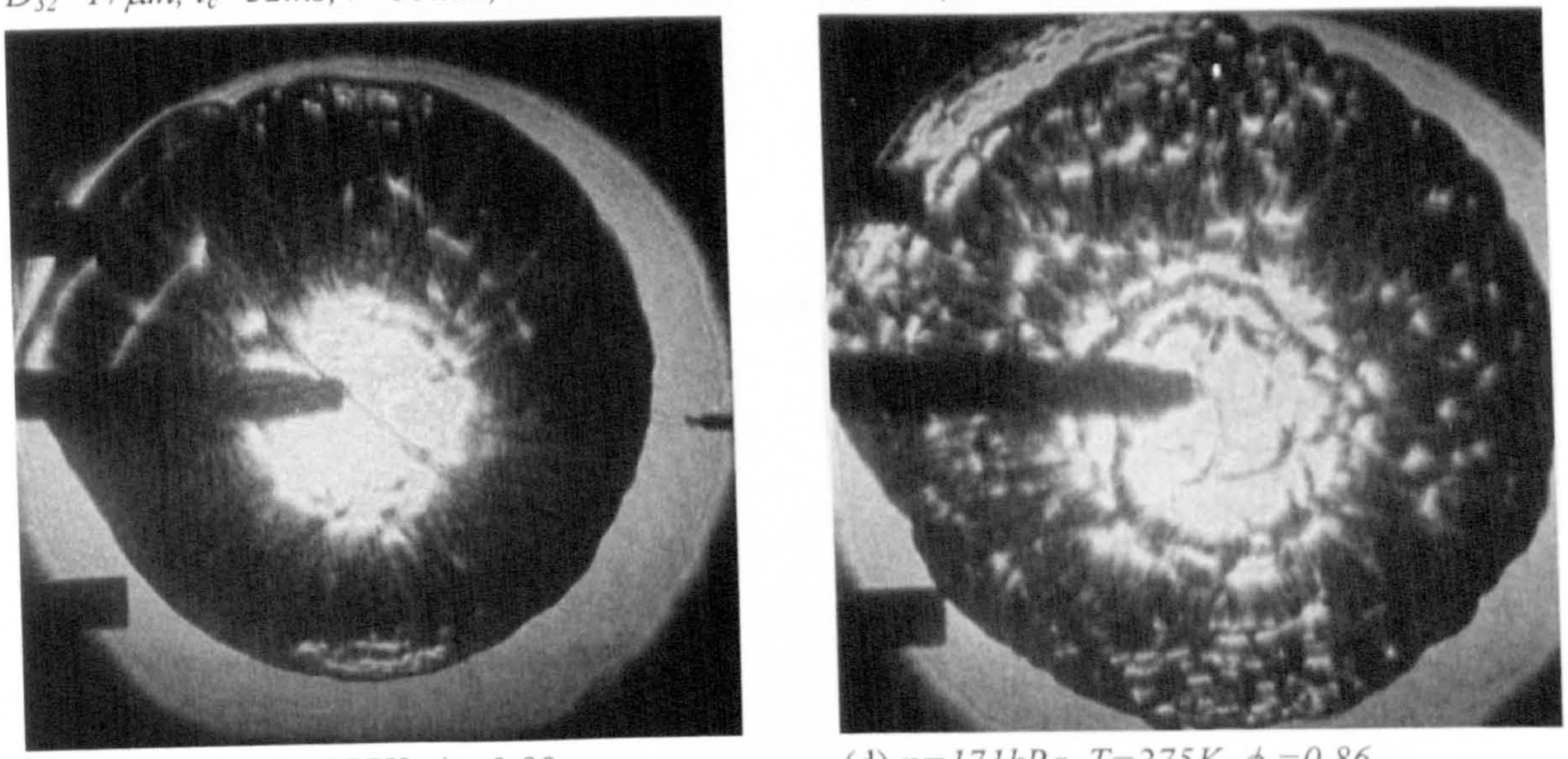

(c) p=182kPa, T=277K, ϕ_g=0.89, D_{32}=24μm, t_c=33ms, r=57mm,

(d) p=171kPa, T=275K, ϕ_g=0.86, D_{32}=25μm, t_c=33ms, r=61mm,

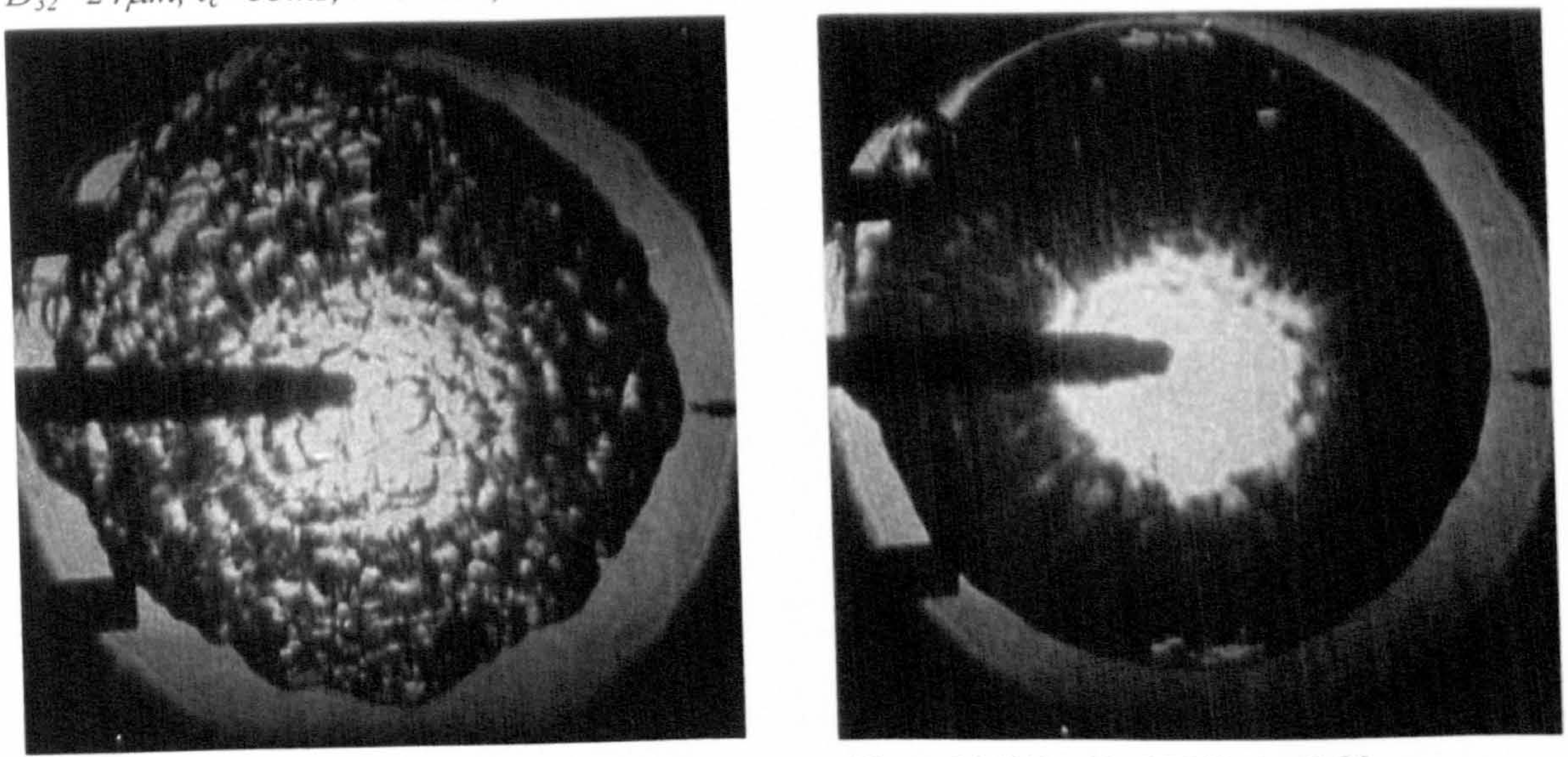

(e) p=162kPa, T=272K, ϕ_g=0.84, D_{32}=27μm, t_c=33ms, r=61mm,

(f) p=154kPa, T=270K, ϕ_g=0.82, D_{32}=28μm, t_c=33ms, r=59mm,

Figure 5.9: *Schlieren photographs of laminar iso-octane-air aerosols with varying aerosol properties,* ϕ_{ov}=*1.0.*

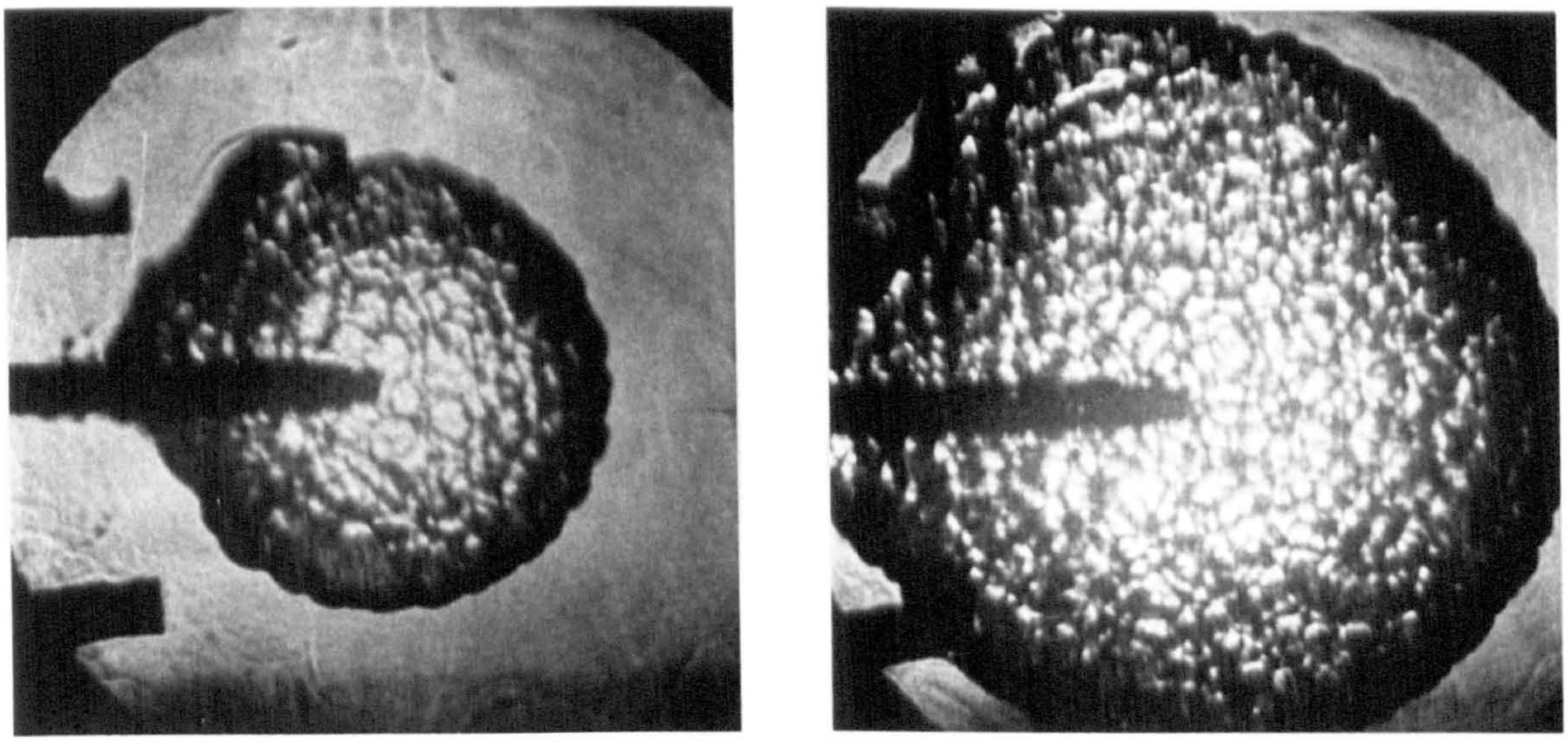

(a) t_c=16ms, r=79mm, (b) t_c=26ms, r=127mm

Figure 5.10: *Schlieren photographs of a laminar iso-octane-air aerosol,* $\phi_{ov}=1.0$, $\phi_g=0.9$, $D_{32}=16\mu m$, $T=286K$, $p=322kPa$.

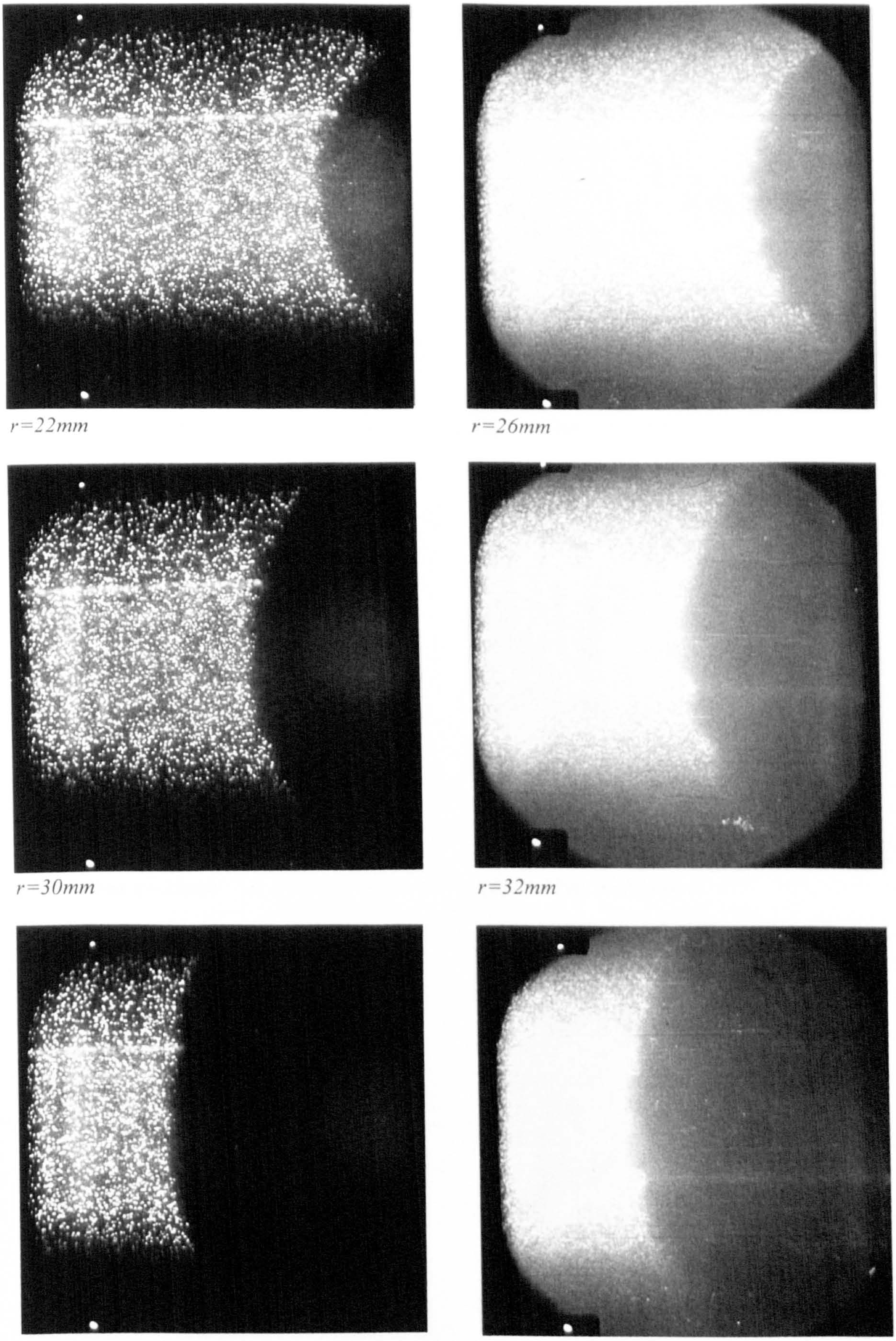

r=22mm

r=26mm

r=30mm

r=32mm

$\phi_{ov}=1.0$, $\phi_g=0.75$, $D_{32}=20\mu m$, $r=40mm$

(a)

$\phi_{ov}=1.2$, $\phi_g=0.93$, $D_{32}=25\mu m$, $r=41mm$

(b)

Figure 5.11: *Sequences of laser sheet images of laminar iso-octane-air aerosol flames, p=109kPa, T≈265K.*

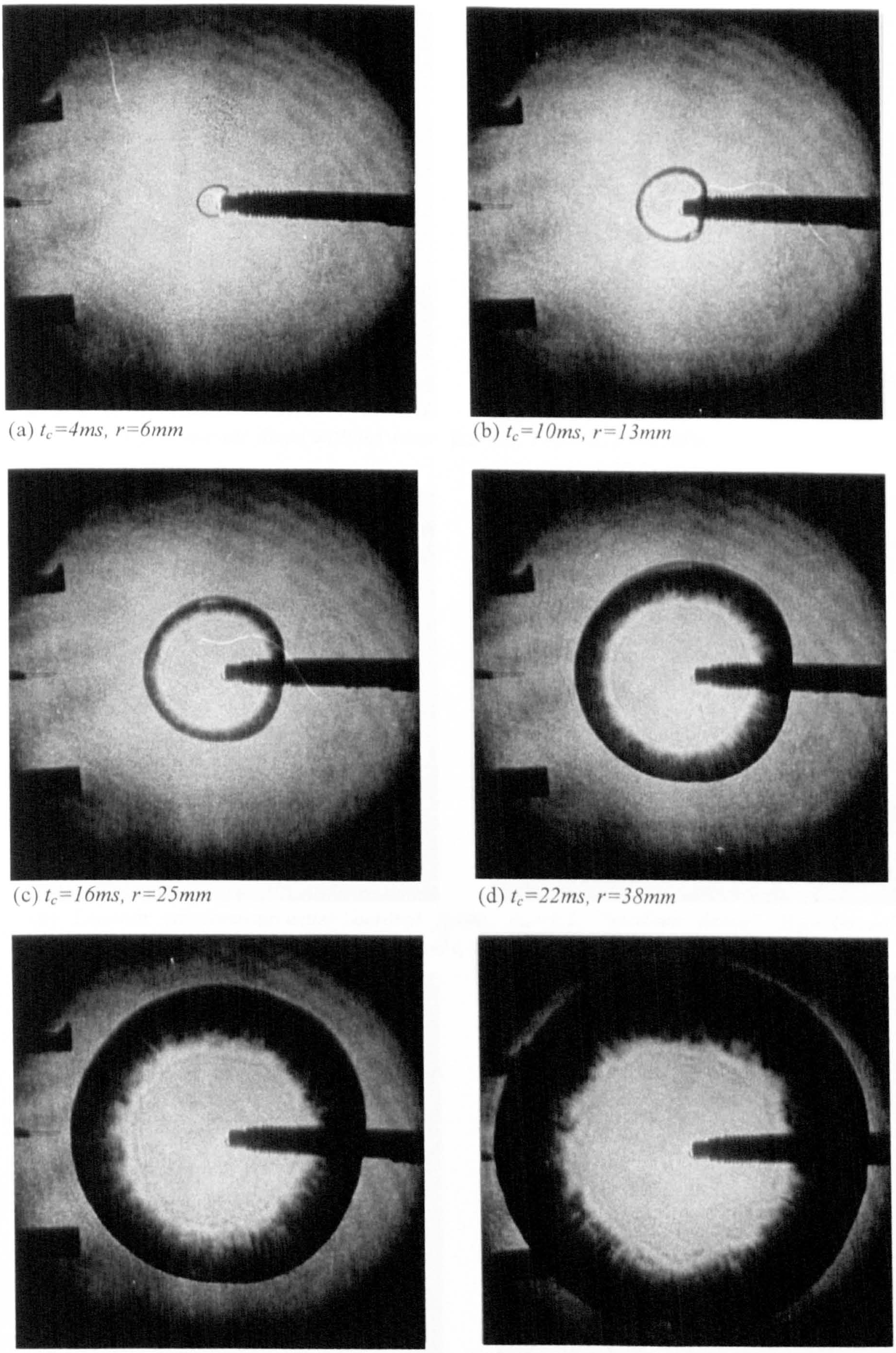

(a) t_c=4ms, r=6mm

(b) t_c=10ms, r=13mm

(c) t_c=16ms, r=25mm

(d) t_c=22ms, r=38mm

(e) t_c=28ms, r=51mm

(f) t_c=32ms, r=60 mm

Figure 5.12: *Effect of 5cm^3 of hollow glass spheres, D_{32}=10-12μm, ρ=1.1g/cm^3, on a laminar gaseous iso-octane-air flame, ϕ_{ov}=1.0, p=100kPa, T=328K.*

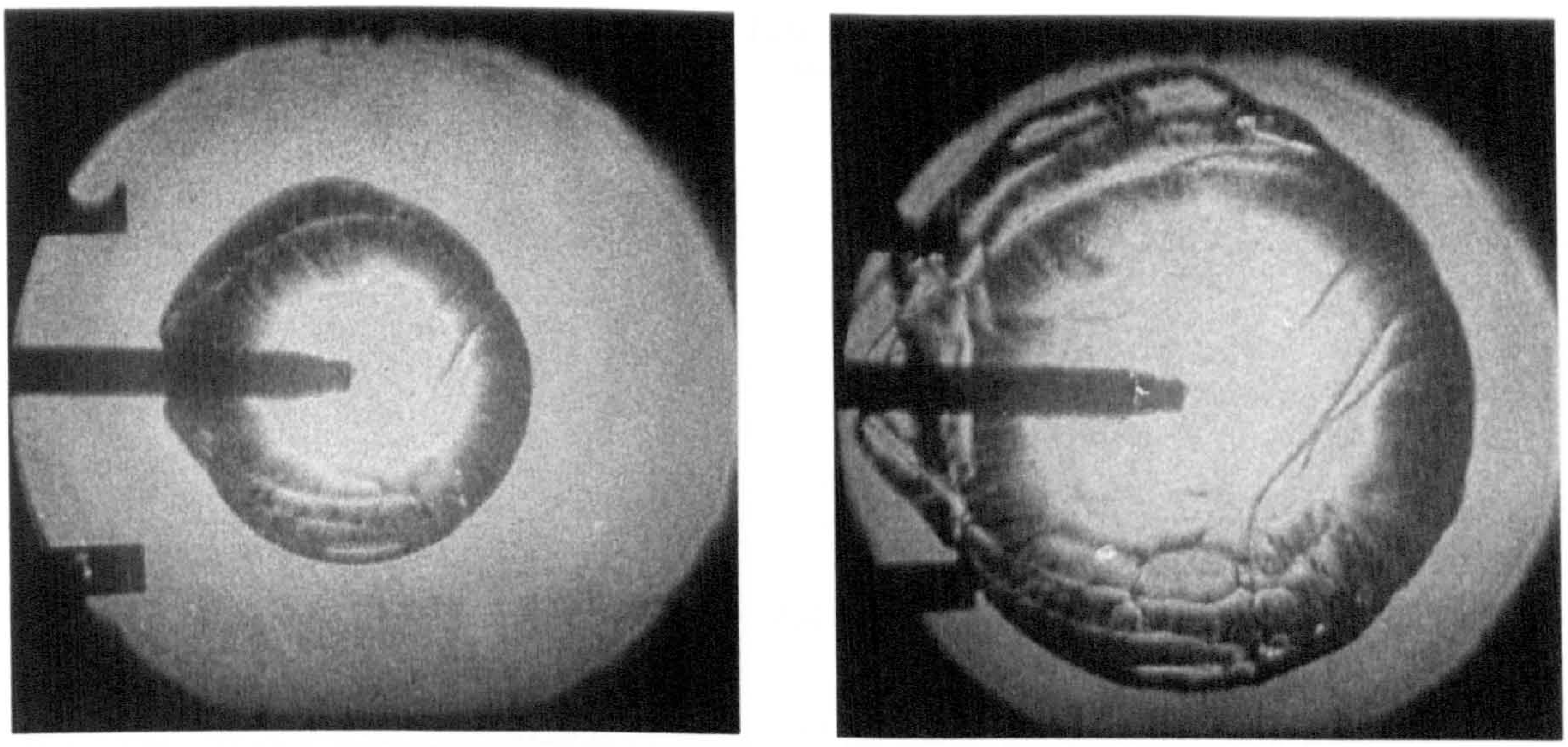

(a) *Laminar propane-air flame without water,* $\phi_{ov}=1.3$, $T\approx250K$, $p\approx105kPa$.
$t_c=16ms$, $r=36mm$ $t_c=26.5ms$, $r=59.5mm$.

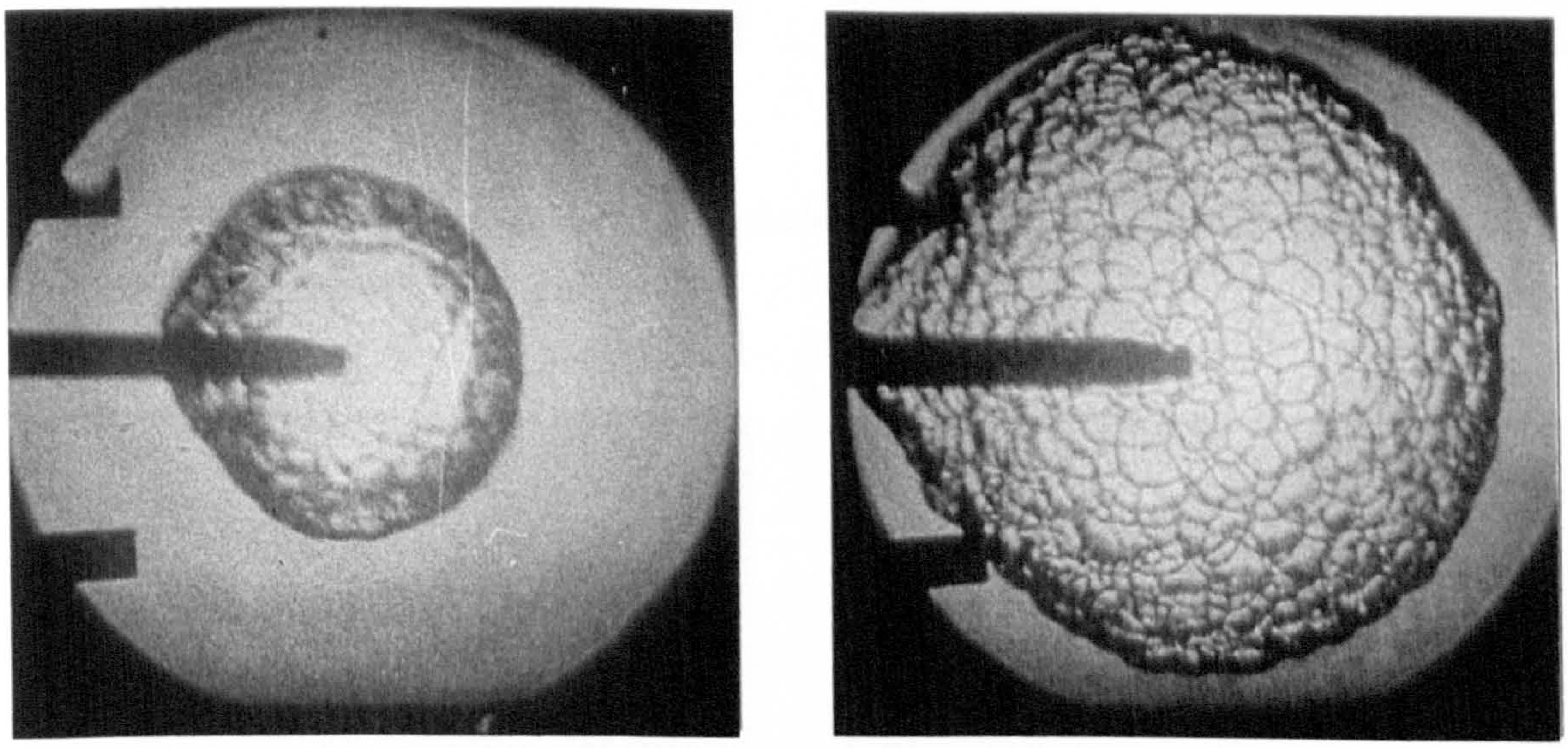

(b) *Laminar propane-air-water aerosol flame,* $\phi_{ov}=1.3$, *"medium dense"* H_2O*-Aerosol* $T\approx265K$, $p=108kPa$, $t_c=16ms$, $r=35.5mm$ *and* $t_c=26.5ms$, $r=60mm$.

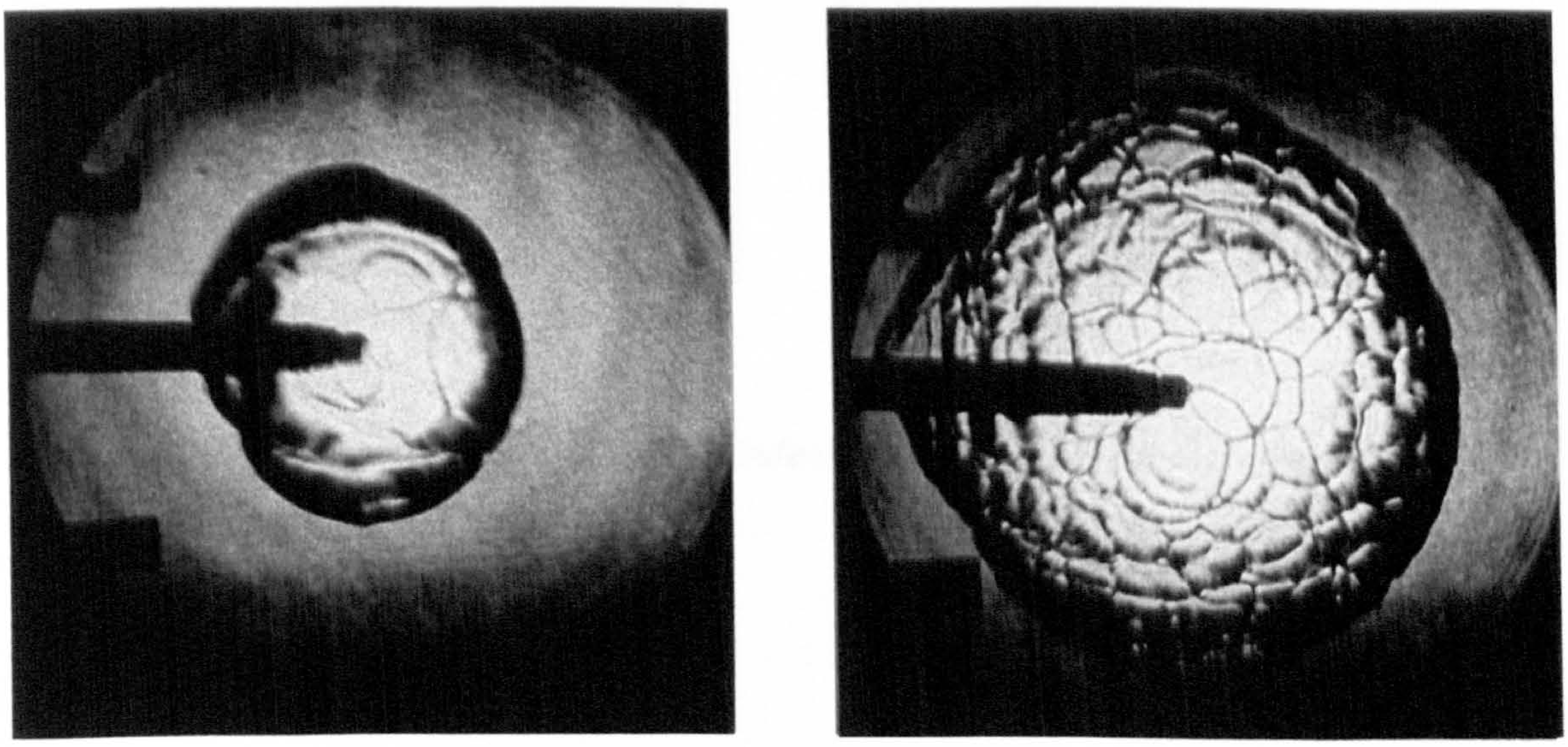

(c) *Laminar propane-air-water aerosol flame,* $\phi_{ov}=1.3$, *"very dense"* H_2O*-Aerosol,* $T\approx265K$, $p=108kPa$, $t_c=16ms$, $r=33mm$ *and* $t_c=26.5ms$, $r=56mm$.

Figure 5.13: *Effect of water-aerosol on gaseous fuel-air flames*

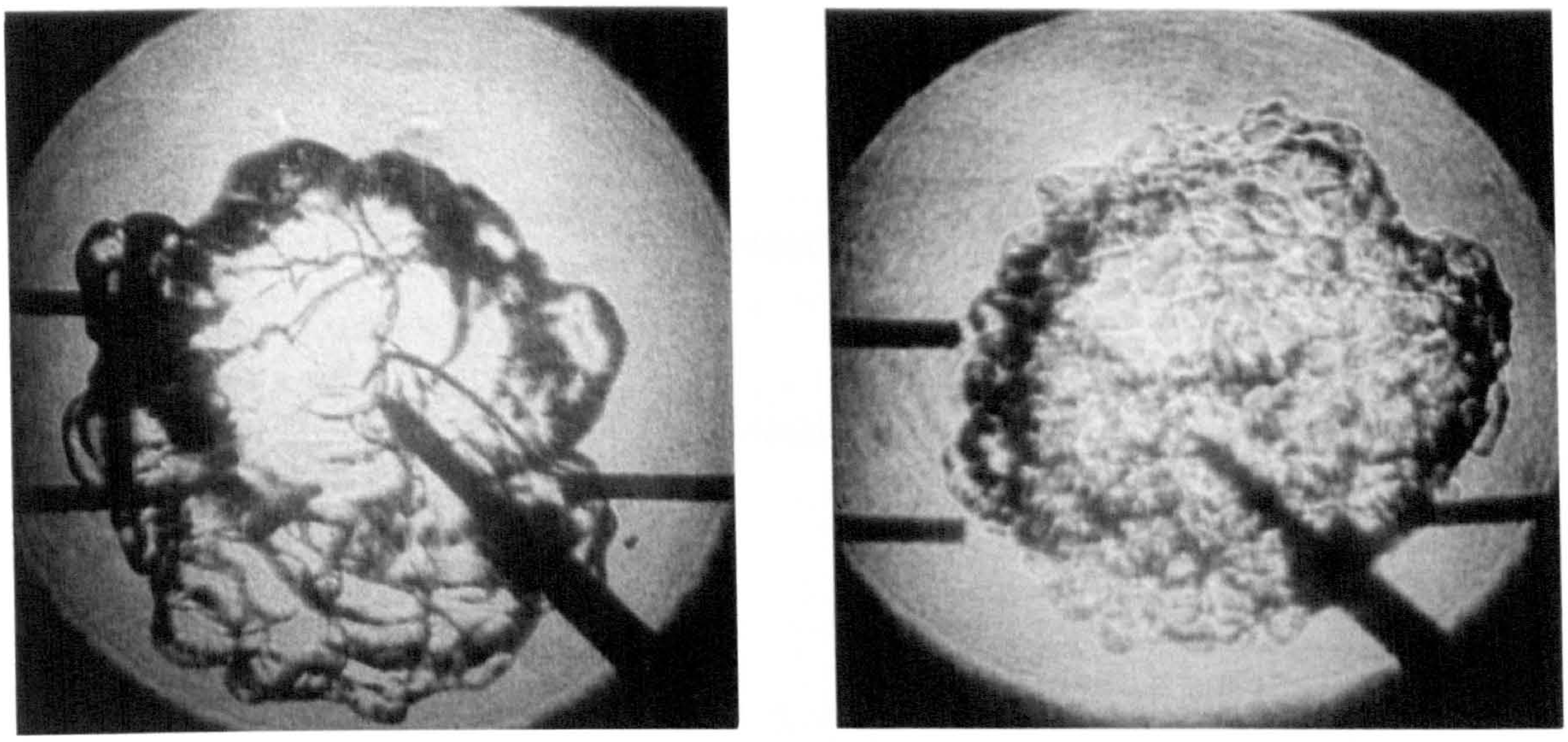

(a) $u'=0.6\ m/s$ (b) $u'=1.2\ m/s$

Figure 5.14: *Schlieren photographs of turbulent gaseous iso-octane-air flames,* $\phi=1.0$, $T=358K$, $p=100kPa$, *(Bradley et al., 1995).*

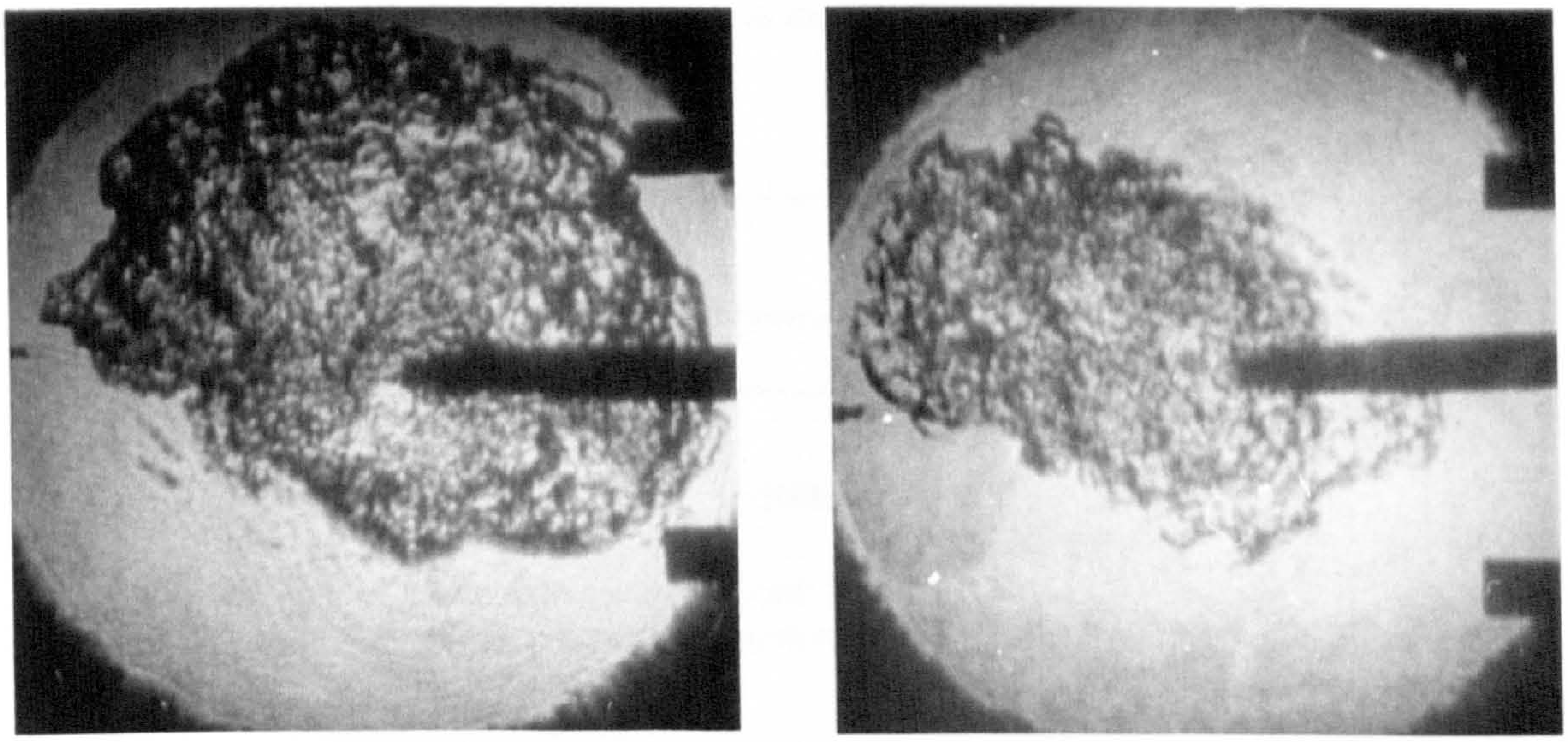

(a) $u'=0.83\ m/s$, $\phi_g=0.87$, $D_{32}=20\mu m$, (b) $u'=1.67\ m/s$, $\phi_g=0.9$, $D_{32}=20\mu m$,

Figure5.15: *Schlieren photographs of turbulent iso-octane-air aerosol flames,* $\phi_{ov}=1.0$, $p=90kPa$, $T=265K$.

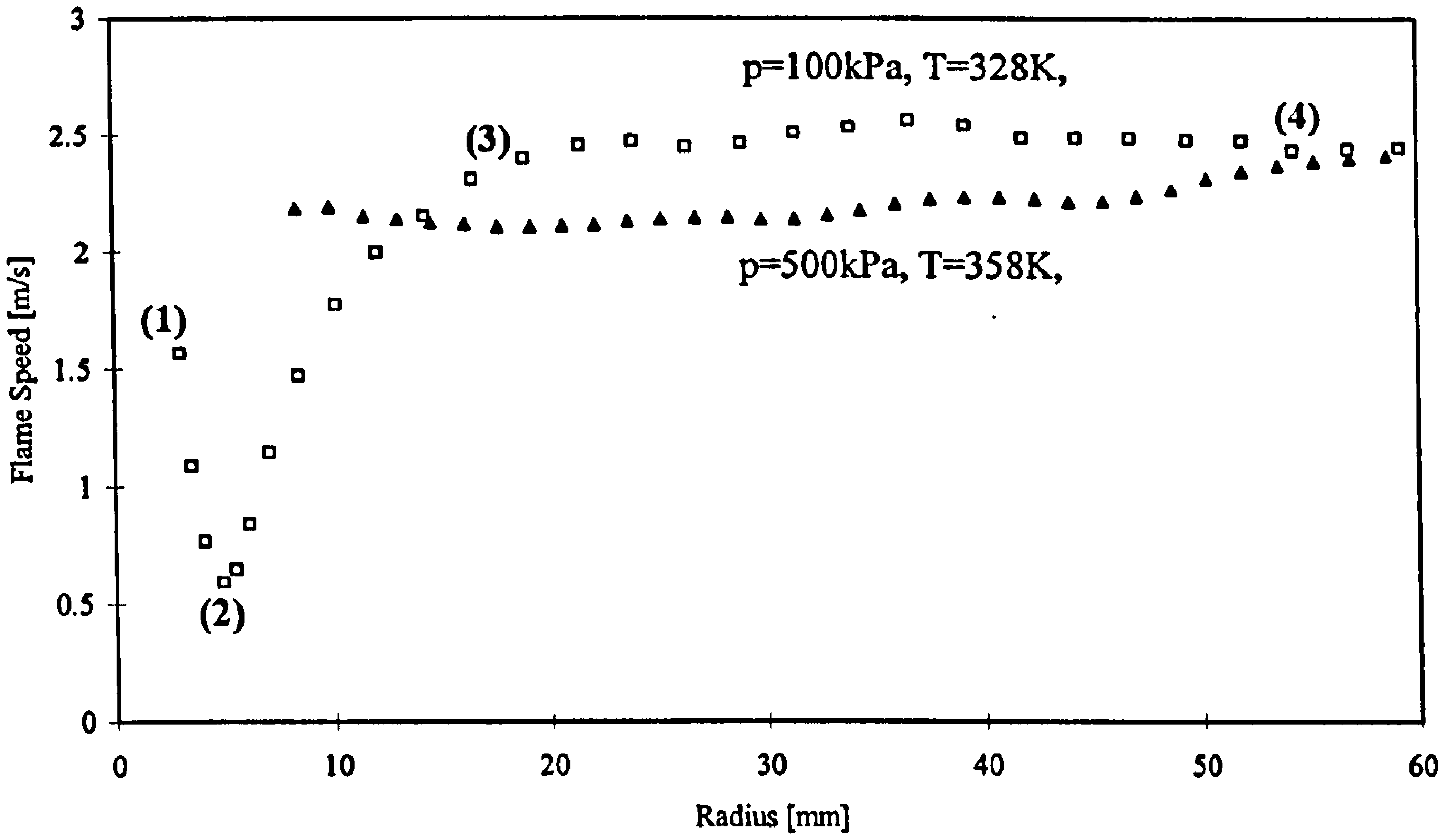

Figure 5.16: *Flame speed against radius for gaseous iso-octane-air flames at different pressures; Numbers indicate combustion regimes explained in the text.*

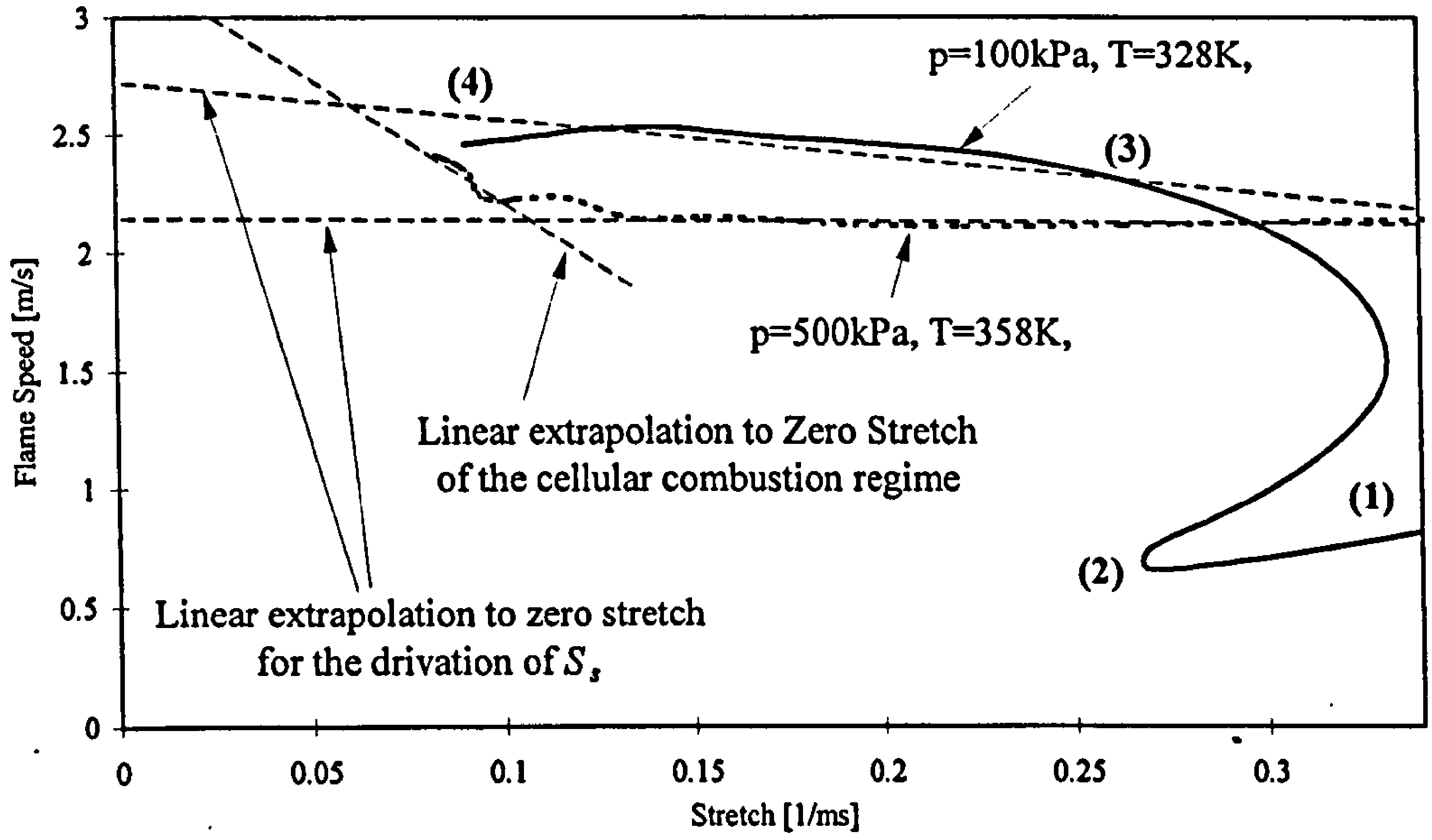

Figure 5.17: *Flame speed against stretch for gaseous iso-octane-air flames at different pressures; Numbers indicate combustion regimes explained in the text.*

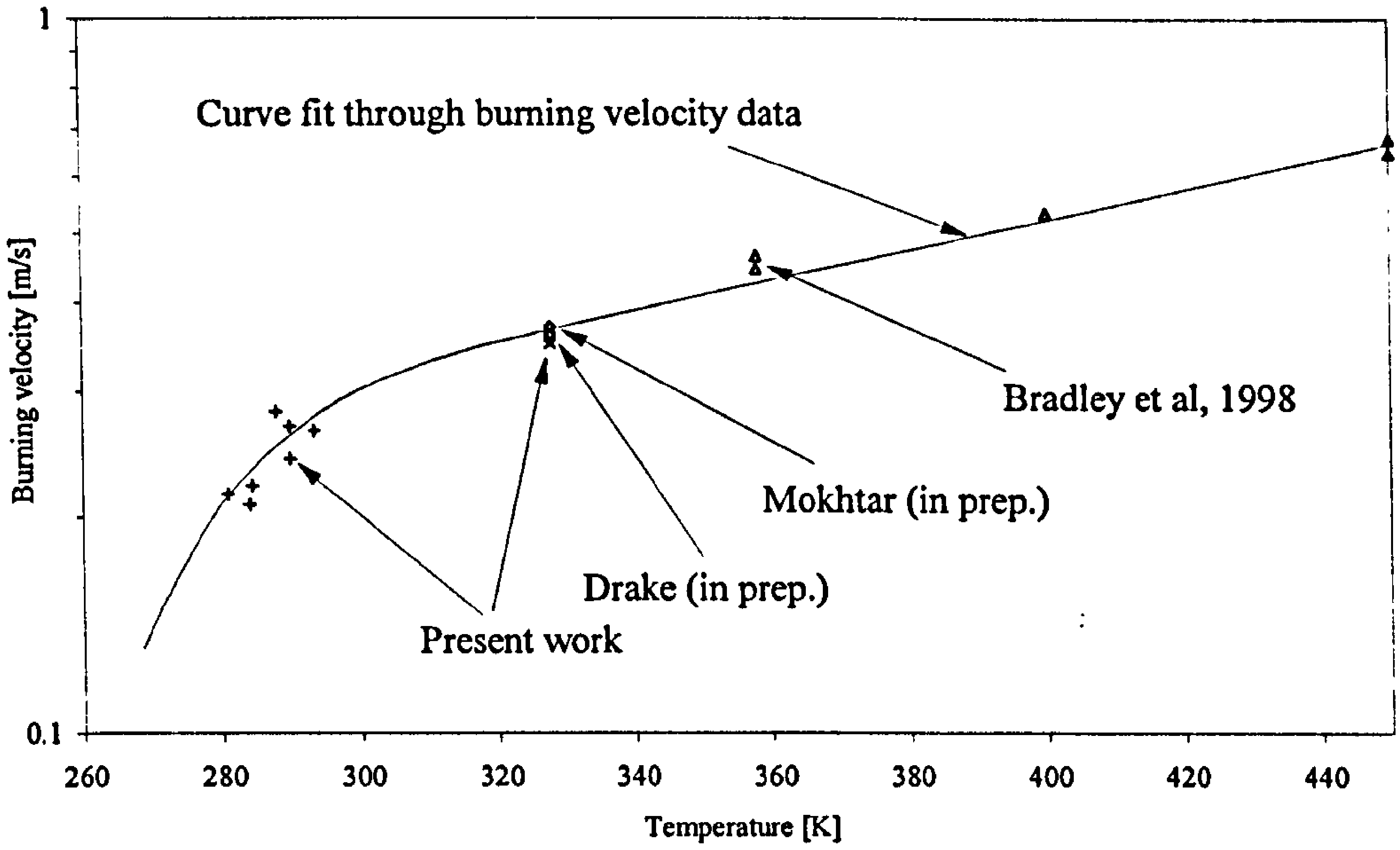

Figure 5.18: *Burning velocity against temperature for stoichiometric gaseous iso-octane-air flames at 100kPa.*

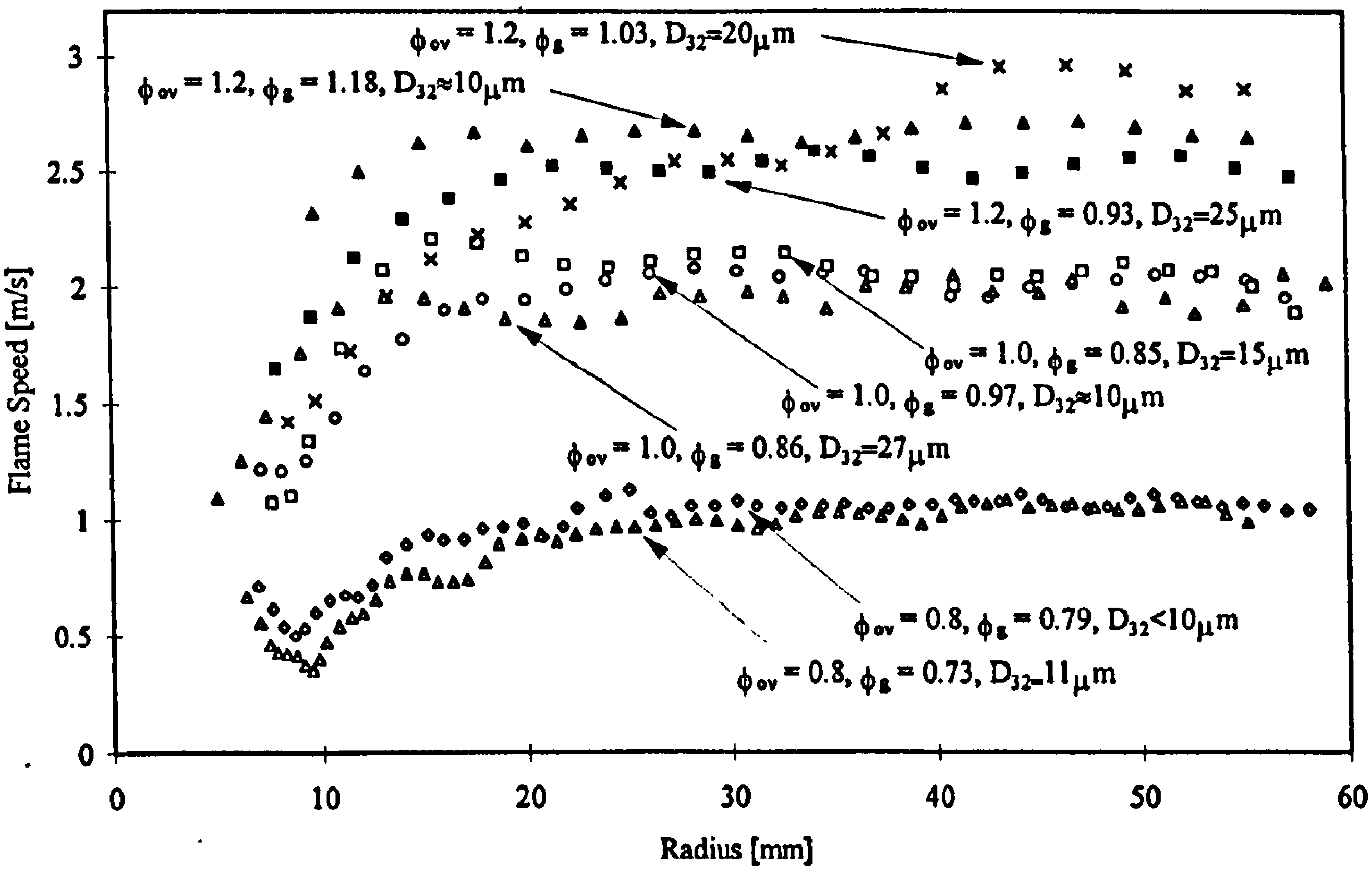

Figure 5.19: *Flame speed against radius for laminar iso-octane-air aerosols at ϕ_{ov}=0.8, 1.0 & 1.2.*

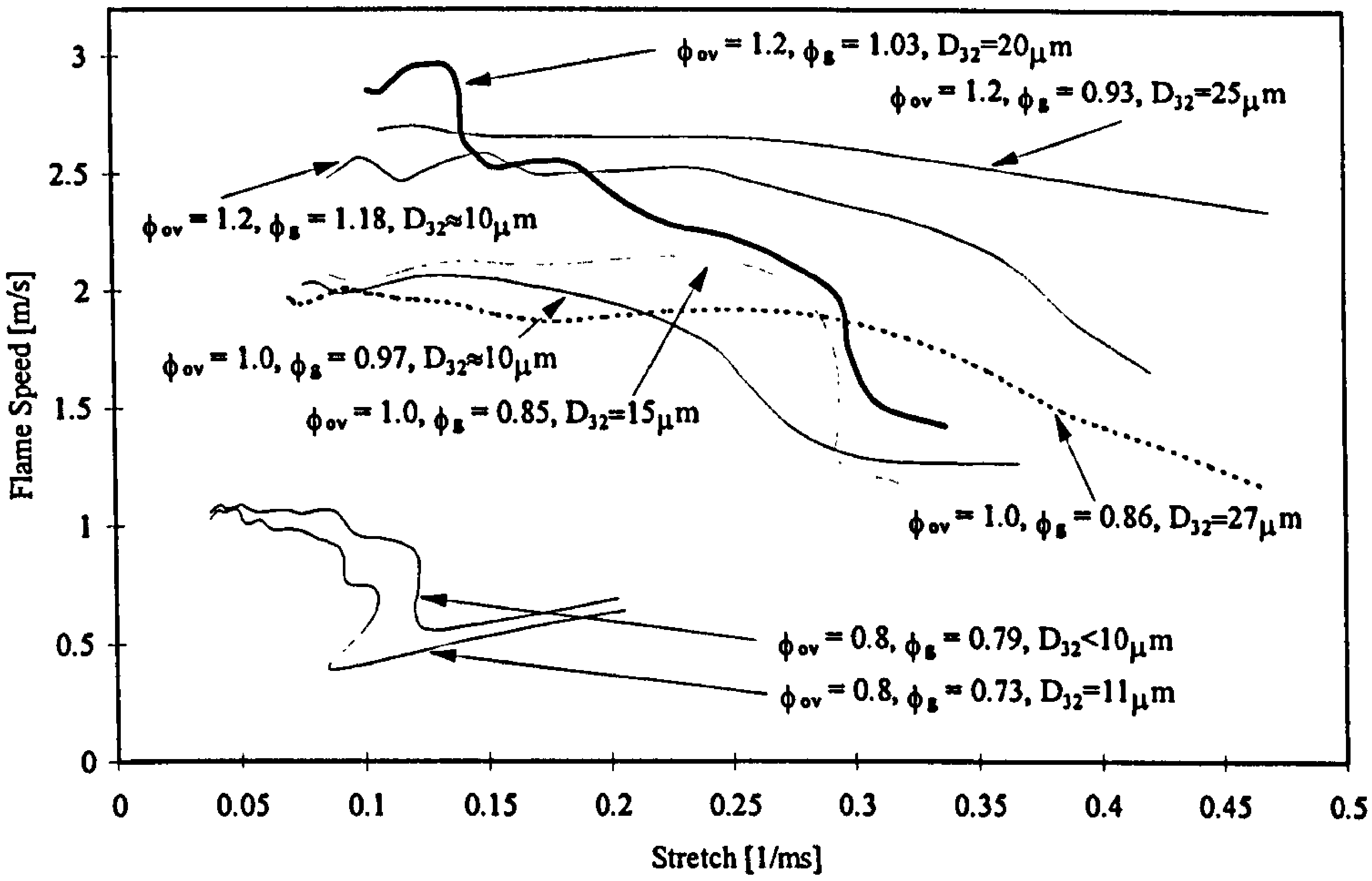

Figure 5.20: *Flame speed against stretch for laminar iso-octane-air aerosols at* ϕ_{ov}*=0.8, 1.0 & 1.2.*

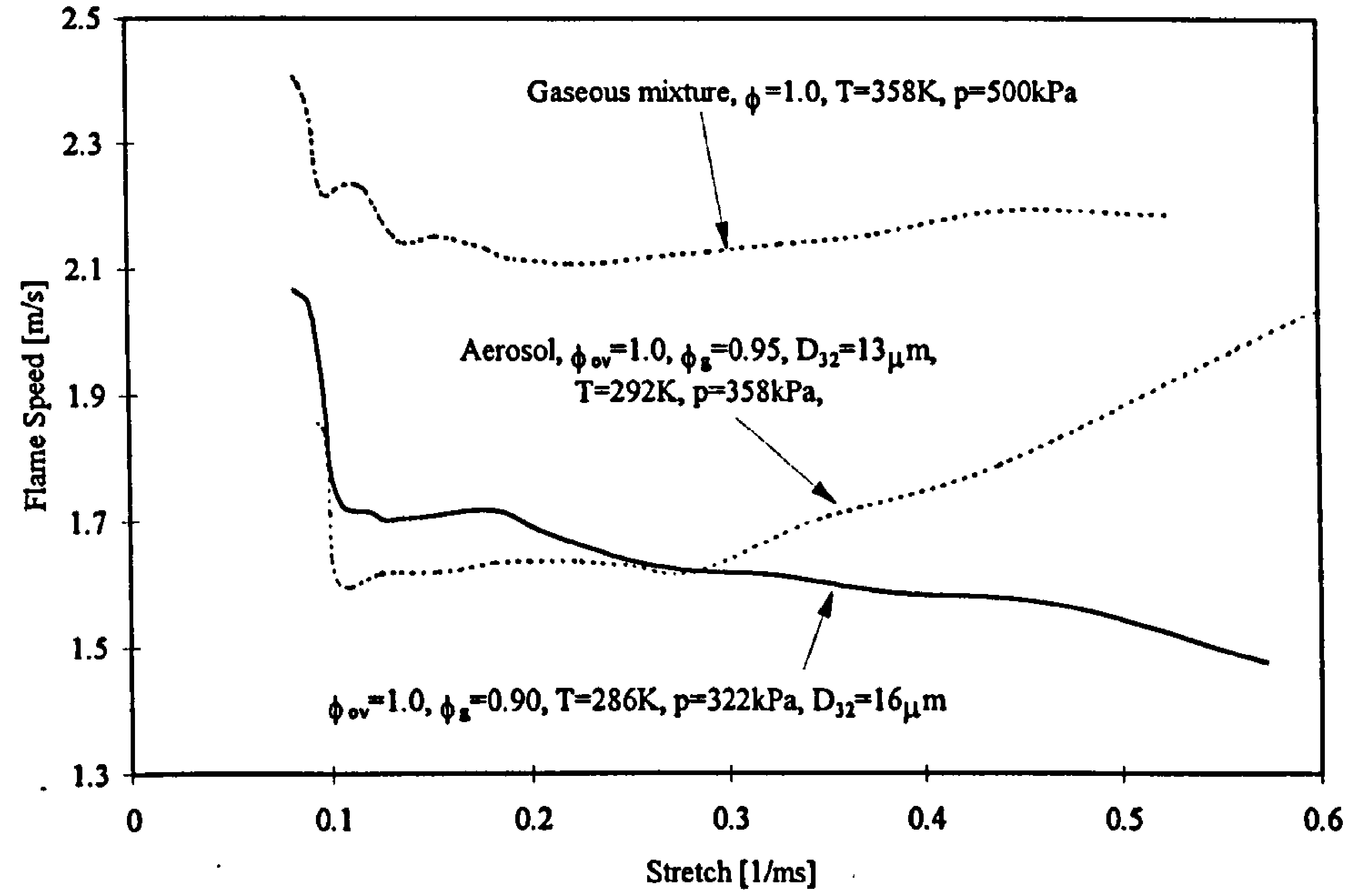

Figure 5.21: *Flame speed against stretch for laminar iso-octane-air aerosols at* ϕ_{ov}*=1.0 and elevated pressure; Also shown is a gaseous stoichiometric flame at 500kPa.*

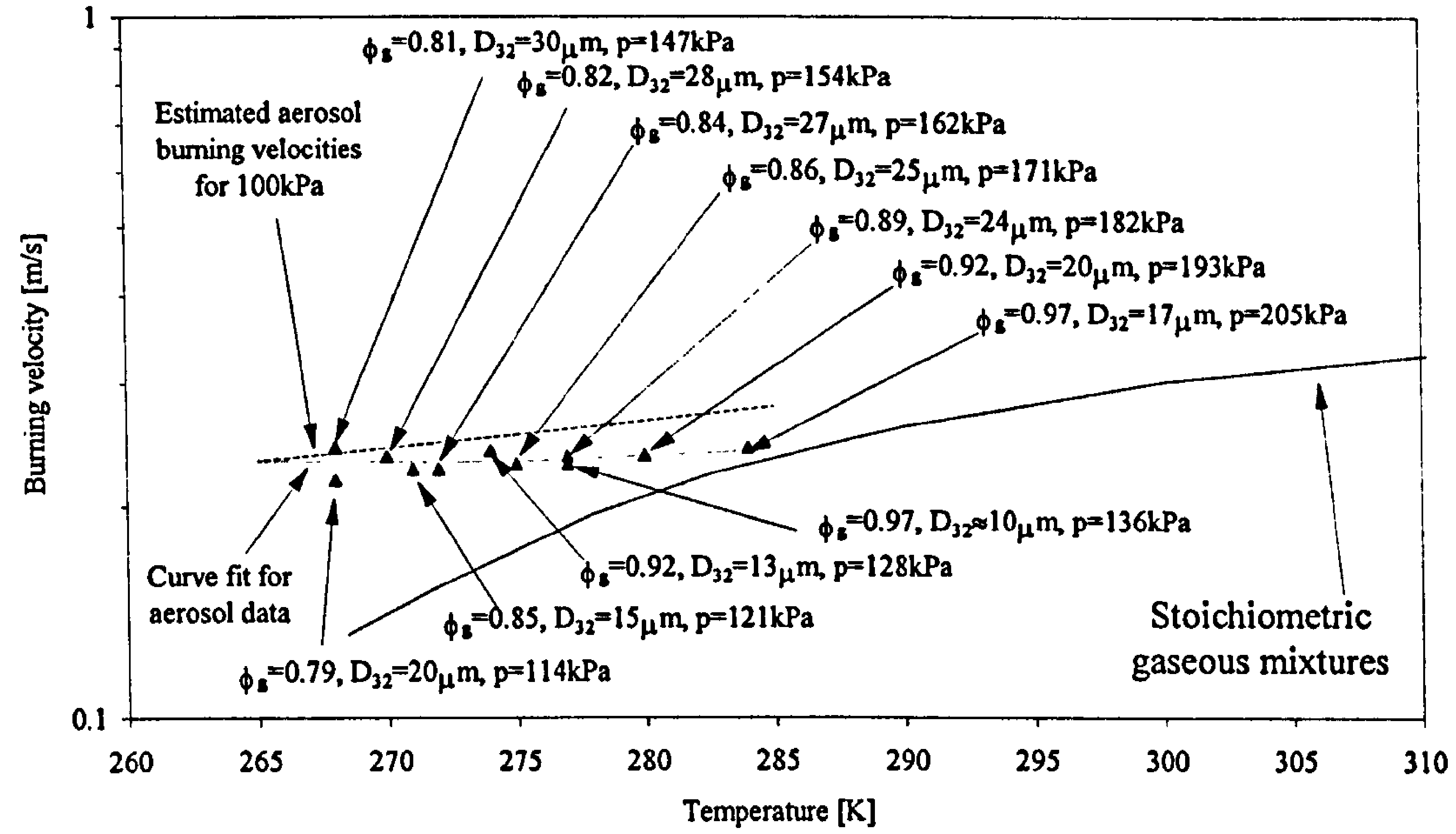

Figure 5.22: *Burning velocity against temperature for iso-octane-air aerosols, $\phi_{ov}=1.0$; Also shown are the gaseous baseline burning velocities and an estimate of the effect of pressure.*

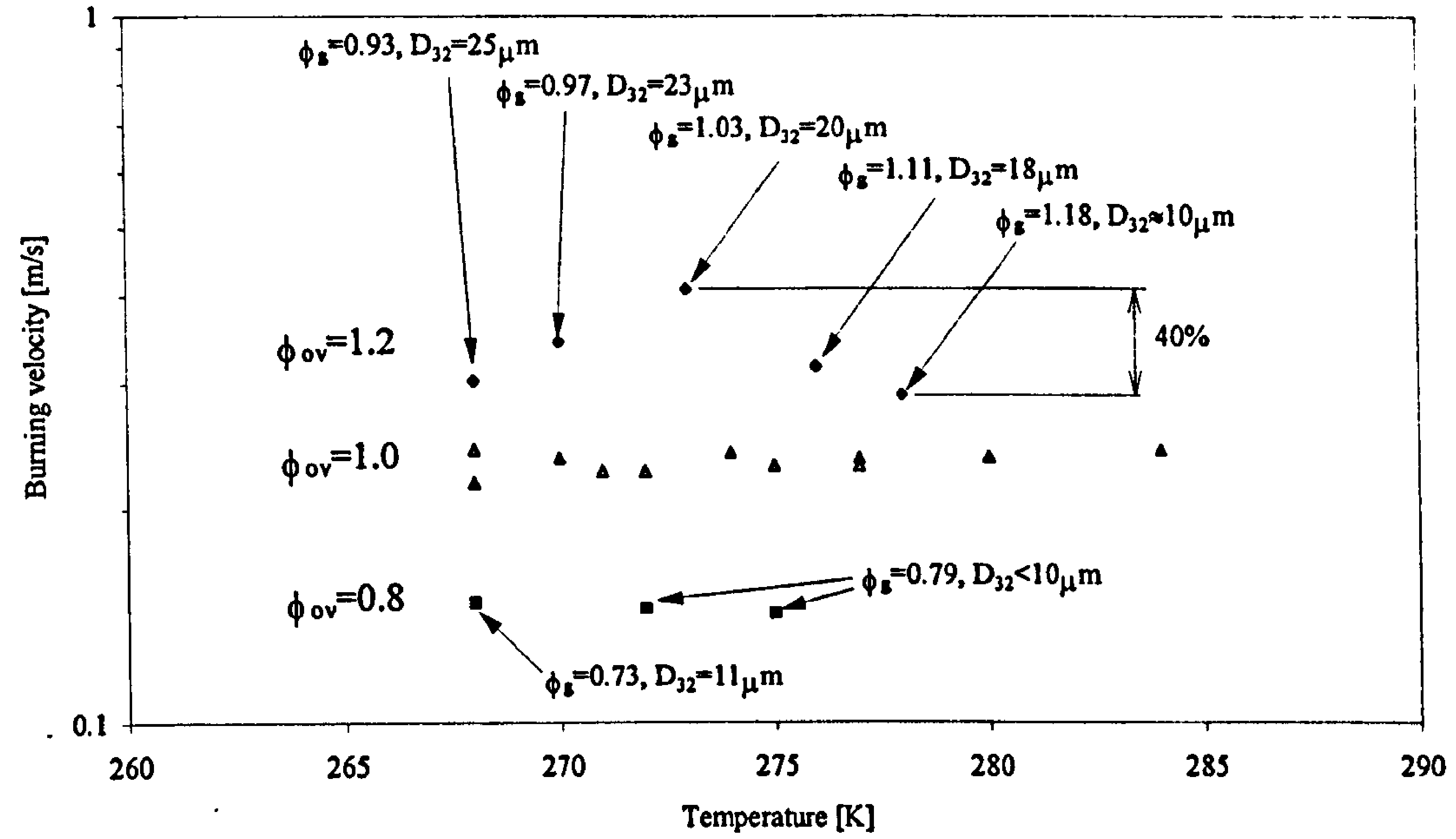

Figure 5.23: *Burning velocity against temperature for iso-octane-air aerosols, $\phi_{ov}=1.2$ & 0.8; Also shown for comparison are the values for $\phi_{ov}=1.0$.*

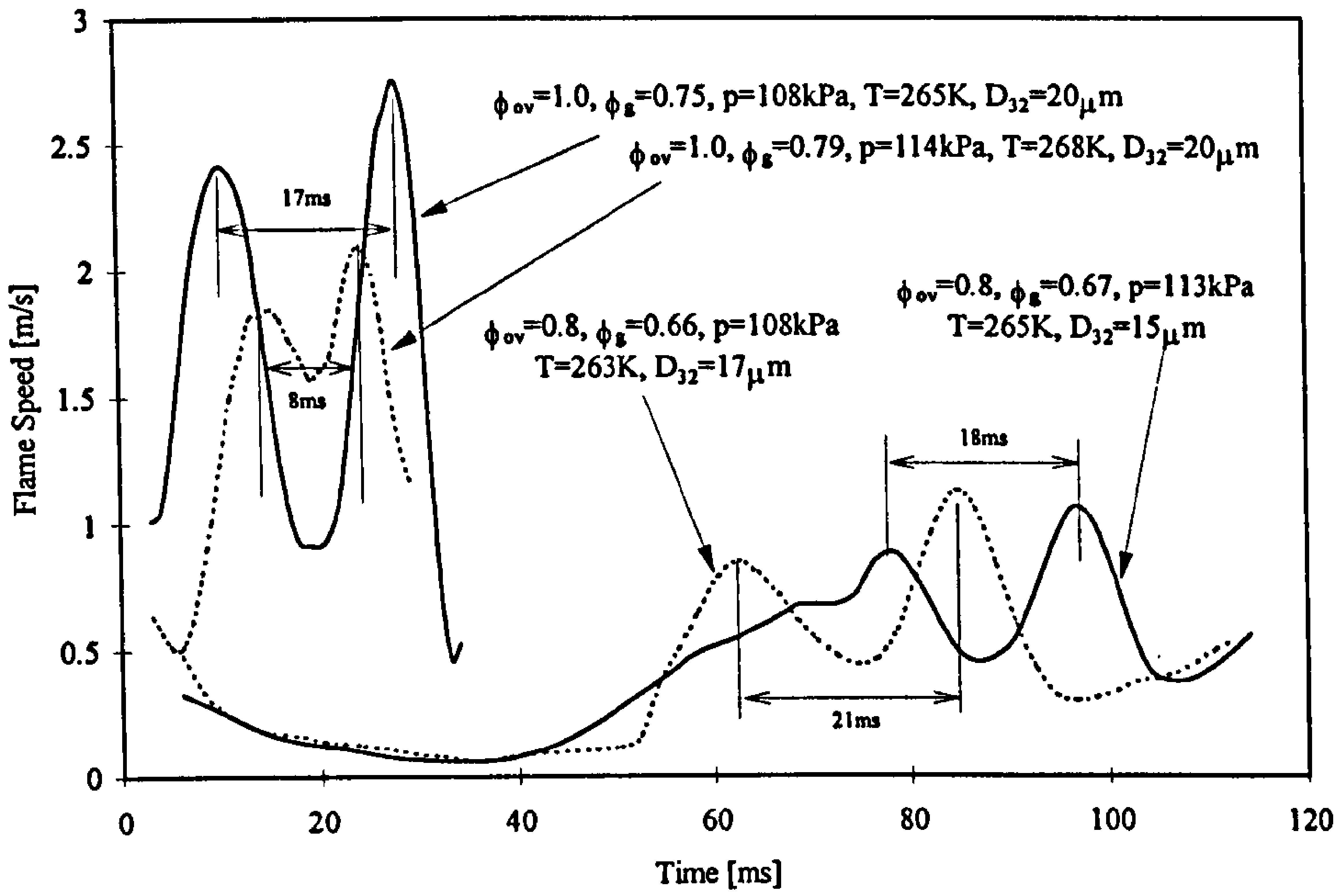

Figure 5.24: *Flame speed against time for oscillating iso-octane-air aerosols at ϕ_{ov}=0.8 & 1.0; Also shown are oscillation periods.*

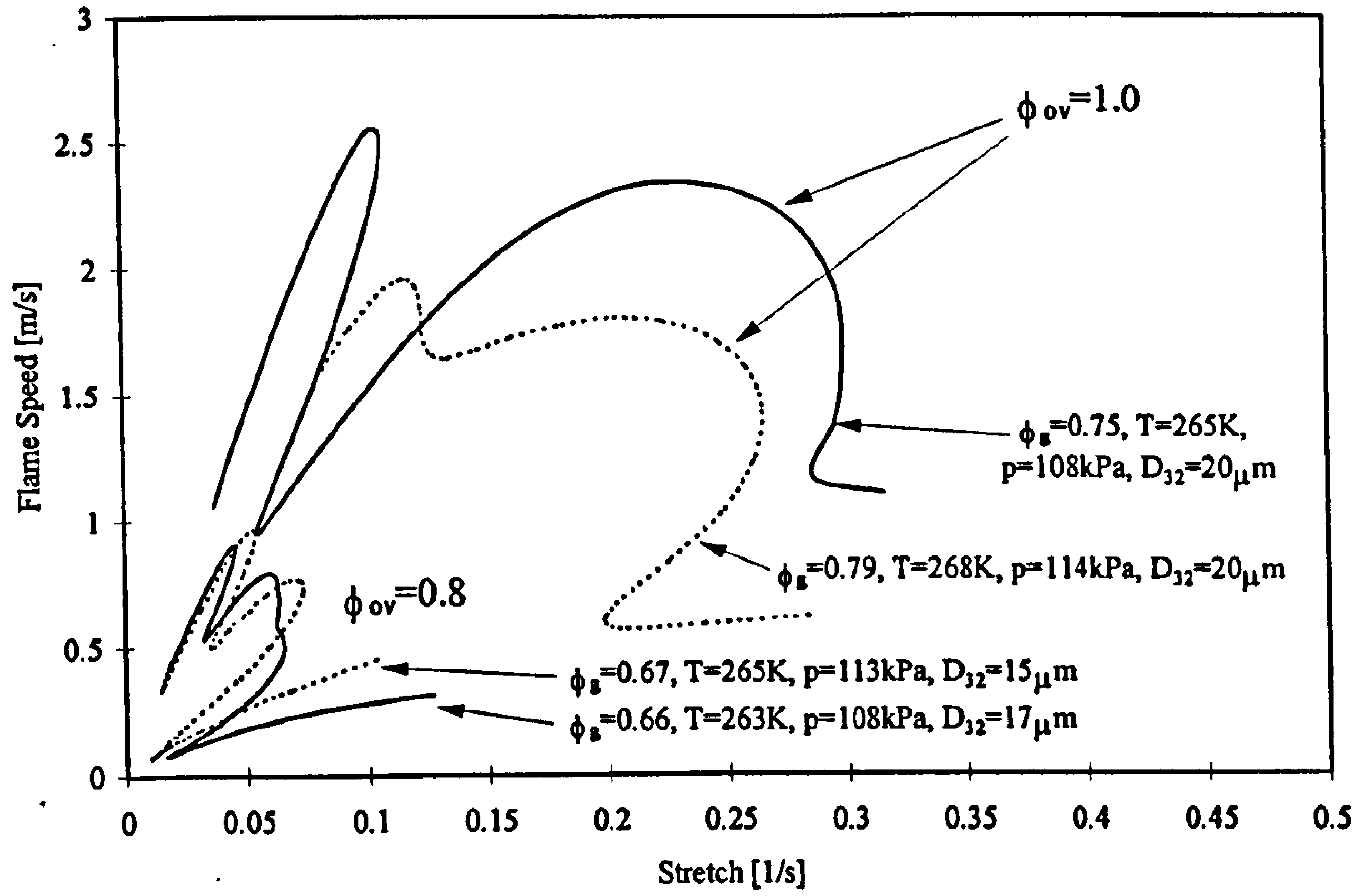

Figure 5.25: *Flame speed against stretch for oscillating iso-octane-air aerosols at ϕ_{ov}=0.8 & 1.0.*

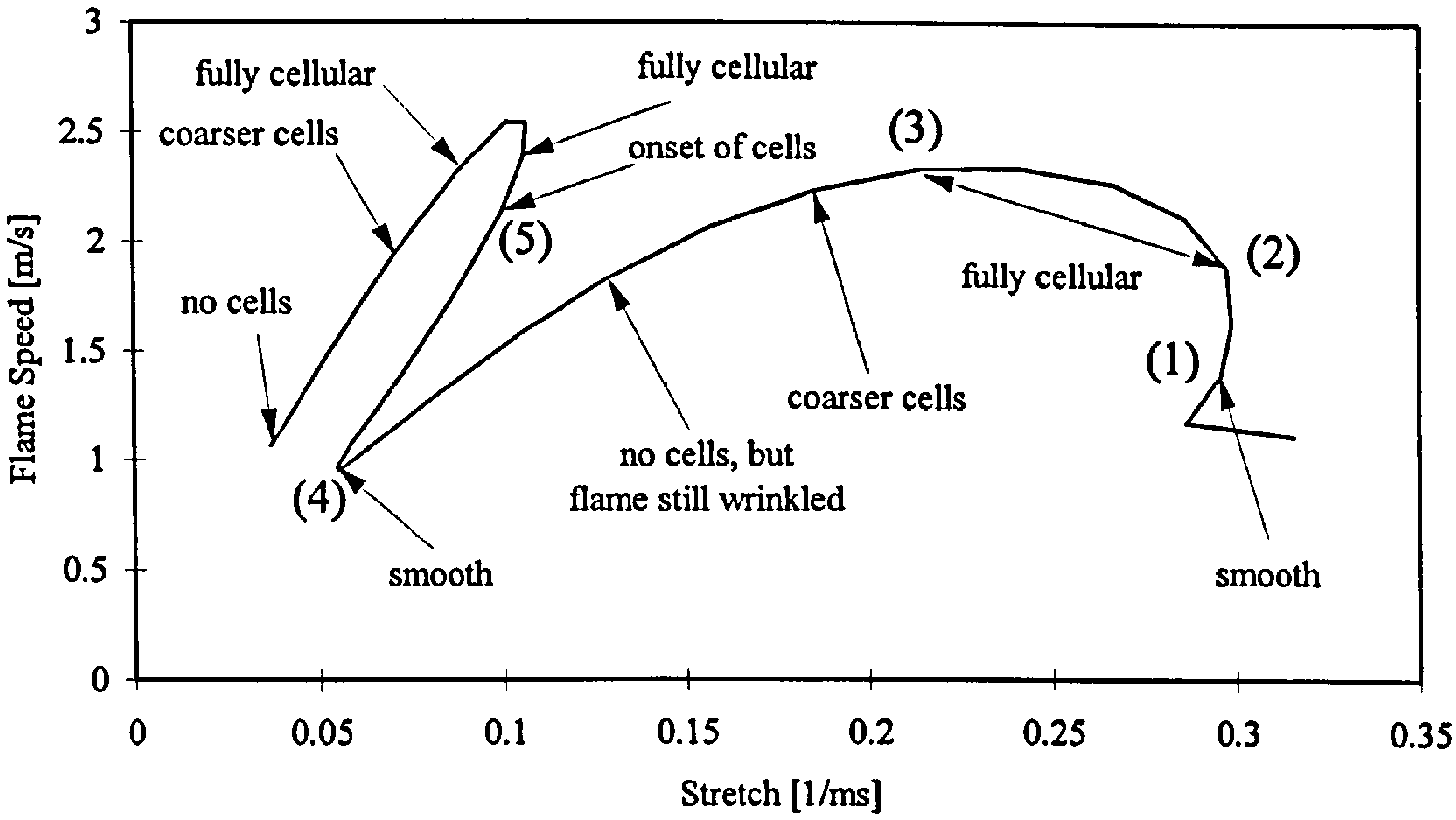

Figure 5.26: *Flame speed against stretch for an oscillating iso-octane-air aerosol at* $\phi_{ov}=1.0$, $\phi_g=0.75$, $D_{32}=20\mu m$, $p=108kPa$, $T=265K$; *Also shown are changes in surface structure during flame propagation.*

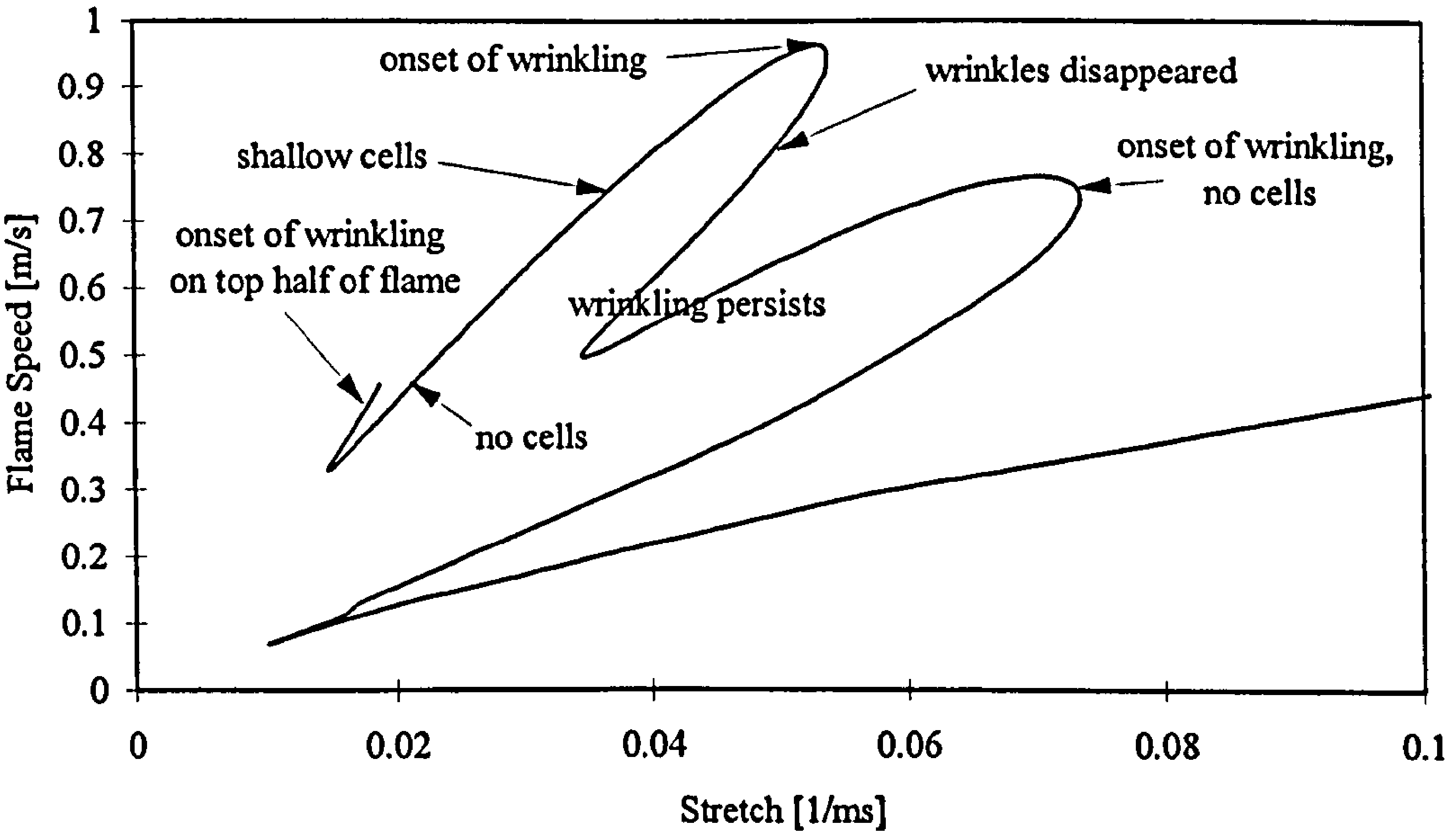

Figure5.27: *Flame speed against stretch for an oscillating iso-octane-air aerosol at* $\phi_{ov}=0.8$, $\phi_g=0.66$, $D_{32}=17\mu m$, $p=108kPa$, $T=263K$; *Also shown are changes in surface structure during flame propagation.*

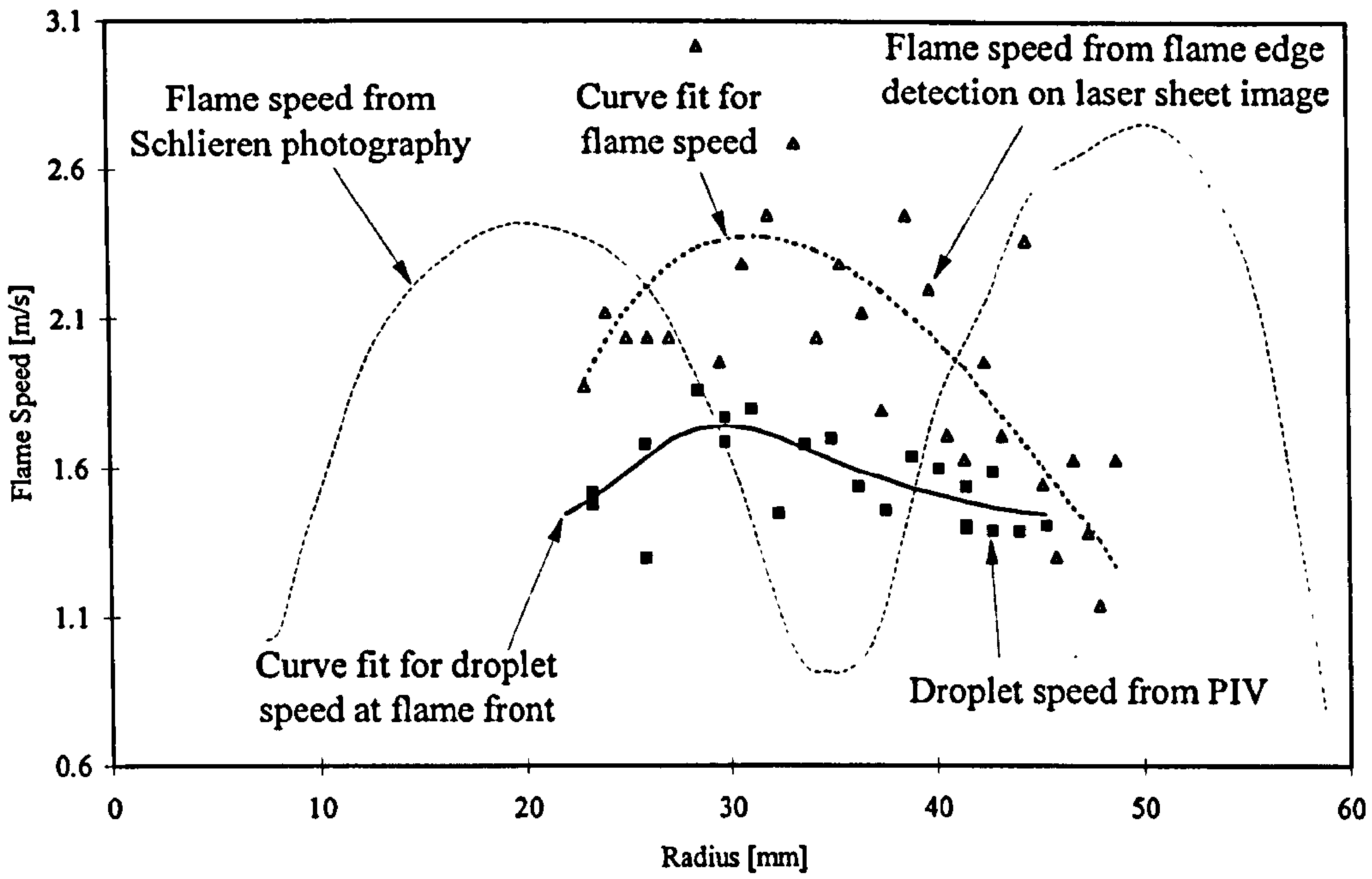

Figure 5.28: *Flame speed and droplet speed against radius for an oscillating iso-octane-air aerosol,* $\phi_{ov}=1.0, \phi_g=0.75, D_{32}=20\mu m, T=265K, p=108kPa$.

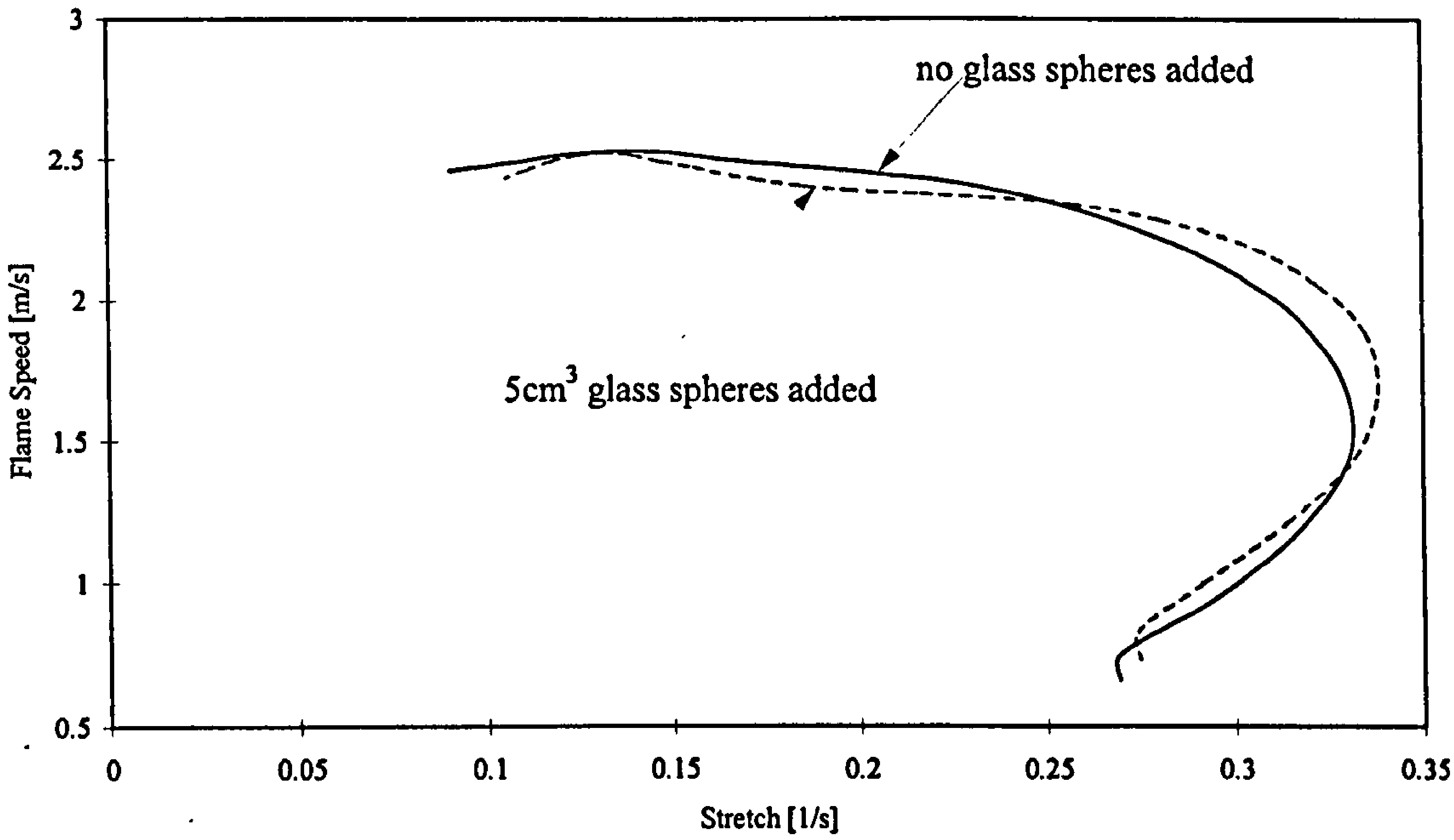

Figure 5.29: *Flame speed against stretch for laminar gaseous iso-octane-air flames with and without spherical glass beads.*

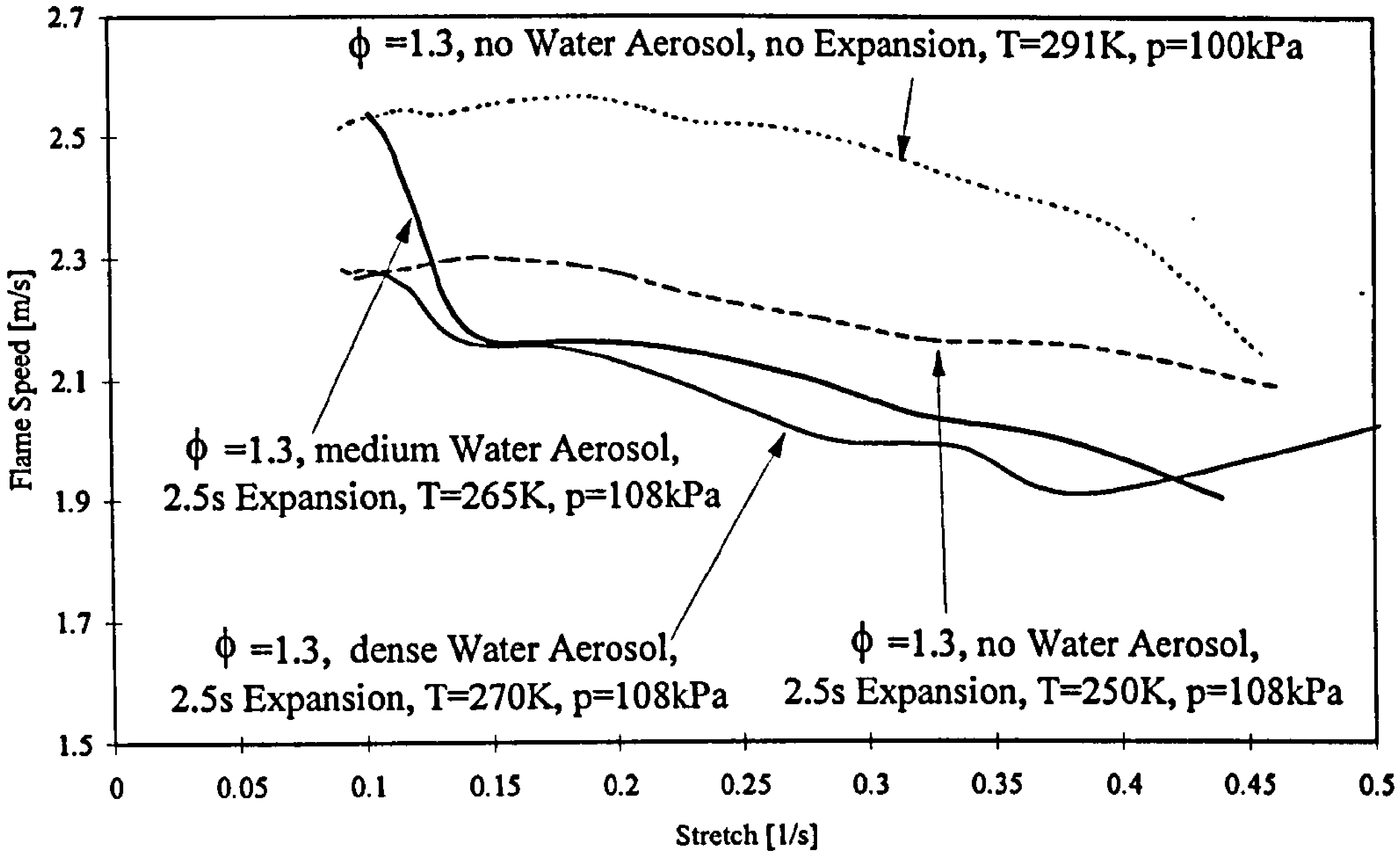

Figure 5.30: *Flame speed against stretch for laminar gaseous propane-air flames with and without water aerosols.*

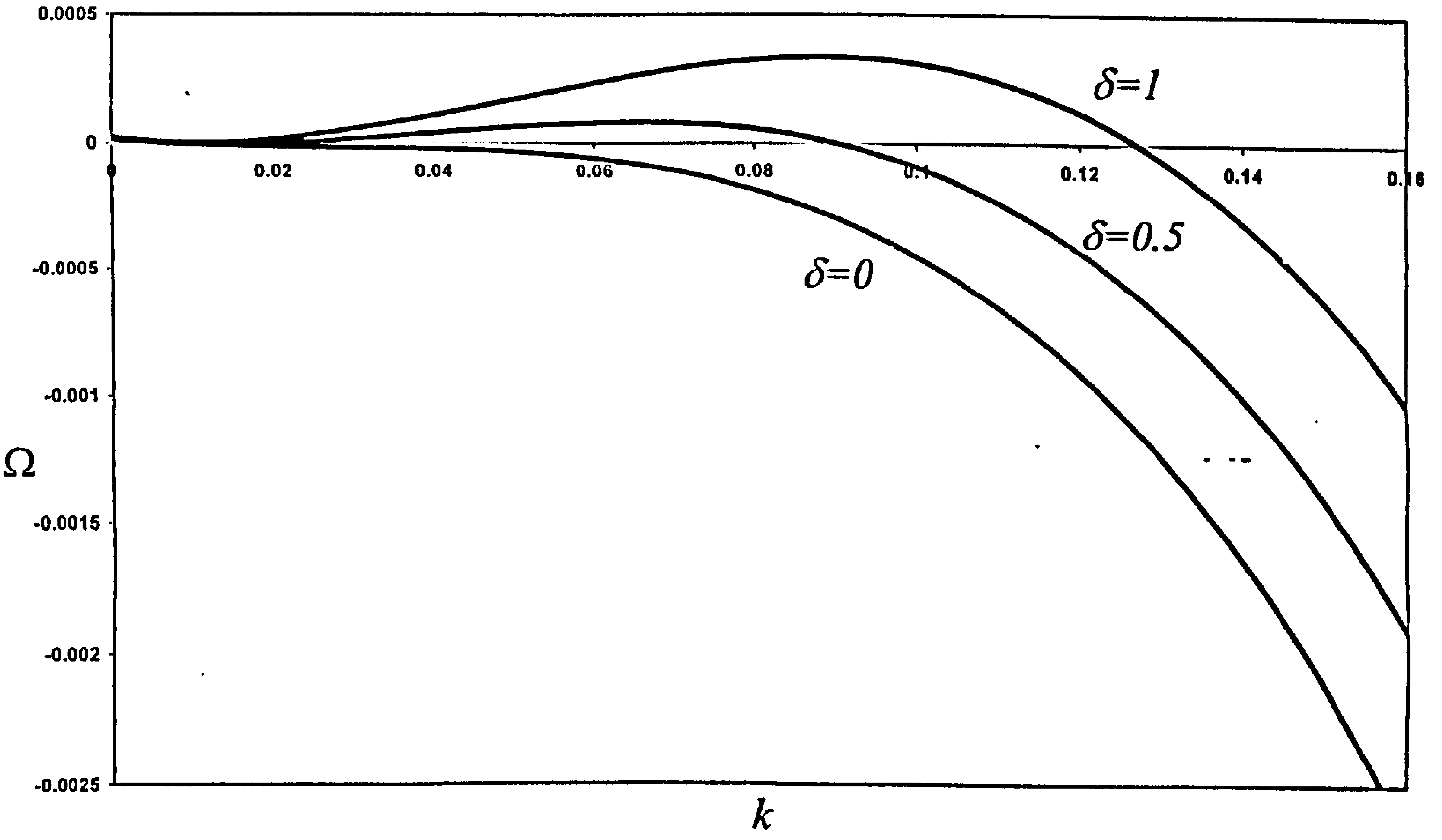

Figure 5.31: *Growth parameter Ω against perturbation wave number k (from Greenberg et al., 1998 & in prep.).*

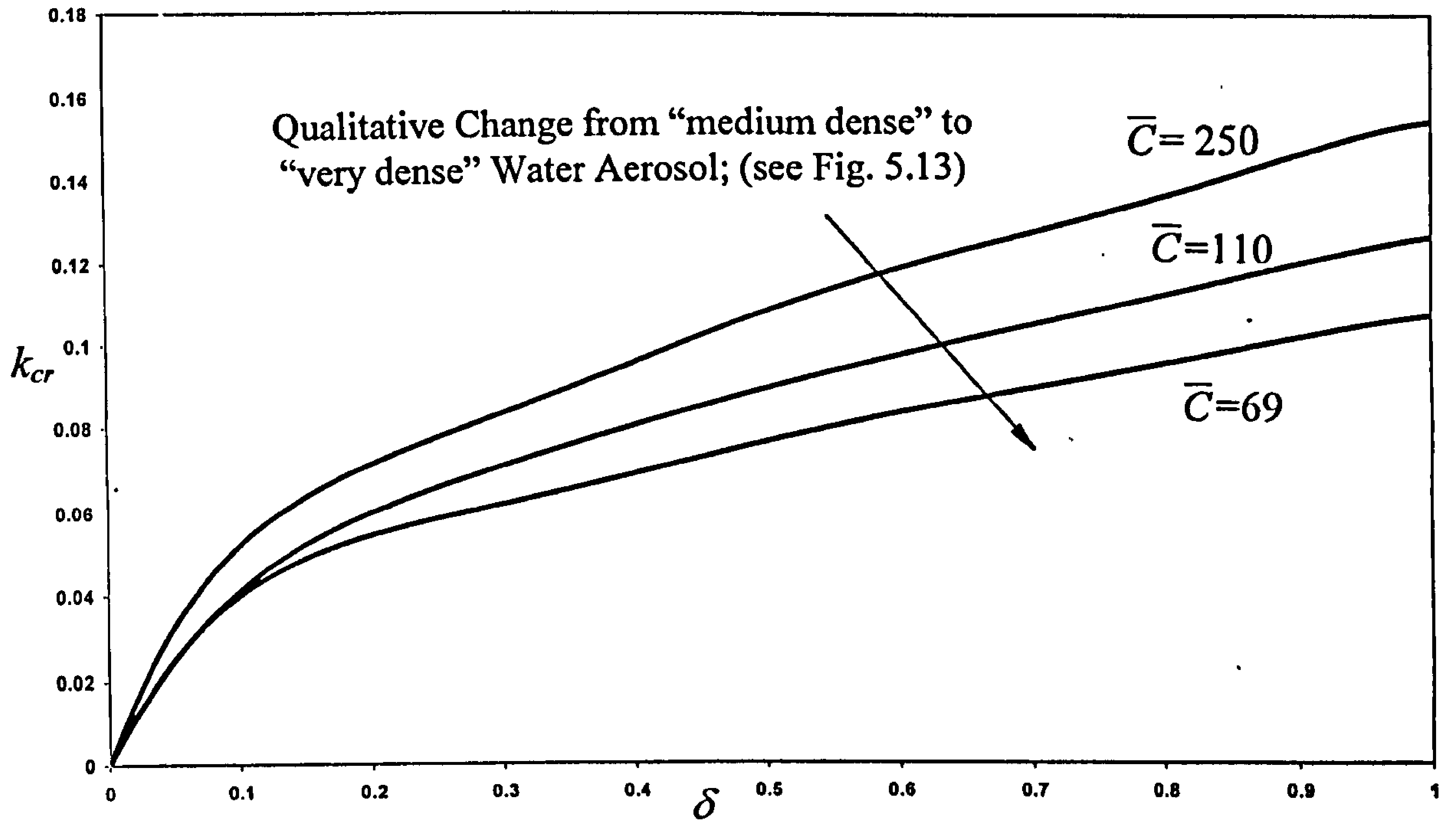

Figure 5.32: *Critical wave number k_{cr} against drop loading δ (from Greenberg et al., 1998 & in prep.).*

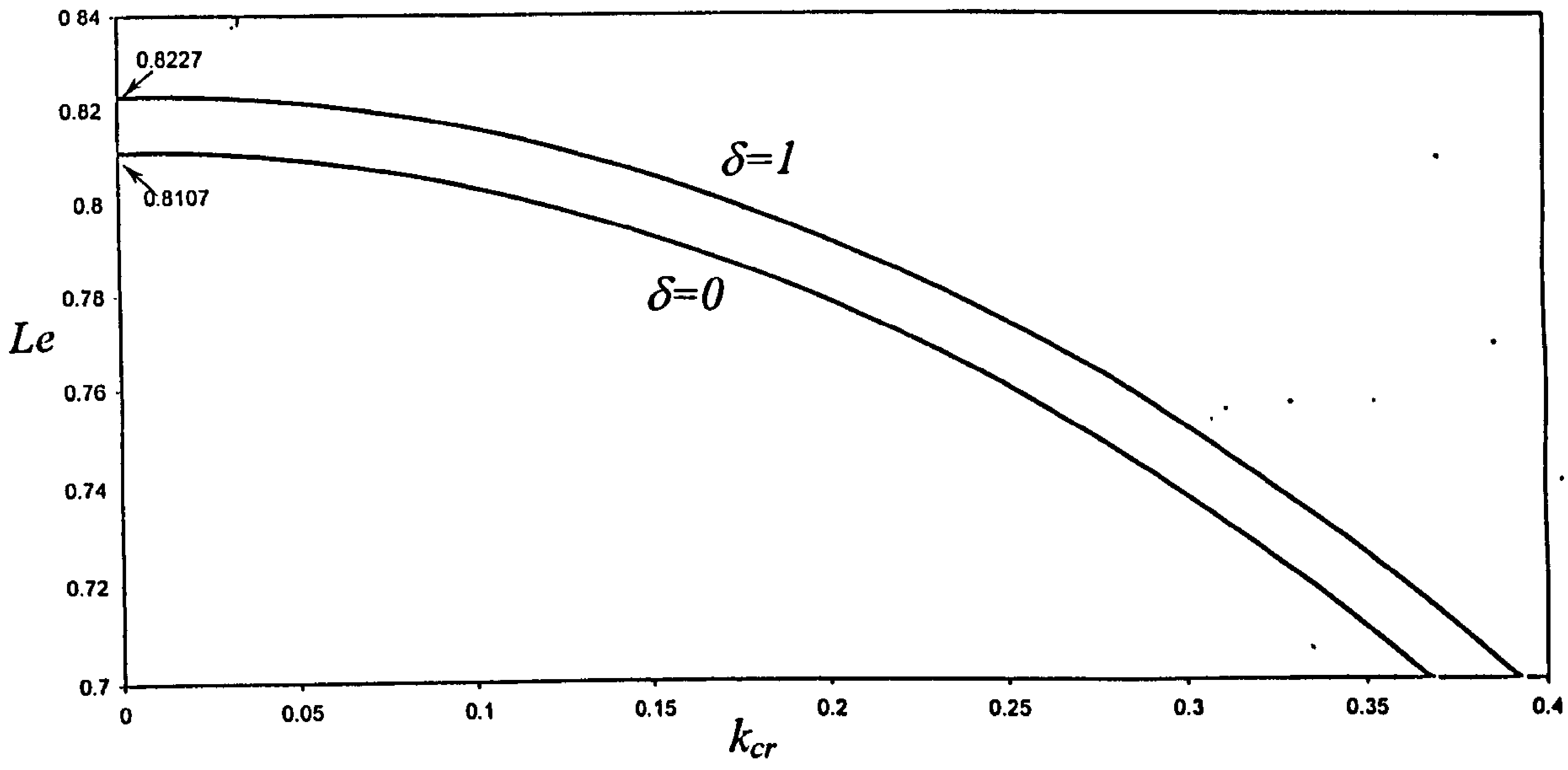

Figure 5.33: *Lewis number against Critical wave number k_{cr} (from Greenberg et al., 1998 & in prep.).*

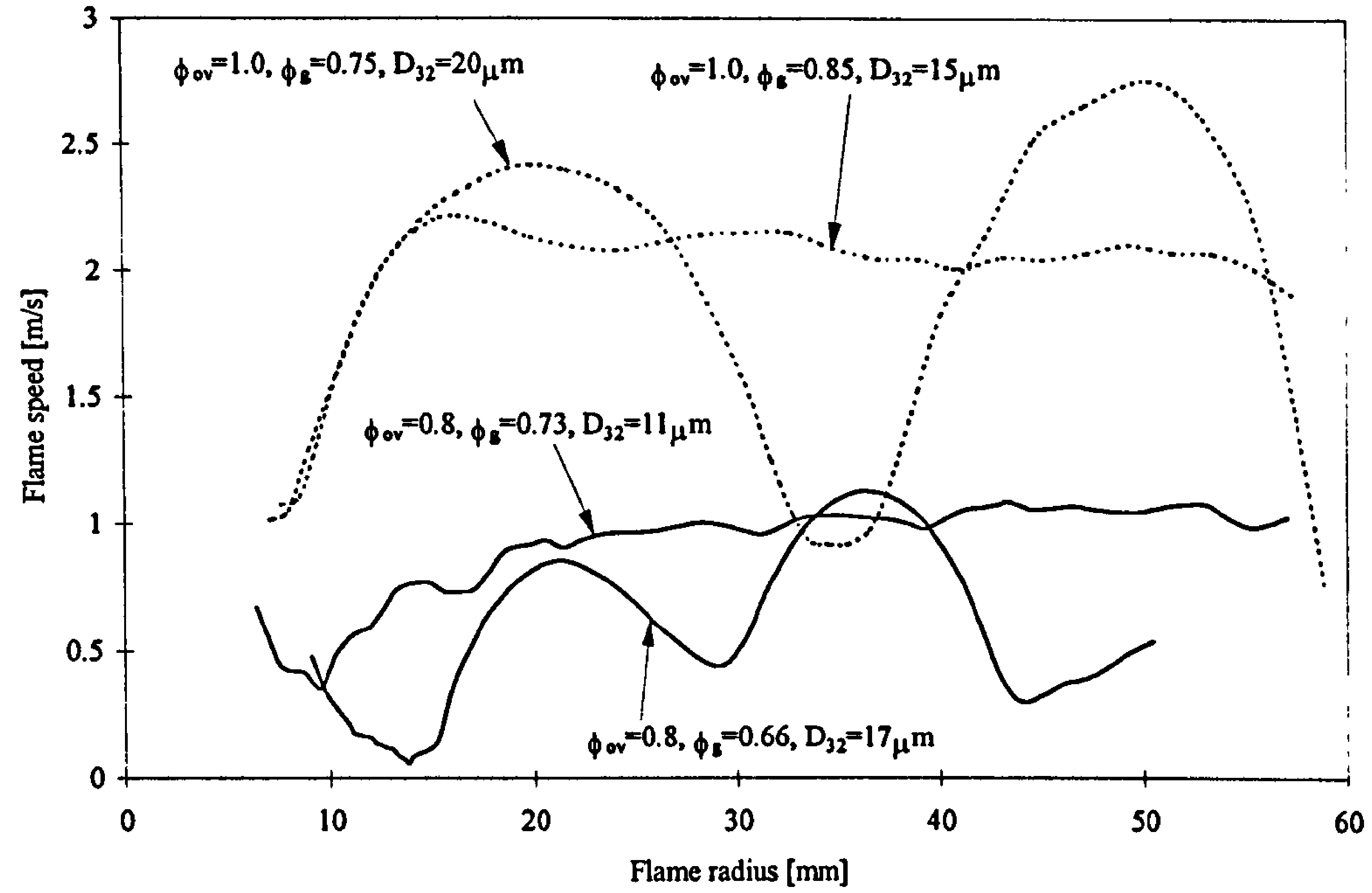

Figure 5.34: *Experimental curves showing the effect of gaseous equivalence ratio on flame speed oscillations in iso-octane-air aerosol flames at $\phi_{ov}=1.0$ & 0.8.*

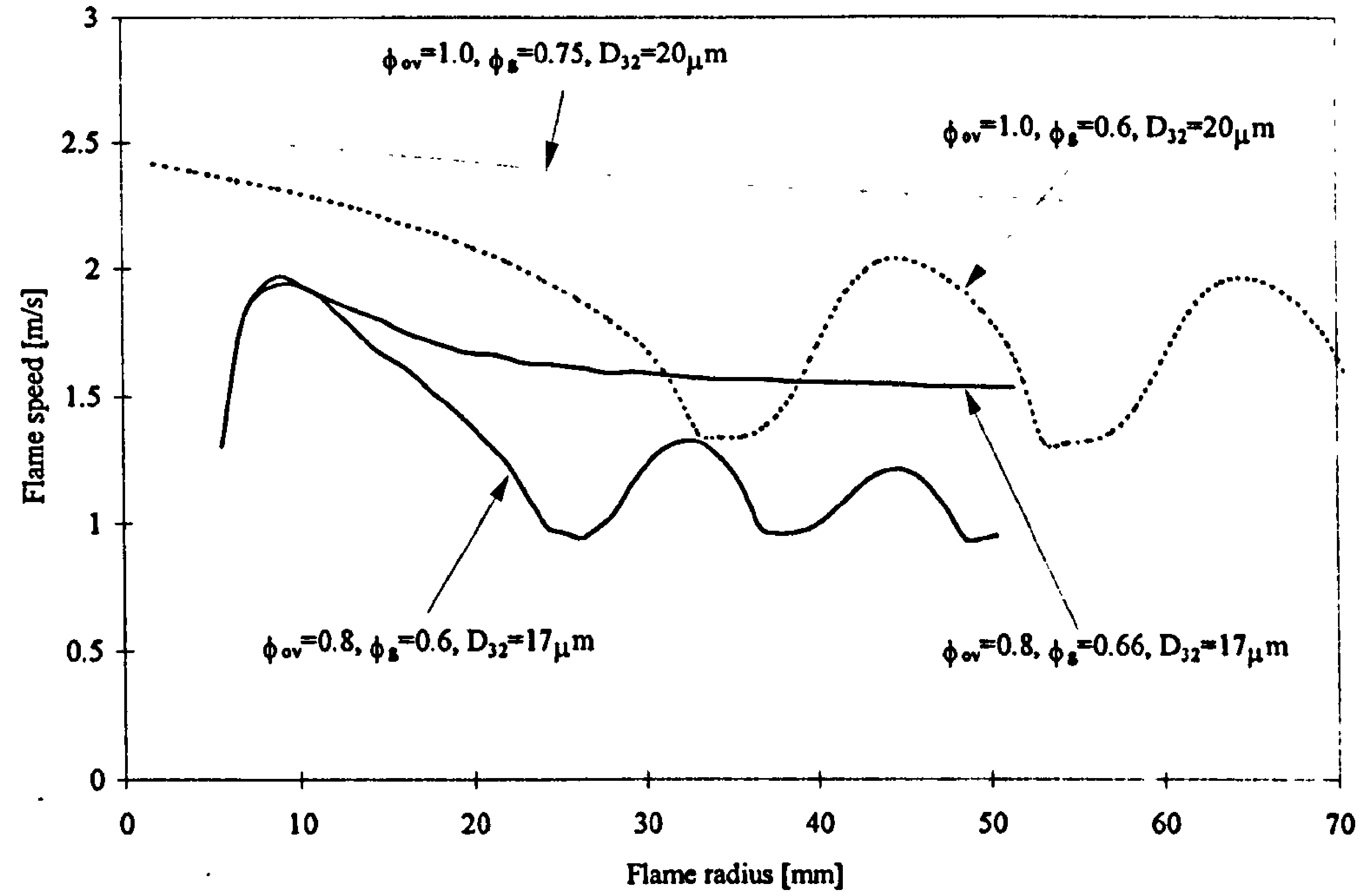

Figure 5.35: *Calculated curves showing the effect of gaseous equivalence ratio on flame speed oscillations in iso-octane-air aerosol flames at $\phi_{ov}=1.0$ & 0.8.*

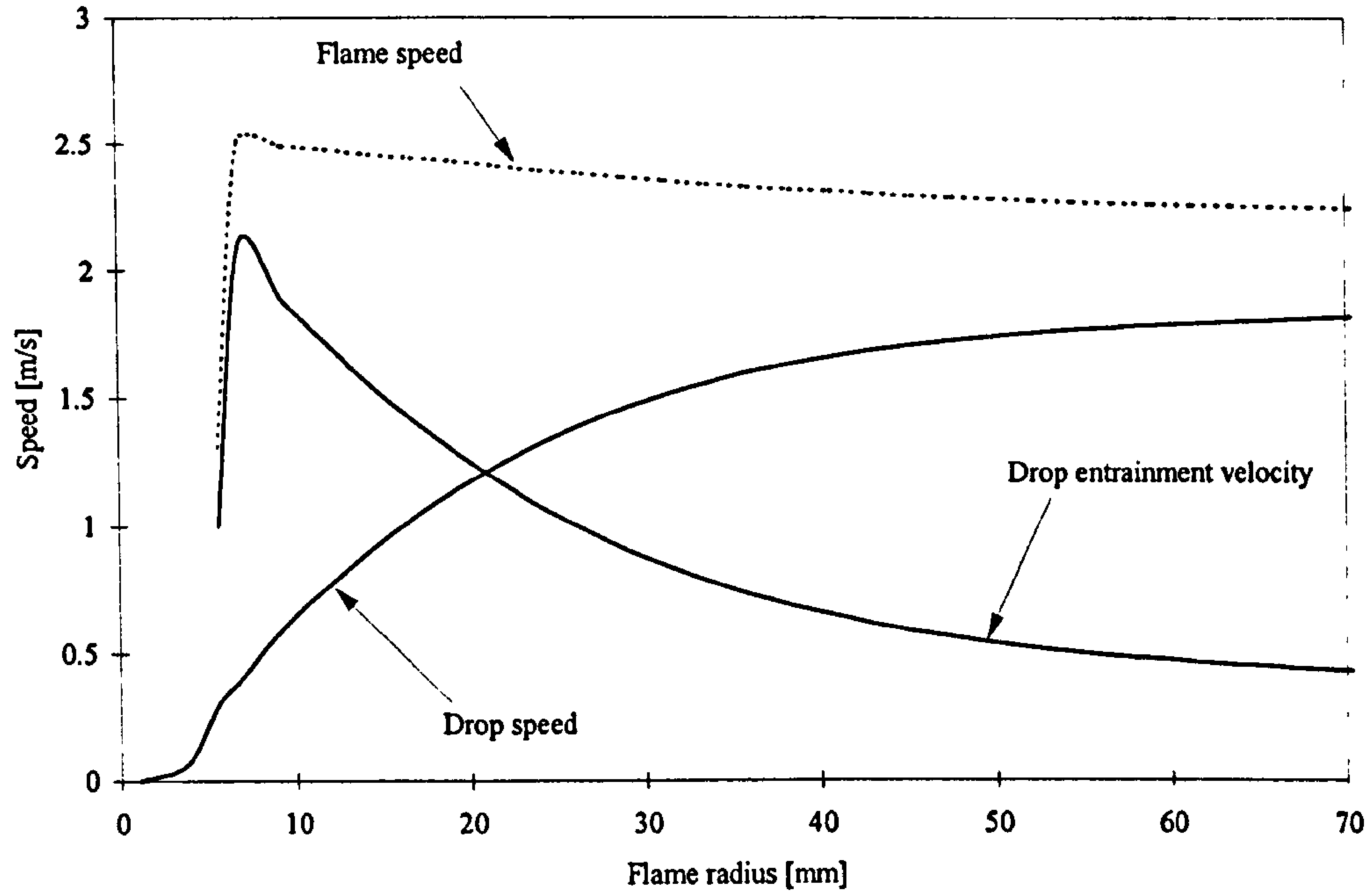

Figure 5.36: *Calculated droplet speed, flame speed and droplet entrainment velocity against radius for a non-oscillating flame at* $\phi_{ov}=1.0, \phi_g=0.75, D_{32}=20\mu m$.

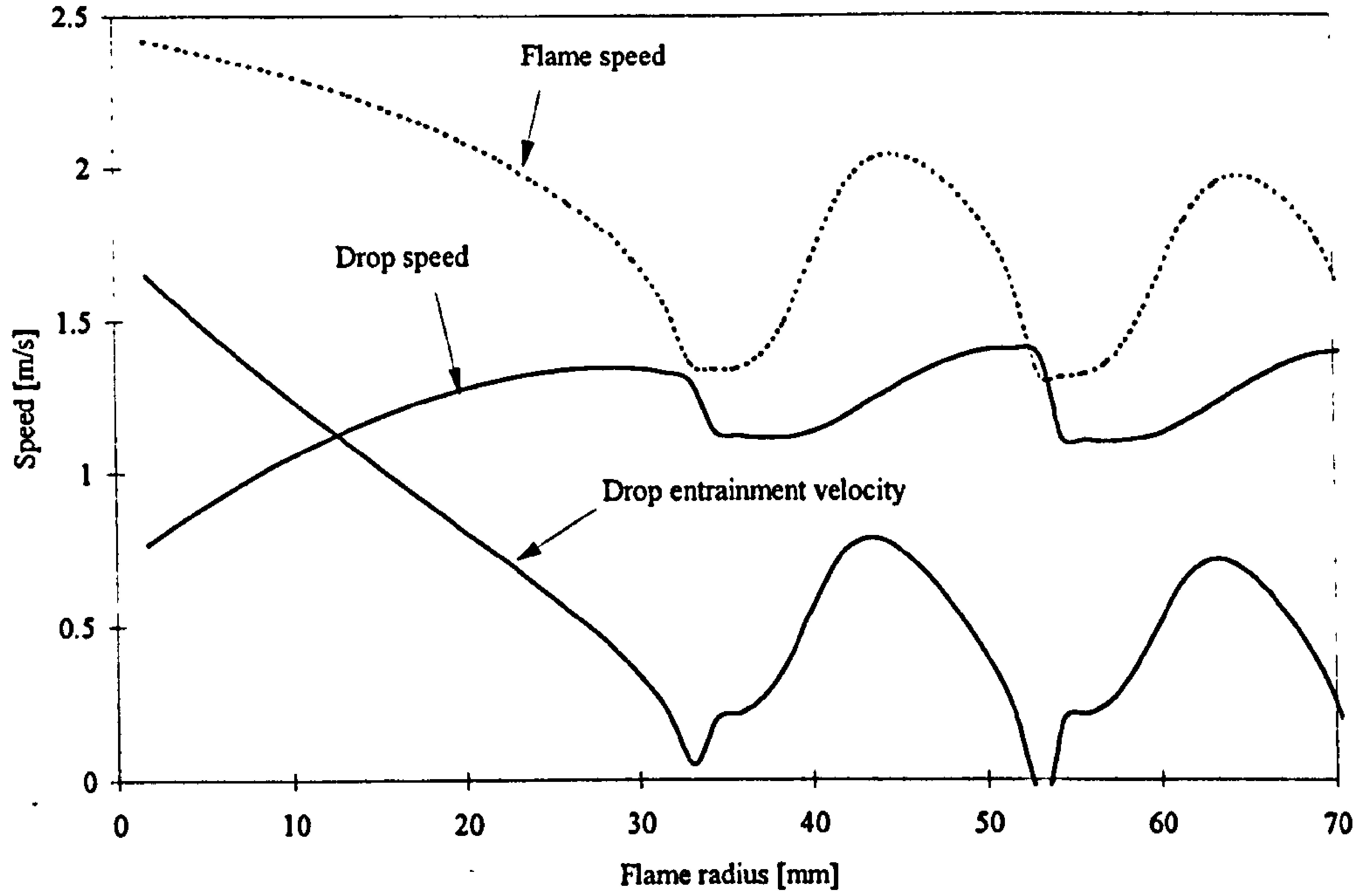

Figure 5.37: *Calculated droplet speed, flame speed and droplet entrainment velocity against radius for an oscillating flame at* $\phi_{ov}=1.0$, $\phi_g=0.6$, $D_{32}=20\mu m$.

6. CONCLUSIONS AND FUTURE WORK

The present thesis comprises a fundamental study of spherical premixed aerosol flames. A novel combustion apparatus has been developed, based on the Wilson cloud chamber principle, that allows the observation of flame propagation in aerosols under both laminar and turbulent conditions. In this apparatus, aerosols have been generated by condensation, which was caused by expansion-cooling of an initially gaseous charge. The effects of changes in overall, gaseous and liquid equivalence ratios, drop size, mixture temperature and pressure on flame propagation have been investigated. Schlieren cine photography and planar laser sheet imaging have been employed to study mainly laminar, but also turbulent flame propagation in iso-octane-air aerosols. The flame photographs, obtained with these techniques, have been used to study changes in flame surface structure due to the presence of droplets, for a wide variety of aerosol mixtures. These photographs also were used to derive aerosol flame speeds and burning velocities, which were compared with the wide range of data available for the gaseous combustion of iso-octane mixtures. The effect of stretch on flame propagation and on the development of flame instabilities was analysed, using the same technique that was hitherto employed for the investigation of stretch in gaseous flames.

A number of additional experiments have been conducted to examine potential causes for flame instability in aerosol mixtures. These include the combustion of mixtures containing inert spherical glass particles and water aerosols.

The experimental results of the present work have been compared to a mathematical analysis of instabilities in aerosol flames, and good qualitative agreement was found.

For some experimental conditions strong flame oscillations were observed and possible causes for this phenomenon were examined with a simple aerodynamic model.

The main conclusions that are drawn from the present work are itemised below.

6.1 CONCLUSIONS

- A number of fundamental studies previously have been conducted in the field of aerosol combustion research. These have revealed important details about the combustion behaviour of aerosol mixtures. However, due to the inherent complexity of aerosol experiments, the results were often apparatus specific and quantitatively of limited general utility.
- A novel combustion apparatus was developed by the present author for the combustion of aerosols in a well controlled environment with respect to aerosol properties, temperature,

pressure and turbulence. Aerosols were generated using the Wilson cloud chamber principle. This method uses the cooling of a fuel-air mixture by expansion to cause the condensation of a part of the initially evaporated fuel into a fog of droplets. Unlike aerosols produced by injection systems, these droplet clouds were homogeneously distributed in space, the droplets were of nearly equal size and the level of turbulence in the combustion chamber, by mixture preparation, was negligible.

- Aerosols were characterised experimentally and theoretically for a range of mixture pressures, temperatures and overall equivalence ratios. The gaseous and liquid fractions of fuel in the mixture and the drop size were the main variables. Although these parameters were not independent of each other, the expansion method offered some flexibility through the use of different pre-expansion pressures, temperatures and equivalence ratios.
- The aerosol combustion studies were based on the investigation of spherically expanding explosions. This experimental method, and its theoretical descriptions, are well established for gaseous combustion and were, for the first time, employed for aerosol studies. A wide range of experimental results for gaseous iso-octane-air flames was available for comparison with the results of the present work.
- Aerosols were combusted at drop sizes of 10 to 30 μm, at pressures between 200 and 100kPa and temperatures of 278 to 263K. A considerable enhancement of the burning velocity of up to 150% was observed for the overall equivalence ratios 1.0 and 1.2 as function of drop size and liquid fraction. Generally, increasing drop size and liquid fraction caused an increase in burning velocity.
- Insufficient data was available for ϕ_{ov}=0.8 and further work is required.
- Droplet enhancement is probably caused by the increase in surface area due to the evolution of instabilities
- The effect of stretch may be important in the suppression of instabilities in aerosol flames. However, this needs further investigation.
- Oscillating flames were observed for temperatures below 268K for the overall equivalence ratios of 0.8 and 1.0 at drop sizes of 15 to 20 μm. These experiments did not allow for the derivation of a burning velocity. However, enhanced flame speeds clearly were observed.
- The phenomenon of flame oscillation was investigated using a simple aerodynamic model. It was assumed that the flame is periodically starved and fed with liquid fuel by a relative movement of the drops and the flame front, which is caused by the acceleration and deceleration of drops, due to the gas motion ahead of the flame front. Although this model offers an explanation for this effect, there are important influences which have been

neglected. Radiative heat transfer from burning droplets also was suggested (Greenberg et al, 1999, Hanai et al., 1998) as a possible cause in the onset of oscillations. Oscillations of this amplitude, hitherto, have not been observed in spherical flames and need further investigation.

- To investigate the effect of temperature, a small number of experiments were conducted at approximately 290K. This dictated an increase in initial mixture pressure to approximately 350kPa, at which gaseous flames of same overall equivalence ratio also become cellular. However, a considerably more rapid cellular acceleration was observed, than is experienced by gaseous flames at the same conditions. Indeed, the flame structure was more representative of gaseous flames at the higher pressure of 500kPa.
- The surface of aerosol flames at elevated temperatures (290K) resembled much more that of gaseous cellular explosions than that observed in aerosol experiments conducted at lower temperatures. At low temperature (<275K) the formation and destruction of wrinkles and cells appeared to be random. However, at higher temperatures the pattern of cell formation and division was progressive and traceable.
- The hydrodynamic effect of a cloud of droplets on the flame was investigated using inert glass particles. These had a similar density to liquid iso-octane and a particle size close to that of the aerosols investigated. The particles did not cause flame wrinkling or cellularity and the value of flame speed was similar to that of a mixture without glass particles.
- The effect of drop evaporation on the flame was isolated from that of heat release from burning droplets, by using a water aerosol. This was generated using the same method as for the fuel aerosol. Mixtures containing water aerosol burned considerably faster (50%) than purely gaseous mixtures. This contradicts the hypothesis that fuel rich pockets might trigger instabilities in aerosols. These flames had a very similar cell-like surface to that of gaseous cellular ones. Also, the process of cell division was traceable throughout the growth of the flame.
- An increase in the number density and size of droplets causes an increase in flame speed. However, when either number density or drop size are increased beyond a critical threshold, flame speed decreases. This implies, that there is an optimum amount of aerosol that will produce the highest burning velocity in a given aerosol. In the present work, this was observed for overall fuel rich iso-octane aerosols and in the experiments using water aerosols. Insufficient data were obtained to confirm this effect for lean mixtures. However, it has been observed by previous workers (e.g. Mizutani, 1973) also for overall lean fuel aerosols.

- Experimental data of the present work were compared with a linear stability analysis (Greenberg et al., 1998, 1999, to be published), in which the heat loss from the flame, due to drop evaporation, is assumed to be the primary cause of instabilities in aerosol flames. Good qualitative agreement between the results of the present work and the predictions of the model was found.

6.2 RECOMMENDATIONS FOR FURTHER WORK

- For a precise quantification of burning velocity enhancement, it is necessary to investigate a wide range of experimental conditions. It would be desirable to extend the values of overall equivalence ratios to cover the range between 0.6 and 1.4. Also, an increase in mixture temperature and pressure is required to examine aerosol combustion at conditions closer to those pertaining in engines. A wider range of experimental conditions is also essential to further investigate the effect of flame stretch in aerosol flames.
- A gaseous baseline for all measured equivalence ratios between 0.6 and 1.4 at temperatures close to mixture saturation is needed, to quantify burning velocity enhancement.
- In order to further investigate the burning velocity enhancement at lean conditions it is recommended that mixtures be expanded from a higher pressure and temperature of 300kPa and 313K, preferably at an overall equivalence ratio of 0.8, to extend the present results. The semi-empirical condensation model, presented by the present author (Chapter 4) should be used to determine favourable conditions for early onset of condensation and, hence, appropriate drop sizes (20-30 μm) at ignition.
- In the present work, the amount of water used in the water aerosol experiments was not controlled as precisely as one would like. Therefore, a method of precisely measuring and vaporising water in the bomb is needed. Also, accurate characterisation of such aerosols is required to further investigate the effect of water aerosol on combustion.
- The generation of aerosols at higher temperatures, e.g. 330K, with the current method is possible, if the pre-expansion pressure is high enough. Since the maximum safe operating pressure of the current vessel is only 300kPa at ignition, the use of the "new" Leeds bomb is recommended. An inexpensive modification of the present exhaust system, without changes to the bomb itself and without the need for an expansion tank, is adequate for this purpose. With the range of pre-expansion pressures increased to 1500kPa a wide variety of conditions can be covered.

- It would be desirable to use drop sizing instrumentation, e.g. PDA or laser diffraction, simultaneously with the flame photography in combustion experiments to facilitate a more accurate determination of the drop size and liquid fraction at ignition. Because the laser diffraction averages across the measurement volume it appears to be the favourable method. Two new laser diffraction instruments suitable for laser obscuration up to 95% and a long optical path length are available (Malvern Instruments Ltd. and Sympatec GmbH).
- In order to reveal the nature of the cell-like structure, observed in the present study, laser induced fluorescence LIF appears to be a promising analytic tool. In combination with schlieren photography this would also allow for the determination of the position of the flame front with respect to the evaporation zone.
- The transition from a random manner of cell formation and destruction at low temperatures (<275K) to a progressive and traceable pattern of cell division at elevated temperature (>290K) needs to be examined. This transformation may mean, that aerosols and gaseous mixtures are more similar in their combustion behaviour, at higher temperature, than hitherto assumed.
- Aerosols flames have a finer cellular structure than gaseous flames at the same pressure. Experiments at high pressures (>1MPa) should reveal, whether this trend also pertains at very high pressures and, hence, flame propagation is promoted at these high pressures.
- The decrease in burning velocity at temperature close to saturation has, to the authors knowledge, not been observed previously. It might be due to a change in diffusivity of the fuel and an investigation into this phenomenon is required.
- First experiments in the combustion of turbulent aerosols have been performed in the present work. The apparatus is well suited for these studies, since turbulence is precisely controlled. The interaction between aerosol induced flame instability and turbulent flame wrinkling may have important implications for gas turbine and engine combustion, particularly with reference to direct injected engines (DI-Diesel, GDI). A fundamental study of turbulent aerosol combustion is required.
- The linear stability analysis of Greenberg et al., (1998, 1999 & to be published) is qualitatively in good agreement with the data of the present work. A non-linear analysis could possibly predict cell size and amplitude, thus providing a measure for the increase in surface area due to the presence of an aerosol. This could be possibly facilitate the prediction of (enhanced) aerosol burning rates.

- The phenomenon of flame oscillations needs further investigation. The current model should be extended to include the effects of burning velocity enhancement and stretch, and possibly radiation.
- The Leeds burning velocity correlation (Bradley et al., 1992) should be extended to include aerosol burning velocities and appropriate dimensionless groups should be identified.
- First successful tests of laser ignition in dense aerosol clouds have been performed by the present author. These trials should be extended to explore the use of such systems in aviation gas turbines (Ronney, 1994) and, possibly, reciprocating engines.

Abdel-Gayed R.G., Al-Kishali K.J. & Bradley D., TURBULENT BURNING VELOCITIES AND FLAME STRAINING IN EXPLOSIONS, Proc. Roy. Soc. London, A 391, pp. 393-414, 1984

Abdel-Gayed R.G., Bradley D. & Lawes M., TURBULENT BURNING VELOCITIES: A GENERAL CORRELATION IN TERMS OF STRAINING RATES, Proc. Roy. Soc. London, A414, pp. 389-413, 1987.

Aggarwal S.K. & Sirignano W.A., UNSTEADY SPRAY FLAME PROPAGATION IN A CLOSED VOLUME, Combustion and Flame, Vol. 62, pp. 69-84, 1985

Akamatsu F., Mizutani Y., Katsuki M., Tsushima S. & Yong D.C., MEASUREMENT OF THE LOCAL GROUP COMBUSTION NUMBER OF DROPLET CLUSTERS IN A PREMIXED-SPRAY STREAM, 26th Symposium (International) on Combustion, pp. 1723-1729, 1996

Akamatsu F., Mizutani Y., Katsuki M., Tsushima S., Yong D.C. & Nakabe K., GROUP COMBUSTION BEHAVIOUR OF DROPLETS IN A PREMIXED-SPRAY FLAME, Atomization & Sprays, Vol. 7, pp. 199-218, 1997

Ali Y., Bradley D., Lawes M. & Mushi E.M.J., PROBLEMS OF THE MEASUREMENT OF MARKSTEIN LENGTHS WITH EXPLOSION FLAMES, The Combustion Institute, Proc. British and German sections, Queen's College Cambridge, 1993

Amelin A.G., THEORY OF FOG CONDENSATION, Israel Program for Scientific Translations, Ed. B.V. Deryagin, Jerusalem, 1967

Andrews G.E. & Bradley D., DETERMINATION OF BURNING VELOCITIES, A CRITICAL REVIEW, Combustion and Flame, Vol. 18, pp. 133-153, 1972

Andrews G.E., LAMINAR AND TURBULENT FLAME PROPAGATION, PhD-Thesis, Dept. of Mech. Eng., University of Leeds, 1972

Annamalai K. & Ryan W., INTERACTIVE PROCESSES IN GASIFICATION AND COMBUSTION, PART I: LIQUID DROP ARRAYS AND CLOUDS, Progress in Energy and Combustion Science, Vol. 18, No.3, pp. 221-295, 1992

Arold M.L., Espey C., Litzinger T.A., Santavicca D.A. & Santoro R.J., STUDY OF NON-SWIRLING AND SWIRLING AND THEIR EFFECTS ON SPRAY FLOW FIELDS AND COMBUSTION IN AN OPTICALLY-ACCESSIBLE DI-DIESEL ENGINE, SAE Transactions, Vol. 99, No. 3, pp. 916-928, 1990

Ashgriz N. & Yao S.C., MECHANISM OF FLAME PROPAGATION IN SPRAYS, Chemical and Physical Processes in Combustion (Combustion Inst.), Vol. 4, pp. 1-70, 1984

Ashurst W.T., DARRIEUS-LANDAU INSTABILITY, GROWING CYCLOIDS AND EXPANDING FLAME ACCELERATION, Combust. Theory Modelling 1, pp. 405-428, 1997

Aslanov S., Kopyt N. & Struchaev A., FLAME PROPAGATION IN A PREMIXED TURBULENT HEAVY HYDROCARBON VAPOUR-DROP SYSTEM, J. Aerosol Sci., Vol. 22, Suppl. 1, pp. 485-488, 1991

Atashkari K., EXPERIMENTAL STUDY OF FLOW AND TURBULENCE IN A V-FLAME BURNER AND A S.I. ENGINE, PhD Thesis, Dept. of Mech. Eng., University of Leeds, 1997

Ballal D.R. & Lefebvre A.H., FLAME PROPAGATION IN HETEROGENEOUS MIXTURES OF FUEL DROPLETS, FUEL VAPOR AND AIR, 18th Symposium (International) on Combustion, pp. 321-328, 1980

Bourgoyne J.H. & Cohen L., THE EFFECT OF DROP SIZE ON FLAME PROPAGATION IN LIQUID AEROSOLS, Proc. Roy. Soc. London, A225, pp. 375, 1954

Bradley D., INSTABILITIES AND FLAME SPEED IN LARGE SCALE PREMIXED GASEOUS EXPLOSIONS, in preparation

Bradley D., Hicks R.A., Lawes M. Sheppard C.G.W. & Woolley R., THE MEASUREMENT OF LAMINAR BURNING VELOCITIES AND MARKSTEIN NUMBERS FOR ISO-OCTANE-AIR AND ISO-OCTANE-N-HEPTANE-AIR MIXTURES AT ELEVATED TEMPERATURES AND PRESSURES IN AN EXPLOSION BOMB, Combustion and Flame, Vol. 101, pp. 126-144, 1998

Bradley D., Gaskell P.H. & Gu X.J., BURNING VELOCITIES, MARKSTEIN LENGTHS, AND FLAME QUENCHING FOR SPHERICAL METHANE-AIR FLAMES: A COMPUTATIONAL STUDY, Combustion & Flame, Vol. 104, pp. 176-198, 1996

Bradley D., Lawes M., Scott M.J,, Sheppard C.G.W., Woolley R., Greenhalgh D., Lockett R.D., Kailasanath K., Oran E.S. & Patnaik G., THE CRACKING OF LAMINAR FLAMES, 26th Symposium (International) on Combustion, WIP-Poster, 1996b

Bradley D., Lawes M., Sheppard C.G.W. & Woolley R., FINAL REPORT JOU2-CT92-0081, ENGINE AND FUEL INTERACTIONS IN GASOLINE ENGINES, Commission of the EU, 1995

Bradley D. & Harper C.M., THE DEVELOPMENT OF INSTABILITIES IN LAMINAR EXPLOSION FLAMES, Combustion and Flame, Vol. 99, pp. 562-572, 1994

Bradley D., Lau A.K.C. & Lawes M., FLAME STRETCH RATE AS A DETERMINANT OF TURBULENT BURNING VELOCITY, Phil. Trans. Roy. Soc. Lond., A338, pp. 359-387, 1992

Bradley, D., in INTERNAL COMBUSTION ENGINEERING: SCIENCE AND TECHNOLOGY, (Ed. J. Weaving), Elsevier Applied Science, pp. 287, 1990

Browning J.A. & Krall W.G., EFFECT OF FUEL DROPLETS ON FLAME STABILITY, FLAME VELOCITY AND INFLAMMABILITY LIMITS, 5th Symposium (International) on Combustion, pp. 159-163, 1954

Brundish K.D., Foster T.J., Gray C.R., Seoud R.E. & Wilson C.D., THE USE OF AXIALLY FUEL STAGED COMBUSTION IN GAS TURBINE COMBUSTORS, Proc. 4th Int. Conf. on Technologies & Combustion for a Clean Environment, Lisbon, Portugal, 1997

Buchave P., PARTICLE IMAGE VELOCIMETRY - STATUS AND TRENDS, Experimental Thermal Fluid Science, Vol. 5, pp. 586-604, 1993

Carey V.P., LIQUID-VAPOR PHASE-CHANGE PHENOMENA, Hemisphere Publishing Corporation, 1992

Cekalin E.K., PROPAGATION OF FLAME IN TURBULENT FLOW OF TWO-PHASE FUEL-AIR MIXTURE, 8th Symposium (International) on Combustion, pp. 1125-1129, 1962

Chiu H.H., Kim H.Y. & Croke E.J., INTERNAL GROUP COMBUSTION OF LIQUID DROPLETS, 19th Symposium (International) on Combustion, pp. 971-980, 1982

Chiu H.H. & Liu T.M., GROUP COMBUSTION OF LIQUID DROPLETS, Comb. Sci. & Tech., Vol. 17, pp. 127-142, 1977

Clavin P., DYNAMIC BEHAVIOUR OF PREMIXED FLAME FRONTS IN LAMINAR AND TURBULENT FLOWS, Prog. Energy Comb. Sci., 11/1, 1985

Clavin P. & Sun J., THEORY OF ACOUSTIC INSTABILITIES OF PLANAR FLAMES PROPAGATING IN SPRAYS OR PARTICLE-LADEN GASES, Comb. Sci. & Tech., Vol. 78, pp. 265-288, 1991

Clanet C., Searby G. & Clavin P., PRIMARY ACOUSTIC INSTABILITY OF FLAMES PROPAGATING IN TUBES: CASES OF SPRAY AND PREMIXED GAS COMBUSTION, J. Fluid Mech., in preparation;

Correa S.M. & Sichel M., GROUP COMBUSTION OF A SPHERICAL CLOUD OF MONODISPERSED DROPLETS, 19th Symposium (International) on Combustion, pp. 981-991, 1982

Darrieus G., PROPAGATION D'UN FRONT DE FLAMME: ESSAI DE THÉORIE DES VITESSES ANOMALES DE DÉFLAGRATION PAR DEVELOPPEMENT SPONTANÉ DE LA TURBULENCE, Presented at the 6th Int. Cong. Appl. Mech., Paris, 1938

Demoulin, F.X., TECHNICAL REPORT T50, Combined Engineering Library, School of Mechanical Engineering, University of Leeds, 1999

Dixon-Lewis, G., STRUCTURE OF LAMINAR FLAMES, 23rd Symposium (International) on Combustion, pp. 305-324, 1990

Dowdy D.R., Smith D.B., Taylor S.C. & Williams A., THE USE OF EXPANDING SPHERICAL FLAMES TO DETERMINE BURNING VELOCITIES AND STRETCH EFFECTS IN HYDROGEN AIR MIXTURES, 23rd Symposium (International) on Combustion, pp 325, 1991,

Drake M., THE FUNDAMENTAL BURNING CHARACTERISTICS OF SPARK IGNITION ENGINE FUELS, PhD-Thesis, School of Mech. Eng., University of Leeds, in preparation

Dugger G.L. & Graab D.D., FLAME VELOCITIES OF HYDROCARBON-OXYGEN-NITROGEN MIXTURES, 4th Symposium (International) on Combustion , pp. 302-310, 1953

Durao D.F.G. & Heitor M.V., MODERN DIAGNOSTIC TECHNIQUES FOR COMBUSTING FLOWS: AN OVERVIEW, Combusting flow diagnostics, Eds. D.F.G. Durao et al., pp. 1-45, Kluwer Academic Publishers, 1990

Edwards C.F., Siebers D.L. & Hoskin D.H., STUDY OF THE AUTOIGNITION PROCESS OF A DIESEL SPRAY VIA HIGH SPEED VISUALIZATION, SAE Paper No. 920058, 1992

EPEFE, Report of the EUROPEAN PROGRAMME ON EMMISSIONS, FUELS AND ENGINE TECHNOLOGIES, compiled by F. Palmer on behalf of ACEA and EUROPIA, 1997

Faeth G.M., SPRAY COMBUSTION PHENOMENA, 26th Symposium (International) on Combustion, pp. 1593-1612, 1996

Faeth G.M., EVAPORATION AND COMBUSTION IN SPRAYS, Prog. Energy Combust. Sci., Vol. 9, pp. 1-76, 1983

Faeth G.M., CURRENT STATUS OF DROPLET AND LIQUID COMBUSTION, Prog. Energy Combust. Sci., Vol. 9, pp. 191-224, 1977

Fuks N.A., DROPLET EVAPORATION AND GROWTH IN A GASEOUS MEDIUM, Izdatel'stvo AN SSSR, 1958

Fujimoto M., Nishida K., Hiroyasu H. & Tabata M., INFLUENCE OF MIXTURE STRATIFICATION PATTERN ON COMBUSTION CHARACTERISTICS IN A CONSTANT-VOLUME COMBUSTION CHAMBER, SAE-Paper 952412, 1995

Gillespie L., IMAGING AND ANALYSIS OF TURBULENT FLAME DEVELOPMENT IN SPARK-IGNITION ENGINES, PhD Thesis, School of Mech. Eng., University of Leeds, 1998

Godsave G.A.E., STUDIES OF THE COMBUSTION OF DROPS IN A FUEL SPRAY - THE BURNING OF SINGLE DROPS OF FUEL, 4th Symposium (International) on Combustion, pp. 818-832, 1952

Greenberg J.B., Brindley J. & McIntosh A.C., INSTABILITY OF A FLAME FRONT PROPAGATING THROUGH A FUEL-RICH DROPLET-VAPOR-AIR CLOUD, 39th Israel Annual Conference on Aerospace Science, 1999

Greenberg J.B., Brindley J. & McIntosh A.C., LINEAR STABILITY ANALYSIS OF LAMINAR FLAME PREMIXED SPRAY FLAMES, in prep.

Greenberg J.B., PERSONAL COMMUNICATIONS, 1999

Greenberg JB, Silverman I. & Tambour Y, ON DROPLET ENHANCEMENT OF THE BURNING VELOCITY OF LAMINAR PREMIXED SPRAY FLAMES, Combustion and Flame, Vol. 113, pp. 271-273, 1998

Greenberg J.B., Silverman I. & Tambour Y., PROPAGATION OF A LAMINAR FLAME THROUGH A POLYDISPERSE SPRAY OF DROPLETS, Combustion and Flame, Vol. 104, pp. 358-368, 1996

Hanai H., Maruta K., Kobayashi H. & Niioka T., PULSATING FLAME PROPAGATION OF PMMA-PARTICLE-CLOUD IN MICROGRAVITY, 27th Symposium (International) on Combustion, 1998

Haq M.Z., FUNDAMENTAL STUDIES OF PREMIXED COMBUSTION, PhD Thesis, School of Mech. Eng., University of Leeds, 1998

Hayashi S., Ohtani T., Iinuma K. & Kumagai S., LIMITING FACTOR OF FLAME PROPAGATION IN LOW-VOLATILITY FUEL CLOUDS, 18th Symposium (International) on Combustion, pp. 361-367, 1981

Hayashi S., Kumagai S. & Sakai T., PROPAGATION VELOCITY AND STRUCTURE OF FLAMES IN DROPLET-VAPOR-AIR MIXTURES, Combustion Science & Technology, Vol. 15, pp. 169-177, 1976

Hayashi S. & Kumagai S., FLAME PROPAGATION IN FUEL DROPLET-VAPOR-AIR MIXTURES, 15th Symposium (International) on Combustion, pp. 445-452, 1975

Heywood J.B., COMBUSTION ENGINE FUNDAMENTALS, McGraw Hill ,1983

Hodkinson J.R., Applied Optics Vol. 5, pp. 839-844, (1966)

Hundy G.F., FLAME PROPAGATION IN A CLOSED VESSEL, PhD-Thesis, Dept. of Mech. Eng., University of Leeds, 1969

James E. H., LAMINAR BURNING VELOCITIES OF ISO-OCTANE-AIR MIXTURE - A LITERATURE REVIEW, SAE Paper 870170, 1987

Jones A.R., INSTRUMENTATION FOR FLOWS WITH COMBUSTION, Ed. A.M.K.P. Taylor, Academic Press, London, 1993

Koshland C.P. & Bowman C.T., COMBUSTION OF MONODISPERSE DROPLET CLOUDS IN A REACTIVE ENVIRONMENT, 20th Symposium (International) on Combustion, pp. 1799-1807, 1984

Kuehl D.K., LAMINAR BURNING VELOCITIES OF PROPANE-AIR MIXTURE, 8th Symposium (International) on Combustion, pp. 510-521, 1962

Labowski M. & Rosner D.E., "GROUP" COMBUSTION OF DROPLETS IN FUEL CLOUDS, 1. QUASI-STEADY PREDICTIONS, Evaporation-Combustion of Fuels, American Chemical Society, Ed. J.T.Zung, Vol. 166, pp. 63-79, 1978

Landau L.D., ON THE THEORY OF SLOW COMBUSTION, Acta Physicochem, 1944

Lauterborn W. & Vogel A., MODERN OPTICAL TECHNIQUES IN FLUID MECHANICS, Annual Rev. Fluid Mech., Vol. 16, pp. 223, 1984

Law C.K., RECENT ADVANCES IN DROPLET VAPORISATION AND COMBUSTION, Prog. Energy Combust. Sci., Vol. 3, pp. 171-181, 1982

Lawes, M., EFFECTS OF TURBULENCE ON COMBUSTION IN ENGINES, PhD Thesis, University of Leeds, 1987.

Lawton B. & Klingenberg G., TRANSIENT TEMPERATURE IN ENGINEERING AND SCIENCE, Oxford University Press, 1996

Lefebvre A.H., ATOMIZATION AND SPRAYS, Hemisphere Publishing Corporation, 1989

Lefevre A.H., GAS TURBINE COMBUSTION, Hemisphere Publishing Corporation, 1983

Maxwell C., Coll. Sci. Paper, Cambridge, Vol. 11, pp. 625, 1890

Merdjani S. & Sheppard C.G.W., GASOLINE ENGINE CYCLE SIMULATION USING THE LEEDS TURBULENT BURNING VELOCITY CORRELATIONS, SAE Paper 932640, 1993.

Mizutani Y. & Nakajima A, COMBUSTION OF FUEL VAPOUR-DROP-AIR SYSTEMS: PART I, OPEN BURNER FLAMES, Combustion & Flame, Vol. 20, pp. 343-350, 1973a

Mizutani Y. & Nakajima A., COMBUSTION OF FUEL VAPOR-DROP-AIR SYSTEMS: PART II - SPHERICAL FLAMES IN A VESSEL, Combustion & Flame, Vol.20, pp. 351-357, 1973b

Mizutani Y. & Nishimoto T., TURBULENT FLAME VELOCITIES IN PREMIXED SPRAYS, PART I: EXPERIMENTAL STUDY, Combustion Science & Technology, Vol. 6, pp. 1-10, 1972

Mokhtar A.S., FUNDAMENTAL STUDY OF THE IGNITION AND COMBUSTION OF TWO-PHASE FLOWS AT GAS TURBINE CONDITIONS, PhD Thesis, School of Mech. Eng., University of Leeds, in preparation

Murphy M.J. & Borman G.L., OXIDES OF NITROGEN EMISSIONS FROM A BURNING FUEL MIST, Comb. Sci. & Tech., Vol. 21, pp. 53-63, 1979

Myers G.D. & Lefebvre A.H., FLAME PROPAGATION IN HETEROGENEOUS MIXTURES OF FUEL DROPS AND AIR, Combustion and Flame, Vol. 66, No.2, pp. 193-210, 1986

Nakabe K., Akamatsu F., Mizutani Y., Katsuki M. & Imoto T., GROUP COMBUSTION BEHAVIOUR OF LIQUID FUEL SPRAY UNDER THE INFLUENCE COHERENT LARGE EDDIES, ASME/JSME Thermal Engineering Conference, Vol. 3, pp. 149-156, 1995

Nakabe K., Mizutani Y., Akamatsu F., Fuchihata M. & ElEmam S.H., SPARK IGNITED SPHERICAL FLAMES PROPAGATING IN A SUSPENDED DROPLET CLOUD, 5th ICLASS-91, NIST Special Publications, 1991a

Nakabe K., Mizutani Y., Hirao T. & Fujioka H., AN EXPERIMENTAL STUDY ON DETAILED FLAME STRUCTURE OF LIQUID FUEL SPRAYS WITH AND WITHOUT GASEOUS FUEL, Combustion and Flame, Vol. 84, pp. 3-14, 1991b

Nakabe K., Mizutani Y., Hirao T. & Tanimura S., BURNING CHARACTERISTICS OF PREMIXED SPRAYS AND GAS-LIQUID COBURNING MIXTURES, Combustion and Flame, Vol.74, No.1, pp. 39-51, 1988

Polymeropoulos C.E. & Das S., THE EFFECT OF DROPLET SIZE ON THE BURNING VELOCITY OF KEROSENE-AIR SPRAYS, Combustion and Flame, Vol. 25, pp. 247-257, 1975

Polymeropoulos C.E., FLAME PROPAGATION IN AEROSOLS OF FUEL DROPLETS, FUEL VAPOR AND AIR, Combustion and Flame, Vol. 40, pp. 217-232, 1984

Polymeropoulos C.E., FLAME PROPAGATION IN LIQUID FUEL, FUEL VAPOR AND AIR MIXTURES, Chemical and Physical Processes in Combustion (Combustion Inst.), pp. 1-4, 1983

Richards G.A. & Lefebvre A.H., TURBULENT FLAME SPEEDS OF HYDROCARBON FUEL DROPLETS IN AIR; Combustion and Flame, Vol.78, No.3-4, pp.299-307, 1989

Ronney P.D., LASER VERSUS CONVENTIONAL IGNITION OF FLAMES, Optical Engineering, Vol. 33/2, pp.510-521, 1994

Shivashinsky G.I., DIFFUSIONAL-THERMAL THEORY OF CELLULAR FLAMES, Comb. Sci. & Tech., Vol.15, pp. 137-146, 1977

Silverman I., Greenberg J.B. & Tambour Y., STOICHIOMETRY AND POLYDISPERSE EFFECTS IN PREMIXED SPRAY FLAMES, Combustion and Flame, Vol. 93, pp. 97-118, 1993

Spalding D.B., THE COMBUSTION OF LIQUID FUELS, 4th Symposium (International) on Combustion, pp. 847-864, 1952,

Strehlow R.A., COMBUSTION FUNDAMENTALS, McGraw-Hill Book Company, 1985

Stroia B.J. & Abata D.L., FLAME SPEED OF LOW-CETANE FUEL IN A DIESEL ENGINE, Journal of Engineering for Gas Turbines and Power, Transactions of the ASME, Vol. 113, No. 3 , pp. 456-463, 1991

Su T.F., Chang C.T., Reitz R.D., Farrell P.V., Pierpont A.D. & Tow T.C., EFFECTS OF INJECTION PRESSURE AND NOZZLE GEOMETRY ON SPRAY SMD AND D.I. EMISSIONS, SAE-Paper 952360, 1995

Taylor A.M.K.P., OPTICALLY-BASED MEASUREMENT TECHNIQUES FOR DISPERSED TWO PHASE FLOW, Combusting flow diagnostics, Ed. D.F.G Durao, Kluwer Academic Publishers, 1992

Tian-Yu X., Zhao-Xiang H., Yi-Zhen W., SOME FACTORS AFFECTING ALTITUDE RELIGHTING PERFORMANCE OF TURBOJET ENGINE COMBUSTOR, ASME 81-JT-49, 1981

Tsushima S., Saitoh H., Akamatsu F. & Katsuki M., OBSERVATION OF COMBUSTION CHARACTERISTICS OF DROPLET CLUSTERS IN A PREMIXED-SPRAY FLAME BY SIMULTANEUOS MONITORING OF PLANAR SPRAY IMAGES AND LOCAL CHEMILUMINESCENCE, 27th Symposium (International) on Combustion, 1998

Van Wylen G.J. & Sonntag R.E., FUNDAMENTALS OF CLASSICAL THERMODYNAMICS, John Wiley & Sons Inc., 1985

Weinberg F., OPTICS OF FLAMES INCLUDING METHODS FOR THE STUDY OF REFRACTIVE INDEX FIELDS IN COMBUSTION AND AERODYNAMICS, Butterworths, 1963

Witchell G., THE IGNITION OF METHANE-AIR MIXTURES, PhD Thesis, University of Leeds Departments of Mechanical Engineering and Fuel and Combustion Science, 1973

Wilson C.T.R., Cambridge Phil. Soc., 1895

Wilson C.T.R., ON A METHOD OF MAKING VISIBLE THE PATHS OF IONISING PARTICLES THROUGH A GAS, Proc. Roy. Soc., London, A85, pp. 285-288, 1911

Wirth M., Keller P. & Peters N., A FLAMELET MODEL FOR PREMIXED TURBULENT COMBUSTION IN S.I. ENGINES, SAE paper 932646, 1993

Wolfhard H.G. & Parker W.G., Journal Inst. Petrol., Vol. 35, pp. 118, 1949

Woolley R., PERSONAL COMMUNICATIONS, 1999

Yaws C.L., HANDBOOK OF VAPOR PRESSURES, VOL. 3, Gulf Publications Co., 1994